



HAL
open science

Light interreflexions in ridged surfaces : influence of surface structure, material and lighting on color

Dorian Saint-Pierre

► **To cite this version:**

Dorian Saint-Pierre. Light interreflexions in ridged surfaces : influence of surface structure, material and lighting on color. Optics [physics.optics]. Université de Lyon, 2020. English. NNT : 2020LY-SES041 . tel-03215591

HAL Id: tel-03215591

<https://theses.hal.science/tel-03215591v1>

Submitted on 5 Oct 2023

HAL is a multi-disciplinary open access archive for the deposit and dissemination of scientific research documents, whether they are published or not. The documents may come from teaching and research institutions in France or abroad, or from public or private research centers.

L'archive ouverte pluridisciplinaire **HAL**, est destinée au dépôt et à la diffusion de documents scientifiques de niveau recherche, publiés ou non, émanant des établissements d'enseignement et de recherche français ou étrangers, des laboratoires publics ou privés.



Order number NNT: **2020LYSES041**

PhD Thesis, UNIVERSITY OF LYON
Completed at the
University Jean Monnet

Doctoral School N° 488
Sciences, Ingénierie, Santé

Publicly defended on 19/11/2020, by:
Dorian SAINT-PIERRE

Light interreflections in ridged surfaces: influence of surface structure, material and lighting on color.

In front of the jury composed of:

ZERRAD, Myriam	Research Engineer HDR, CNRS, Institut Fresnel	Reporter
MENEVEAUX, Daniel	Professor, Poitiers University	Reporter
ANDRAUD, Christine	Professor, Museum National d'Histoire Naturelle	Examiner
JACQUEMOUD, Stéphane	Professor, Paris University	Examiner
HÉBERT, Mathieu	Professor assistant HDR, Jean Monnet University	Director
SIMONOT, Lionel	Professor assistant HDR, Poitiers University	Co-director



N° d'ordre NNT : **2020LYSES041**

THESE de DOCTORAT DE L'UNIVERSITE DE LYON

Opérée au sein de
L'Université Jean Monnet

Ecole Doctorale N° 488
Sciences, Ingénierie, Santé

Soutenue publiquement le 19/11/2020, par :
Dorian SAINT-PIERRE

**Interréflexions lumineuses sur surface structurée :
influence de la structure de surface, du matériau et de
l'éclairage sur la couleur**

Devant le jury notamment composé de :

ZERRAD, Myriam	Ingénieure de Recherche HDR, CNRS, Institut Fresnel	Rapporteuse
MENEVEAUX, Daniel	Professeur, Université de Poitiers	Rapporteur
ANDRAUD, Christine	Professeure, Museum National d'Histoire Naturelle	Examinatrice
JACQUEMOUD, Stéphane	Professeur, Université de Paris	Examineur
HÉBERT, Mathieu	Maître de Conférences HDR, Université Jean Monnet	Directeur
SIMONOT, Lionel	Maître de Conférences HDR, Université de Poitiers	Co-directeur

This work has been founded by

Océ Print Logic Technologies and Canon

under the supervision of

**Maria Ortiz Segovia
Christophe Leynadier
Frans Gaykema**

with the support of **ANRT**

within the framework of the CIFRE program (Grant 2017/411)

and of **ANR**

(grant ANR-15-CE38-0005 “MATERIAL”)



A CANON COMPANY

Canon



Acknowledgements

My absolute gratefulness first goes to my supervisor Mathieu Hébert who made this project happen from the start. His guidance and benevolence throughout my student years, combined with his undying enthusiasm and his colorful sense of creativity, provided me with the best environment possible for this work at the Hubert Curien Laboratory. I extend this salutation to my co-supervisor, Lionel Simonot, who taught me more than I could have envisioned, with nothing but the highest precision and meticulousness that characterizes him.

My sincere gratitude to the members of the jury who accepted to dedicate their time to the task of reporting this thesis, Myriam Zerrad and Daniel Meneveaux. Many thanks to Christine Andraud and Stephane Jacquemoud who accepted with enthusiasm to be part of this final step as examiners. Special salutations to Christophe Leynadier and Maria Ortiz-Segovia for attending the defense after being my principal coaches for the industrial part of this project. I wouldn't have come this far if it wasn't for your guidance. I am also thankful for Frans Gaykema's presence, who made sure that I could bring this PhD to completion without any additional worries.

I want to thank all the people I had the immense pleasure to work with, or met at a conference, or shared a drink with, sometimes all three at the same time: Lou Gevaux, Raphael Clerc, Mehdi Daanoune, Nicolas Dalloz, Frédéric Jolivet, Fabien Momey, Anthony Berdeu, Théo Phan Van Song, Marine Page, Anthony Cazier, Caroline Ponte, Isabelle Verrier, Julien Eymard, Jean-Marie Campiglia and Cédric Valade. All of you made the PhD adventure worth living and helped me more than you could imagine. I also want to thank all the people of the MATERIALS project I had the pleasure to meet.

I want to have a small but meaningful thought for two very dear beings who departed for the longest journey this year: my grandmother and my cat. The loving memories I have from you will forever overcome the pain of your absence.

This penultimate paragraph goes to my friends and family, who made me into the person I am today. I am forever in your debt for the unconditional love, friendship and support you showed me way before the beginning of this PhD thesis. I'm sorry for not naming all of you, but I'm rather sure you will all recognize yourself in these few words.

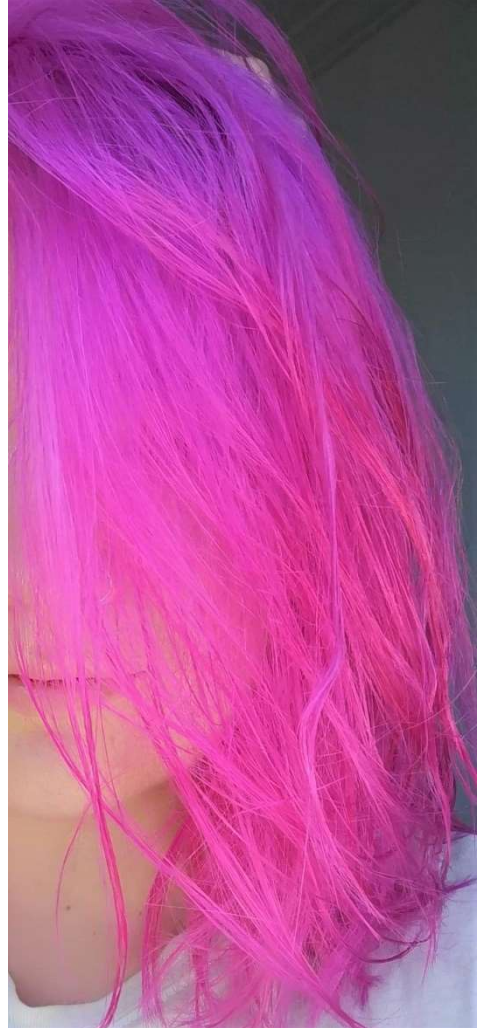
Finally, my most precious thoughts are addressed to Caroline. You entered my desaturated life without a warning and made sure I discovered a whole new world; with wonders one could only dream of after reading them in the rarest of books. Thank you for being always by my side, for being my best friend, my partner, and my soul mate.

Table of content

Abstract	15
Résumé	17
Chapter 1. Introduction	19
1.1 Why V-cavities?	22
1.2 Optical phenomena at play: light interreflections	23
1.3 What kind of material?	25
1.4 Structure of the manuscript	27
Chapter 2. Preliminary reminder in optics and colorimetry	29
2.1 Elements of radiometry	29
2.1.1 Geometrical concepts	30
2.1.2 Radiometric quantities	32
2.1.3 Lambert's law	33
2.2 Radiometric concepts for surfaces	33
2.2.1 BRDF	33
2.2.2 Reflectance	34
2.2.3 Reflectance factor	35
2.3 Measurement and representation of a reflectance	36
2.3.1 Spectrophotometer	36
2.3.2 Integrating sphere	37
2.3.3 Lambert transformation – Reflectance Maps	38
2.4 Radiometric properties of some special surfaces	39
2.4.1 Perfectly matte surfaces: Lambert's model	39
2.4.2 Reflection and transmission of light by smooth interfaces	39
2.4.3 Lambertian background with a flat interface	44
2.5 Basic notions of colorimetry	46
2.6 Conclusions	48

Chapter 3. Light interreflections in a Lambertian V-cavity	49
3.1 Introduction.....	49
3.2 General case.....	51
3.3 Special case of a V-cavity of infinite length.....	54
3.4 Illumination Geometries	57
3.4.1 <i>Light interreflections under a directional illumination.....</i>	<i>58</i>
3.4.2 <i>Light interreflections under a diffuse illumination.....</i>	<i>60</i>
3.5 Influence of the lighting geometry.....	61
3.5.1 <i>Mixing a frontal collimated lighting with a diffuse one.....</i>	<i>65</i>
3.6 Influence of the observation direction.....	68
3.7 Influence of the V-cavity's shape	71
3.8 Metamerism and interreflections.....	77
3.9 V-cavity with two different colors	79
3.10 Conclusions.....	81
Chapter 4. Light interreflections in a specular only V-cavity.....	83
4.1 Introduction.....	83
4.2 Multiple reflections process in a mirror-like V-cavity	86
4.3 Model for radiance attenuation in a specular V-cavity.....	89
4.4 Optical and color analysis of periodically grooved specular surfaces.....	91
4.4.1 <i>Directional-hemispherical reflectance.....</i>	<i>92</i>
4.4.2 <i>Hemispherical-directional reflectance.....</i>	<i>93</i>
4.4.3 <i>Bi-hemispherical reflectance.....</i>	<i>97</i>
4.5 Approximate models.....	99
4.5.1 <i>First approximate model: light remaining unpolarized.....</i>	<i>99</i>
4.5.2 <i>Second approximate model: separate polarization components</i>	<i>100</i>
4.5.3 <i>Comparison of the models.....</i>	<i>101</i>
4.6 Experimental verifications.....	104
4.7 Optical and colorimetric analysis of randomly grooved specular surfaces.....	107
4.7.1 <i>Bi-hemispherical reflectances.....</i>	<i>107</i>
4.7.2 <i>Conventional microfacets models for rough surfaces.....</i>	<i>109</i>
4.8 Conclusions.....	110

Chapter 5. Light interreflections in an interfaced Lambertian V-cavity	112
5.1 Introduction.....	112
5.2 Overview of the model.....	114
5.3 Components of the model	117
5.3.1 Irradiance of the Lambertian material: vector E'_{in}	117
5.3.2 Interreflections within the cavity: Matrix K'	118
5.3.3 Exiting rays: Matrix M'_{out}	120
5.3.4 Vector L_s	122
5.4 Simulations of V-cavities made with Lambertian material with an interface ...	123
5.5 Conclusions	125
Chapter 6. Conclusion.....	128
6.1 Most relevant parameters for interreflections	128
6.2 Experimental verification.....	130
6.3 Further developments.....	130
References	132



Example of light interreflections in hair dyed with a magenta coloration. Credits: Karolina Starzecka.

Abstract

The present manuscript explores an optical phenomenon that hasn't been extensively studied: light interreflections. It happens on every non-flat surface and more precisely, in their concavities either big or small, and affects their colored appearance. This effect comes from the fact that every illuminated point in a concavity will then re-illuminate the other points, after reflection of the light. This process of mutual illumination can indefinitely happen if the surface is scattering. It is now established that accounting for many successive reflections in the case of matte and light surfaces is crucial, at the risk of creating high discrepancies when simulating the colored appearance otherwise. Thankfully, proposals of models allowing for the rigorous and exhaustive description of these multiple reflections with equations have been published, and their more recent versions offer an almost analytical resolution. On the downside, these models are only valid for perfectly matte surfaces, i.e. Lambertian, which corresponds to a very limited part of real structured surfaces.

Beyond the possible approaches to deal with this subject, we selected physical modeling based on optical equations, despite its limitation to ideal structured surfaces. The chosen topology is a periodically ridged surface, with infinitely long V-cavities, identical and parallel. The material is opaque, each cavity reflects light independently of the others, which allows for the study of one ridge to be enough to describe the whole surface behavior. The panels of the cavity can have different optical properties, each being the object of a dedicated chapter:

- Strongly scattering surfaces and perfectly matte, called Lambertian surfaces. The model allows for the simulation of the perceived radiance and the color as a function of the dihedral angle of the V-cavity, the spectral absorbance of the material, the lighting geometry (frontal, oblique or diffuse), and the observation direction. The model rigorously accounts for the fact that some parts of the cavity are not necessarily visible nor receive light, which depends on both the point of view and the lighting configuration. It can quantify the color difference obtained when structuring two materials being metamers when flat.
- Mirror-like surfaces, such as metallic ones. Our model fully embraces the starting point of an ideal surface: in a precise photometric approach, it can describe all the trajectories of light rays entering the V-cavity without any trade-off on the shadowing and masking modeling. We study the evolution of the surface color under a perfectly diffuse lighting, as a function of the cavities dihedral angle, of the spectral optical index of the materials and

of the observation direction. We put the emphasis on the evolution of the light polarization through the multiple reflections, given it is unpolarized when entering the structure. Experimental measures on metallic V-cavities allowed us to confirm the validity of the model, despite the difficulties encountered during the set-up.

- Scattering surfaces possessing a smooth interface with air also called “interface Lambertian surface”. The model is limited to a single case study of lighting and observation geometry, yielding no shadowing nor masking. It is similar to a combination of the two previous models, considering the light goes through an interface each time it enters or exits the material, and can undergo multiple reflections in the process. These reflections can happen in the air (specular reflections between the panels interfaces) or on the side of the material (scattering between the interface and the matter itself).

Numerous figures are gathered in a portfolio and allow for the visualization of the effects we want to highlight.

Because it is based on ideal structures, the models do not permit the precise prediction of the change in color induced by a complex change of the topology. Nevertheless, they form a useful toolbox to get an idea of the different parameters influencing color, which evolution to expect and to what extent their influence is significative in order to explain the physical reasons behind these changes. The described evolutions can be generalized to more complex structures than the one we effectively studied.

Résumé

Le présent mémoire explore un phénomène optique relativement peu étudié, qui se produit sur les surfaces non-planes, plus précisément dans leurs concavités petites ou grandes, et qui affecte de manière sensible leur apparence colorée : les interréflexions lumineuses. Ce phénomène provient du fait que chaque point éclairé dans une concavité de la surface rééclaire à son tour, après avoir réfléchi la lumière, les autres points de la cavité. Ce processus d'éclairage mutuel des différents points de la cavité peut se produire indéfiniment si la surface est diffusante, et il est maintenant établi qu'il est crucial de prendre en compte un très grand nombre de réflexions successives dans le cas des surfaces mates et claires, sans quoi l'erreur commise dans la simulation de leur apparence colorée peut s'avérer très grande. Heureusement, des modèles permettant de décrire ces réflexions multiples par des équations de manière rigoureuse et exhaustive ont été proposés dans le passé, et leurs dernières versions offrent une résolution quasi-analytique. Malheureusement, ces modèles ne sont valables que lorsque les surfaces sont parfaitement mates, c'est-à-dire lambertiennes, ce qui ne correspond qu'à une frange limitée des surfaces texturées de la vie quotidienne.

Parmi les multiples méthodes possibles pour aborder ce sujet, nous avons privilégié la modélisation physique basée sur les équations optiques, malgré sa limitation à des structures simples et idéales. Le type de structure choisi est une surface striée périodique, formée de cavités en V infiniment longues, identiques et parallèles. La matière est opaque, chaque cavité réfléchit la lumière indépendamment des autres, de sorte que l'étude de la réflexion lumineuse par une cavité suffit pour décrire la réflexion lumineuse par toute la surface striée. Les panneaux latéraux de ces cavités peuvent présenter des propriétés optiques diverses. Trois types ont été étudiés, chacun faisant l'objet d'un chapitre dédié :

- Les surfaces très diffusantes et parfaitement mates, dites lambertiennes. Le modèle permet de simuler la luminance perçue, ou la couleur, en fonction de divers paramètres tels que l'angle dièdre de la cavité en V, l'absorbance (spectrale) de la matière, les conditions d'éclairage (collimaté frontal, collimaté oblique, ou parfaitement diffus) ou l'angle d'observation. Le modèle permet de prendre en compte rigoureusement le fait que certaines parties de la cavité peuvent ne pas être éclairées selon l'angle d'éclairage, ou ne pas être vues selon l'angle d'observation. Il permet aussi de quantifier l'écart de couleur qu'on obtient en texturant une surface faite de deux matériaux lorsque ceux-ci sont métamères s'ils forment des surfaces planes.
- Les surfaces à panneaux parfaitement spéculaires, notamment métalliques. Notre modèle tire tout l'avantage de partir d'une surface idéale : il peut décrire de manière

photométriquement rigoureuse la trajectoire des tous les rayons entrant dans la cavité et donc traiter sans approximation les phénomènes d'ombrage et de masquage. Nous cherchons à voir l'évolution de la couleur de la surface sous un éclairage parfaitement diffus en fonction de l'angle dièdre des cavités, de l'indice spectral du matériau, ou de l'angle d'observation. Nous étudions particulièrement la manière dont la polarisation de la lumière, non polarisée lorsqu'elle entre dans la cavité, évolue au cours des réflexions successives. Des mesures expérimentales portant sur des cavités métalliques ont permis de confirmer la validité du modèle, malgré leur difficulté de mise en œuvre.

- Les surfaces diffusantes ayant une interface lisse avec l'air, dites "surfaces lambertiennes interfacées". Le modèle correspondant se limite à une seule configuration d'éclairage et d'observation, où les problèmes d'ombrage et de masquage ne se posent pas. Il s'apparente à une combinaison des deux modèles mentionnés ci-dessus, prenant en compte le fait que la lumière franchit une interface chaque fois qu'elle entre ou sort de la matière, et qu'elle peut subir des réflexions multiples aussi bien côté air (des réflexions spéculaires entre les interfaces planes des deux panneaux de la cavité) que côté matière (des réflexions diffuses entre l'interface et la matière elle-même).

De nombreuses figures rassemblées dans un portfolio permettent de visualiser les effets que nous souhaitons mettre en valeur.

Parce que basés sur des surfaces idéales, les modèles ne permettent pas encore de prédire précisément les changements de couleur induits par un changement trop complexe de topologie de surface. Néanmoins, ils forment une boîte à outil très utile pour se faire une idée des paramètres influant sur la couleur, à quelle évolution de couleur s'attendre, dans quelle mesure leur influence est significative, et de savoir expliquer les raisons physiques de ces évolutions. Les évolutions décrites peuvent, elles, se généraliser à des structures surfaces plus complexes que celles que nous effectivement étudiées.

Chapter 1.

Introduction

The sensations produced by the human visual system during its perception process of objects result from an interpretation of the light signal captured by the eyes: the light signal issued from the object itself, and the one issued from its surrounding. The interpretation is based on an empirical understanding, acquired unconsciously during life, of the strong correlation between the object's appearance and the light-matter interaction that is at the origin of the light signal captured. More conscious is the correlation between appearance and material: the work of artists and craftsmen is mostly based on the experience of this correlation. But the crucial role played by light in it remains mostly confidential, accessible to a few scientific experts, and its study is quite young – barely more than a century – in comparison to Art History, which coincides with Human History.

The light-matter interaction which underlies the appearance of objects is a combination, often too complex to be comprehensively described at the thinnest scale, of optical phenomena such as absorption, reflection, refraction, scattering, diffraction, interferences, etc. Selective absorption according to wavelength of light is probably the best-known optical phenomenon for its correlation with *color*, one of the main visual attributes for objects. It is also known that light scattering into the material also plays a role on the color rendering of the object, as well as on its *translucency*, another visual attribute, whereas light scattering by the object's surface rather influences the *gloss*. Light scattering by materials and surfaces is still an active subject of research today, aiming at predicting as precisely as possible object appearances for a wide range of materials, structures and lighting conditions. Citing only research works carried out in France recently in this domain, the PhD dissertation by Colette Turbil [1] has tackled the problem of accurately modelling the diffusion of light by rough surfaces, using real samples and comparing different approaches based on physical and geometrical optics to predict their appearance. She showed that the widely used microfacet models fall short of faithfully predicting their visual aspect. The work by Simon Desage [2] in computer vision highlights the importance of visual patterns and characteristic visual criteria for the recognition of objects, combining a classic pattern identification with the visual sensation. Marine Page [3] worked extensively in the field of relief printing, modulating the roughness of a surface by printing translucent varnish micro-pillars as a way of controlling the glossy or matte appearance of printed samples, and were applied cultural heritage preservation. The research conducted by Theo Phan Van Song [4] used a four-

flux approach to better predict the appearance of stack of multiple inks layers by modeling the numerous light-ink interactions. All these works have in common the scattering of light by thin microstructures of the material, and its role in the appearance of the various surfaces that we can encounter every day, working as a link between their topology and their visual aspect.

Much less studied in the scientific literature is the strong influence that the shape of the object may have on its appearance, not only because of the specific cues it offers to the perceptual process of the human visual system, but also because the object's shape allows for specific light paths that a flat object made of the same material would not allow. This influence of shape on appearance is illustrated through a couple of art pieces of tableware shown in Figure 1. The variable thickness of glass in the vase by Lalique produces different green shades, due to the different light path lengths across the material, as well as dark areas because of the absence of light refracted by the object towards the observer in these areas. The interior of the goblet in sterling silver by Chris Knight, coated with a thin layer of gold (parcel-gild technique), exhibits a color gradient due to the mutual reflections of the different parcels of the surface: the deeper points of the goblet look brighter than the ones near the external edge. The influence of the shape of an object on its appearance will be main subject of the present work, by considering opaque materials. In particular, we are interested in see to which extent the shape of the object has an impact on its spectral reflectance, thereby on its color (independently of perceptual considerations). For example, the optical mechanisms explaining the color gradient observed in the metallic goblet will be addressed, whereas the color variation observed on the glass vase are out of our scope, the material being transparent.

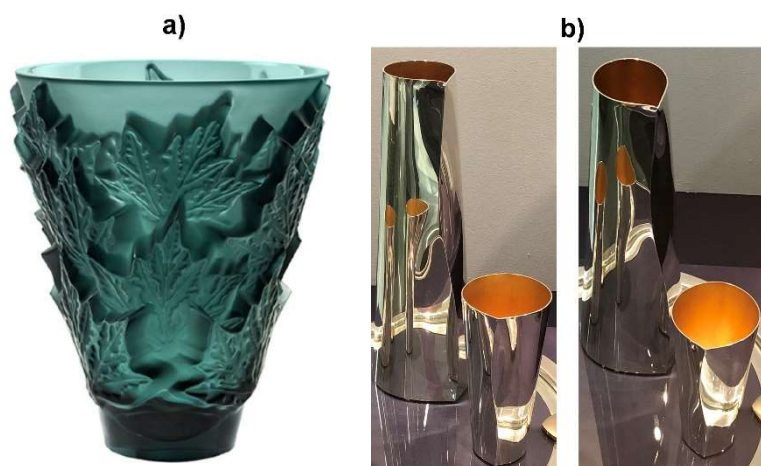


Figure 1 - Example of objects in which the macroscopic shape have a strong influence on appearance. a) Vase "Champs-Elysée" by Lalique, 1951. b) Pitcher and goblet by Chris Knight, 1993, under two points of view.

If the appearance of art objects such as the ones previously shown is fully mastered and controlled by the know-how of the craftsmen, it is not the case of object generated by automated processes like 3D printing systems. Instead of a try-error or experience-based

Introduction

work of the matter until the expected appearance is reached, the automated system converts the digital file – visible only through a more or less realistic preview on a computer screen – thanks to a digital driver of the machine. The obtained appearance is consistent with the expected one only if all optical phenomena underlying it have been anticipated, i.e., if the driver relies on an appropriate optical model. 3D printing has therefore a crucial need in terms of management of color and other appearance attributes. It is necessary to quantify these attributes, to model their correlation with the optical signal received by an observer, being either a sensor or the human eye, and to better predict this optical signal according to the material considered, its geometrical configuration, and the lighting used. Since 3D printing mainly uses colored polymers with smooth surface (at least at the microscopic scale, i.e., at the scale of one ink drop or thread), our final goal was to be able to address the case of opaque materials with a refractive index close to 1.5 and a flat interface with air.

To apprehend these points, two approaches are possible. The first approach is the *empirical one*. It consists in the production of a large number of samples while varying multiple manufacturing parameters, then the measurement of their optical responses with appropriate tools, an interpolating of the collected data, and finally the derivation of a law linking the surface structure parameters to their optical response. The second approach is the *theoretical one*. It relies on a model describing the optical response of the material according to the manufacturing parameters, by starting with simple configurations (lighting, material, object shape...) and extending the model in order to cope with more and more complex configurations until the response of the considered object in its surrounding can be comprehensively described.

The empirical approach has the advantage of being physically based with absolute correctness, provided the measurements are representative of what an observer can see in another context. Gathering measurements and data ensure the robustness of the process linking the samples to the desired appearance and gives a roadmap of how to obtain a certain type of visual aspect by modulating a set of parameters. The main drawback to this method is that it can require many samples in order to accurately quantify the extent of the different parameters influence. Another drawback is that the deduced law for appearance prediction is not necessarily transposable to different materials in different scenes. One example is commonly used in printing, where in order to calibrate the offset printers and be sure to print the exact same colors on every sample, a large set of color patches is printed, the patches are measure one by one, and a look up table containing all printable colors is created by interpolation of the measured colors. This can be really time consuming and is often device dependent.

The theoretical approach has the advantage of trying to find a general model allowing the prediction of a material appearance in any case. It can even allow to find an analytical formulation for the optical response of an object surface, and then be easily programmed to simulate the desired result. The main drawback is that this approach often considers ideal cases that are not often met in the real life.

In this work, we decided to adopt the theoretical approach, being aware that this orientation is opposed to the one mainly used today, i.e., the empirical approach based on neural networks which is often so efficient but so greedy in measured data. We are convinced that understanding deeply the optical phenomena underlying the appearance of structured materials have some interest today and can be useful in the long term, at least by focusing people's attention on visual effects that are rarely addressed and probably not often anticipated in object's design renderers. It is also of interest of understanding how the optical response of the object varies according to the optical properties of materials (e.g., absorbance), the nature of the material (metal, diffusing matter...), the shape of the surface, and the lighting.

The problematic is therefore to determine the influence of the surface structure of a material onto its optical response and the color sensation produced, with a comprehensive consideration of the lighting and observation geometry.

The chosen surface structure for this study is restricted to one particular shape: V-shaped ridges, infinitely long, with planar sides. An illustration of such a surface is visible in Figure 2. This structure enables to study optical effects such as anisotropy, shadowing and masking, and of course light interreflections.

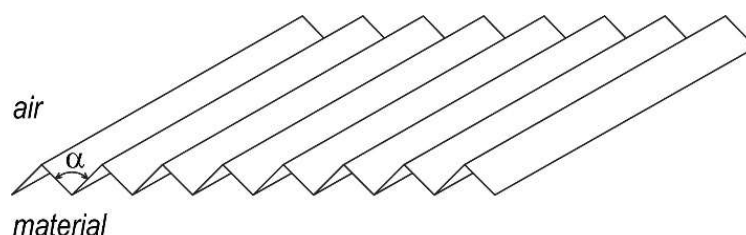


Figure 2 - Structured surface with parallel, periodical, and identical V-shaped ridges of dihedral angle α .

1.1 Why V-cavities?

We justify the choice of this structure by the fact that the optical phenomena which occur in it, especially the light interreflections, are also present in more complex structures that we will not discuss in the manuscript, such as massive materials with rough surfaces, woven fabrics, etc. It is certain that the interreflections play a role, probably an important one, in the way these complex surfaces reflect light, and in their color appearance in various observation and light scenarios. By studying the interreflection phenomenon in the specific case of V-ridged surfaces, we do not claim addressing all surface structures, but at least we think that the influence of the different structural (dihedral angle of the cavity), optical (absorbance, refractive index of the material), or environmental (geometry of lighting and observation) parameters should be rather similar.

Introduction

This type of surface also has an interest since it is derived from the usual way of simulating a rough surface. The microfacet model approach developed first by Torrance & Sparrow [5], and then mostly by Cook & Torrance [6], is used in computer graphics and considers a surface made of small planar facets acting as mirrors. Their orientation follows a random distribution producing the studied optical response of the surface at the macroscopic scale. The facets are facing each other, creating concavities and reliefs, for example V-cavities (symmetrical or not) and often have the same elevation. Colette Turbil [1] showed that the microfacet model is far from the reality of rough surfaces, and that the simulated optical response is not coherent with what measurements show. Nevertheless, this approach is still widely in use today, and is therefore justified for our case study.

This choice is also motivated by the simplicity of the V-cavities geometry, which facilitates the development of a thorough optical model as a solid base for the precise study of phenomena such as light interreflections and shadowing. It is also a model being independent of the scale, whether the V-ridged sample is made with a folded paper sheet, a metallic roof, or a ridged surface at the microscopic scale. This consideration is valid if the scale is not below the μm , under which wave optics phenomena such as diffraction would become significant, whereas the present work relies on geometrical optics.

The whole work presented in this manuscript relies on the assumption of opaque materials. Thus, no light can transit from one V-cavity to a neighboring one. Corollary, we can focus the study on one V-cavity only and assume that every other V-cavity being identical to the one considered has the same optical response. The overall behavior of the surface is therefore an average made on all the parallel and periodical ridges.

For less periodical and less perfect structures, the optical phenomena would mostly be the same, with only a change in their respective contribution to the light scattering operated by the whole surface. We will not discuss these cases because of a lack of time, but the mechanisms that will be presented later have the credit of constituting a strong case study for optical effects happening in every kind of structured surface.

1.2 Optical phenomena at play: light interreflections

Light interreflections is a phenomenon happening everywhere a concavity in a surface is illuminated. They enhance the perceived lightness and tend to saturate the initial color when the light is collimated and directional, even more so if it is frontal, or on the contrary tend to darken the overall aspect when the light source is diffuse. Both cases are respectively illustrated in Figure 3 and Figure 4.

This phenomenon has gained a lot of attention in computer graphics in order to improve the rendering quality of scenes where various objects exchange light between each other (typically a colored object close to a white wall) [7, 8, 9]. It has also been studied in the domain of computer vision, in order to remove this effect from images of an

object in order to retrieve the object's 3D shape (shape-from-shading methods) [10-15] or its spectral reflectance as well as the illuminant spectral power distribution [16, 17].

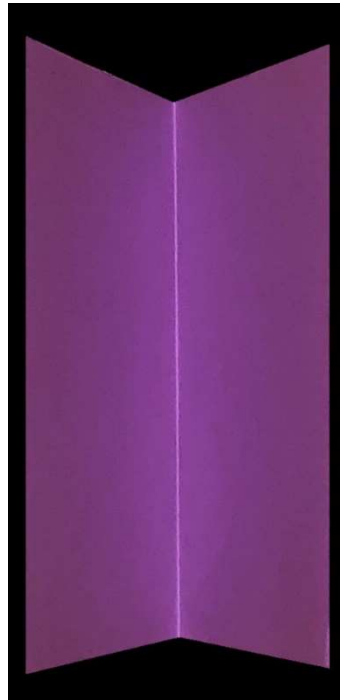


Figure 3 - Cavity made of two diffusive and planar adjacent panels, under a frontal collimated lighting.

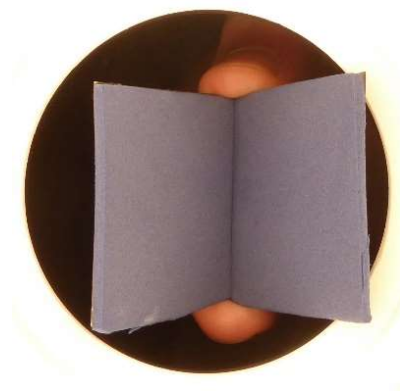


Figure 4 - V-cavity with an angle of 45° between the two panels made of a gray Lambertian material, illuminated by perfectly diffused light in an integrating sphere.

In most previous studies, interreflections are modeled by considering only two or three reflections of the light, especially for computation efficiency when working with ray tracing. Recent work by Rada Deeb [18] showed that in the case of Lambertian surfaces with high reflectance, at least in a given part of the visible spectrum, it is necessary to take into account all successive reflections until infinity in order to obtain an accurate prediction of the radiances displayed by the object. This is a problem that a discrete

Introduction

version of the interreflection equation, or radiosity equation by Koenderink [19] can tackle. This was the starting point of our work.

The main question resulting from this observation is to know to which extent interreflections, which increase the perceived radiance in the concavities of the surface, compensates shadowing, which decreases the irradiance, according to the shape of the surface, its reflectance, the illumination and observation geometries.

1.3 What kind of material?

Historically, Lambertian surfaces are a well-used starting point when it comes to model matte rough diffusive surfaces [20]. Therefore, assuming a Lambertian surface in order to build an interreflection model is an approach that we used for the prediction and analysis of a material's appearance. The prediction model relies on the radiosity equation also called the interreflection equation [19], which stands only for Lambertian surfaces. It is therefore natural to start our study with this kind of surface, even though it is rarely met in the everyday life. Some very matte papers, like colored paper sheets produced by Munsell, can be assumed Lambertian surfaces except at grazing angles. The surfaces shown in Figures 3 and 4 have these properties. At a different scale, powdery snow can also be assumed Lambertian.

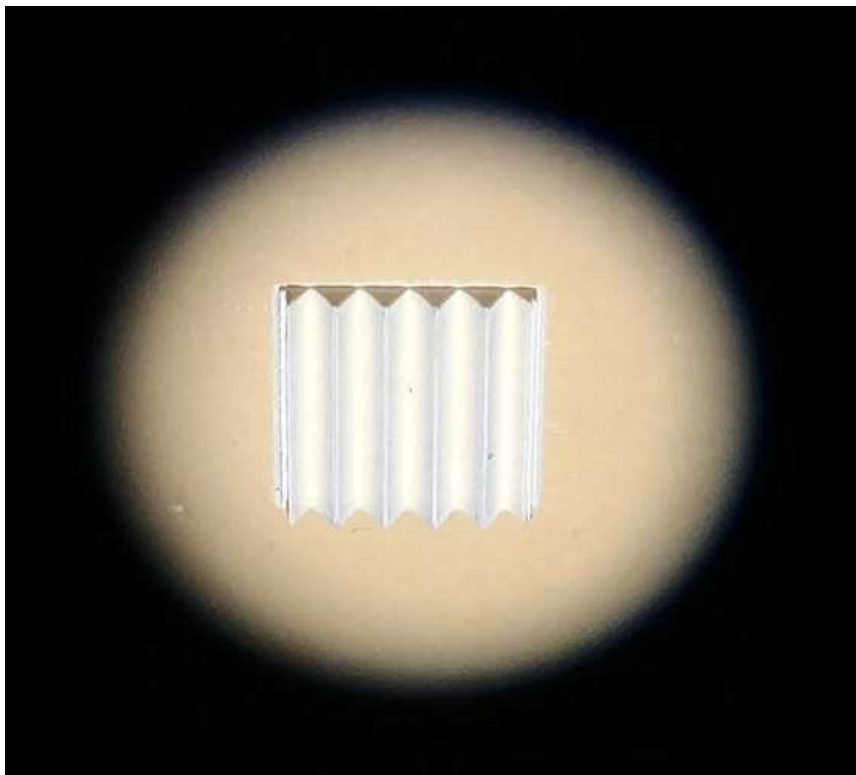


Figure 5 - 2.5D printed sample with white ink, under frontal lighting, forming a 45° V-shaped ridged surface pattern. The sample is 1 × 1 cm, 2.4 mm height with a 2 mm period.

However, as aforementioned, the type of materials that we want to address with our work is typically the one that can be found in 2.5D printing, i.e., samples produced with stacks of solidified inks creating a relief. When the relief is mainly created by white ink before application of the colored inks, the surface is rather opaque and enters the scope of our study. Figure 5 shows a V-ridged surface printed in relief with white ink only.

Even though the white ink is strongly scattering, the surface cannot be considered as Lambertian because of the air-ink interface and the Fresnel reflections and transmissions that it provokes. Therefore, before addressing the case of such "interfaced Lambertian" surfaces, we focused our attention to the light interreflections occurring in a cavity where only the air-matter interface is involved, namely into cavity whose panels are mirrors. This intermediate case of mirror cavities is particularly interesting on an optical point of view: as far as we could see, no previous work described comprehensively the different successive reflections taking place into the cavity according to the orientation and position of the incident ray. The evolution of the polarization state of the ray along its path within of the cavity was also an open question, to which we decided to answer. In the specific case where the material is a colored metal, such as gold or copper, and to a lower extent silver, the study is also interesting on a colorimetric point of view: we can clearly see an evolution of the color of the surface according to the depth of the cavities, or their dihedral angle. A deeper structure yields a more saturated color than the one displayed by a flat mirror – a phenomenon that we can easily observe in the goblet shown in Fig. 1-1. The model that we will present later in this manuscript is far different from the radiosity model applicable to Lambertian surfaces, but as this latter model, it relies on analytical equations.

Coming back to the interfaced Lambertian surfaces that are the final target of our study, the approach that we adopted is an extension of the radiosity model in order to take into account the Fresnel reflections and transmissions of light at the interfaces. Like in the radiosity model, we describe the light transfers between every pair of parcels of the cavity, these parcels being located at the surface of the strongly scattering material, just beneath the interface. We incorporate into the model the different specular reflections that can occur in the cavity (i.e., in air), before the light enters the material and after it exits it, as well as the multiple internal reflections taking place within the material between the material itself and its interface, whose importance has been put into evidence for a long time in the context of flat surfaces [21-24]. The model for interfaced Lambertian materials can therefore be a combination of the models for Lambertian cavities and mirror-like cavities. Even though its complexity is substantially increased in comparison to the radiosity model for Lambertian surfaces, we still have an analytical model. For lack of time, we could address only one special illumination and observation geometry for one colored material, but this already enables drawing some comparison between the reflectances and colors of Lambertian and interfaced-Lambertian V-ridged surfaces.

All the models that will be presented are used to produce simulations obtained thanks to MATLAB© programming.

1.4 Structure of the manuscript

Chapter 2 will go over the basis concept useful to build our study. Chapter 3 will present the first model for Lambertian materials that are ridged with infinitely long V-cavities. Chapter 4 will continue the presentation with another light interreflection model, this time for V-cavities with mirror like panels. Finally, the Chapter 5 will tackle the purpose of this work and will try to finish the answer to the proposed problematic by developing a model of Lambertian V-cavities with their interface with air, before we draw our conclusions in Chapter 6.

Chapter 2.

Preliminary reminder in optics and colorimetry

The work presented in this manuscript is mostly based on two sciences: radiometry and color science. Radiometry helps to quantify the amount of light transferring from the light source to the observer after interaction with objects. The geometric and energetic notions are reminded here, as well as the quantities relative to surfaces and the properties of certain types of ideal surfaces. In order to investigate the predictions of the material appearance by the models we offer to present after, we need to visualize the results under different aspects. One of them is the influence of the structured surface on the perceived color. Therefore, after the sections on radiometric quantities, a paragraph will introduce a few notions of color science.

2.1 Elements of radiometry

Radiometry is the science of measuring radiations. It consists in the analysis of radiation emissions by sources, and their detection, reflection and transmission through various entities such as material surfaces, optical systems, etc. It is different from the field of classical optics because it is focused on the measurement of energy without considering the type of material encountered. Therefore, we prefer to think in terms of absolute power, and express the quantities studied in energy units. But one fact remains adamant: it is important to precisely know the properties of the light to perform accurate measurements, even if in most cases, radiometry considers incoherent radiations included in the scope of geometrical optics.

In color reproduction, and more specifically in the case of this work focused on the prediction of materials appearance, the most interesting part of the electromagnetic spectrum is comprised between the wavelengths 380 nm and 780 nm. This domain corresponds to the visible light for the human eye, and the science that studies it is called *photometry*. In this field, the radiant power at each wavelength is weighted by a visual sensitivity function modeling the human eye sensitivity. As a result, the measured

quantities are expressed in *luminous units* such as *lumen*, *candela* (one of the seven base units of the International System of Units), and *lux*.

The interest of radiometry for material appearance resides in the possibility of modeling and measuring the amount of light being in interaction with an object of interest. Thanks to radiometric quantities, the description of the light distribution in space can be done, from a light source, through or reflected on an object, and ending on a detector. The properties of an object such as reflection or transmission can be derived from ratios of these quantities. In the following sections a presentation of the radiometric quantities useful to our work on material appearance is made.

When describing the trajectory of the light, from its source to an observer through an object of interest, we can start by defining two points P_1 and P_2 in space, through which a ray of light passes. The model of the light ray is acceptable to assess all the light passing through the two points but isn't enough anymore when it comes to the description of the spatial repartition of the light in space. So instead, considering a small area around each point, and therefore considering a small number of directions, is more convenient.

2.1.1 Geometrical concepts

Solid angle

The first concept used in radiometry to describe the spatial repartition of a light beam is called a *solid angle*, and its unit is the *steradian* (sr). It is defined for a point from which a set of directions are exiting towards a surface.

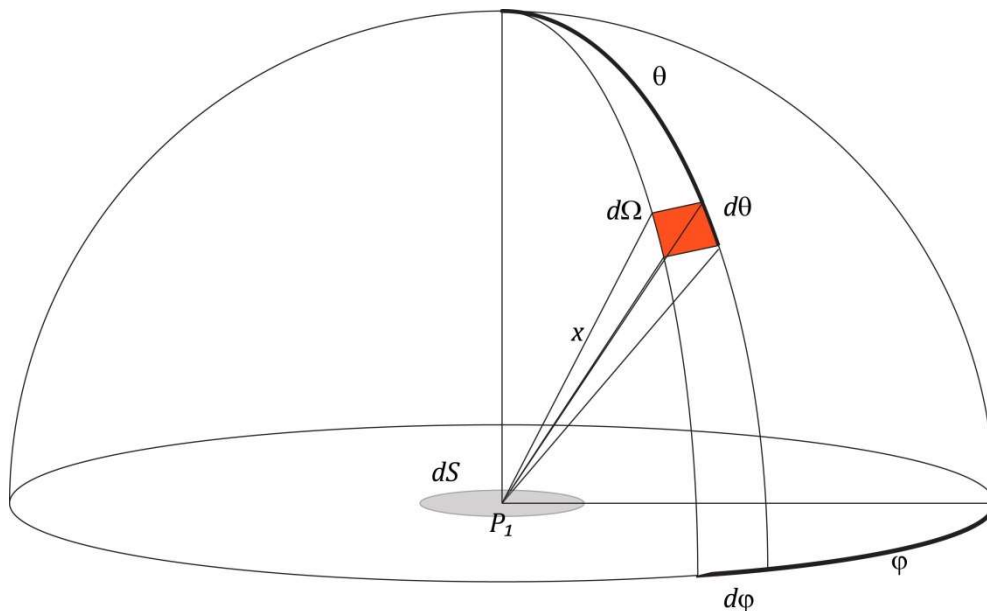


Figure 6 - Differential solid angle in the direction (θ, φ) .

To formalize this concept, a common practice is to specify an infinitesimal solid angle $d\Omega$ thanks to a given point P_1 on an infinitesimal surface dS pointing towards a direction

Preliminary reminder in optics and colorimetry

specified by its spherical coordinates. The polar and azimuth angles (θ, φ) are defined within the coordinate system taking its origin in P_1 . On Figure 6 it is shown that the small set of directions on the described configurations intercepts an area $x^2 \sin\theta d\theta d\varphi$ on the sphere of radius x . The infinitesimal solid angle is therefore:

$$d^2\Omega = \sin\theta d\theta d\varphi \tag{2.1}$$

Geometrical extent

In this paragraph, we describe this time a light beam propagating from one elemental surface to another. The geometry of such a light pencil is called the *geometrical extent*. We consider the light propagating between two small surface elements dS_1 and dS_2 to which belong the two points P_1 and P_2 . As shown on Figure 7, if we assume the distance x between the two areas to be finished, we can assume that the rays received by dS_2 come from the point P_1 , and reciprocally for the rays going from P_2 to the elementary surface dS_1 .

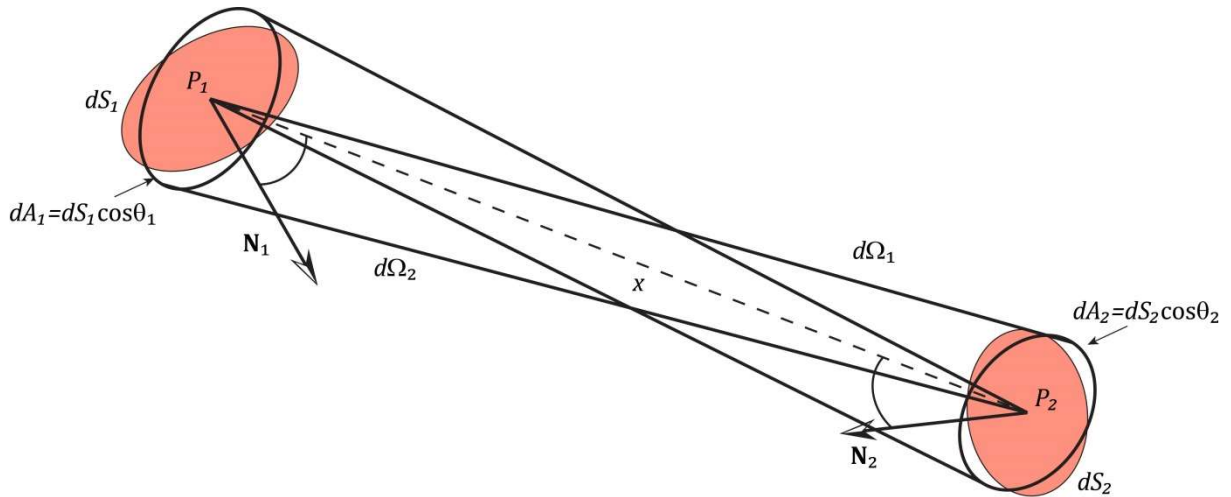


Figure 7 - Geometrical extent between two elementary areas dS_1 and dS_2 .

From this consideration we deduct that the solid angle $d\Omega_1$ defined by the point P_1 and the elementary area dS_2 intersects an area dA_2 , which is tangent in P_2 to the sphere of radius x centered in P_1 . dA_2 is called the *apparent surface*. Since the considered surfaces are infinitesimal, the apparent surface and the surface on the sphere coincide. Therefore:

$$d\Omega_1 = \frac{dA_2}{x^2} = \frac{dS_2 \cos\theta_2}{x^2} \tag{2.2}$$

The elementary geometrical extent d^2G of the light pencil, presented in Figure 7, is:

$$d^2G = dA_1 d\Omega_1 = dA_2 d\Omega_2 = \frac{1}{x^2} (dS_1 \cos\theta_1) (dS_2 \cos\theta_2) \quad (2.3)$$

2.1.2 Radiometric quantities

Using the previously defined geometrical concepts, we will now present the definitions of some radiometric quantities.

In radiometry, the *flux*, or *radiant flux*, is the energy radiated per unit of time. It is expressed in watts (W) and will be denoted F throughout this manuscript.

The *Irradiance* E is the density of flux per unit of area, which is incident on a given point belonging to a specific area. It is expressed in $\text{W}\cdot\text{m}^{-2}$, and if we consider a flux dF relatively to a surface dS , the corresponding irradiance is:

$$E = \frac{dF}{dS} \quad (2.4)$$

When light is emitted from the surface instead, the concept equivalent to irradiance is the *exitance*, usually denoted M .

The *radiance* L is the flux per unit of geometric extent it arrives through. It is attached to a specific point on a surface and follows a particular direction. Therefore, its unit is $\text{W}\cdot\text{m}^{-2}\cdot\text{sr}^{-1}$ and it can be defined as:

$$L = \frac{d^2F}{d^2G} \quad (2.5)$$

From the radiance and its link with the geometrical extent, we can deduce the principle of *radiance invariance*. Indeed, if we consider two elemental surfaces and the small light pencil propagating between them, with the assumption of not encountering any absorbing or diffusing element, we can be sure that the radiance emitted by one is equal to the radiance received by the other. The elemental geometrical extent d^2G is derived from an elemental surface dS viewed from another surface, with an angle θ in the relation to the surface's normal, and under the solid angle $d\Omega$. We can say that the elemental geometrical extent is $d^2G = dS \cos\theta d\Omega$. Therefore we can transform Eq. (2.5) as:

$$L(\theta, \varphi) = \frac{d^2F}{dS \cos\theta d\Omega} \quad (2.6)$$

The term d^2F/dS corresponds to the elemental irradiance. The relationship between this irradiance and the radiance is then:

$$dE(\theta, \varphi) = L(\theta, \varphi) \cos\theta d\Omega \quad (2.7)$$

2.1.3 Lambert's law

In this manuscript, an extensive use of the concept of diffuse light is made. To describe diffuse light in radiometry, the *Lambert's law* is of importance. It states that a perfectly diffusing surface displays the same radiance in every direction over the hemisphere centered in a point belonging to the surface. We then speak about a *Lambertian surface* or *Lambertian reflector*. Following the idea of Eq. (2.7), the elemental exitance from the surface towards a given direction (θ, φ) in a coordinate system defined according to the surface normal, is:

$$dM(\theta, \varphi) = L \cos\theta d\Omega \quad (2.8)$$

with the radiance L being a constant in this case. It also means that by summing every elemental exitance over the hemisphere, the relationship between the exitance and the radiance as a result is:

$$M = \int_{\varphi=0}^{2\pi} \int_{\theta=0}^{\pi/2} L \cos\theta \sin\theta d\theta d\varphi = \pi L \quad (2.9)$$

2.2 Radiometric concepts for surfaces

To help characterizing a surface's optical properties, especially under a diffuse illumination, we need to introduce some additional concepts.

2.2.1 BRDF

The *Bidirectional Reflectance Distribution Function*, or BRDF, is according to Nicodemus [25] the description of the light reflection process by a surface. It is denoted f_R and links the elemental irradiance dE_i coming from each direction (θ_i, φ_i) in relation to the surface's normal, and the reflected radiance dL_r into each direction (θ_r, φ_r) :

$$dL_r(\theta_r, \varphi_r) = f_R(\theta_i, \varphi_i; \theta_r, \varphi_r) dE_i(\theta_i, \varphi_i) \quad (2.10)$$

It is expressed in sr^{-1} and can also be defined in terms of incident radiance $L_i(\theta_i, \varphi_i)$:

$$dL_r(\theta_r, \varphi_r) = f_R(\theta_i, \varphi_i; \theta_r, \varphi_r) L_i(\theta_i, \varphi_i) \cos\theta_i d\Omega_i \quad (2.11)$$

One could consider for example a nonabsorbing Lambertian reflector, the total exitance M_r is equal to the incident irradiance. Since the reflected radiance is M_r/π in every direction, the BRDF is therefore equal to $1/\pi$.

2.2.2 Reflectance

Reflectance denotes a ratio of fluxes: it is computed by dividing the reflected flux by the incident flux. When these two are relative to the same surface element, reflectance is therefore a ratio of exitance to irradiance. This quantity is dimensionless, and wavelength, direction, polarization and position dependent. As a general approximation throughout this manuscript, we will consider that the materials' surface we consider are isotropic, with reflection properties being independent of position over a characteristic area of a few square millimeters. Note that this statement will be valid when considering a flat materials surface, and not a structured one, as we will see later. We also consider a natural light source in the visible spectral domain, making every radiometric quantity spectral and independent of the polarization

One example of reflectance is for a situation where the light is incident through a cone Γ_i , and reflected following a cone Γ_r , as seen on Figure 8. In the incident cone, an incident radiance $L_i(\theta_i, \varphi_i)$ following the direction (θ_i, φ_i) creates, according to Eq.(2.7), the elemental irradiance $dE(\theta_i, \varphi_i) = L_i(\theta_i, \varphi_i) \cos\theta_i d\Omega_i$.

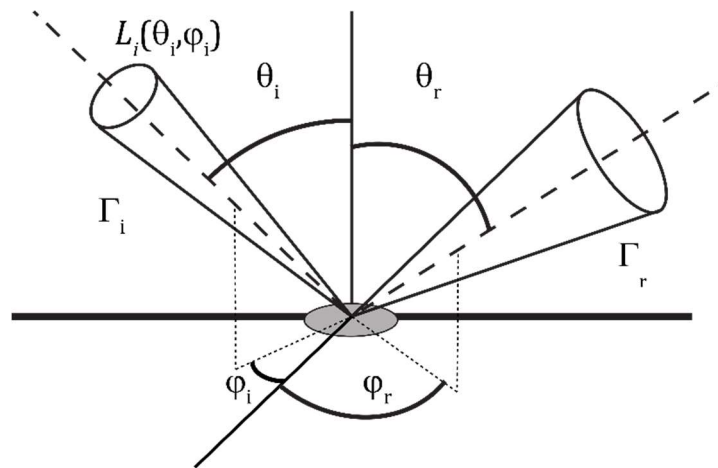


Figure 8 – Incident light with the radiance $L_i(\theta_i, \varphi_i)$ through a solid angle Γ_i being reflected into the solid angle Γ_r .

The total irradiance coming from the incident set of directions Γ_i is:

$$E_{\Gamma_i} = \int_{(\theta_i, \varphi_i) \in \Gamma_i} L_i(\theta_i, \varphi_i) \cos\theta_i d\Omega_i \quad (2.12)$$

The link between some incident radiance $L_i(\theta_i, \varphi_i)$ and one reflected radiance $L_r(\theta_r, \varphi_r)$ is made with the BRDF. According to Eq. (2.11), the corresponding elemental exitance is:

$$d^2M(\theta_i, \varphi_i; \theta_r, \varphi_r) = f_R(\theta_i, \varphi_i; \theta_r, \varphi_r) L_i(\theta_i, \varphi_i) \cos\theta_i d\Omega_i \cos\theta_r d\Omega_r \quad (2.13)$$

Preliminary reminder in optics and colorimetry

By summing all the contributions of the incident radiances contained in the cone Γ_i , we obtain the elemental exitance in the direction (θ_r, φ_r) :

$$dM(\Gamma_i; \theta_r, \varphi_r) = \int_{(\theta_i, \varphi_i) \in \Gamma_i} f_R(\theta_i, \varphi_i; \theta_r, \varphi_r) L_i(\theta_i, \varphi_i) \cos\theta_i d\Omega_i \cos\theta_r d\Omega_r \quad (2.14)$$

Then, by accounting for every elemental exitances going through the cone of observation Γ_r , the total exitance is obtained:

$$M(\Gamma_i; \Gamma_r) = \int_{(\theta_r, \varphi_r) \in \Gamma_r} \int_{(\theta_i, \varphi_i) \in \Gamma_i} f_R(\theta_i, \varphi_i; \theta_r, \varphi_r) L_i(\theta_i, \varphi_i) \cos\theta_i d\Omega_i \cos\theta_r d\Omega_r \quad (2.15)$$

Finally, the ratio defining the reflectance computed by dividing the total exitance by the incident irradiance is therefore [25]:

$$R(\Gamma_i; \Gamma_r) = \frac{\int_{(\theta_r, \varphi_r) \in \Gamma_r} \int_{(\theta_i, \varphi_i) \in \Gamma_i} f_R(\theta_i, \varphi_i; \theta_r, \varphi_r) L_i(\theta_i, \varphi_i) \cos\theta_i d\Omega_i \cos\theta_r d\Omega_r}{\int_{(\theta_i, \varphi_i) \in \Gamma_i} L_i(\theta_i, \varphi_i) \cos\theta_i d\Omega_i} \quad (2.16)$$

Practically, when one wants to perform a reflectance measurement, the CIE recommends [26] different geometries of measure, some of them listed in Table 1.

Table 1 - Selection of geometries recommended by the CIE for reflectance measurements

<i>Geometry designation</i>	<i>Illumination</i>	<i>Capture</i>
Diffuse/8°, specular component included (di:8°)	Hemispherical	Directional (radiance at 8°)
Diffuse/8°, specular component excluded (de:8°)	Hemispherical	Directional (radiance at 8°)
Diffuse/diffuse (d:d)	Hemispherical	Hemispherical
Alternative diffuse geometry (d:0°)	Hemispherical	Directional (radiance normal to the surface)
45° annular/normal (45°a:0°)	Annular	Directional (radiance normal to the surface)
45° directional/normal (45°x:0°)	Directional	Directional (radiance normal to the surface)

2.2.3 Reflectance factor

In practice, in order to determine the reflectance of a surface, one needs to measure the reflected flux, and the incident flux. Most instruments today contain a detector for the first one, but it is usually tedious to know the second one. Instead, the incident flux is measured indirectly with the help of a perfect white diffuser able to reflect the light uniformly over the hemisphere, without absorption. As a result, the measured flux by the

detector is proportional to the incident flux. The ideal case of white standard is a Lambertian, nonabsorbing and diffusing sample. It has a reflectance equal to 1 and a BRDF equal to $1/\pi$ for every pair of incident/observation direction.

Such a sample does not exist. The best white standards are made of pressed barium sulfate or PTFE (known as Alfolon, Halon or Spectralon) and comes with a calibration certificate. They are fabricated in order to have a reflectance superior to 0.99 in a diffuse/ 0° geometry over the visible spectrum. Then, the object to analyze and the white standard are illuminated and observed with the same geometry. The ratio \hat{R} of the measured flux reflected from the object F_{sample} and the measured flux from the white reference is called *reflectance factor*:

$$\hat{R} = \frac{F_{sample}}{F_{reference}} \quad (2.17)$$

This quantity is exactly a reflectance only in the case of a perfect Lambertian reflector. It can occur that the sample reflect more light towards the detector than the white reference does. It is the case for example, when a mirror with a reflectance R is illuminated by a directional light with an incident flux F_i at an angle θ_i and observed in the specular direction. The detector captures the flux $F = R(\theta_i)F_i$ and the flux $F_{ref} = F_i/\pi$ from the diffuser. In this configuration, the reflectance factor will overpass the unity at every wavelength where $R(\theta_i) > 1/\pi$.

2.3 Measurement and representation of a reflectance

The previous radiometric quantities have been defined without precisely considering their dependence to the wavelength. In practice, what is often measured is the *spectral flux* F_λ , which is the spectral distribution of the radiation defined as flux per unit wavelength. Quantities like the spectral irradiance E_λ and the spectral radiance L_λ are similarly defined.

2.3.1 Spectrophotometer

The type of device to measure such a flux is called a *spectrophotometer*. Its sensor captures the incident flux in successive spectral bands with a given $\Delta\lambda$ bandwidth. If it is small enough, the measured flux is equal to $F_\lambda\Delta\lambda$, and if it is larger bandwidth comprised between λ_1 and λ_2 , the measured flux is:

$$F_{[\lambda_1, \lambda_2]} = \int_{\lambda_1}^{\lambda_2} F_\lambda d\lambda \quad (2.18)$$

The spectral sampling varies according to the application targeted. For example, in color reproduction, it can be comprised between 0.2 and 10 nanometers. To select narrow

Preliminary reminder in optics and colorimetry

bandwidths, the light is decomposed by using a prism or a diffraction grating [27]. The position on the bar of photodetectors then determines the measured wavelength.

For example, to measure a spectral reflectance using a spectrophotometer, one needs to compute the ratio of the reflected spectral flux to the incident reflected spectral flux, both defined on the same small bandwidth. As mentioned before, this type of device often uses a white reference in its calibration process. This is done in order to give a reflectance factor as output, both the reference and the sample being illuminated by the same source of light and with the same geometrical configuration.

2.3.2 Integrating sphere

The reflectance measurement devices contain either a directional or a Lambertian white light source, and capture the reflected light in one given direction, several, or over the complete hemisphere. To perform this type of measurement, an integrating sphere is used. This device takes the form of a spherical cavity coated with a non-absorbing diffusing material (typically BaSO_4) and possessing a preferably high reflectance [28, 29]. Its purpose is to either produce a Lambertian illumination or to collect all the reflected light on a sample to analyze, coming from all over the sphere. The source of light used generally possesses a spectral distribution with a continuous spectrum, usually a halogen lamp, or a Xenon-arc lamp. The reflected flux by the sample is captured by a spectrophotometer.

On Figure 9 are represented two situations, whether we want to produce a Lambertian illumination, or to collect the reflected light over the hemisphere. In the $d:0^\circ$ geometry, the integrating sphere has the function of producing a diffuse illumination. The reflected light by the sample is then captured at a 0° angle (or an 8° angle) from the surface's normal of the sample. In the case where one wants to exclude the specular component, a hole is found in the regular direction with respect to the position of the detector. In this configuration, we measure a hemispherical-directional reflectance.

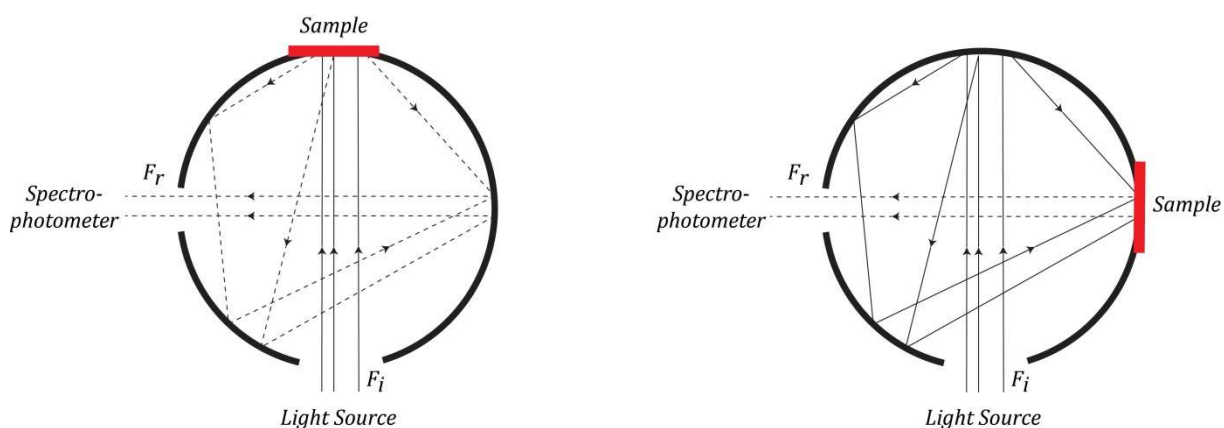


Figure 9 - Integrating spheres being used with a $0^\circ:d$ geometry (left) and a $d:0^\circ$ geometry (right).

In the 0° :d geometry, the integrating sphere has the function of collecting all the flux reflected by the sample being illuminated directly by a directional beam. This time, it is a directional-hemispherical reflectance that is measured.

2.3.3 Lambert transformation – Reflectance Maps

As presented, the BRDF is function with many parameters. It depends on the four angles describing the direction of incidence and the direction of observation, and on the wavelength, the polarization state, the position on the surface... This complexity makes impossible to plot a full BRDF on a 2D graphics, and the use of a 3D visualization software is preferred. An alternative that we used in this work is planar mapping [30], in order to represent for example a *hemispherical-directional reflectance map*. This kind of map describes the response of a surface in terms of reflectance to a Lambertian illumination (the “hemispherical” part) and gives the observed reflectance for each direction of observation over the hemisphere (“directional” part).

The mapping used is called the Lambert azimuthal equal-area projection [31]. Its convenience resides in its property of conserving the areas: a portion of the hemisphere of area A corresponds to a portion of a disk with the same area A . In other words, an elemental area on this map is directly proportional to a solid angle. To every direction (θ, φ) corresponds a point (u, v) within a disk of radius $\sqrt{2}$ whose coordinates are:

$$\begin{cases} u = 2 \sin(\theta/2) \cos \varphi \\ v = 2 \sin(\theta/2) \sin \varphi \end{cases} \quad (2.19)$$

An illustration of this mapping is visible on Figure 10. In practice, this mapping results in an image containing as many channels as wavelengths, and each pixel on the image corresponds to a given direction (θ, φ) , therefore a given solid angle

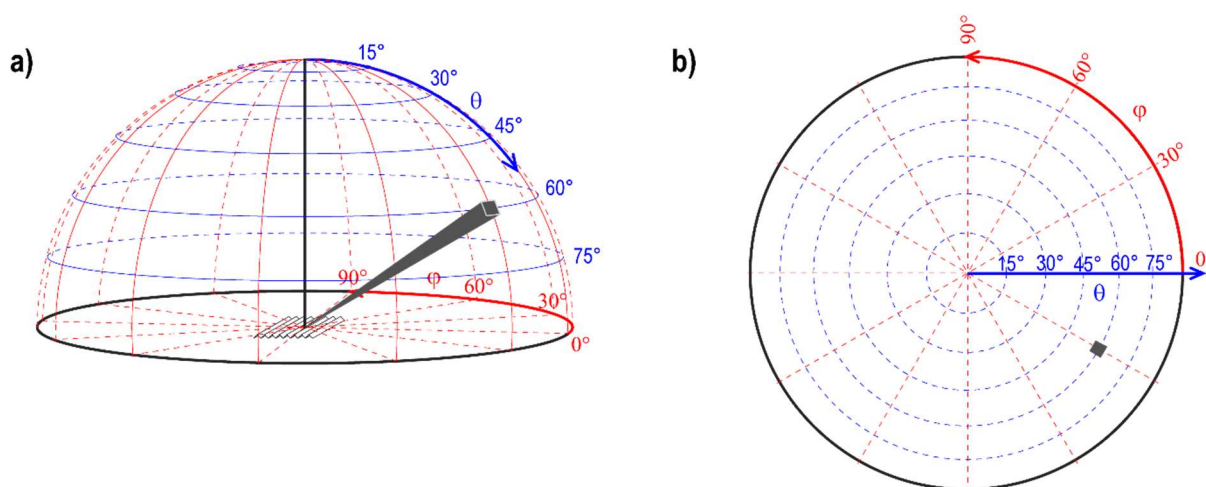


Figure 10 - When the hemisphere (a) is mapped onto a disk (b) according to the Lambert azimuthal equal area projection, any portion of the hemisphere with area A (gray solid angle) is mapped into a portion of the disk with same area A (gray square).

2.4 Radiometric properties of some special surfaces

In order to properly model the phenomena contributing to a material surface's appearance, such as the interreflection effect, one must properly consider the type of light source to use. We will first consider the photometrical behavior of special case of surfaces. We will then precise each case by making the distinction between two lighting geometry, a diffuse and a directional one. The first one is simple to model, and one must be careful of the angle of incidence onto the surface, leading to an irradiance attenuation following a cosine law. The same goes for a diffuse light source, but this time for every direction in space, and not always with the same, radiance attached to every one of them. Mixed illuminations could also be considered, as natural light is typically a mix between a directional source with a given direction of incidence, like sunlight, and a diffuse light source, like the blue sky, with light coming from every possible direction. One must then model the interaction between the incident light and the reflection and transmission properties of the surface encountered.

In this section, we first define a Lambertian light source, and then go on to develop the reflection and transmission properties of a material's interface with air, through the presentation of Fresnel's coefficients. We extend this presentation to the reflection

2.4.1 Perfectly matte surfaces: Lambert's model

As presented in section 2.1.3, a surface following the Lambert's law displays a uniform radiance independently of the direction of observation and emission. It displays a matte finishing due to the uniform scattering occurring when light encounters it. Formally, we will say that the scattered radiance by the surface is $L=constant$, without any dependence on the lighting geometry solid angle, whether it is diffuse or directional, and without any dependence on the observation solid angle as well.

This is a convenient way to model an object surface because it allows us to accurately describe any incident direction and its path after being reflected, refracted, or diffused by the surface, with comprehensive knowledge of the photometric and geometrical parameters along the way.

2.4.2 Reflection and transmission of light by smooth interfaces

When talking about material appearance under a given illumination type, one must consider the influence of a critical parameter: the interface between the media of incidence, and the media of the material. The fact that they have a different optical index is adamant to predict correctly the appearance of a material. In this work, the media of incidence will always be the air, with a refractive index equal to the unity, but the material considered will be either a dielectric or a metallic material. The interface is considered perfectly flat afterward.

Directional light: Fresnel's formulae

The fraction of light reflected by the interface between the air and the material is called *angular reflectance*, and is given by Fresnel's formulae, established by writing the equation of passage of an electromagnetic wave through the interface. It is dependent on the angle of incidence θ_1 , on the relative refractive index noted $n = n_2/n_1$, with n_1 and n_2 being respectively the media of incidence and the media after the interface. As said before, in this manuscript $n_1 = 1$.

In most cases, the incident light is considered unpolarized and modeled as the sum of two linearly polarized lights. The polarization being the orientation of the electric field in respect to the plane of incidence, we can consider the cases where the electric field oscillates in a parallel and perpendicular way to the incidence plane. These polarizations are called "parallel" and "perpendicular", symbolized by the letters p and s .

For an incident light pencil coming from the first medium with an angle of incidence θ_1 , the reflectance for the p -polarized light is

$$R_{p12}(\theta_1) = \left| \frac{n \cos \theta_1 - \cos \theta_2}{n \cos \theta_1 + \cos \theta_2} \right|^2 \quad (2.20)$$

where $\theta_2 = \arcsin(\sin \theta_1 / n)$ is the angle of refraction into the second medium obtained by Snell's law for refraction. For the s -polarized light, the reflectance is

$$R_{s12}(\theta_1) = \left| \frac{\cos \theta_1 - n \cos \theta_2}{\cos \theta_1 + n \cos \theta_2} \right|^2 \quad (2.21)$$

They both can be rewritten as functions of the angle of incidence only using the expression of θ_2 as

$$R_{p12}(\theta_1) = \left| \frac{n^2 \cos \theta_1 - \sqrt{n^2 - \sin^2 \theta_1}}{n^2 \cos \theta_1 + \sqrt{n^2 - \sin^2 \theta_1}} \right|^2 \quad (2.22)$$

and

$$R_{s12}(\theta_1) = \left| \frac{\sqrt{n^2 - \sin^2 \theta_1} - \cos \theta_1}{\sqrt{n^2 - \sin^2 \theta_1} + \cos \theta_1} \right|^2 \quad (2.23)$$

Considering an unpolarized source of light means it contains the same quantity of p - and s - polarizations, therefore can be expressed as the mean of both the angular reflectances:

Preliminary reminder in optics and colorimetry

$$R_{12}(\theta_1) = \frac{1}{2} [R_{p12}(\theta_1) + R_{s12}(\theta_1)] \quad (2.24)$$

It is important to keep in mind that the parallel and perpendicular polarizations are reflected in different amount, the only exception being for a normal incidence. In the case of a dielectric material, one particular angle called the *Brewster angle*, is such as the p -polarized light is not reflected at all. This angle $\theta_b = \arctan(n)$ is therefore often used in practice to obtain a totally s -polarized light.

It is important to acknowledge that the angular reflectance is the same, whether light comes from the first medium with an angle θ_1 , or from the second media with an angle θ_2 , these angles being linked by Snell-Descartes's law. Independently of the polarization, this means that:

$$R_{*12}(\theta_1) = R_{*21}(\theta_2) \quad (2.25)$$

with * being either p - or s - polarized light.

When considering the refracted component, and given that no light is absorbed at the interface, one can deduce the *angular transmittance*:

$$T_{*12}(\theta_1) = 1 - R_{*12}(\theta_1) \quad (2.26)$$

A direct consequence of Eq. (2.25) is therefore:

$$T_{*12}(\theta_1) = T_{*21}(\theta_2) \quad (2.27)$$

This consideration is crucial when working with material appearance. Since the incident light coming from the air onto a material's surface is bound to go through a material's interface, it can be diffused, transmitted, and reflected by the material itself. Then it can be transmitted back into the air, thus modifying the properties of the incident pencil of light.

Radiance reflection and transmission

A direct consequence one can derive from Snell's laws and Fresnel's formulae is the relationship between the incident, reflected and refracted radiances. The fact is that when a pencil of light changes of medium, its geometrical extent is modified as well. On Figure 11 we see an incident radiance L_1 coming from a medium 1. It is defined by the flux element $d^2F(\theta_1, \varphi_1)$ coming from the direction (θ_1, φ_1) through the elementary solid angle $d\Omega_1 = \sin\theta_1 d\theta_1 d\varphi_1$ and illuminating the elementary area dS :

$$L_1 = \frac{d^2F(\theta_1, \varphi_1)}{dS \cos\theta_1 \sin\theta_1 d\theta_1 d\varphi_1} \quad (2.28)$$

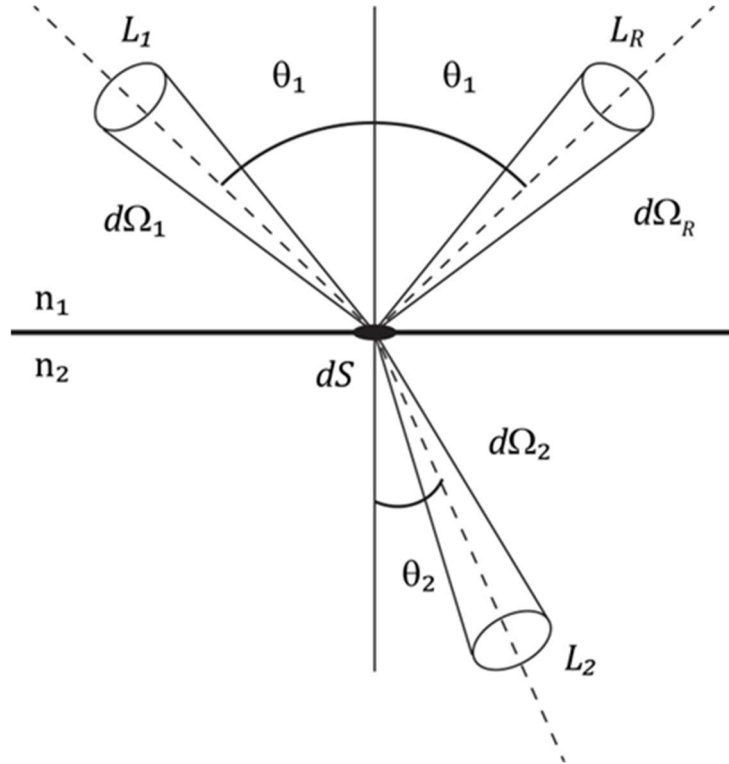


Figure 11 - Interface between two media of indices n_1 and n_2 , with $n_2 > n_1$, and the incident, reflected and refracted radiances.

The denominator of this fraction stands for the geometrical extent. Since according to Snell's law, the angle of reflection is the same as the angle of incidence, the geometrical extent of the reflected light pencil is also the same. The reflected radiance L_R can be expressed as:

$$L_R = R_{12}(\theta_1)L_1 \quad (2.29)$$

with $R_{12}(\theta_1)$ being the angular reflectance of the interface between medium 1 and 2. Regarding the refracted pencil, the Snell's law for refraction states that:

$$n_1 \sin\theta_1 = n_2 \sin\theta_2 \quad (2.30)$$

By differentiating Eq. (2.30), one obtains that:

$$n_1 \cos\theta_1 d\theta_1 = n_2 \cos\theta_2 d\theta_2 \quad (2.31)$$

Since the incident and refracted azimuth angles form a fixed angle of π , an infinitesimal variation on one implies the same variation on the other. Therefore from Eq. (2.31), one can arrive to

$$n_1^2 dS \cos\theta_1 \sin\theta_1 d\theta_1 d\varphi_1 = n_2^2 dS \cos\theta_2 \sin\theta_2 d\theta_2 d\varphi_2 \quad (2.32)$$

Preliminary reminder in optics and colorimetry

which is

$$n_1^2 d^2 G_1 = n_2^2 d^2 G_2 \quad (2.33)$$

This result means that the quantity $n_i^2 d^2 G_i$ remains invariant. It also means that the geometrical extent is multiplied by the square ratio of the optical indices when the light goes from one medium to another. To summarize, the refracted radiance is:

$$L_2 = \left(\frac{n_2}{n_1} \right)^2 T_{12}(\theta_1) L_1 \quad (2.34)$$

This result is a crucial one to keep in mind when talking about modeling material appearance when dealing with light encountering the interface of an object of which we want to predict the aspect.

Diffuse light: Lambertian reflectance and transmittance

We analyzed the behavior of light being incident on an interface for one ray of light. Now if we consider a diffuse Lambertian source illuminating an interface between two media 1 and 2, with n being the relative index, we can deduce directly from the reflectance in Eq.(2.16) the *bi-hemispherical* reflectance, also called *Lambertian reflectance*, denoted r_{12} , and given by:

$$r_{12} = \int_{\theta_1=0}^{\pi/2} R_{12}(\theta_1) \sin 2\theta_1 d\theta_1 \quad (2.35)$$

where θ_1 is the incidence angle from medium 1 onto the interface, relatively to its normal. This reflectance is only a function of the relative index and may be computed discretely with a small sampling. The integral computation of this expression was proposed by Duntley [Ref Duntley 37 poly Mathieu] and results in the following expression:

$$\begin{aligned} r_{12} = & \frac{1}{2} + \frac{(n-1)(3n+1)}{6(n+1)^2} - 2n^3 \frac{(n^2+2n-1)}{(n^4-1)(n^2+1)} + \dots \\ & \dots 8n^4 \frac{(n^4+1)\ln(n)}{(n^4-1)^2(n^2+1)} + n^2 \frac{(n^2-1)^2}{(n^2+1)^3} \ln\left(\frac{n-1}{n+1}\right) \end{aligned} \quad (2.36)$$

At the interface, the light flux is reflected all over the hemisphere, but is not necessarily Lambertian anymore, because of the angle dependency. The conservation of energy at the interface translates to the *Lambertian transmittance* being:

$$t_{12} = 1 - r_{12} \quad (2.37)$$

Following the same line of reasoning, when the light is incident from the medium 2 towards the medium 1, the bi-hemispherical reflectance is:

$$r_{21} = \int_{\theta_2=0}^{\pi/2} R_{21}(\theta_2) \sin 2\theta_2 d\theta_2 \quad (2.38)$$

It is important to know that $R_{12}(\theta_1)$ and $R_{21}(\theta_2)$ are equal, but r_{12} and r_{21} aren't, because of the possible total reflections happening in medium 2 but not in medium 1. The relationship between the two quantities is:

$$1 - r_{21} = \left(\frac{1}{n^2}\right)(1 - r_{12}) \quad (2.39)$$

Eq. (2.39) results in:

$$t_{21} = \frac{1}{n^2} t_{12} \quad (2.40)$$

2.4.3 Lambertian background with a flat interface

In this work, most of the materials encountered are strongly scattering, therefore resulting in an effort to develop models based on a Lambertian background. We saw that this type of surfaces reemits light with the same radiance in every direction over the hemisphere. But this hypothesis isn't true anymore when we consider the surface with its interface, especially if the latter is flat, and leads to specular reflections. Nonetheless, under the interface, the material is still Lambertian and its behavior is described by Lambert's law with Eq. (2.8).

To correctly describe the reflectance and transmittance of such a configuration, one can use a line of reasoning using upward and downward fluxes, as seen on Figure 12.

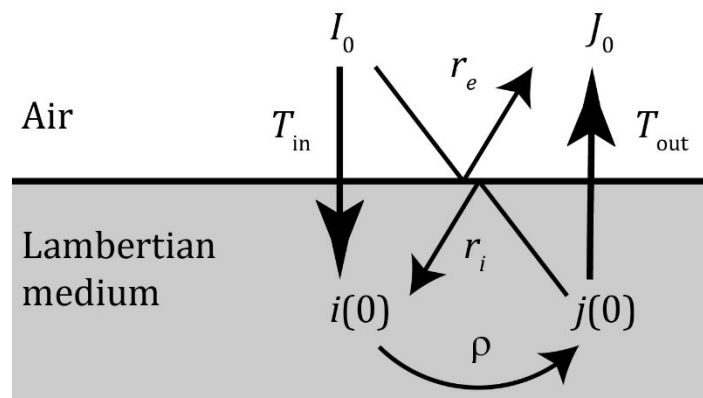


Figure 12 - Reflection and transmission processes for diffuse light at the interface between air and a Lambertian material

Preliminary reminder in optics and colorimetry

In this section, if we denote R the effective reflectance of the Lambertian material layer with its interface with air, then R is equal to the ratio of the outgoing flux J_0 over the incoming flux I_0 :

$$R = \frac{J_0}{I_0} \quad (2.41)$$

We can also denote ρ the reflectance of the Lambertian without its interface, also called *intrinsic reflectance*. It is defined as the ratio of upward and downward fluxes, but just at the surface of the material, at a null depth:

$$\rho = \frac{j(0)}{i(0)} \quad (2.42)$$

When the light hits the interface, a fraction r_e is reflected, called the *external reflectance*, whereas a fraction T_{in} is transmitted into the material. The same phenomenon happens for light when it exits the medium : a fraction r_i , called *internal reflectance* is reflected, and a fraction T_{out} is transmitted into the air. To formalize these two processes, one can sum them up with two equations:

$$\begin{cases} i(0) = T_{in}I_0 + r_i\rho i(0) \\ J_0 = r_eI_0 + T_{out}\rho i(0) \end{cases} \quad (2.43)$$

From these equations, the effective reflectance of a Lambertian material layer with an interface is derived:

$$R = r_e + \frac{T_{in}T_{out}\rho}{1 - r_i\rho} \quad (2.44)$$

This formula is known as the Saunderson equation [21] and was developed to offer a correction to another model for diffusing layers, the Kubelka-Munk model [32, 33], which wasn't taking into account the influence of the material's interface with another medium.

An important precision is that the terms in Eq. (2.44) depend on the illumination and observation geometries. For example, if the geometry is hemispherical-directional, with an observation at an angle θ from the normal, then the term r_e becomes $R_{12}(\theta)/\pi$ and T_{out} is expressed by $T_{12}(\theta)/\pi n^2$, with $R_{12}(\theta)$ and $T_{12}(\theta)$ being the Fresnel angular reflectance and transmittance defined in Eqs. (2.24) and (2.26), the factor $1/\pi n^2$ for T_{out} coming from the fact that only a fraction of the incident flux is exiting towards the observer, while changing of medium.

2.5 Basic notions of colorimetry

Modeling the appearance of an object is inseparable of correctly modeling its color. Color is a physiological sensation resulting from the brain's interpretation of the signal sent by our visual system and is highly subjective. It differs from one person to another. It is for this reason that the CIE established a "standard observer" from a series of experimentations. It can be seen as an "average person" in terms of human color perception. From these experiments, it has been derived that mainly three parameters are enough to classify colors: the brightness, the hue and the saturation. It also has been observed the human eye uses three different types of cone cell for color perception: short, medium, and long, standing for the range of wavelengths they capture. Each one of them possesses a specific spectral sensitivity plotted in Figure 13, with overlaps existing.

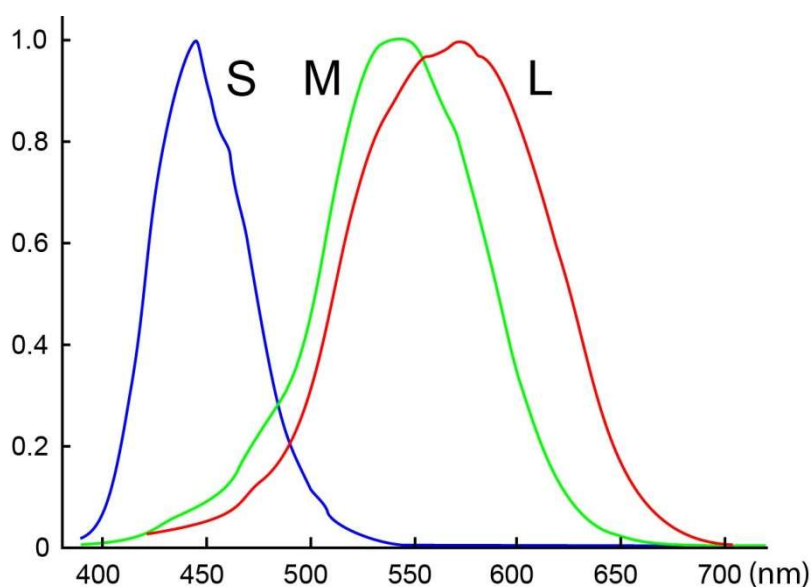


Figure 13 - Normalized spectral sensitivity of human cone cells in the short (S), medium (M) and long (L) wavelengths ranges. [34]

By weighting any type of light stimulus by the spectral sensitivity of each of these cells gives what is called the *tristimulus values*, effectively describing the perceived color. But the accurate knowledge of the eye spectral responsivity is rather recent.

Since when a stimulus arrives on the fovea of the eye, either two or the three types of cell can be activated. It is therefore complicated to model every tristimulus values in a physical model. For example, it is impossible to model a value that would be non-zero for one type of cell and zero for the other, because of the overlapping of the sensitivity curves. Therefore, it first led the CIE in 1931 to produce the RGB *color matching functions* in 1931, for two different standard observers, one with a 2° arc on the fovea (CIE 2° RGB), and later the other with a 10° arc (CIE 10° RGB) in 1964. These functions translate the amount of red, green, and blue light needed to match with a monochromatic stimulus at any

Preliminary reminder in optics and colorimetry

wavelength. Therefore, if a spectral radiance $L(\lambda)$ arrives on the fovea, the modeled RGB color is obtained with:

$$\begin{aligned} R &= \int_{\lambda} \bar{r}(\lambda) L(\lambda) d\lambda \\ G &= \int_{\lambda} \bar{g}(\lambda) L(\lambda) d\lambda \\ R &= \int_{\lambda} \bar{b}(\lambda) L(\lambda) d\lambda \end{aligned} \quad (2.45)$$

where \bar{r} , \bar{g} and \bar{b} are the CIE 1931 RGB color matching functions.

One problem remains. These color matching functions can have negative values. It especially happens when one tries to match a monochromatic light with a very high saturation or chroma by combining the RGB primaries. This why in order to obtain a precise color, we mix it with the three primaries and reach an equalization.

For this reason, the CIE1931 XYZ color space was created. The RGB color matching functions were transformed into a set of fictive new ones, the XYZ primaries, by using other color matching functions: \bar{x} , \bar{y} and \bar{z} . The transformation has been defined so that all the tristimulus values are positive.

$$\begin{aligned} X &= \int_{\lambda} \bar{x}(\lambda) L(\lambda) d\lambda \\ Y &= \int_{\lambda} \bar{y}(\lambda) L(\lambda) d\lambda \\ Z &= \int_{\lambda} \bar{z}(\lambda) L(\lambda) d\lambda \end{aligned} \quad (2.46)$$

The RGB and XYZ color spaces hold one difficulty: they are not uniform in the perception sense of the term, and therefore are complicated to use when one wants to represent colors and differences between them in a way that would suit the human color perception better. To solve this problem, the CIE suggested a more uniform color space, called the CIE 1976 L*a*b* color space, represented in Figure 14. The triplet of L*a*b* values can be easily computed from the XYZ tristimulus values. The most used metric in this color space to measure distances between colors is the ΔE 2000 color distance, which is not a Euclidean distance between the colors due to the non-uniformity of the space, but it is preferred to adapt the measure and conserve the color space.

The CIE 1976 L*a*b* color space is suitable to represent the colors yielded the models of this study. Efforts were made to include the chromatic adaption the human brain does when confronted with a white reference in the scenery. Therefore, when using this color space, one must specify the white reference from which the colors would be compared to. For example, to accurately represent the perceived color of a painting in a museum, it is important to clarify the white reference coming from the white wall behind, of even the light source if it is in the field of view.

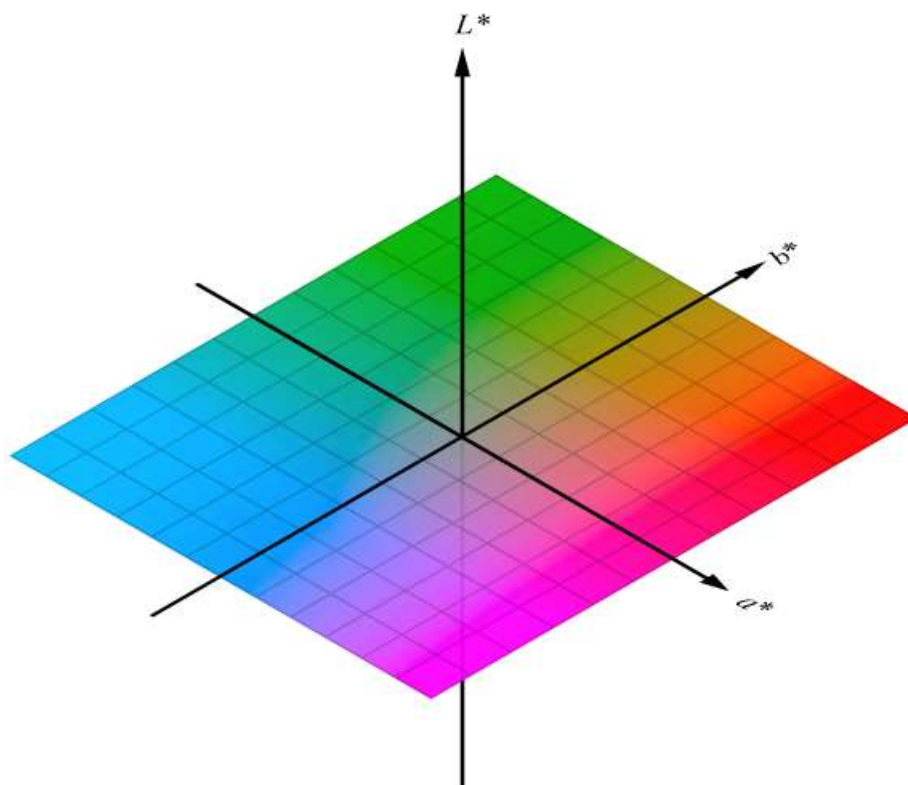


Figure 14 - 3D representation of the CIE 1976 $L^*a^*b^*$ color space. [35]

The parameters L^* , a^* , and b^* also aim to represent the behavior of our visual system, specialized in the detection of contrasts between luminosity and colors. The extremities of the three axes are antagonist colors. L^* is the lightness, going from 0 to 100, where 0 is the darkest black and 100 is the whitest component of the scenery. The a^* axis is the green-red component, with green being in the negative direction, and red in the positive direction. b^* axis stands for the blue-yellow component, with blue in the negative values, and yellow in the positive values. As a result, a color with the values $a^* = b^* = 0$ is a true neutral gray. This color space was designed to be closer to the color perception of the human visual system when looking at a surface.

In the same year, in cylindrical coordinates, the CIE also recommended the CIE 1976 $L^*C^*h^*$ color space. L^* is also the lightness, C^* is the chroma, and h^* is the hue angle.

2.6 Conclusions

We presented all the necessary concepts for the basis of our study. The approach using radiometry-based models will enable the analysis of the interreflection phenomenon and its influence on a structured material surface appearance, modeled with ideal surfaces as the ones presented in this chapter. The radiometric quantities and their properties are at the core of the models we now offer to develop in the three following chapters.

Chapter 3.

Light interreflections in a Lambertian V-cavity

The different areas of a concave object illuminate each other by a multiple light reflection process, called interreflections, depending on the geometries of the object and the lighting. For an accurate prediction of the radiance perceived from each point of the object by an observer or a camera, an interreflection model is necessary, taking into account the optical properties and the shape of the object, the orientation(s) of the incident light which can produce shadows, and the infinite number of light bounces between the different points of the object. The present chapter focuses on the irradiance of two adjacent Lambertian planar panels (V-cavity) illuminated by collimated light from any direction of the hemisphere, or by diffuse light. According to the reflectance of the material and the angle of the cavity, as well as the observation direction of the structure, the loss of irradiance near the fold due to the shadowing effect is partly compensated by the gain in radiance due to the interreflections. It can lead to significant change the lightness and chroma of the structure towards colors given by wavelengths that are weakly absorbed at first. The interreflections can also cancel the metamerism, as well as change the perception of ridged surfaces with two colors.

3.1 Introduction

In this chapter, we will consider the case of Lambertian materials displaying a periodical surface pattern of V-ridges, as presented in the general introduction. The purpose is to consider a perfect theoretical surface to accurately describe the interreflections and derive an analytical formulation, to help produce simulations of appearance.

With the interreflection phenomenon, the characteristic gain in lightness and chroma is illustrated by Figure 15. The material presented is rather Lambertian and orange, and the gradient of luminosity is well visible when the incident light is rather frontal and illuminates the whole surface.

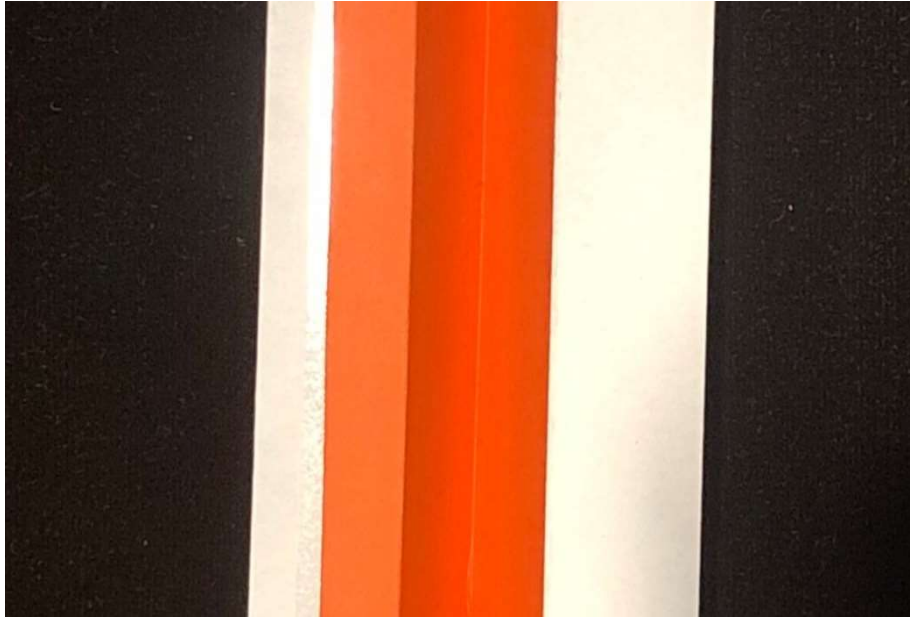


Figure 15 – Orange 45° V-cavity made of matte orange paper under a frontal lighting.

However, in the case of oblique lighting, the concavities may be only partly illuminated because of shadowing, and partly visible due to masking. Moreover, in case of diffuse lighting the shadowing effect diminishes the irradiance of the surface in the concavities, and the visual effects consequently lessen.



Figure 16 – Icelandic house during winter under a perfectly diffuse illumination, in a very scattering environment. Credits : Dorian Saint-Pierre.

Light interreflections in a Lambertian V-cavity

The picture in Figure 16 of an Icelandic house during winter shows that under a perfectly diffuse lighting, a snowy landscape, therefore a highly scattering one, can appear without any light reflections and only display some shadows where concavities are to be found, only to darken the overall visual aspect.

The main question resulting from this observation is to know to which extent interreflections can be in competition with shadowing, and how this can alter the perception of the surface topology. To answer it, it is assumed that the surface is perfectly scattering, i.e., Lambertian. The model is based on the radiosity equation such as the one proposed by Koenderink and Van Doorn [19], extended after by Seitz *et al.* [12] to offer a linear matrix transformation of the problem, and more recently by Rada Deeb [18] for spectral estimations in computer vision.

This interreflection model is presented in Section 3.2, in the general case of a 3D-shaped Lambertian material, then in the special case of a V-cavity of infinite length. We then address the question of the illumination geometry and the shadowing model in Section 3.4, which finishes the presentation of the model. The influence of illumination geometry is then addressed in Section 3.5. After this, a part focused on the influence of the observation direction is presented in Section 3.6, followed by the influence of the shape in section 3.7. Two studies using the interreflection model for V-cavities of infinite length made of Lambertian materials are conducted in Sections 3.8 and 3.9, regarding respectively metamerism and structured surfaces with two different colors. The section 3.10 will draw the conclusions of this chapter.

3.2 General case

One way of writing the observed radiance from a 3D-shaped Lambertian surface S is by taking into account the contribution of the multiple light bounces between each pair of points P_i and P_j on the surface. This helps derive a continuous equation known as the radiosity equation, or interreflection equation, which expresses the total radiance $L(P_i)$ perceived from every point P_i as the sum of two terms. The first term is the radiance $L_1(P_i)$ after one bounce, corresponding to the observed photons issued from the light source of irradiance $E_0(P_i)$ and reflected once on the surface of reflectance r_i in P_i :

$$L_1(P_i) = \frac{r_i}{\pi} E_0(P_i) \quad (3.1)$$

The second term is the radiance after multiple bounces, corresponding to the observed photons issued from every other point P_j of the surface and reflected one more time on the surface in P_i . The following reasoning line will establish this second term.

Each point P_i emits the radiance $L(P_j)$ in every direction, therefore towards point P_i . The elemental irradiance received in P_i from P_j is then:

$$K(P_i, P_j)L(P_j)dP_j \quad (3.2)$$

where $K(P_i, P_j)$ is a function called geometrical kernel (or interreflection kernel) related to the geometrical extent subtended by points P_i and P_j on the surface, defined by Eq.(2.3) :

$$K(P_i, P_j) = \frac{d^2G(P_i, P_j)}{dP_i dP_j} V(P_i, P_j), \quad (3.3)$$

$V(P_i, P_j)$ being a visibility function that gives 1 when both elementary areas dP_i and dP_j can see each other, and 0 otherwise. In order to better understand how the radiance after multiple reflections is constructed, let us consider first every elemental irradiance received in P_i after one reflection. They are coming from every point P_j , and by summing them, the total irradiance after one reflection is obtained:

$$E_1(P_i) = \int_{P_j \in S} \frac{r_j}{\pi} E_0(P_j) K(P_i, P_j) dP_j \quad (3.4)$$

Following the same line of reasoning, taking into consideration a second reflection before reaching the point of interest P_i means summing every irradiance contribution received in every point P_j that have been reflected once from other points $P_{j'}$, therefore leading to:

$$E_2(P_i) = \int_{P_{j'} \in S} \int_{P_j \in S} \frac{r_{j'} r_j}{\pi^2} E_0(P_{j'}) K(P_i, P_j) K(P_j, P_{j'}) dP_j dP_{j'} \quad (3.5)$$

In order to account for three reflections before reaching P_i , incidentally the irradiance received is:

$$E_3(P_i) = \int_{P_{j''} \in S} \int_{P_{j'} \in S} \int_{P_j \in S} \frac{r_{j''} r_{j'} r_j}{\pi^3} E_0(P_{j''}) K(P_i, P_j) K(P_j, P_{j'}) K(P_{j'}, P_{j''}) dP_j dP_{j'} dP_{j''} \quad (3.6)$$

Since the material considered here is Lambertian, this process continues until infinity. This consideration also means that since the same radiance is being reflected in every direction, it is therefore possible to state that the radiance after multiple bounces, which incorporates the elemental irradiances in P_i formed by the light coming from all other points P_j of the surface S , is therefore

$$\frac{r_i}{\pi} \int_{P_j \in S} K(P_i, P_j) L(P_j) dP_j \quad (3.7)$$

and the total radiance $L(P_i)$ displayed by point P_i is given by:

Light interreflections in a Lambertian V-cavity

$$L(P_i) = \frac{r_i}{\pi} \left[E_0(P_i) + \int_{P_j \in S} K(P_i, P_j) L(P_j) dP_j \right] \quad (3.8)$$

thus, considering every contribution from the other points.

The integral equation (3.8) is an inhomogeneous Fredholm equation [36] of the second kind and has no analytical solution in the general case. It can be solved numerically or, more conveniently, converted into a discrete version thanks to a Neumann series, after sampling the surface, thus represented by a collection of n microfacets having same area, as proposed by Nayar *et al.* [10].

By considering both radiance and reflectance constant over each facet, represented by a point P_i and its finished area dP_i , the integral equation (3.8) becomes:

$$L(P_i) = \frac{r_i}{\pi} \left[E_0(P_i) + \sum_{j \neq i} K_{ij} L(P_j) \right] \quad (3.9)$$

where

$$K_{ij} = \int_{P \in \Delta P_j} K(P_i, P) dP \quad (3.10)$$

This allows for transforming the geometrical kernel into a matrix

$$\mathbf{K} = \begin{pmatrix} 0 & K_{12} & \cdots & K_{1n} \\ K_{21} & 0 & \cdots & K_{2n} \\ \vdots & \vdots & \ddots & \vdots \\ K_{n1} & K_{n2} & \cdots & 0 \end{pmatrix} \quad (3.11)$$

which is symmetrical as $K_{ij} = K_{ji}$ for every i and j .

Since each facet has its proper spectral reflectance, we gather all facet's reflectances into an $n \times n$ diagonal matrix whose i th entry on the diagonal is the reflectance of facet i :

$$\mathbf{R} = \begin{pmatrix} r_1 & 0 & \cdots & 0 \\ 0 & r_2 & & \vdots \\ \vdots & & \ddots & 0 \\ 0 & \cdots & 0 & r_n \end{pmatrix} \quad (3.12)$$

The incident irradiance E_0 , the radiance L and the radiance after one reflection, L_1 , can also be defined for a collection of small areas on the surface (e.g. corresponding to a tessellation of the surface), and are in this case represented under the form of vectors:

$$\begin{aligned} \mathbf{E}_0 &= [E_0(P_1) \quad E_0(P_2) \quad \cdots]^T \\ \mathbf{L} &= [L(P_1) \quad L(P_2) \quad \cdots]^T \end{aligned} \quad (3.13)$$

where the superscript T denotes the transpose operator.

We can finally write Eq. (3.9) as:

$$\mathbf{L} = \frac{1}{\pi} \mathbf{R} [\mathbf{E}_0 + \mathbf{K} \mathbf{L}] \quad (3.14)$$

where vectors \mathbf{L} and \mathbf{E}_0 stands for the radiance and irradiance in each point of the scene, gathered in vectors. The equation (3.14) is equivalently:

$$\mathbf{L} = \frac{1}{\pi} \left(\mathbf{I} - \frac{1}{\pi} \mathbf{R} \mathbf{K} \right)^{-1} \mathbf{R} \mathbf{E}_0 \quad (3.15)$$

where \mathbf{I} is the $n \times n$ identity matrix. All terms contained in this general matrix equation are wavelength dependent. The equation is therefore written for each wavelength of light.

Remark: the computation of the terms K_{ij} defined by equation (3.10) needs an important comment. When points P_i and P_j are far from each other, we can assume that function $K(P_i, P_j)$ is nearly constant over the integration domain and therefore that equation (3.10) can be simplified as

$$K_{ij} \approx K(P_i, P_j) \Delta P_j \quad (3.16)$$

However, this approximation is not valid for adjacent facets, i.e., when P_i and P_j are close to each other. In this case, K_{ij} must be computed by integration as defined in equation (3.10), either analytically when possible, or numerically.

3.3 Special case of a V-cavity of infinite length

We now consider the interreflections in a V-cavity drawn by two adjacent planar panels forming an angle α , as shown in Figure 17. The two panels will be labelled 1 and 2. The common edge of the panels, assumed to be of infinite length, defines the x -axis of the 3D Cartesian space. The width of both panels is set to unity (it could be equivalently any other value: the width has no impact on the interreflection effect in this configuration as we will show later). The y - and z -axes belong to the plane orthogonal to the x -axis, the z -axis being in the bisector plane between the two panels. Hence, each panel forms an angle $\alpha/2$ with the z -axis. Moreover, the position of points in the panels will be described by proper bi-dimensional coordinate systems: (x, y') in panel 1 and (x, y'') in panel 2, where the y' and y'' axes belong respectively to panel 1 and panel 2 and are perpendicular to the x axis. Since the V-cavities considered in this paper have an infinite length according to the x -axis, their geometry depends only on angle α .

Light interreflections in a Lambertian V-cavity

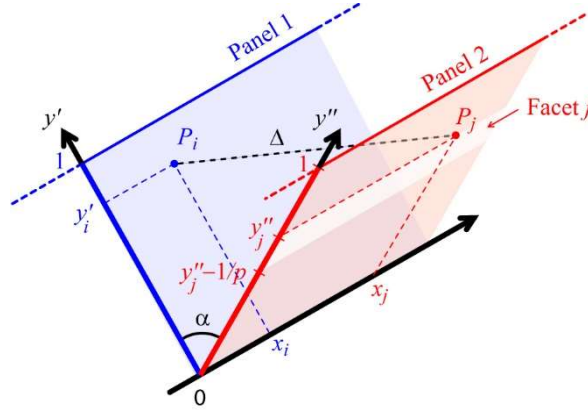


Figure 17 - Geometrical configuration where a point P_i on panel 1 sees a facet of infinite length on panel 2.

The general interreflection equation(3.15), in particular the matrices \mathbf{R} and \mathbf{K} , can be adapted to the V-cavity of infinite length made of a uniform Lambertian material as follows.

Regarding matrix \mathbf{R} , since the two panels are uniform and made of the same Lambertian material, all facets have the same reflectance r . Hence, matrix \mathbf{R} is a diagonal matrix where all terms on the diagonal are r , and can therefore be replaced with $r\mathbf{I}$, where \mathbf{I} is the $2p \times 2p$ unity matrix. Eq. (3.15) can therefore be written as:

$$\mathbf{L} = \frac{r}{\pi} \left(\mathbf{I} - \frac{r}{\pi} \mathbf{K} \right)^{-1} \mathbf{E}_0 \quad (3.17)$$

Regarding matrix \mathbf{K} , it is built according to a tessellation of the panels into $2p$ facets and has therefore the dimension $2p \times 2p$. Each of the two panels is decomposed into p facets of infinite length (according to the x -axis) and finite width (according to the y' or y'' axis, accordingly). Since the total width of each panel is unity, the width of each facet is $1/p$. The entries K_{ij} of matrix \mathbf{K} are computed according to Eq.(3.16), where function $K(P_i, P_j)$ is defined by Eq.(3.3). The visibility function $V(P_i, P_j)$ introduced in equation (3.3) is 0 for facets belonging to the same panel, and 1 for facets belonging to different panels. The geometrical extent $d^2G(P_i, P_j)$, also introduced in equation , must take into account the fact that we have here facets of infinite length. It has an analytical expression that we propose to derive now.

Let us consider on panel 1 a point P_i of coordinates (x_i, y_i') in the (x, y') -coordinate system used for panel 1, and a point P_j of coordinates (x_j, y_j'') in the (x, y'') -coordinate system used for panel 2, as featured in Figure 17. We also consider on panel 2 a facet of infinite length whose edges are parallel to the x -axis. Its highest edge meets point P_j at the ordinate y_j'' and, since every facet has a width $1/p$, its lower edge is at the ordinate $y_j'' - 1/p$. We want to express first the geometrical extent subtended by elemental areas dP_i and dP_j around points P_i and P_j , then the geometrical extent subtended by dP_i and the whole facet j .

In the 3D Cartesian system introduced in Figure 17, the points P_i and P_j have the coordinates

$$P_i = \begin{pmatrix} x_i \\ -y'_i \sin(\alpha/2) \\ y'_i \cos(\alpha/2) \end{pmatrix} \quad \text{and} \quad P_j = \begin{pmatrix} x_j \\ y''_j \sin(\alpha/2) \\ y''_j \cos(\alpha/2) \end{pmatrix} \quad (3.18)$$

and the normal of dP_i and dP_j , corresponding to the normals \mathbf{N}_1 and \mathbf{N}_2 of panels 1 and 2, respectively, are:

$$\mathbf{N}_1 = \begin{pmatrix} 0 \\ \cos(\alpha/2) \\ \sin(\alpha/2) \end{pmatrix} \quad \text{and} \quad \mathbf{N}_2 = \begin{pmatrix} 0 \\ -\cos(\alpha/2) \\ \sin(\alpha/2) \end{pmatrix} \quad (3.19)$$

The angles θ_i and θ_j formed by the line $(P_i P_j)$ and the normals \mathbf{N}_1 , respectively \mathbf{N}_2 , therefore satisfy the equations:

$$\cos\theta_i = \frac{1}{\Delta} \begin{pmatrix} x_j - x_i \\ y''_j \sin(\alpha/2) + y'_i \sin(\alpha/2) \\ y''_j \cos(\alpha/2) - y'_i \cos(\alpha/2) \end{pmatrix} \cdot \begin{pmatrix} 0 \\ \cos(\alpha/2) \\ \sin(\alpha/2) \end{pmatrix} \quad (3.20)$$

and

$$\cos\theta_j = \frac{1}{\Delta} \begin{pmatrix} x_i - x_j \\ -y'_i \sin(\alpha/2) - y''_j \sin(\alpha/2) \\ y'_i \cos(\alpha/2) - y''_j \cos(\alpha/2) \end{pmatrix} \cdot \begin{pmatrix} 0 \\ -\cos(\alpha/2) \\ \sin(\alpha/2) \end{pmatrix} \quad (3.21)$$

where symbol \cdot denotes the dot product between vectors, and Δ denotes the length $P_i P_j$:

$$\begin{aligned} \Delta &= \sqrt{(x_i - x_j)^2 + (y'_i + y''_j)^2 \sin^2(\alpha/2) + (y'_i - y''_j)^2 \cos^2(\alpha/2)} \\ &= \sqrt{(x_i - x_j)^2 + y_i'^2 + y_j''^2 - 2y'_i y''_j \cos\alpha} \end{aligned} \quad (3.22)$$

After computation, one obtains:

$$\cos\theta_i = \frac{y''_j \sin\alpha}{\Delta} \quad \text{and} \quad \cos\theta_j = \frac{y'_i \sin\alpha}{\Delta} \quad (3.23)$$

The elemental area dP_i around P_i can be written $dx_i dy'_i$ and the elemental area dP_j around P_j , $dx_j dy''_j$.

Finally, according to Eqs. (2.3), (3.22) and (3.23), the geometrical extent is written:

Light interreflections in a Lambertian V-cavity

$$d^4G = \frac{y'_i y''_j \sin^2 \alpha}{\left[(x_i - x_j)^2 + y_i'^2 + y_j''^2 - 2y'_i y''_j \cos \alpha \right]^2} dx_i dy'_i dx_j dy''_j \quad (3.24)$$

and the interreflection Kernel defined by Eq. (3.16) becomes

$$K(x_i, y'_i, x_j, y''_j) = \frac{y'_i y''_j \sin^2 \alpha}{\left[(x_i - x_j)^2 + y_i'^2 + y_j''^2 - 2y'_i y''_j \cos \alpha \right]^2} \quad (3.25)$$

Regarding the non-zero entries of matrix \mathbf{K} , defined by Eq. (3.11) in the case where P_i and P_j belong to different panels, they are obtained by integrating the interreflection Kernel $K(x_i, y'_i, x_j, y''_j)$, given by Eq. (3.25), over the facet, i.e., between $-\infty$ and ∞ along the x -axis, and between $y''_j - 1/p$ and y''_j along the y'' -axis:

$$K_{ij} = \int_{x=-\infty}^{\infty} \int_{y''=y''_j-1/p}^{y''_j} \frac{y'_i y''_j \sin^2 \alpha dx dy''}{\left[(x_i - x)^2 + y_i'^2 + y''^2 - 2y'_i y'' \cos \alpha \right]^2} \quad (3.26)$$

This double integral has an analytical solution, given by:

$$K_{ij} = F_i(y''_j) - F_i\left(y''_j - \frac{1}{p}\right) \quad (3.27)$$

with

$$F_i(u) = \frac{\pi}{2} \frac{u \cos \alpha - y'_i}{\sqrt{y_i'^2 + u^2 - 2y'_i u \cos \alpha}} \quad (3.28)$$

Unsurprisingly, K_{ij} is independent of x_i . This is due to the infinite length of the V-cavity which generates an invariant interreflections process along the x axis.

Finally, matrix \mathbf{K} in Eq. (3.17) is a $2p \times 2p$ matrix whose entries are 0 for pairs of facets belonging to the same panel, and are given by Eq. (3.27) for pairs of facets belonging to different panels, knowing that $K_{ij} = K_{ji}$.

3.4 Illumination Geometries

In the radiance of Eq. (3.17), the term \mathbf{E}_0 denotes the direct irradiance of the different facets in the V-cavity (without taking into account the interreflections), which depends on the geometrical configuration of illumination. In this study, we consider that the lighting is spatially uniform (in x and y) and covers the whole V-cavity aperture. Three configurations are considered, featured in Figure 18: frontal directional lighting, where the incoming light is parallel to the z -axis; oblique directional lighting where the incoming light is parallel to a vector \mathbf{e} , featured in by a green arrow, forming a polar angle θ in respect to the z -axis and an azimuthal angle φ in respect to the (y, z) -plane; and perfectly

diffuse lighting, characterized by a radiance uniformly distributed over the hemisphere. The aim of this section is to study the influence of the angular distribution of incident light on the radiance displayed by the cavity in each point by considering the possible shadows that one panel may cast onto the other panel.

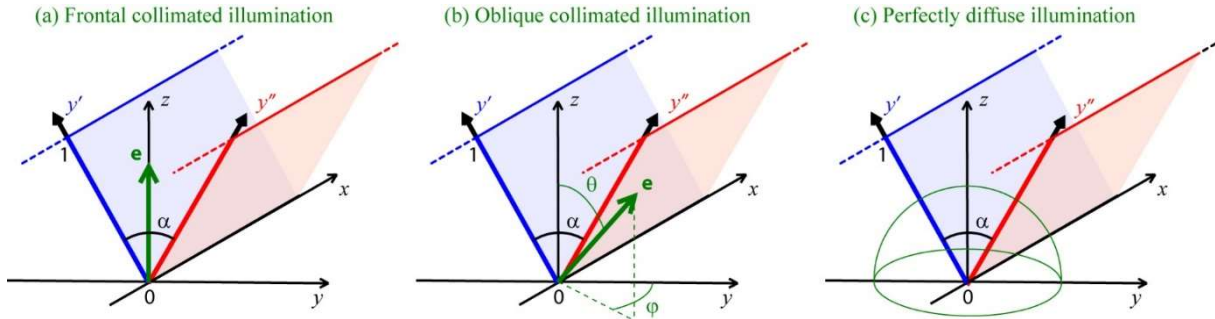


Figure 18 Geometry of the V-cavity under the considered lighting configurations

3.4.1 Light interreflections under a directional illumination

We first consider a frontal collimated lighting, parallel to the z -axis, i.e., $\mathbf{e} = (0 \ 0 \ 1)^T$. The horizontal plane (x, y) receives an irradiance denoted as E_z . It is the maximum direct irradiance that a panel can receive. Under this frontal illumination, since both panels form an angle $\alpha/2$ with the vector \mathbf{e} , each one receives an irradiance $E_z \sin(\alpha/2)$. All entries of vector \mathbf{E}_0 are therefore identical:

$$\mathbf{E}_0 = E_z \sin(\alpha/2) (1 \ \dots \ 1)^T \quad (3.29)$$

Under an oblique illumination, where the collimated light is parallel to the vector

$$\mathbf{e} = (\sin\theta \sin\varphi \ \sin\theta \cos\varphi \ \cos\theta)^T \quad (3.30)$$

the panels receive an irradiance given by

$$E_z \langle \mathbf{e} \cdot \mathbf{N}_i \rangle \quad (3.31)$$

where the symbol $\langle \cdot \rangle$ denotes the clamped dot product between the illumination vector \mathbf{e} and the normal \mathbf{N}_i of the panel $i = 1$ or 2 , given by Eq. (3.19), or equal to 0 when the dot product is negative since the surface is not illuminated when the angle between the incident light direction and the surface normal exceeds 90° .

Hence, for an oblique illumination, the entries of vector \mathbf{E}_0 are $E_z (u \sin\theta \cos\varphi \cos(\alpha/2) + \cos\theta \sin(\alpha/2))$ with $u = 1$ for the p first entries attached to the facets on panel 1, and $u = -1$ for the p last entries attached to the facets on panel 2.

Moreover, part of a panel may also be not illuminated because of shadowing by the other panel. Shadowing can be taken into account into the interreflection equation (3.17) by simply setting to 0 the entries of the irradiance vector \mathbf{E}_0 corresponding to the non-

Light interreflections in a Lambertian V-cavity

illuminated facets, thanks to a diagonal matrix \mathbf{S}_h of size $2p \times 2p$ whose j^{th} entry on the diagonal is 1 if the j^{th} facet is illuminated, and 0 otherwise. The interreflection equation modified as follows automatically considers the fact that some facets may be not directly illuminated by the light source:

$$\mathbf{L} = \frac{r}{\pi} \left(\mathbf{I} - \frac{r}{\pi} \mathbf{K} \right)^{-1} \mathbf{S}_h \mathbf{E}_0 \quad (3.32)$$

The Boolean values in this diagonal matrix \mathbf{S}_h are given by a function $S_j(\theta, \varphi)$ depending on the orientation of illumination, computed according to a condition that the central point F of each facet j of the V-cavity satisfies or not, and that we propose to introduce now.

First, we can observe that shadowing does not occur if vector \mathbf{e} is parallel to the (x, z) plane. It occurs only if the vector \mathbf{e}^\perp obtained by projection of vector \mathbf{e} onto the (y, z) plane forms an angle larger than $\alpha/2$. This projected vector \mathbf{e}^\perp can be defined by its coordinates (y_e, z_e) in the (y, z) plane:

$$\mathbf{e}^\perp = \begin{pmatrix} y_e \\ z_e \end{pmatrix} = \begin{pmatrix} \sin\theta \cos\varphi \\ \cos\theta \end{pmatrix} \quad (3.33)$$

In Figure 19, the projections of panels 1 and 2 onto the (y, z) plane are represented by a blue segment OA and a red segment OB, respectively. Vector \mathbf{e}^\perp , represented by a green arrow, is based on the central point F of a facet located on panel 1, at a distance y'_F from the fold (point O):

$$\mathbf{F} = \begin{pmatrix} y_F \\ z_F \end{pmatrix} = \begin{pmatrix} -y'_F \sin(\alpha/2) \\ y'_F \cos(\alpha/2) \end{pmatrix} \quad (3.34)$$

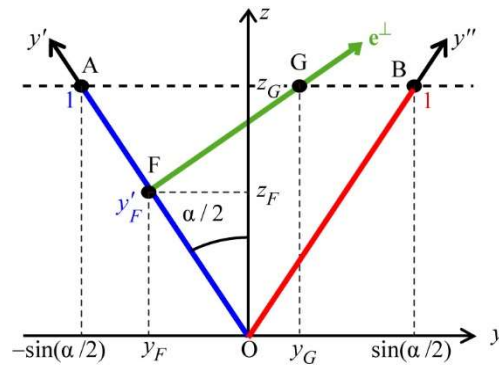


Figure 19 - Geometry of the V-cavity and the illumination vector projected onto the plan (y, z) plane.

The line parallel to vector \mathbf{e}^\perp that meets point F intersects line (AB) in a point G whose coordinates in the (y, z) plane satisfy both line equations:

$$\begin{aligned} \text{(AB): } z_G &= \cos(\alpha/2) \\ \text{(FG): } z_G &= z_F + (y_G - y_F) \frac{z_e}{y_e} \end{aligned} \quad (3.35)$$

By solving this system of two equations and using Eq.(3.34), one obtains:

$$y_G = (1 - y'_F) \tan \theta \cos \varphi \cos(\alpha/2) - y'_F \sin(\alpha/2) \quad (3.36)$$

The condition for this point F on panel 1 to be illuminated is that G is between A and B, i.e., that $|y_G| < \sin(\alpha/2)$, which yields the condition:

$$\left| (1 - y'_F) \tan \theta \cos \varphi \cos(\alpha/2) - y'_F \sin(\alpha/2) \right| < \sin(\alpha/2) \quad (3.37)$$

The Boolean function $S_i(\theta, \varphi)$ used to determine the values of the first p entries on the diagonal of matrix \mathbf{S}_h is 1 if the central point F of the i^{th} facet satisfies the inequality (3.37), and 0 otherwise.

Similar reasoning line applies when the point F is on panel 2, except that its coordinates in the (y, z) plane are:

$$\mathbf{F} = \begin{pmatrix} y_F \\ z_F \end{pmatrix} = \begin{pmatrix} y''_F \sin(\alpha/2) \\ y''_F \cos(\alpha/2) \end{pmatrix} \quad (3.38)$$

and the inequality of Eq. (3.37) becomes

$$\left| (1 - y''_F) \tan \theta \cos \varphi \cos(\alpha/2) + y''_F \sin(\alpha/2) \right| < \sin(\alpha/2) \quad (3.39)$$

The Boolean function $S_j(\theta, \varphi)$ used to determine the values of the last p entries on the diagonal of matrix \mathbf{S}_h is 1 if the central point F of the $p+j^{\text{th}}$ facet satisfies the inequality (3.39), and 0 otherwise.

3.4.2 Light interreflections under a diffuse illumination

Another type of lighting geometry is the perfectly diffuse light, also called Lambertian illumination (see Figure 5.c). Under this lighting, a horizontal plan would receive same radiance L_0 from every direction of the hemisphere, forming on the (x, y) plane a total irradiance E_z related to L_0 by:

$$E_z = \int_{\varphi=0}^{2\pi} \int_{\theta=0}^{\pi/2} L_0 \cos \theta \sin \theta d\theta d\varphi = \pi L_0 \quad (3.40)$$

In the case of the V-cavity, because of the shadowing effect, the panels are not homogeneously illuminated: the points near the edges are more illuminated than the ones near the fold. The irradiance $E_{0,j}$ on each facet j of the V-cavity can be computed thanks to the Boolean function introduced previously:

Light interreflections in a Lambertian V-cavity

$$E_{0,j} = \int_{\varphi=0}^{2\pi} \int_{\theta=0}^{\pi/2} L_0 S_j(\theta, \varphi) \cos\theta \sin\theta d\theta d\varphi \quad (3.41)$$

The entries of the vector \mathbf{E}_0 are computed according to this Eq. (3.41), and the interreflection equation (3.17) can be used to predict the radiance observed from the facets of the cavity.

Figure 20 shows the irradiance distribution on panel 1 along the y' -axis, for various cavities characterized by different angles α between the panels, all illuminated by a Lambertian lighting that produces an irradiance unity ($E_z = 1$) on a horizontal flat surface ($\alpha = 180^\circ$). Similar distribution would be observed on panel 2 along the y'' -axis. As α decreases, the irradiance is decreased by a factor $\sin(\alpha/2)$ in every position y' [see Eq. (3.29)], and is even more decreased as y' tends to zero due to the shadowing effect.

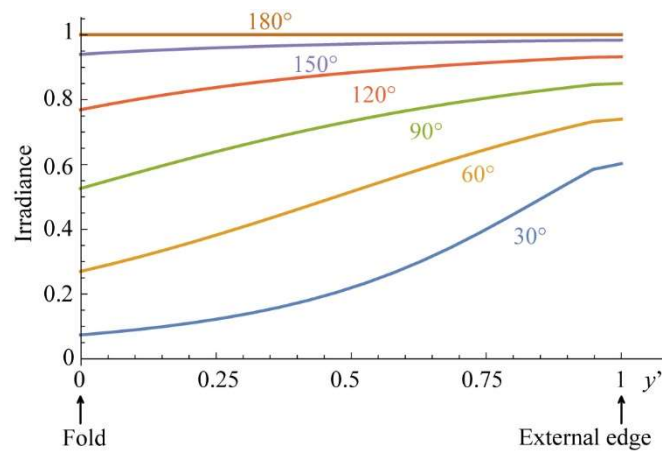


Figure 20 - Direct irradiance on panel 1 along the y' axis, from 0 (fold) to 1 (external edge), for a panel of V-cavities characterized by different angles α under a Lambertian illumination producing an irradiance $E_z = 1$ on the horizontal plane.

Now that the overview of the model for Lambertian V-cavities has been done, we will go on to present the simulations results. The three following sections will discuss three parameters: the lighting geometry, the observation geometry and the shape of the V-cavity.

3.5 Influence of the lighting geometry

In this section we will illustrate how the lighting geometry can impact the appearance of a grooved surface. Using the model presented earlier, simulation results will extensively show how such a surface structure impacts the reflected radiance displayed, as well as its color. Three cases of lighting geometry are used: a frontal directional one, with a direction of incidence being $(\theta, \varphi) = (0^\circ, 0^\circ)$, a directional oblique one being $(\theta, \varphi) = (45^\circ, 0^\circ)$, and a diffuse one, accounting for every direction of incidence over the hemisphere. These three types of illumination are presented on Figure 21. A sample of a

single V-cavity was fabricated. The length of the cavity along its folding axis is sufficiently long to be considered infinite compared to its width. The dihedral angle is 45° and made with orange matte paper and white matte paper. The cavity is presented alongside flat areas of the material for comparison purposes.

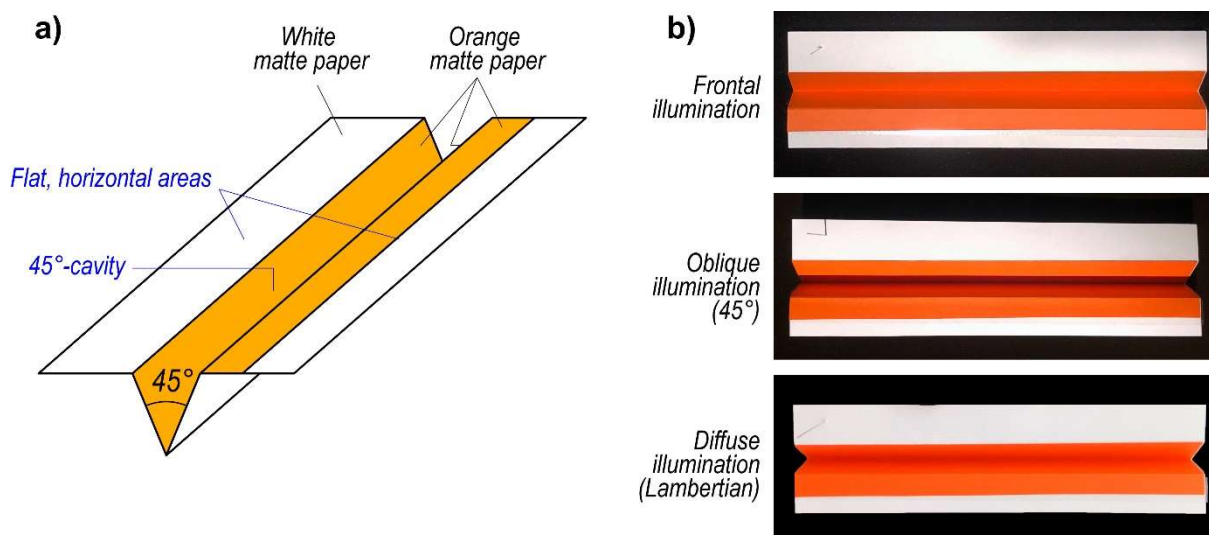


Figure 21 - Structure of paper sample presenting two flat, horizontal areas and a 45° -cavity, made of white and orange matte 120 g/m^2 paper. b) Color pictures of this sample (non-calibrated color) under different illumination geometries (see details in Figure) and observe under a frontal point of view..

A detailed version of the sample is presented in Figure PF3-1 on the left page. The first configuration (top picture) is a frontal collimated light $((\theta, \varphi) = (0^\circ, 0^\circ))$ direction of incidence within the coordinate system defined earlier). The cavity displays a radiance gradient along its sides, with a stronger radiance at the fold, due to the interreflections of the light. The increased radiance near the fold gives an impression like luminescence, while edges are darker and less saturated. In the second case (middle picture), a directional lighting with a $\theta = 45^\circ$ zenith angle, the interreflections are still present but are hidden by the shadowing effect. As a result, only the directly illuminated part displays a strong radiance, and the contribution of the interreflections is visible on the other side of the cavity, with a weaker radiance gradient. Notice that this gradient has a maximum roughly around the middle of the shadowed panel, corresponding the maximum amplitude of the interreflections. The last lighting geometry (bottom picture) is a diffuse one, with light coming from all the directions over the hemisphere. The shadows prevail over the interreflections, resulting in the opposite appearance of the frontal illumination: the fold is darker than the edges.

Aside from these pictures of the real cavity, simulations are shown on Figure PF3-1 on the right page. They correspond to the same cavity shape, and the same three illumination geometries. As data entries for these simulations, we consider a reflectance

Light interreflections in a Lambertian V-cavity

corresponding to a magenta material consisting of a stack of five sheets of non-fluorescent white paper, of density 80 g/m² with matte finishing, the last sheet being printed in inkjet with a magenta ink. The stack of sheets is used here to simulate an opaque white Lambertian material, opaque enough to simulate an infinite number of layers. In fact, the reflectance of this opaque stack was measured and used with the magenta color to purposefully have a configuration where the fabricated spectral radiance of the samples used is nearing 1 in the visible spectrum above 600nm. Therefore, displaying a stronger interreflection phenomenon when illuminated in a collimated fashion is possible.

For these simulations, we remind the interreflection model for Lambertian materials:

$$\mathbf{L} = \frac{r}{\pi} \left(\mathbf{I} - \frac{r}{\pi} \mathbf{K} \right)^{-1} \mathbf{S}_h \mathbf{E}_0 \quad (3.42)$$

We used an incident irradiance with a value of $E_z = \pi$ when it is illuminating a flat surface made of the same material and parallel to the horizontal plan (x,y) . When considering the frontal collimated lighting, the light beam is propagating parallelly to the z -axis. If a perfectly white, Lambertian and flat surface was illuminated by this irradiance, the observed radiance would be $L = E_z / \pi = 1$. The same irradiance value is used for the diffuse illumination. Therefore, the components of the vector \mathbf{E}_0 from the model equation (3.42) are computed with consideration of the obliqueness of the cavity's panels. In fact, the irradiance effectively hitting the panels represents 39% of the initial value, in the case of 45° V-cavity under a frontal collimated lighting, because its value is $E_z \sin(\alpha/2)$.

The geometry of the V-cavity itself, represented by the matrix \mathbf{K} in Eq.(3.42) was computed using the analytical model for a V-cavity of infinite length presented in Eqs. (3.26), (3.27) and (3.28). A cavity was generated using 64 microfacets in total (32 per panel), with the form of narrow bands of infinite length along the x -axis. The chosen scale is 2.5 mm of width for a microfacet, giving a total 80 mm height for a panel. This is purely for an informative purpose, because as mentioned earlier, the interreflection phenomenon takes place at any scale with the condition of having a structure size significantly larger than the wavelength. The number of microfacet is sufficiently high to properly observe the different events in the V-cavity without under sampling them.

Finally, the reflectance r is the spectrum of the flat magenta material, measured with a spectrophotometer X-Rite Color i7 using a Xenon lamp and an integrating sphere.

An important point of interest to keep in mind is the appearance of the grooved surface as whole, seen from a distance, without the perception of the details. Therefore, the average perceived radiance of one V-cavity is computed from the results of the interreflection model. As such, the average is computed on all the spectral radiances from each visible microfacets. In the current section, the observation direction at 0° is such as every microfacet is visible. But as we will see in the following section, it is not always the case.

The corresponding spectra displayed by all facets across the cavity are represented on the right side of the right page, with a solid line standing for a spectrum on the edge of the cavity ($y' \rightarrow 1$), a dashed line representing a facet at the fold of the cavity ($y' \rightarrow 0$), a dashed magenta line symbolizing the reflectance of the flat surface made with the same material, and a solid red line representing the average reflectance displayed by the cavity seen from afar, following the frontal direction.

On the left side of the right page are represented the color gradient of the cavity. These gradients are computed using colorimetric functions programmed on MATLAB. From the set of spectra, a conversion is made to the CIE 1931 XYZ color space using a D65 standard illuminant. Then from the XYZ primaries, a conversion to the CIE 1976 $L^*a^*b^*$ color space is done using a perfect unit white reference. Finally, to display the gradients, a conversion from the $L^*a^*b^*$ to the sRGB color space is done using a D65 illuminant.

On the top figure, under a frontal lighting, the structure displays a radiance gradient on its sides, with a brighter fold and darker edges, with a sensation of luminescence. This translates to the spectra observed on the graphics on the right. The highest spectrum, represented by a dashed line is from the fold, and the spectrum drawn in a solid line is from the edge. The interreflections are such as the mean reflectance on the cavity observed under the frontal direction is even higher than the flat surface's reflectance for the weakly absorbed wavelength range. On the contrary, the wavelengths that are already greatly absorbed result in an even weaker spectral radiance, mainly due to the obliqueness of the cavity's panels and interreflections being weak. As a result, the whole cavity appears to be darker but with a more saturated color, similarly to the picture of the orange sample under a frontal lighting.

For the oblique directional lighting at 45° (middle figure), we observe the same behavior as the picture presented before. The right side doesn't receive any light, the fold is darker due to the shadowing effect, but we can see a radiance gradient resulting from the interreflections with the illuminated part of the left side. On average, the cavity seen from afar will appear darker. A more detailed view of what the cavity is reflecting is presented on Figure 22.

The normalized and frontal irradiance represented by a green curve is illuminating the cavity in an oblique way, and the reflected radiance by the cavity is represented by the orange curve, and by the gray level gradient underneath the curve plot. We can observe that the right panel and the fold are completely shadowed, but we can also quantify the contribution of the interreflections happening with the illuminated left panel.

Light interreflections in a Lambertian V-cavity

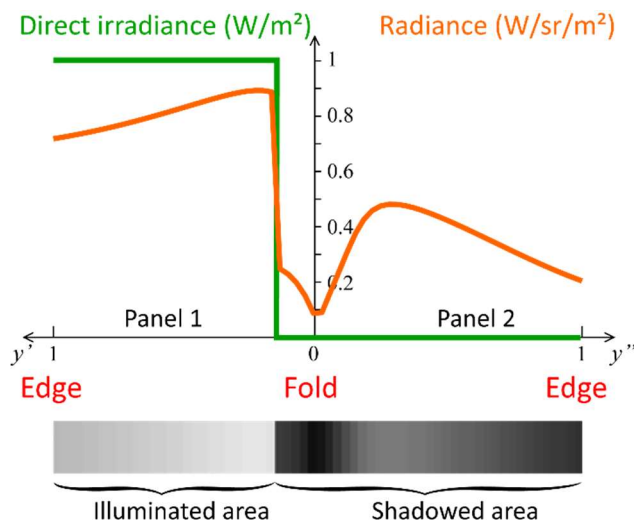


Figure 22 - Simulated spectral radiance (orange) perceived from the two panels of a V-cavity of angle $\alpha = 45^\circ$ and reflectance $r = 1$, illuminated by oblique collimated normalized irradiance (green) coming from the direction $(\theta, \varphi) = (45^\circ, 0^\circ)$. A slice of the cavity perpendicular to the x -axis, is shown in gray level below the graph.

Finally, under a diffuse illumination (Figure PF3-1, bottom), the shadowing effect is predominant. Therefore, as seen on both the picture and the simulated gradient, the radiance gradient is weaker near the fold and brighter at the edge. The spectra graphics shows that under a diffuse illuminant, the structured surface is always darker than the flat surface. The loss in radiance is mostly due to the obliqueness of the panels for the edges, and mainly to both the obliqueness and the shadows near the fold. Interreflections are still happening but in a more discreet amount.

3.5.1 Mixing a frontal collimated lighting with a diffuse one

Natural light is often a mix of both a directional light source, for example sunlight, and a diffuse light source, like the blue sky. It can be entirely composed of diffuse light, like during a very cloudy day, but never entirely of direct sunlight. A simple way to model this kind of natural light source is to simply compute a linear combination between a frontal and a diffuse light source, with multiplication factor b between them that varies between 0 and 1:

$$E_{total} = (1 - b) \cdot E_{frontal} + b \cdot E_{diffuse} \quad (3.43)$$

To further the study on the lighting geometry influence, simulations were performed in the case of a monochromatic material, one with a spectral reflectance of 1, being a perfectly white diffuser, and another with a spectral reflectance of 0.8, a gray material. Both materials are used to form a 45° dihedral angle of cavity, and they are put under a hybrid illumination. Using Eq. (3.43), we vary the proportion of frontal collimated and diffuse light, with 0.2 steps of the b factor.

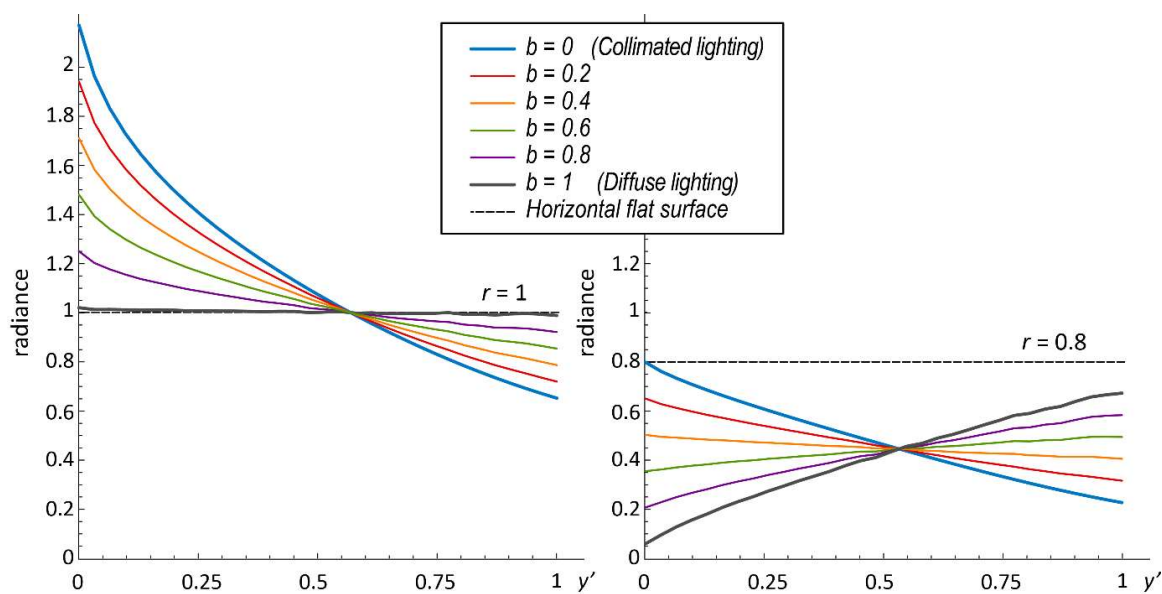


Figure 23 - Variation of the perceived radiance along the y' -axis on panel 1 in a V-cavity with angle $\alpha = 45^\circ$ and reflectance **a)** $r = 1$ or **b)** $r = 0.8$, for various illumination geometries obtained by mixing a fraction b of perfectly diffuse light and a fraction $(1 - b)$ of frontal collimated light.

When illuminated by perfectly diffuse light, the perfectly non-absorbing cavity (Figure 23a) displays a constant radiance equal to unity over the whole panel: it looks similar as a flat, horizontal surface made of the same material, which also displays a uniform radiance equal to unity. As soon as the illumination geometry contains a fraction of collimated light, the areas near the fold display a higher radiance and thus look brighter than the horizontal flat surface; in opposition, the areas near the external edge are darker than the horizontal flat surface. At a position on the panel around $y' = 0.6$, the radiance unity is displayed independently of the illumination geometry. For the material with reflectance $r = 0.8$, which is slightly absorbing, all points of the panel display a lower radiance than a horizontal flat surface of the same material, which would display a radiance 0.8. The areas near the fold are brighter than the ones near the external edge when the proportion of collimated light is high (low b values) but they look darker when the proportion of collimated light is low (high b values). As for the non-absorbing material, there is a position on the panel, around $y' = 0.55$, where the displayed radiance is independent on the illumination geometry.

One illustration for these simulations is the appearance of snow, being typically a very scattering and highly reflective medium. Under a very sunny day, with predominantly a directional sunlight, it becomes easy to perceive all the snow bumps and the shadows gradients for example on a ski trail (Figure 24). But as the simulations show, a very reflective and scattering structured surface under a Lambertian illumination tends to display the same reflectance as a flat surface made of the same material, meaning the structure isn't perceivable anymore. On Figure 25, we can observe such a case, where the snow bumps and the topography are hard to distinguish under what is also called a "flat light".

Light interreflections in a Lambertian V-cavity



Figure 24 – A ski trail under a directional sunlight. The bumps and the light gradients are visible. (credits : http://www.mechanicsofsport.com/snow_weather.html)



Figure 25 – a ski trail under a cloudy sky. The snow bumps are indistinguishable and no shadows are casted, rendering difficult the perception of the topography. (credits : http://www.mechanicsofsport.com/snow_weather.html)

Different variations as the ones displayed in Figure 23 would be obtained with other material reflectance values: the displayed radiance strongly decreases as the reflectance decreases. The cavity angle α , fixed to 45° this section, also have a strong impact on the radiance gradient displayed by the cavity panels, as shown in a following section. A lower angle value of cavity strengthens both interreflection and shadowing effects, the first one tending to increase the displayed radiance near the fold, and the second one tending to decrease it. There is therefore a competition between the two phenomena, being generally in favor to the interreflection effect (brighter areas near the fold) under a rather frontal lighting, and in favor to the shadowing effect (brighter areas near the external edges) under a rather diffuse lighting.

Following this study on the illumination geometry influence, we will now move on to the influence of the observation direction in the following section.

3.6 Influence of the observation direction

The observation direction also has a strong influence on the perceived radiance, especially at grazing angle where only the areas closest to external edge of one panel are visible, the other areas being masked by the other panel. Masking can be treated by defining a similar Boolean function as for shadowing with Eq. (3.39).

Taking the masking effect into account translates to adding a masking matrix \mathbf{M}_a to the interreflection model for Lambertian surfaces, with components computed thanks to the aforementioned condition, this time for the observation direction. In other words, the masking matrix is built by following the same process as for the shadowing matrix.

$$\mathbf{L} = \mathbf{M}_a \frac{r}{\pi} \left(\mathbf{I} - \frac{r}{\pi} \mathbf{K} \right)^{-1} \mathbf{S}_h \mathbf{E}_0 \quad (3.44)$$

To illustrate this model, we first show on Figure PF3-2 what the observation direction implies in terms of visible area of the V-cavity. Using a V-cavity with a 45° angle, made of the same magenta material as before, we simulate the spectral radiance and color gradient across the structure for a lighting geometry following the $(45^\circ, 0^\circ)$. We want to emphasize the fact that this is purely for the sake of illustration.

On the top part of the figure, we can see that the structure is fully viewed for a zenith angle going from -22.5° to 22.5° , corresponding to the half value of the cavity angle. The average perceived spectral radiance would therefore be computed on the whole structure.

On the bottom part of the picture, four different points of view are represented, each of them perpendicular to the cavity, and a 30° , 45° , 60° and 70° zenith angle. The greater the angle of observation is, the smaller visible area of the cavity is. The main difference resides in the average spectral radiance displayed by the cavity.

Light interreflections in a Lambertian V-cavity

When the cavity is fully viewed, the average is done on the whole structure, and since it is partially illuminated, the shadowed part will diminish the average. Then, if the observation direction shifts towards the illuminated panel, the structure will appear lighter and lighter, with an optimum of retro diffusion located at 30° where all the illuminated zone is observed, in the case of the 45° V-cavity. When the visible zone is only contained in the illuminated area (a zenith angle of 75° for example), the structure will appear very luminous to the observer. For the shadowed panel, the average radiance consequently appears darker and darker with the zenith angle of observation increasing.

To further analyze of the observation direction's influence, simulations were done using the same magenta material as before, as well as a cyan patch printed on the same opaque and Lambertian material. The cyan color was chosen due to its weaker lightness, resulting in weaker interreflections but still with enough saturation to observe a change of aspect under the different lighting geometries, in respect with a varying observation direction. The observation varies from the direction $\theta = -75^\circ$ to 75° with a 15° increment for the zenith angle. On the following pages are presented the average spectra of simulated magenta and cyan V-cavities with a 45° dihedral angle. The lighting geometries are a frontal lighting, a directional 45° lighting and a diffuse lighting. On the right of the spectra, left page, are represented the evolution of the average luminosity and chroma of each cavity, in an L^*C^* diagram computed in the CIE 1976 $L^*a^*b^*$ color space. On the second page, left, are presented the evolution of the average cavity colors in the a^*b^* diagram. On the right of the left page is the evolution of the color distance ΔE_{2000} , computed with the $L^*a^*b^*$ coordinates, with the view from the frontal direction as reference. The parameters for the incident irradiance as well as for the geometry of the cavity are the same as in section 3.5.

On Figure PF3-3 on the left page for the 45° magenta V-cavity, since the lighting geometry is symmetrical, there's no difference between the positive and negative range of the observation point. The L^*C^* diagram on the right of the left page shows that the more the observation is grazing, the more the lightness and chroma diminish, coherently so with the gradient observed on the cavity sides in such a configuration. On the right page, the a^*b^* diagram reveals a small change of hue angle, meaning the interreflections allied with a changing point of view not only changes the perceived lightness and chroma of the structure, but also its hue. The color distance ΔE_{2000} quantifies the strongest difference between the frontal point of the view and the most grazing one up to 5, meaning the differences are visible for the human eye.

Under the oblique 45° illumination, the symmetry doesn't exist anymore. As seen in Figure PF3-2, the change of observation direction impacts the visible area of the cavity, and therefore changes the average spectral radiance perceived. We can clearly see the lightness increasing with the zenith angle of observation going from 0° to 75° , because of the average being computed on more and more lighted microfacets, compared to a lower spectral radiance when the cavity is fully viewed. The maximum average is obtained for a 45° zenith angle of observation, being the same as the lighting direction. Just below is 60°

and then 75° , due to the obliqueness between the point of view and the viewed panel increasing. On the other side, for the negative zenith angle of observation, we can see a decrease of the radiance, except for -45° zenith angle of observation being higher than the others, because of the interreflections maximum on the shadowed panel. The L^*C^* diagram shows a high range of change for the lightness, but a change of chroma as important as the change observed for the frontal illumination, meaning that the change of directional lighting geometry also changed the evolution of the color saturation as a function of the observation. The a^*b^* diagram also shows a consequent change in the perceived hue, yielding a strong gonio-dependence of the color for this kind of anisotropic surface structure, especially with an asymmetrical lighting. The color distance ΔE_{2000} quantifies the strong dispersion of the perceived colors compared to the frontal point of view and takes values as high as 19 for the observation direction coinciding with the lighting direction.

Finally, for Figure PF3-3, the magenta V-cavity under a diffuse illumination shows a smoother evolution of the average spectral radiance with the observation direction than in the two previous cases. The fact that the shadowing effect is dominating the structure's appearance shows on the corresponding L^*C^* diagram that the chroma barely changes while the lightness increases with the zenith observation angle, the observer getting a smaller and smaller visible area being lighter on the edges. The change of hue angle represented in the a^*b^* diagram is rather small and comparable to the change of hue for the frontal illumination and leads to the same kind of color distance evolution.

On Figure PF3-4 the same study was conducted for a 45° cyan V-cavity. As one can observe, the tendencies of the curves are very similar to the case of the magenta, with little differences.

Under a frontal collimated lighting the average spectra never overpass the unity because of cyan being a darker color to begin with, therefore yielding weaker interreflections. The L^*C^* diagram shows a small change in lightness and chroma, but a higher change of hue in the a^*b^* diagram is visible, overall leading to a rather small evolution of the color distance compared to the frontal observation.

The fact that the interreflections are weaker for a cyan V-cavity shows that the observation angle dependence of the perceived radiance and color is even greater due to the stronger influence of the shadowing effect when considering a 45° oblique illumination. Since the interreflections are weak, they can't compete with the shadows and the cavity will more rapidly evolve from a lighter to a darker appearance.

Finally, the diffuse lighting geometry shows the same kind of smooth evolution as for the magenta structure but with a noticeable difference for the color distance. The ΔE_{2000} being a metric more sensitive for the blue colors yields that even with weaker interreflections, the human eye would more sensitive to the change of appearance in the case of a cyan grooved surface than in the case of a magenta grooved surface.

3.7 Influence of the V-cavity's shape

The next parameter of the presented interreflection model for Lambertian surfaces we offer to analyze is the shape of the V-cavity, more precisely its dihedral angle α , fixed at a 45° value until now. To investigate the influence of the shape, we now choose an angle of cavity taking the following values: 30°, 45°, 60°, 90°, 120°, 150° and the flat surface at 180°. We also want to analyze the influence of the structure on the color. To do so, a selection of different colors has been made. The same opaque material as before, with a measured reflectance of a stack of five sheets of non-fluorescent white paper, of density 80 g/m² with matte finishing constitute the base, with a magenta, a cyan and a yellow patch printed on it with an inkjet printer. The reflectances of the respective sample are then measured using the spectrophotometer from X-Rite: the model Color i7. In addition to these materials, two Munsell patches of reference were selected from the Munsell Book of Color from X-rite: an orange patch with a Munsell value of 7 and a chroma of 14, and a green patch with a Munsell value of 7 and a chroma of 10. These values were selected to obtain a good trade-off between the lightness of the samples and their chroma, but we will observe that even with these parameters, the interreflections are quite discreet. Finally, we study the stack of paper sheets itself as a white Lambertian material without any ink printed on it, as well as a material, represented by the reflectance of a single sheet of the same paper, being slightly less reflective.

The equation model used in this section considers a frontal direction of observation, yielding no masking effect:

$$\mathbf{L} = \frac{r}{\pi} \left(\mathbf{I} - \frac{r}{\pi} \mathbf{K} \right)^{-1} \mathbf{S}_h \mathbf{E}_0 \quad (3.45)$$

Since no masking is present in this section, all the average spectra are therefore computed on the whole structure.

The irradiance is still spatially uniform and taken such as it yields a unitary radiance when illuminating a white Lambertian reference. The lighting geometry is computed for two cases: a frontal collimated illumination and a diffuse illumination. The geometrical kernel matrix \mathbf{K} is computed according to Eq. (3.26), for each value of cavity's angle, with the same parameters as previously presented.

On Figure PF3-5, for both types of illumination, a magenta V-cavity has been simulated. For each value of dihedral angle, the spectral radiance from each microfacets was plotted. The highlighted spectral radiances are the one of the flat surface, represented by a magenta dashed line, the average spectral radiance of the whole cavity, represented by a solid red line, the spectrum from a microfacet situated on the edge, represented by a solid black line, and the one from a microfacet near the fold, with a dashed black line. Under each graphics is represented the equivalent color gradient of the cavity, computed

with all the spectra from the microfacets, and using the same pipeline of conversion from spectrum to sRGB values as presented in Section 3.5.

On the top part of Figure PF3-5 are plotted the different cavities under a frontal collimated lighting. The evolution from the flat surface to a very closed structure with a 30° angle shows the interreflection phenomenon becoming stronger and stronger. This is due to the decreasing distance between the microfacets, reinforcing the contribution of the reflected diffuse light across the cavity. We can even observe that some microfacet have a spectrum overpassing the unit value when observing the cavity, to the point where for an angle of cavity of 45° or lower, the average perceived radiance is also superior to the unity, and most importantly superior than the flat surface's reflectance as well, for weakly absorbed wavelengths.

On the bottom part of Figure PF3-5 are plotted the different cavities under a diffuse illumination. The shadowing effect is predominant on the interreflections, leading to an overall darker structure with a less saturated colors. We can observe that when the V-cavity's angle decreases, the collection of spectra from the microfacets is spreading, due to the increasing obliqueness of the panels as well as the closing of the cavity reinforcing the shadowing effect. The main thing to retain here is that the spectral radiance displayed by such a structure under a diffuse illumination is always lower than the flat surfaces. The color gradients also show the color becoming more and darker.

Following this first analysis, a set of figures on double pages is presented. For each pair or pages, the case for one color of material is presented. First comes the magenta, then cyan, yellow, orange, green, gray and finally, white. For each of these materials, we plot the average spectra displayed by the cavity, for each angles of the cavity. These spectra are then converted into CIE 1976 $L^*a^*b^*$ color space coordinates and plotted in an L^*C^* diagram as well as an a^*b^* diagram, following the same reasoning as in Section 3.5. The evolution of the ΔE_{2000} color distance is plotted, with the flat surface marked as a reference. Finally, these processes are repeated for two types of lighting geometries presented before: the frontal collimated light, and the diffuse one.

On the first double page is Figure PF3-6 and the case of a magenta V-cavity. The interreflection phenomenon is strongly visible under a frontal collimated lighting, as seen on the left page, top picture. We can observe that when the dihedral angle increases, the part of the spectrum that is weakly absorbed is gaining in lightness, but on the other side, the part that are strongly absorbed are lowered. This phenomenon is stretched to the point where we can observe a crossing between the different spectral radiances for each angle, and we can derive that there is threshold existing above which the interreflection effect can induce an increase of lightness, and is the strongest in very closed structures because of the small distance separating the Lambertian microfacets. The L^*C^* diagram for the magenta under a frontal lighting shows a consequent drop in lightness with the dihedral angle decreasing, and a rather small change in chroma. On the contrary, the a^*b^* diagram on the right page displays a huge change of hue between a flat surface and a 30° V-cavity, notifying the strong influence evolution of the interreflections in this case when

Light interreflections in a Lambertian V-cavity

the cavity's shape is "closing". The evolution of the ΔE_{2000} color distance translates the great disparity between the 30° angle of cavity and the flat surface.

For the diffuse illumination (bottom picture, left page), since the shadowing effect is predominant, we observe once again the fact that all the structured surfaces are always darker and less saturated than the flat reference. The L^*C^* diagram shows a decrease in lightness but a very small change of chroma. In the same fashion as for the frontal lighting, the hue in the a^*b^* diagram undergoes a great change when going from flat to a very closed angle of cavity. In this case the evolution of the color distance is comparable as well.

On the second double page, Figure PF3-7, are the simulations for a varying dihedral angle of the cavity for a cyan structure. This time, the average spectral radiances under a frontal lighting on the left page shows that the interreflections phenomenon is weaker, to the point where all the structured surfaces display a lower radiance than the flat surface. The case of diffuse illumination shows a very similar behavior, but for both type of illumination, the change of hue and chroma is still consequent and this is even more visible with the evolution of the color distance. The more the concavity of a grooved surface is marked, the more the perceived color and radiance is changed, leading to a color distance superior to 20 in the case of a 30° angle of cavity, compared to the flat surface.

The following cases of yellow, green, orange, gray and white mostly follow the same trend as magenta and cyan. The main differences lay in whether the colors are

On Figure PF3-8 is presented the influence of the V-cavity shape for a yellow material. In this case, the considered sample is highly reflective. Under a frontal lighting, it leads to a very strong interreflection effect taking place in the V-cavity. As seen the on the top left graphics on the left page, the observer will get a strong sensation of fluorescence while looking at the surface. The interreflections are reinforcing the gain in lightness and the color saturation to the point where the structure will seem to emit some lights itself. The L^*C^* diagram on the top right of the left page shows an increasing chroma as a result of the interreflections. The a^*b^* diagram translates the strong interreflections into a consequent change of hue. A change that is not as significant as for the cyan material because as the corresponding color distance graphics shows, since the human eye is less sensitive when it comes to yellow, the difference between the flat surface and the structured one is not as great as in the previous cases.

Under a diffuse illumination, the yellow V-cavity for different angles is still shows a strong spectral radiance, but always lower than the equivalent flat surface. It also means that for a highly reflective and scattering material like the yellow patch, the shadowing effect doesn't alter the appearance of the structure much, as illustrated with the case of a perfectly white structured surface in Section 3.5.

On Figure PF3-9 is presented the case of a green Munsell patch. Its behavior is similar to the one of cyan, being a rather cold color with a low spectral maximum, whether it is under a frontal illumination, or a diffuse one, with the difference of an anecdotal change of hue.

The same type of behavior is observable for the orange Munsell patch, on Figure PF3-10. This time, the sample being slightly more reflective than the green one, we can observe that both under a frontal and a diffuse illumination, there is a decrease in lightness alongside a small increase in chroma when the cavity angle is decreasing. For both the frontal and diffuse lighting, since the interreflections are not dominant but still happening, meaning that the weakly absorbed wavelengths are amplified, and that the wavelengths already low are lowered, we can see in both a^*b^* diagrams that the orange V-cavity becomes more red with the aperture becoming smaller (the value are tending towards the a^* axis).

For the last two double pages, we studied the case of the Lambertian background alone used as a support for the previous colors. Figure PF3-11, under a frontal lighting, the single layer paper appears gray, and not reflective enough to display a strong interreflection phenomenon. This is also because the paper is not opaque, therefore transmitting light, which is not diffused by the material and reflected into the formed V-cavity. The decrease in lightness observed is then solely explained by the obliqueness of the panels compared to the direction of incidence. Since the paper appears gray, the influence of the shape is only marked by the evolution of the color distance between the different angles, with a more closed structure appearing darker than a less closed one.

The behavior is similar under a diffuse illumination, even more so because of the shadowing effect being dominant in this case, leading to a DE2000 color distance spreading further from the flat surface for small angles of cavity such as 45° and 30° .

On the contrary, on Figure PF3-12, the interreflections are consequently stronger, even leading to the spectral radiances for different cavity angles crossing each other, as illustrated on the top left picture on the left page. It also leads to the appearance of the material deriving a bit towards a yellowish color. This is due first because of the interreflections taking place in the stack of paper sheets, and then to the interreflections taking place in the V-cavity. They reinforce the sensation by increasing the weakly absorbed wavelengths and decreasing the others. As shown on the L^*C^* diagram for the frontal lighting, we can observe a shift of chroma without a decrease of lightness, and without a noticeable shift of hue in the a^*b^* diagram.

Under a diffuse illumination, the stack of paper layers appears darker than the flat surface in average, and with the angle of the V-cavity diminishing, we can observe the same shift of chroma accompanied this time by a decrease in lightness due to the shadowing.

To summarize the influence of the shape of the V-grooved surface, we concatenate all the a^*b^* diagrams into one in Figure PF3-13. If it appears clearly that the lighting geometry has a strong impact on the spectral radiance and the displayed chroma by the V-cavities, compared to the flat surface, it has on the contrary less impact, if an impact at all, on the hue evolution with the aperture angle of the structure. For each one of the simulated colors, and under both the frontal and diffuse lighting, the 30° V-cavities exhibits colors with (a^*, b^*) values testifying of the hue shift compared to the one of the

Light interreflections in a Lambertian V-cavity

flat surface. This evolution of the hue is mainly due to the interreflections, because the darkening due to the obliqueness and to the shadowing in the case of the diffuse lighting would imply a linear variation of the spectral radiance, which is not the case with the interreflections.

Even if the interreflection phenomenon depends on the initial irradiance of the cavity's microfacets, which is not exactly the same whether the lighting is frontal or diffuse, the dependence is weak considering that in both cases, the interreflections amplify the spectral radiance in the wavelength range where it is the highest (or decrease it in the opposite case). Therefore, the more a V-cavity's aperture is small, the more concentrated is the radiance around the weakly absorbed wavelengths, and the color of the structure tends to the corresponding wavelength: orange and magenta become more red (a^* axis), the yellow becomes yellower, the cyan becomes more blue (b^* axis), and the green almost keeps the same hue.

As we could observe through the previous simulations, it sometimes happens that the mean perceived radiance of a cavity illuminated frontally and viewed frontally overpasses the one of the flat surfaces made of the same material, at least at some wavelengths. It was visible in Figure PF3-3 for a 45° magenta cavity, as well as in Figure PF3-6 for different cavity apertures α . Same observation is made for the yellow and white cavities (Figure PF3-8 for the yellow and Figure PF3-12 for the white stack of paper), but it is not the case for the other colors (Figure PF3-7 for the cyan, Figure PF3-9 for the green Munsell, Figure PF3-10 for the orange Munsell, Figure PF3-11 for the gray single sheet paper). This happens when the material reflectance, at these wavelengths, overpasses a certain threshold that we denote here as ρ_x .

To investigate this issue, we generated a material with a "ramp" reflectance, ranging from 0 to 1 on the visible spectrum. This way it allows us to plot the resulting radiance after interreflections and find the threshold ρ_x . This is illustrated by the graph in Figure 26a the radiance issued from the facets of a 45° cavity (illuminated and viewed frontally), the mean radiance, and the radiance perceived from a flat surface are plotted as functions of the material reflectance ρ .

Below the limit value $\rho_x = 0.93$, the mean radiance issued from the cavity remains below the radiance issued from the flat surface. Beyond that limit, the opposite is observed. This threshold ρ_x depends upon the cavity aperture α , as shown in Figure 26b for two reasons:

- The irradiance of the facets in the cavity (same in all facets as the cavity is illuminated frontally here) is proportional to $\sin(\alpha/2)$. This tends to darken the cavity as angle α decreases: the flat surface has the highest irradiance, whereas a very closed cavity (e.g., $\alpha = 30^\circ$) has a much lower irradiance.
- Secondly, the interreflections, are stronger as the cavity aperture decreases. This tends to brighten the cavity as angle α decreases.

There is therefore a competition between the darkening effect due to the obliquity of panels and the brightening due to the interreflections. The two effects depend on α but in different ways. This explains the presence of a minimum for ρ_x in the curve plotted in Figure 26b, around 0.93, at α around 40°. This cavity aperture is the most favorable to the brightening effect due to the interreflections in front of the darkening effect due to the facets obliquity, and the reflectance value from which the interreflections bring a gain in mean radiance in comparison to the flat surface is the lowest.

Notice from Figure 26a that when the reflectance ρ is lower than the limit value ρ_x , the mean radiance is strongly attenuated in comparison to the one of the flat surface. This can be interpreted as an increased absorbance by the V-cavity.

The consequence of this loss or gain in radiance, in terms of color appearance, is variable. It depends on whether this concerns a small or large spectral domain. In the case of the white cavity, as the material reflectance is higher than the threshold ρ_x , the spectral radiance of the 45° cavity overpasses the one of the flat surfaces on the whole spectrum.

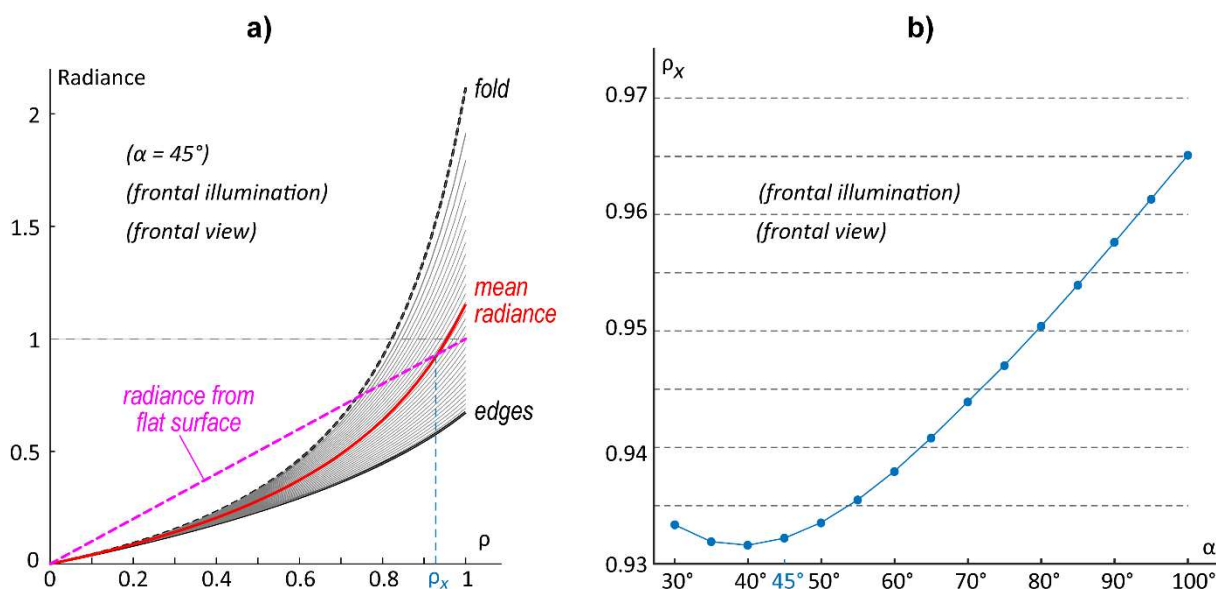


Figure 26 – **a)** Variation as a function of the material reflectance ρ of the perceived radiance issued from a flat surface of this material (dashed purple line), a 45° V-cavity frontally illuminated and frontally viewed (mean radiance, red line), and various facets of this cavity: facets near the fold (solid black line), facets near the edges (dashed black line), other facets elsewhere in the cavity (thin lines). The limit value ρ_x corresponds to the reflectance beyond which the 45° V-cavity is more reflective than a flat surface of same material. **b)** Variation of the limit reflectance ρ_x value as a function of the cavity aperture α .

This is translated into a gain of lightness (see Figure PF3-12a and b). But this is not true for the yellow cavity (see Figure PF3-8a and b): we observe a gain in radiance beyond 530 nm and a loss below that wavelength. This is translated into a very small gain in lightness, and a strong gain in chroma. In the case of magenta, the gain in radiance beyond 640 nm (therefore in a spectral domain where the sensitivity of the visual system is rather

Light interreflections in a Lambertian V-cavity

low) is not enough to compensate the loss in radiance in the rest of the spectrum. This is translated into a gain in chroma, but a loss in lightness (Figure PF3-6a and b). For every other color, the fact that the radiance of the cavity is lower than the one of the flat surface for all wavelengths results systematically in a loss in lightness; and the fact that the lowest radiance values are more attenuated than highest ones explains that in some cases we can have a slight gain in chroma.

Obviously, some microfacets in the V-cavity are the closest to the fold, and therefore can reemit a stronger spectral radiance under a frontal illumination than the flat surfaces do, even if the average spectral radiance doesn't overpass it. It is important to notice that for this to happen, the material reflectance needs to be high enough coherently with the aperture of the cavity, to compensate the darkening linked to the obliquity of the panels). For more open V-cavities, the limit value of reflectance for this to happen is lower. For an almost flat cavity (with a dihedral angle of 179° for example), this limit reflectance is around 0.55, which means that for a reflectance lower than this value, no microfacets can be brighter than the flat surface.

3.8 Metamerism and interreflections

Metamerism is a phenomenon analyzed in colorimetry, where two samples will display the same color under the same illuminant, while having two different spectral power distributions. The colors that matching are then called metamers for the given illuminant. This phenomenon is quite common when considering colors that are close to grays, but becomes scarcer with bright and saturated colors, such as the ones we observed in this chapter. The classical method to lift the metamerism is then to change the illuminant. One could also formulate the hypothesis that two metamers would become distinguishable when structured in a V-groove pattern creating shadows and interreflections, depending on the lighting used. To verify this, we took two spectral distribution powers, extracted from the *Munsell Book of Color* from X-rite, and the other completely fabricated for it to reach metamerism with the first sample, under the equal energy illuminant we are considering so far.

Both the spectra were then used in the model for Lambertian materials to generate a 45° V-cavity structure, under both frontal and diffuse illumination, with a frontal observation. On Figure PF3-14 pp. 26-27 are represented the color gradients of both the metamers, flat and formed in a 45° V-cavity, alongside the average spectra computed for the whole cavity, and the corresponding CIE 1976 $L^*a^*b^*$ coordinates plotted in the L^*C^* and a^*b^* diagrams. This analysis is done for a frontal lighting on Figure on the left page, and for a diffuse lighting on Figure on the right page.

Under a frontal illumination (left page) as well as under a diffuse one (right page), we first observe the metamerism of the flat material's surfaces. When folded into a 45° V-cavity and under both types of illumination, the first material tends to display a more

turquoise color, with the interreflections reinforcing the green sensation at the bottom of the cavity for the frontal illumination. The second material displays a bluer hue.

This is also observable Figure PF3-14c, for the frontal lighting. Once the first material is made into a 45° V-cavity, the interreflection phenomenon steps in and we can see that the mean spectral radiance (dotted purple curve) display a sharper peak around 500 nm, meaning the color becomes greener and a bit less blue. On the contrary, the flat surface's radiance of the second material is lower to begin with, meaning the interreflections will be less intense when the material is folded. As observed with the dotted green curve, the 45° V-cavity displays a lower mean radiance, with a peak as wide as the peak of the flat surface. This corresponds to a greater blue component in the spectrum, illustrated by the bluer gradient.

Under a diffuse illumination, given the fact that the shadowing effect is predominant on the interreflections, the differences between the two folded metamers are slightly less pronounced. As seen on the spectra plot, the spectral radiance of material 1 (dotted purple curve) has a lower peak than under a frontal illumination, but still narrow, leading to a turquoise color as mentioned earlier, but a bit closer to the average color displayed by material 2 folded into a 45° V-cavity.

The disappearance of the metamerism is also observable on the L*C* and a*b* diagrams for both illuminations (Figure PF3-14d, on both pages). Under a frontal lighting on the left page, the metamers display two colors that are separated by roughly 10 units of chroma, and we can see the shift in color on the a*b* diagram, where the folded material 1 tends towards the negative part of a* axis, so a greener color, whereas the folded material 2 color evolved roughly along the line formed the origin of the diagram and the color of the flat material, thus meaning an average color staying bluer. The resulting DE2000 color distance is 4.7, as opposed to 1.87 when the materials are flat. Under a diffuse illumination, on the right page, the diagrams translate the smaller gap between the two structured materials with mostly the shadowing effect intervening, and the resulting color distance is 4.2. Figure PF3-14b on both pages also shows that the color distance doesn't have a monotonous evolution across the V-cavity. In fact, for the frontal illumination, the microfacets located near the fold are showing the highest color distance (around 7), due to interreflections being more intense between close surfaces. On Figure PF3-14b, right page, the predominant shadowing effect under the diffuse illumination shows the highest color distance for the areas that are more shadowed, with still a small contribution of the interreflections. Even though the effects are evolving in opposite directions between the frontal and the diffuse lighting, the color distance curves are quite similar.

The study presented in this section has the interest of showing the impact on metamerism of a structured surface. As an example of use, a widely known problem in sectors like brand management and marketing is the color constancy over various types of support, such as glass, paper, metal... A brand could succeed in obtaining the same apparent color on two types of diffusing background, thus reaching a form of metamerism,

Light interreflections in a Lambertian V-cavity

and a small structure of surface could then alter it to the point of having two distinct colors afterwards. Another example could be found in printed documents security. One could easily verify the authenticity of a document by simply folding an apparent official document in such a way that interreflections would be generated, under a given light and a given angle of folding. The color then displayed would either be the same as the referenced color, or slightly different, revealing a document that would've been forged using a different type of ink.

3.9 V-cavity with two different colors

The last aspect we propose to analyze with the model for Lambertian material is the one where the panels of the V-cavity don't have the same reflectance. Indeed, in the model equation:

$$\mathbf{L} = \frac{1}{\pi} \left(\mathbf{I} - \frac{1}{\pi} \mathbf{R} \mathbf{K} \right)^{-1} \mathbf{R} \mathbf{E}_0 \quad (3.46)$$

we explained that the reflectance matrix \mathbf{R} is a diagonal matrix containing the reflectances of every facet taken across the cavity. If we are to consider that the ridged surface pattern consists of an alternance of two colors, for example cyan and yellow, the reflectance matrix would then be a diagonal matrix with half the diagonal being the reflectance of cyan printed on a Lambertian material, and the other half being yellow ink.

We now offer to study the simulations of two cases. As seen on Figure PF3-15, the first case, illustrated on the upper part of the figure, with **a**, **b**, **c** and **d**, is a V-cavity where the colors of the panels alternate between cyan and yellow being printed on a stack of 5 sheets of non-fluorescent paper. The second one consists of the same material, with two occurrences of cyan followed by two occurrences of yellow, and so on, and is illustrated on the bottom part of the figure, graphs **e**, **f**, **g** and **h**. The dihedral angle of cavity used here is 45° . Four lighting geometries are studied: frontal, two directional collimated light source with directions of incidence being respectively $(\theta, \varphi) = (45^\circ, 0^\circ)$ and $(-45^\circ, 0^\circ)$, and diffuse. To complete the analysis, we vary the observation from the direction with a zenith angle of -75° to 75° , with a 15° , similarly to what is presented in section 3.6. Each observed average spectral radiance are then computed on the visible area of the structure (the visible area of the structure can evolve, as illustrated in section 3.6), and plotted. Above each spectra plot are represented the frontal view of the structure under the specified illumination.

For the first configuration alternating between cyan and yellow, and under a frontal illumination, the average spectral radiance displayed by the structure is represented in Figure PF3-15a. The main observation here is that when the V-cavity is fully visible, between -22.5° and 22.5° , the average spectral radiance displayed is a mix between the cyan and the yellow panels, with a greenish color. The high reflectance of the yellow is

attenuated by the interreflections taking place with the cyan having a lower reflectance. As soon as masking is intervening, we observe either predominantly cyan or yellow. For the same type of lighting, but this time with the second configuration presented on Figure portfolio e, we observe the same greenish and rather dark color for every point of view. The reflectance being quite low, the interreflections are weak. Since the alternance of colors is symmetrical, the direction of observation offers little change in the perceived average color.

For an oblique lighting such as the one presented on Figure PF3-15e, with a 45° zenith angle of incidence, the first configuration displays mostly a cyan color, this panel being the only one to be illuminated. We can furthermore observe that this color is more saturated than under a frontal illumination. The combination of the cyan panel being directly illuminated with the interreflections taking place with the yellow panel being completely shadowed but possessing a high reflectance, is resulting in a brighter and more saturated cyan. The brightness and saturation increase with the observation angle being more and more grazing. As soon as the observation direction includes the shadowed part, the displayed color is instantly darker and located in the deep greens.

The same line of reasoning applies if the lighting geometry is switched to a -45° zenith angle. This time, it's the yellow panel being directly illuminated, on Figure PF3-15c, with the average spectral radiance rapidly decreasing with the observation direction zenith angle including the shadowed cyan part.

For the second configuration, the ridged surface displays the same green color being brighter or darker depending on the observation, since the color pattern is symmetrical.

Finally, under a diffuse illumination, the first configuration, in Figure PF3-15d, displays an average spectral radiance with a brighter color than under a frontal lighting. This is mainly due to the shadowing effect being predominant on the interreflection phenomenon, leading to less interactions between the two panels. We can observe for example that the reflectance of the yellow panel seen from a grazing angle of -75° is higher (between 0.6 and 0.7 for the less absorbed wavelengths) than the yellow seen from the same angle under a frontal lighting, with a reflectance around 0.4 for the most reflected wavelengths.

This section showed the interest in accurately modeling the interreflection phenomenon for structured and scattering materials. The anisotropy of the ridges pattern itself already delivers a strong anisotropy in the perceived color and average radiance, but it can be reinforced with different colors printed either on one side or the other. The interreflections phenomenon can then attenuate both colors and create another color sensation from mixing them under a frontal lighting, or it can make one of them appear even more saturated because of the diffused light by the other color, under an oblique lighting.

On the contrary, one could create interesting effects using the interreflection phenomenon, displaying brighter and saturated colors with a mix of others, and at the

Light interreflections in a Lambertian V-cavity

same time being able to guarantee the appearance under different types of lighting for every point of view, by simply using a color pattern as the one presented in the bottom part of Figure PF3-15. An example can be found in the work of Teun Baar *et al.* [37], with lenticular relief printings, where they analyzed the apparition of image ghosts when printing two different images on a topography allowing one image or the other to appear depending on the observation direction. The light interreflections were not identified as a cause of this phenomenon but could very well be at the root of these ghost images.

3.10 Conclusions

In this chapter, we analyzed the interreflection effects occurring in concave surfaces under various illumination geometries, from a frontal collimated lighting to an oblique directional one, to a perfectly diffuse lighting, through the simple case of V-cavities of infinite length made of a Lambertian material. Interreflections are known to increase the radiance exhibited by the concavities or the corners of the surface, but this stands mainly for a frontal collimated illumination. In case of diffuse lighting, shadowing tends to decrease the irradiance of the surface in the concavities or corners, and therefore to make them darker than would be a flat surface of the same material. The reflectance of the material and the dihedral angle of the cavity, as well as the direction of observation, have also a strong impact on the competition between the interreflection effect and the shadowing effects, which can result in a higher radiance near the fold of the cavity than near its external edges, or in the opposite situation. The coincidence of these phenomena can also lead to change in the perceived color in terms of saturation and change of hue. The latter mostly happens around the wavelengths that are weakly absorbed, and that are reinforced by the interreflections also lowering the already absorbed other wavelengths.

The use of a perfect Lambertian material, which is not physically realistic, shows nevertheless that we can generate correct predictions of the overall aspect of a structured surface, when compared to pictures taken in real life. It allows us to deeply understand the mechanisms of diffuse interreflections and their role in human vision.

Chapter 4.

Light interreflections in a specular only V-cavity

In this chapter, we develop a model of multiple specular reflections in a V-cavity simply made of two flat interfaces (mirror-like surfaces). The model accounts for ray position and orientation and polarization effects occurring at each reflection. We study the change in luminance and chroma for a selection of materials, including metals. Spectral reflectances were predicted for the different materials and various dihedral angles of cavities, under diffuse illumination. We also compare this model with two approximated variants where the light polarization is treated in a simpler way. In most cases, the original model and its approximations predict very similar bi-hemispherical reflectances, but the hemispherical-directional reflectances can vary noticeably in certain observation directions. We finally extend the model to randomly ridged surfaces, where the dihedral angle of the V-cavities varies randomly. This study might help achieving more physically realistic rendering of dielectric or metallic ridged surfaces, for example in computer graphics.

4.1 Introduction

In the previous chapter we developed a model for ridged surface considered made of Lambertian materials. We have shown that the presence of periodical ridges modifies the color of the material in comparison to the case where its surface is flat, in different ways according to the ridge shape and the illumination conditions. Specifically, the color of the ridge surface can be brighter and more saturated than the one of the flat surfaces under frontal collimated illumination, but it is darker and less saturated under diffuse illumination. More importantly, this model was also developed without considering the interface of the material with the air because of their strong scattering properties, rendering virtually negligible the influence of a potential specular reflection. But in the reality, no materials are perfectly Lambertian. Although a surface can show a very scattering and quasi-Lambertian behavior, it still possesses an interface that leads to specular reflection at a grazing angle. For a structure surface with a mirror-like behavior,

it is visible that a certain number of specular reflections takes place and influence the overall aspect of the surface. As illustrated by Figure 27, a building forming a V with only windows on its facades generates several reflections impacting the perceived brightness and color. This chapter will therefore only focus on a structure made of V-cavity that behave in a specular reflection only fashion.



Figure 27 – Building forming a V, with windows generating several specular reflections between the two sides. Credits: Gaël Obein

Recently two studies have addressed the case of non-scattering materials such as metals or clear dielectric materials [38, 39]. They consider surfaces with periodical V-shaped structure like the one used in this manuscript, without the infinite length and periodical hypothesis for the first two, and by assuming that the faces of the ridges are flat, behaving like mirrors. They use what is called a kaleidoscope model, presented first by Zipin [40], where the path of the light in the V-cavity is “unfolded”. It was originally designed to describe the heat transfer in metallic V-grooves, and mostly used today by Mulford *et al.* [41] in the field of radiative transfers.

Light interreflections in a specular only V-cavity

In these studies, different, although similar analytical expressions are derived for the description of the interreflections, which are in this case a finite number of specular reflections depending on the orientation and position of the incident rays in respect to the illuminated ridges, as well as the angular aperture α of the ridges and the refractive index of the material. The first study by Xie et al., dedicated to computer graphics, presents an analytical model of Bi-directional Reflectance Distribution Function (BRDF) for a distribution of specular V-grooves, the second study by Lee *et al.*, also dedicated to computer graphics, extends the application to anisotropic rough surfaces. The model presented in this chapter focuses on the angular radiance perceived from any angle when the surface is illuminated by a completely diffuse light. The first two models assume that incident light is unpolarized, as it often is, and remain unpolarized during the whole multiple reflection model.

To go further on our study, the chapter presents a proposal to model rigorously the polarization of light along the multiple reflection process, in order to see to which extent, the approximation made by the previous studies stands according to the considered material, metal or dielectric. We then use this rigorous model to analyze further the influence of the non-scattering ridged structured on the perceived color of a specular only V-grooved surface. Given its building, the model also implicitly considers the shadowing effect, on the contrary of what is traditionally done in computer graphics, typically in the works of Xie and Lee. Therefore, we also analyze its use in the simulation of a surface with a random roughness. Finally, we compare this rigorous model with two approximate models where light is assumed to remain unpolarized all along (first approximate model), or where the p- and s-polarized components are treated separately (second approximate model). Notice that we assume the same hypothesis on the structures scale: the facets are large enough, e.g. larger than a few tens of micrometers, to prevent visible effects of diffraction, which would be inevitable with such periodically structured facets if they were smaller.

The chapter is organized as follows: we firstly introduce in section 4.2 the formalization of multiple light reflections in a V-cavity with specular facets and derive in section 4.3 the analytical formulas describing the attenuation of the radiance along its path into the cavity, according to the three models. Then, in section 4.4, we sum up the radiances in order to obtain hemispherical-directional and bi-hemispherical reflectances. Predictions are made with various materials, including a dielectric, a semi-conductor, and metals, in order to study the influence of the surface shape (precisely the dihedral angle of the cavities) on their respective spectral reflectances and their color. The differences between the predictions given by the model and two approximated approaches are analyzed for efficiency matters in section 4.5. Section 4.6 deals with an experimental verification of the model. We then propose a study where the model presented is used in order to simulate surfaces with a random roughness in section 4.7. Section 4.8 finally draws the conclusions.

4.2 Multiple reflections process in a mirror-like V-cavity

The schematic view of the V-cavity and its geometry is the same as the one used in previous chapters and is reminded in Figure 28. We consider a direction of incidence for the light, determined by its spherical coordinates (θ, φ) , impacting on one of the two panels forming a dihedral angle α of a V-cavity of infinite length along the x -axis. The width of the panels is normalized to 1.

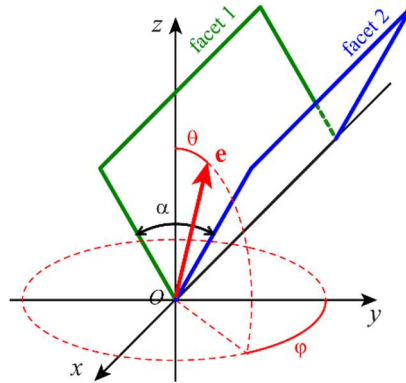


Figure 28 – 3D geometry of one cavity, and vector \mathbf{e} representing the direction of illumination.

Once a light ray enters a cavity, it may undergo one or several successive reflections on the facets. After each reflection, the direction of the ray is modified according to Snell's laws. However, in geometrical optics, it is classical to unfold the rays into their virtual prolongation, which is aligned with the incident ray, as shown on Figure 29 through the example of two rays.

By using this representation for the cavity, the path of one ray is represented by a straight line crossing the successive images of the facets: after a reflection on facet 1, the ray reaches the image of facet 2 (which forms an angle α with facet 1), then the image of facet 1 (which also forms an angle α with the image of facet 2), and so on.

The number of reflections within the cavity depends on both orientation and position of the ray. This is visible in Figure 29, where the two rays are parallel (thus characterized by the same vector \mathbf{e}) and strike facet 2 in different positions: one ray (represented in red; color version online) undergoes 4 reflections, whereas the other ray (represented in orange) undergoes 3 reflections. We remind that the incident irradiance is characterized by a unit vector \mathbf{e} :

$$\mathbf{e} = (\sin\theta\sin\varphi \quad \sin\theta\cos\varphi \quad \cos\theta)^T \quad (4.1)$$

The ray light paths in broken straight lines are featured on Figure 29b, in a projection onto the (yOz) plane of the 3D scene represented on Figure 29a. In the (yOz) plane, the projection of vector \mathbf{e} , denoted as \mathbf{e}^\perp , is:

Light interreflections in a specular only V-cavity

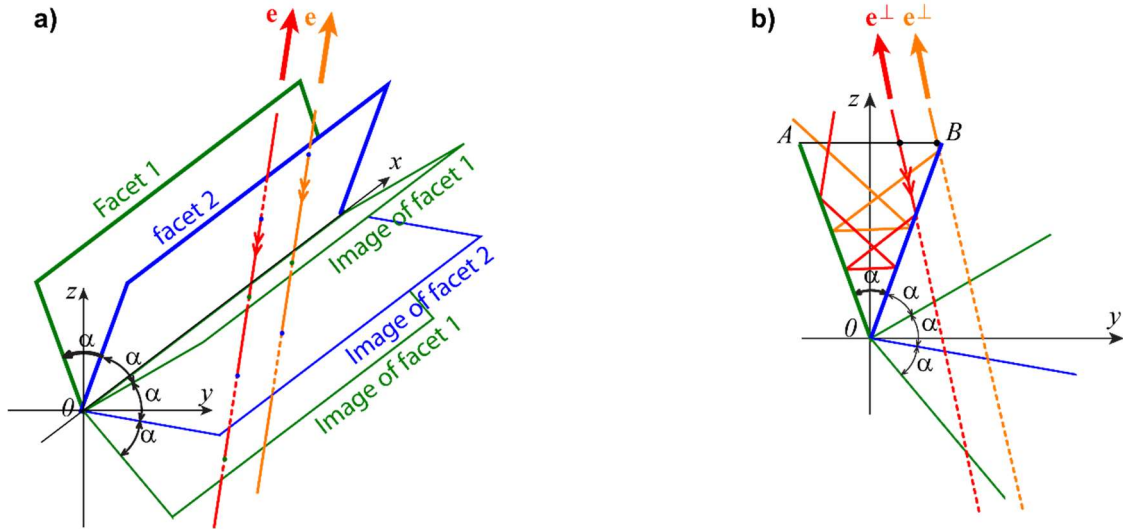


Figure 29 – **a)** Representations of two light rays parallel to the unit vector \mathbf{e} , striking the cavity on facet 2 in different positions. **b)** 2D representation of the two same light rays projected onto the (yOz) vertical plane. The light path can be represented by a straight line joining the successive images of the facets. The projection of the real light paths in broken straight lines is also represented. Geometry for the calculation of the number of reflections, for a same position y_p of the ray, and two different orientations.

$$\mathbf{e}^\perp = (\sin\theta' \cos\theta')^T \quad (4.2)$$

with

$$\theta' = \arctan(\tan\theta \cos\varphi) \quad (4.3)$$

The number of reflections according to the orientation and position of the ray is computed according to the following geometrical considerations, in the (yOz) plane. The orientation of the ray is denoted by the angle θ' given by Eq. (4.3). Its position is described by the point P where the ray meets the line (AB) which joins the extremities of the facets in the (yOz) plane, drawn in Figure 30. This point P has the coordinates $P = (y_p, \cos(\alpha/2))$. The ray meets the unit circle centered in point $O = (0,0)$ in two points: first in point $G = (\sin\beta_G, \cos\beta_G)$, then in point $H = (\sin\beta_H, \cos\beta_H)$. Figure 30 shows two examples for the same position y_p but two different orientations of the ray. In Figure 30a, the ray strikes first facet 1, in Figure 30b, it strikes first facet 2. The facet first met is determined by the following condition: if the meeting point $Q = (y_Q, 0)$ of the ray and the y -axis has a negative abscissa y_Q , facet 1 is met first, otherwise, facet 2 is met first. With some geometric calculations, we find that abscissa y_Q is given by:

$$y_Q = \frac{\sin(\beta_H - \beta_G)}{\cos\beta_G - \cos\beta_H} \quad (4.4)$$

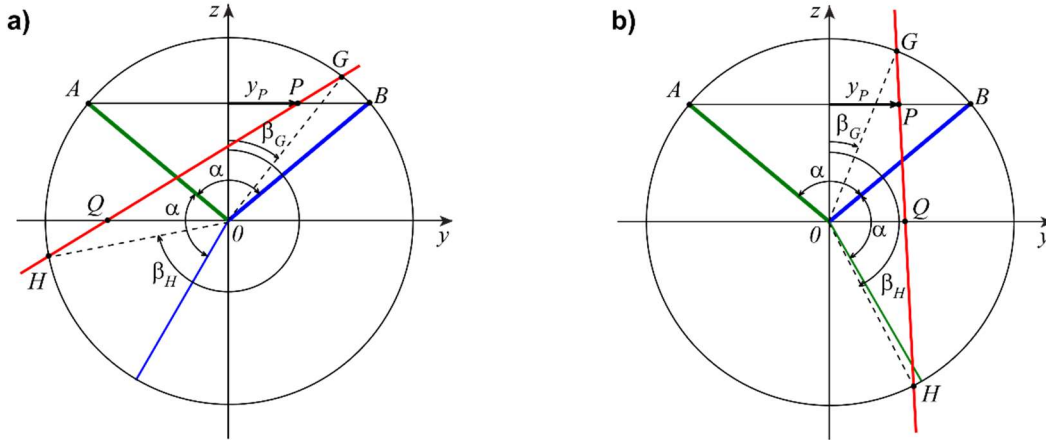


Figure 30 – Geometry for the calculation of the number of reflections, for a same position y_P of the ray, and two different orientations.

where the angles β_G and β_H are computed as follows.

Since

$$\mathbf{PG} = \left(\sin\beta_G - y_P, \cos\beta_G - \cos\left(\frac{\alpha}{2}\right) \right) \quad (4.5)$$

and \mathbf{e}^\perp are collinear, we have:

$$\det \begin{pmatrix} \sin\beta_G - y_P & \sin\theta' \\ \cos\beta_G - \cos\left(\frac{\alpha}{2}\right) & \cos\theta' \end{pmatrix} = 0 \quad (4.6)$$

After some calculations, Eq. (4.6) can be written

$$\sin(\beta_G - \theta') = y_P \cos\theta' - \cos\left(\frac{\alpha}{2}\right) \sin\theta' \quad (4.7)$$

and by noticing that $\beta_G - \theta' < \pi/2$, we obtain

$$\beta_G = \theta' + \arcsin \left[y_P \cos\theta' - \cos\left(\frac{\alpha}{2}\right) \sin\theta' \right] \quad (4.8)$$

Likewise \mathbf{PH} and \mathbf{e}^\perp are collinear, and by following similar reasoning as above with point H in place of point G , therefore with angle β_H in place of β_G , we obtain:

$$\sin(\beta_H - \theta') = y_P \cos\theta' - \cos\left(\frac{\alpha}{2}\right) \sin\theta' \quad (4.9)$$

This time, we can notice that $\beta_H - \theta' > \pi/2$, therefore we have:

$$\beta_H = \theta' + \pi - \arcsin \left[y_P \cos\theta' - \cos\left(\frac{\alpha}{2}\right) \sin\theta' \right] \quad (4.10)$$

Light interreflections in a specular only V-cavity

Figure 30 illustrates the fact that the ray strikes first facet 1 when $y_Q < 0$, and strikes first facet 2 when $y_Q > 0$. Finally, the number of reflections occurring after the first reflection of the first facet met is the number of times angle $\gamma_H - \alpha/2$ contains α . By introducing the angle γ_H defined as:

$$\gamma_H = \begin{cases} 2\pi - \beta_H & \text{when } y_Q < 0 \\ \beta_H & \text{when } y_Q > 0 \end{cases} \quad (4.11)$$

the total number of reflections is given by:

$$m = \text{floor} \left[\frac{\gamma_H}{\alpha} - \frac{1}{2} \right] + 1 \quad (4.12)$$

where the symbol floor [...] denotes the integer part of the number in argument.

4.3 Model for radiance attenuation in a specular V-cavity

Now that the number of light reflections has been determined, we can express the global attenuation undergone by the radiance attached to a given light ray. We then present a model which considers that when the light is reflected in a specular fashion across the V-cavity, it is accompanied by the evolution of the polarization state after each reflection.

The multiple reflections occurring in the cavity bring to the fore the question of the polarization of the light. Even if the light source is incoherent and unpolarized, each reflection partially polarizes the light. It is necessary to rigorously develop the calculation describing the transformation of the polarization and more precisely of its two components s (perpendicular to the incidence plane on the current facet) and p (parallel to it). That enables us to better apprehend the influence of the polarization on the final reflectance of the surface.

Let us compute the Fresnel reflection coefficients for both the s and p components of light. Remind that at each reflection on a facet, or equivalently, at each intersection of the light ray with the images of the V-cavity facets as shown on Figure 30, the incidence plane changes.

At first, the incident wave is represented by its electric field of amplitude E_0 . Because it varies very rapidly in a random manner, this wave is said to be incoherent and unpolarized. It can be represented by the sum of two wave components which are temporally decorrelated, vibrating perpendicularly to each other, and of respective amplitudes E_{0p} and E_{0s} [42]. After their reflection on the first facet, we have:

$$\begin{cases} E_{1p} = r_{1p} E_{0p} \\ E_{1s} = r_{1s} E_{0s} \end{cases} \quad (4.13)$$

which is more conveniently written in matrix form

$$\begin{pmatrix} E_{1p} \\ E_{1s} \end{pmatrix} = \mathbf{R}_1 \begin{pmatrix} E_{0p} \\ E_{0s} \end{pmatrix} \quad (4.14)$$

where

$$\mathbf{R}_1 = \begin{pmatrix} r_{1p} & 0 \\ 0 & r_{1s} \end{pmatrix} \quad (4.15)$$

The wave components of amplitude E_{1p} and E_{1s} are respectively vibrating parallel and perpendicular to the incidence plane 1, and then arrive on facet 2. The incidence plane related to facet 2, labeled 2, a dihedral angle with the incidence plane, denoted as ψ_{12} , and will be computed later.

In this incidence plane 2, the new wave components of amplitude E'_{1p} and E'_{1s} , whose vibration directions are respectively parallel and perpendicular to the new incidence plane, can be derived from the previous amplitudes E_{1p} and E_{1s} , and are given by:

$$\begin{cases} E'_{1p} = E_{1p} \cos \psi_{12} + E_{1s} \sin \psi_{12} \\ E'_{1s} = -E_{1p} \sin \psi_{12} + E_{1s} \cos \psi_{12} \end{cases} \quad (4.16)$$

If we now use the following rotation matrix:

$$\mathbf{M}(\psi_{12}) = \begin{pmatrix} \cos \psi_{12} & \sin \psi_{12} \\ -\sin \psi_{12} & \cos \psi_{12} \end{pmatrix} \quad (4.17)$$

and the diagonal matrix containing the Fresnel reflection coefficients:

$$\mathbf{R}_2 = \begin{pmatrix} r_{2p} & 0 \\ 0 & r_{2s} \end{pmatrix} \quad (4.18)$$

we can then write:

$$\begin{pmatrix} E_{2p} \\ E_{2s} \end{pmatrix} = \mathbf{R}_2 \mathbf{M}(\psi_{12}) \begin{pmatrix} E_{1p} \\ E_{1s} \end{pmatrix} = \mathbf{R}_2 \mathbf{M}(\psi_{12}) \mathbf{R}_1 \begin{pmatrix} E_{0p} \\ E_{0s} \end{pmatrix} \quad (4.19)$$

Iterating for the m reflections, we obtain:

$$\begin{pmatrix} E_{mp} \\ E_{ms} \end{pmatrix} = \mathbf{R}_m \mathbf{M}(\psi_{m-1,m}) \dots \mathbf{R}_3 \mathbf{M}(\psi_{23}) \mathbf{R}_2 \mathbf{M}(\psi_{12}) \mathbf{R}_1 \begin{pmatrix} E_{0p} \\ E_{0s} \end{pmatrix} \quad (4.20)$$

We thus have:

Light interreflections in a specular only V-cavity

$$\begin{cases} E_{mp} = aE_{0p} + bE_{0s} \\ E_{ms} = cE_{0p} + dE_{0s} \end{cases} \quad (4.21)$$

where a, b, c, d are the resulting entries of the matrix product in Eq. (4.20).

By using the fact that the two incident wave components of amplitudes E_{0p} and E_{0s} are temporally decorrelated, we can write the flux F_{mp} and F_{ms} attached to them as:

$$\begin{aligned} F_{mp} &= a^2 F_{0p} + b^2 F_{0s} = (a^2 + b^2) F_0 / 2 \\ F_{ms} &= c^2 F_{0p} + d^2 F_{0s} = (c^2 + d^2) F_0 / 2 \end{aligned} \quad (4.22)$$

where F_0 , F_{0p} and F_{0s} are the fluxes attached to the incident wave and its p and s components.

Finally, the total reflected flux is:

$$F_m = F_{mp} + F_{ms} = (a^2 + b^2 + c^2 + d^2) \frac{F_0}{2} \quad (4.23)$$

The last missing point in the description of the model is the computation of the dihedral angles ψ_{12} , ψ_{23} , etc. In the geometrical configuration we considered in Figure 29, the direction of propagation of the ray in the whole reflection process is given by vector \mathbf{e} , Eq.(4.1). It is contained in the incidence plane j ($j = 1, \dots, m$) with the normal $\mathbf{N}_k^{(j)}$ of the facet $k = 1, 2$. Hence, the normal vector of the incidence plane j , denoted as \mathbf{S}_j , is collinear to $\mathbf{e} \times \mathbf{N}_k^{(j)}$, where symbol \times denotes the cross product operator:

$$\mathbf{S}_j = \frac{\mathbf{e} \times \mathbf{N}_k^{(j)}}{\|\mathbf{e} \times \mathbf{N}_k^{(j)}\|} \quad (4.24)$$

Since the dihedral angle $\psi_{j,j+1}$ between the two planes of incidence is also the angle between their normal vectors, we have:

$$\cos \psi_{j,j+1} = |\mathbf{S}_j \cdot \mathbf{S}_{j+1}| \quad (4.25)$$

4.4 Optical and color analysis of periodically grooved specular surfaces

From the reflectance attached to each incident radiance within the cavity, we now want to display the global results of the model. We propose to first derive the directional-hemispherical reflectance of the structured surface for a directional illumination in each direction (θ, φ) and a collection of light over the hemisphere. This reflectance is equal to the hemispherical-directional reflectance based on a geometric configuration where the

illumination is Lambertian over the hemisphere, and the observer is placed in direction (θ, φ) , as seen in Figure 31.

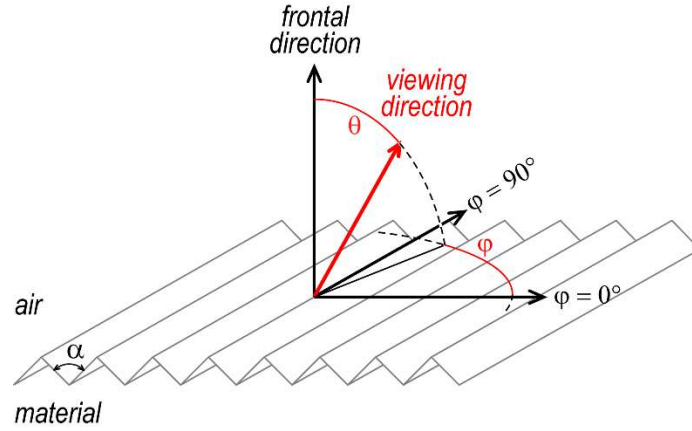


Figure 31 – Representation of the direction of observation of the V-shaped ridged surface.

This representation of the spectral reflectance will allow us to present the model predictions, in terms of perceived average color. Finally, by integrating the hemispherical-directional reflectance over the hemisphere, we obtain the bi-hemispherical reflectance [25], giving information on the global behavior of the surface in response to a diffuse illumination.

4.4.1 Directional-hemispherical reflectance

Let us consider that the cavity is illuminated by directional light from a direction (θ, φ) over a band joining the two edges of the cavity, of length $2\sin(\alpha/2)$ along the y axis and of width Δx along the x axis. We assume that same radiance L_i strikes each point of the band, which therefore receives a uniform irradiance

$$E_i = L_i \cos\theta \Delta\omega \quad (4.26)$$

where $\Delta\omega$ denotes the small solid angle of illumination. Since the illuminated area is $2\sin(\alpha/2)\Delta x$, the incident flux on the band is $F_i = 2\sin(\alpha/2)\Delta x E_i$. On each elementary area within the band, centered around the position y_p and of size $\Delta x dy_p$, the elementary flux is $dF_i = \Delta x dy_p E_i$.

The different elementary fluxes are reflected in various directions according to the microfacet that each one meets first and the number of reflections. By collecting the whole reflected flux, in practice with a measurement device equipped with an integrating sphere, the captured flux F_r is given by

$$F_r = \Delta x E_i \int_{y_p = -\sin(\alpha/2)}^{\sin(\alpha/2)} R(\theta, \varphi, y_p) dy_p \quad (4.27)$$

Light interreflections in a specular only V-cavity

The directional-hemispherical reflectance of the band associated with this orientation of the incident light, and by extension of the whole structured surface made of a juxtaposition of identical bands, is therefore:

$$R(\theta, \varphi; h) = \frac{F_r}{F_i} = \frac{1}{2 \sin(\alpha / 2)} \int_{y_p = -\sin(\alpha/2)}^{\sin(\alpha/2)} R(\theta, \varphi, y_p) dy_p \quad (4.28)$$

4.4.2 Hemispherical-directional reflectance

According to the reverse path principle, this directional-hemispherical reflectance $R(\theta, \varphi; h)$ is also the hemispherical-directional reflectance $R(h; \theta, \varphi)$, corresponding to the measurement geometry where the surface is observed from the direction (θ, φ) and illuminated by Lambertian light. This geometry is the one that we will consider later in our simulations, as it is more consistent with practical observation scenarios, for example a grooved surface placed under a forecast sky and visually observed from any direction.

The picture in Figure 32 shows an example of a V-cavity made of gold with a dihedral angle of 45° , placed in an integrating sphere in order to have a Lambertian illumination, and observed from a direction $(\theta \approx 30^\circ, \varphi \approx 90^\circ)$. On the top of the picture, near the edge of the cavity, we see the different images of each facet by the other one. As the number of reflections increase, the color looks darker and more saturated, an effect that will be studied in more details in the next sections. We also concretely see what was suggested by Figure 29: the number of reflections varies according to the position into the cavity, along the y axis. The red rectangle drawn on Figure 32 represents the area where the cavity can be considered as a cavity of infinite length, without edge effects. The hemispherical-directional reflectance given by Eq. (4.28), and its related color, correspond to the average reflectance, respectively average color, captured over this area.

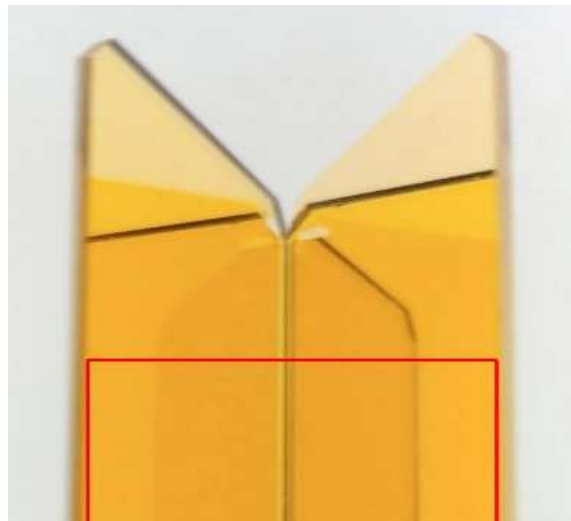


Figure 32 - RGB picture of a V-cavity made of gold with dihedral angle of 45° , placed in an integrating sphere and observed from a direction $(\theta \approx 30^\circ, \varphi \approx 90^\circ)$. The red rectangle features the area where the cavity can be considered as a cavity of infinite length.

In this hemispherical-directional geometry, the specular reflections on the facets do not modify the geometrical extent of the rays; the radiance L_r , perceived in one direction (θ, φ) is therefore:

$$L_r(\theta, \varphi) = R(\theta, \varphi)L_i \quad (4.29)$$

It is possible to display the reflectance given by Eq. (4.28) according to the observation direction on a 2D map thanks to the Lambert azimuthal equal area projection, presented in section 2.3.3.

In order to apprehend the change in reflectance and color due to the dihedral angle of cavity and/or the viewing angle, we computed the hemispherical-directional reflectance by using the model presented in section 4.3, for each wavelength of the light from 380 nm to 730 nm in steps of 10 nm, for different materials, and different dihedral angle values: 180° (flat surface), 150°, 120°, 90°, 60° and 45°. We chose to use the same type of irradiance $E_z = \pi$ all over the hemisphere, as in the Chapter 4. Since this irradiance is then normalized, the reflectance is equivalent to the radiance.

The materials are opaque black glass (refractive index assumed to be 1.5), and materials whose spectral complex refractive indices have been found in the database refractiveindex.info [43]: silicon, a semi-conductor with a behavior similar to a dielectric material in the visible range, and pure metals: gold, silver, copper, and aluminum. Silicon is an interesting study case; the real part of its refractive index in the visible spectrum is very high (around 4) and the imaginary part is low. Since the gap between the two polarizations for this material can be high, it is the best example to study the influence of the polarization model used on the reflectance of the structured surface. For each observation direction (i.e., each point in a map), the spectral reflectance computed is converted by following the same pipeline as presented in chapter 4: a first conversion into CIE 1931 XYZ tristimulus values by considering a D65 illuminant, then, for a better visualization, into CIE1976 L*a*b* color values by considering a perfectly white diffuser under the same illuminant as white reference for the chromatic adaptation. We finally convert these L*a*b* values into sRGB color values in order to obtain displayable digital images. The color maps thus generated are shown in Figure PF4-1.

In addition to the color maps, we computed maps of the maximum number of reflections for each observation direction. In directions where the captured light has undergone one reflection, whatever its entrance position in the cavity is, the corresponding point of the map is colored in light gray (area labeled 1). Other colors for labels 2, 3 and 4 are used when the captured light is subject to have undergone 2, 3 or 4 reflections, respectively. This is represented on the first line of Figure PF4-1.

By observing the color maps related to the dielectric material (black glass) in Figure PF4-1, we can see that the reflectance is globally very weak, except at grazing incidence angles (periphery of the disks) when the cavity dihedral angle is large (reflectance reaches 1 at these grazing angles in the case of the flat surface, i.e., when $\alpha = 180^\circ$). This is coherent

Light interreflections in a specular only V-cavity

with the angular variation of the Fresnel reflectance. For other dihedral angles of the cavity, the highest reflectance peaks are located near the zones where the azimuthal angle $\varphi = \pi/2$, i.e., when the incident light and the x-axis are contained in the same plane of incidence. These directions are the one corresponding to the lowest apparent relief, and always for grazing angles of observation, but it is quite conceivable that the hypothesis of an infinitely long V-cavity made this effect more visible than it would be in a realistic case.

We can also distinguish some discontinuities in the maps, which correspond to the directions at which the number of reflections within the cavity is incremented by one. For example, on the map attached to an aperture of 90° , a central area is lighter than the rest of the graph: it corresponds to rays undergoing one reflection, whereas in the rest of the graphs, rays undergo two reflections. Since the Fresnel reflectance at non-grazing incidence angles is low (less than 0.05 under 45° of incidence), radiance trends rapidly toward zero as the number of reflections increases.

For silicon, a semi-conductor with high refractive index but low extinction coefficient in the visible spectrum of light, the influence of the surface structure is similar as the one observed with black glass but amplified. It looks darker in direction where the number of reflections in the cavity is the highest.

Metals have a higher reflectance than the previous materials due to a higher extinction coefficient. The influence of the surface structure, i.e., of the dihedral angle of cavity, is consequently lower than for black glass and silicon, but remains comparable.

For gold, the Fresnel reflectance depends on the wavelength of light, being much higher for long wavelengths than for short wavelengths. This is at the origin of the intense yellow color displayed in case of small dihedral angles. The color variations concern the chroma rather than the lightness. Comparable effects are observed with copper. For achromatic metals with high reflectance, the attenuation of light at each reflection is low, and the number of reflections has a weak impact on the amount of light that exits the cavity: the reflectance is very high in every observation direction. This is especially true for silver, whose reflectance, near 1, looks constant over the whole hemisphere. With aluminum, an attentive observation of the maps allows us to distinguish the effect of the dihedral angle of cavity, which is like the one observed with the other metals.

Following the same line of reasoning as for the reflectance maps presented in Figure PF4-1, two chromatic metals, copper and gold were selected and for each dihedral angle of the V-cavity presented earlier, three directions of observation were extracted from the reflectance maps: the frontal observation with a zenith angle $\theta = 0^\circ$ and an azimuth angle $\varphi = 0^\circ$, the oblique and perpendicular to the x-axis direction with $\theta = 45^\circ$ and $\varphi = 0^\circ$, called "oblique-perpendicular", and the oblique and parallel to the x-axis direction with $\theta = 45^\circ$ and $\varphi = 90^\circ$, called "oblique-parallel" hereinafter. These directions are illustrated in Figure 31.

For each observation direction, dihedral angle and metal, the spectral hemispherical-directional reflectance factor is plotted in the top part of Figure PF4-2, along with the

corresponding CIE 1976 $L^*a^*b^*$ coordinates in their respective L^*C^* diagrams below. The graphics display the reflectance factors for each angle of cavity and each direction of observation. The frontal observation ($0^\circ, 0^\circ$) is represented by a solid line, the oblique and perpendicular direction ($45^\circ, 0^\circ$) by a dashed line, and the oblique and parallel direction ($45^\circ, 90^\circ$) by a dotted line.

On the top left of Figure PF4-2 is the hemispherical-directional reflectance factors for the copper. In green is plotted the flat surface, and under a diffuse illumination, all the other reflectance factors are lower, and decreasing with the dihedral angle, as observed before in the case of Lambertian materials. Depending on the point of view, in the case of an angle of cavity of 60° for example, the frontal and the oblique-parallel often coincide since both these directions are not subjected to masking. On the other hand, the oblique-perpendicular observation direction bears some masking, since the zenith angle is at 45° . Therefore, similarly to the masking effect and its influence, illustrated in section 3.6, only the visible part is used to predict the perceived radiance attached to this reflectance factor. Since as illustrated in Figure PF4-1 this area corresponds to a given number of specular reflections, in this case, 1 or 2 reflections possible, the angular domain where 3 reflections can happen in a 60° V-cavity is masked. Another example of the importance of masking's influence is that the 90° V-cavity viewed under the oblique-perpendicular direction is even higher than the 120° V-cavity viewed under the same configuration. The corresponding curve is not visible because confounded with the flat surfaces. This is caused by the fact that the visible area in the 90° V-cavity corresponds to a zone where only 1 reflection is happening, because one of the panels is viewed frontally, but up to 2 reflections are possible in the 120° one.

This difference is also translated through the L^*C^* on the bottom left part of Figure PF4-2. We can see that the lightness is decreasing along with the cavity angle, similarly to the results observed in chapter 4. We can also observe that the chroma is increasing as well, since the more closed are the cavities, the more saturated is the perceived color, enhanced by the specular interreflections. The strong dependence to the observation direction is also visible here. The point representing the 90° V-cavity under an oblique-perpendicular observation (yellow triangle) is confounded with the flat surface. As expected, the lightness and chroma displayed by this configuration is more luminous and with a less saturated color than the one for the frontal and the oblique-parallel observation (yellow circle and cross). The same thing happens for the other angles, depending of the areas intercepted by the observer, conditioning the number of reflections observed, and therefore the lightness and color saturation.

On the right part of Figure PF4-2, the same observations can be done for the case of gold. But since gold is a more reflective metal than copper, the decrease in lightness is less shown, but still with an important increase of chroma with a decreasing angle of V-cavity.

These results show the strong importance of an interface between the air and the material, and emphasize the fact that the contribution of the specular reflections to the interreflection phenomenon could constitute a great part in the overall appearance of a

Light interreflections in a specular only V-cavity

ridged periodical surface, under a diffuse illumination as well as a directional one. They also illustrate the importance of considering every reflection possible in a given configuration, because doing otherwise could underestimate the difference of change in lightness and chroma between two different points of observation, even though the anisotropy of the surface would strongly differentiate between them in the first place.

4.4.3 Bi-hemispherical reflectance

The bi-hemispherical reflectance corresponds to a measurement geometry where the sample is illuminated by Lambertian light, and the reflected light is collected all over the hemisphere. It is obtained by integrating over the hemisphere the angular reflectance given by Eq. (4.28). It is a general definition for the ratio of the flux reflected into the hemisphere to that which is incident over the hemisphere. As such, it characterizes here the transfer function of a ridged specular surface in response to a diffuse illumination.

The irradiance on the structured surface is related to the radiance L_i according to the equation:

$$E_i = \int_{\theta=0}^{\pi/2} \int_{\varphi=0}^{2\pi} L_i \cos\theta \sin\theta d\theta d\varphi = \pi L_i \quad (4.30)$$

and the flux reflected by a band of area $2\sin(\alpha/2)\Delta x$ on the surface is given by Eq. (4.27). The exitance is the sum of the reflected radiances expressed by Eq. (4.29):

$$M = \int_{\theta_r=0}^{\pi/2} \int_{\varphi_r=0}^{2\pi} L_r(\theta_r, \varphi_r) \cos\theta_r \sin\theta_r d\theta_r d\varphi_r \quad (4.31)$$

Finally, the bi-hemispherical reflectance is given by:

$$\bar{R} = \frac{M}{E_i} = \frac{1}{\pi L_i} \int_{\theta_r=0}^{\pi/2} \int_{\varphi_r=0}^{2\pi} L_r(\theta_r, \varphi_r) \cos\theta_r \sin\theta_r d\theta_r d\varphi_r \quad (4.32)$$

which yields, according to Eqs. (4.28) and (4.29),

$$\bar{R} = \frac{1}{2\pi \sin(\alpha/2)} \int_{\theta_r=0}^{\pi/2} \int_{\varphi_r=0}^{2\pi} \int_{y_p=-\sin(\alpha/2)}^{\sin(\alpha/2)} R(\theta_r, \varphi_r, y) dy_p \cos\theta_r \sin\theta_r d\theta_r d\varphi_r \quad (4.33)$$

Using Eq. (4.33) with $R(\theta_r, \varphi_r, y)$ predicted by the rigorous model, we computed the spectral bi-hemispherical reflectances for the same dihedral angles of cavity and materials as in Fig. 6. The values at one wavelength, 550 nm, are presented in Table 2.

The spectral bi-hemispherical reflectances obtained for chromatic metals such as gold and copper, and also for silver, aluminum and silicon are plotted in Figure PF4-3 to PF4-

7, pp 36-40 of the portfolio, in the left column of each page. The reflectances are represented alongside the CIE1976 L*a*b* color space L*C* and a*b* diagrams.

Table 2 - Bi-hemispherical reflectance at 550 nm (in %)

<i>Material</i>	<i>Dihedral angle of the V-cavity</i>					
	45°	60°	90°	120°	150°	180°
Black glass	0.9	1.6	3.5	5.5	7.3	8.6
Silicon	11.0	16.6	26.4	34.0	36.8	37.3
Gold	66.3	72.9	80.0	83.6	85.1	85.4
Silver	89.7	92.1	94.4	95.6	96.0	96.1
Copper	33.9	42.8	54.4	61.2	63.9	64.6
Aluminum	77.1	82.2	87.4	90.2	91.0	90.9

All these values and spectra confirm the tendencies featured by the color maps shown in Figure PF4-1: as the dihedral angle decreases, reflectance also decrease and the surface has a darker appearance, because of a higher number of light reflections in the cavity which provokes more successive attenuations. This attenuation effect is stronger at wavelengths for which the material is less reflective or more absorbing, which explains that cavities with a smaller dihedral angle exhibit a more chromatic color, chroma being generally correlated with the contrast between highest and smallest reflectance values in the visible spectrum of light. This is clearly visible and especially true for chromatic metals such as copper and gold, as shown in the picture of Figure 32. In the case of non-chromatic metals like silver and aluminum, the changes are more discreet due to their high reflectivity. In the case of a dielectric such as silicon, the drop in lightness is significant, due to the shadowing effect and polarization components being totally transmitted for some geometrical configurations of incidence during the multiple reflections process.

Although the color of metals becomes more chromatic with the aperture decreasing, it is worth noticing that the hue remains unchanged in the case of gold and copper. For the more achromatic metals, we also see very small difference, with the exception of silver. Compared to aluminum, silver is a bit yellower, and this difference is accentuated by the size of the V-cavity aperture.

Remind that the fact that the surface looks darker with smaller dihedral angles of cavity has to do with shadowing or masking effects, widely used in models for light scattering by rough surfaces [44]. In our model, shadowing is implicitly but rigorously accounted for, as all possible ray paths are considered from their entrance to their exit of the cavity. With facets of reflectance 1, all rays would exit the cavity and the bi-hemispherical reflectance would be 1.

4.5 Approximate models

We have already presented a model for V-grooved surfaces with a mirror-like behavior, with a precise computation of polarization state change throughout the multiple specular reflections process. We offer to present two approximated models and compare their results, to analyze the possible trade-offs that could be made between accuracy of the models and efficiency of the computations.

4.5.1 First approximate model: light remaining unpolarized

Let us consider an unpolarized light ray reflected on an interface between a first medium, in our case always air, and a second medium. It is coming from the first medium with a local incidence angle θ_i . The reflectance, denoted as $R(\theta_i)$, is the average of the squared modules of the Fresnel coefficients for the s (perpendicular) and p (parallel) components [23]:

$$R(\theta_i) = \frac{1}{2} \left(|r_p(\theta_i)|^2 + |r_s(\theta_i)|^2 \right) \quad (4.34)$$

Then, by multiplying the successive Fresnel reflectances $R(\theta_i)$ corresponding to the different reflections on facets, we obtain the total reflectance for one path of the light. We insist on the fact that the interface of the material does not polarize the light at all. This is of course untrue but allows for an approximated formulation of the problem. Note that we also ignore the part of the light transmitted into the material (we can consider that it is absorbed, as it is the case for metals and dark dielectrics).

For each reflection, we compute the local incidence angle θ_i . It can be easily obtained through the dot product between vector \mathbf{e} , which describes the direction of the ray, and the normal of the facet, or image of facet, on which the considered reflection occurs.

We remind that the facets have the normal vectors \mathbf{N}_1 and \mathbf{N}_2 given by

$$\mathbf{N}_1 = \begin{pmatrix} 0 \\ \cos(\alpha/2) \\ \sin(\alpha/2) \end{pmatrix} \quad \text{and} \quad \mathbf{N}_2 = \begin{pmatrix} 0 \\ -\cos(\alpha/2) \\ \sin(\alpha/2) \end{pmatrix} \quad (4.35)$$

The local incident angle for the first reflection depends on whether the ray first meets facet 1 or facet 2, therefore on the sign of the parameter y_ρ defined by Eq. (4.4):

$$\theta_i^{(1)} = \begin{cases} \arccos(\mathbf{e} \cdot \mathbf{N}_1) & \text{if } y_\rho < 0 \\ \arccos(\mathbf{e} \cdot \mathbf{N}_2) & \text{if } y_\rho > 0 \end{cases} \quad (4.36)$$

where symbol " \cdot " denotes the dot product.

The next reflections, if any, occur on images of facets whose normal vector are denoted as $\mathbf{N}_1^{(j)}$ or $\mathbf{N}_2^{(j)}$ if the first reflection occurs on facet 1, respectively on facet 2. These normal vectors, for $j = 1$ to the number of reflections m given by Eq. (4.12), are given by:

$$\mathbf{N}_1^{(j)} = \begin{pmatrix} 0 \\ \cos(\alpha/2 + (j-1)\alpha) \\ \sin(\alpha/2 + (j-1)\alpha) \end{pmatrix} \quad (4.37)$$

and

$$\mathbf{N}_2^{(j)} = \begin{pmatrix} 0 \\ -\cos(\alpha/2 + (j-1)\alpha) \\ \sin(\alpha/2 + (j-1)\alpha) \end{pmatrix} \quad (4.38)$$

and the local incident angle is given by

$$\theta_i^{(j)} = \begin{cases} \arccos(\mathbf{e} \cdot \mathbf{N}_1^{(j)}) & \text{if } y_q < 0 \\ \arccos(\mathbf{e} \cdot \mathbf{N}_2^{(j)}) & \text{if } y_q > 0 \end{cases} \quad (4.39)$$

Finally, the global attenuation of the radiance according to its position y_p between $-\sin(\alpha/2)$ and $\sin(\alpha/2)$, and its orientation (θ, φ) , is given by the reflectance:

$$R(\theta, \varphi, y_p) = \prod_{j=1}^m R[\theta_i^{(j)}] \quad (4.40)$$

Notice that according to the Helmholtz reciprocity principle, a ray following the same path within the cavity but in opposite direction would undergo the same attenuation. Hence, $R(\theta, \varphi, y_p)$ can denote the attenuation for the ray entering or exiting the cavity at the angle (θ, φ) through the position y_p .

4.5.2 Second approximate model: separate polarization components

Regarding the polarization of light along the multiple reflection process within the cavity, a second approximate model is built by assuming that the p and s polarized components of the incident light (half the total radiance for each one) follow the same multiple reflection process. The p -polarized light component remains p -polarized after each reflection (therefore vibrating alongside each successive incidence plane), and the s -polarized light component remains s -polarized (therefore vibrating perpendicularly to each successive incidence plane). The model is similar to the first approximate model, except that Eq.(4.40) is computed twice, a first time by substituting the Fresnel reflectance for unpolarized light, $R[\theta_i^{(j)}]$, with the one for p -polarized light, $R_p[\theta_i^{(j)}]$, and

Light interreflections in a specular only V-cavity

a second time by substituting $R[\theta_i^{(j)}]$ with the Fresnel reflectance for s-polarized light, $R_s[\theta_i^{(j)}]$. Two reflectance components are obtained, $R_p(\theta, \varphi, y_p)$ and $R_s(\theta, \varphi, y_p)$, and their average forms the total reflectance:

$$R(\theta, \varphi, y_p) = \frac{1}{2} [R_p(\theta, \varphi, y_p) + R_s(\theta, \varphi, y_p)] \quad (4.41)$$

4.5.3 Comparison of the models

In order to see how much the approximate models presented in section deviate from the rigorous model, we propose to compare reflectance maps, colors and lightness values predicted by the three models, for a selection among the materials and dihedral angles of cavity considered in section 4.4 by favoring the ones which exhibit the highest differences. In Figure 33, the hemispherical-directional reflectance maps are shown for silicon at a dihedral angle of 45° . There is a sensible difference between the three models for observation in the direction of the ridge (φ around 90°) at a grazing zenith angle (upper part of the hemisphere projection): the non-approximated model predicts a lower reflectance in this case.

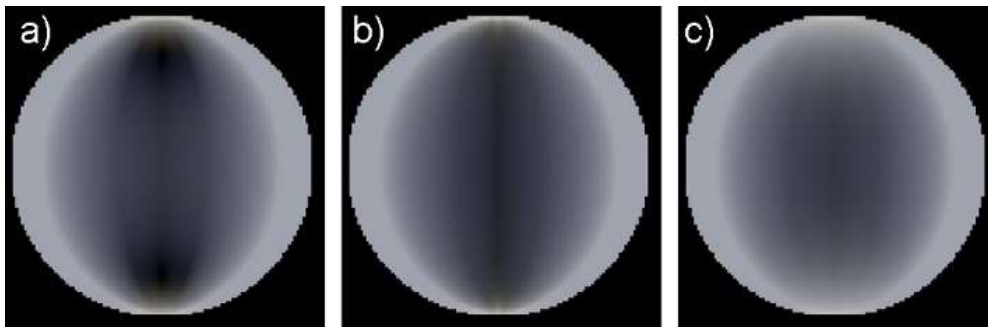


Figure 33 - Color maps of the hemispherical-directional reflectance thanks to the Lambert azimuthal equal area projection, generated for silicon, with a dihedral angle of cavity of 45° , by using **a)** the rigorous model taking into account the polarization of light, **b)** the first approximate model assuming that light remains unpolarized after each reflection, and **c)** the second approximate model where the p - and s -components are assumed to be multiply reflected in parallel, independently from each other.

In Figure 33, the lightness profile of these three maps are compared along the horizontal diameter of the maps (observation perpendicular to the ridge, i.e., $\varphi = 0$ or π) and their vertical diameter (observation parallel to the ridge, i.e., $\varphi = \pi/2$ or $3\pi/2$). The difference between the rigorous model and its two approximate versions is once again well visible, except in graph a) where the rigorous and 2nd approximate model are equivalent when $\varphi = 0$: all multiple reflections occur in the same incidence plane, therefore the p -polarized component remains p -polarized and the s -polarized component remains s -polarized all along the multiple reflection process. In graph b), however, the three models differ dramatically. The fact that the lightness approached 0 near 63° is

because light strikes a facet with an incident angle near the Brewster angle while being almost totally p -polarized, which can be rendered only by the rigorous model, not the approximate ones. Comparable differences are obtained with gold, as well as the other materials, although it is less visible (color maps not reproduced here).

Finally, in Table 3, we compare, using the CIE2000 ΔE metric the color differences associated with the bi-hemispherical reflectance predicted by the rigorous and the first approximate models for various materials, once again according to the dihedral angle of cavity. The color differences are very small for most materials, except at small dihedral angles of cavity for silicon, the material for which we have shown that the differences between the different models are the more pronounced. For this material, we also compare the colors issued from the rigorous and second approximate model, the deviations being even higher than the ones observed between the rigorous and first approximate model. For the other materials, and other angles for the silicon, the colorimetric distance CIE 2000 is low, therefore almost non distinguishable.

Table 3 - CIE 2000 ΔE values between colors corresponding to spectral reflectances predicted by different models

<i>Material^a</i>	<i>Dihedral angle of the V-cavity</i>					
	45°	60°	90°	120°	150°	180°
Black Glass ^a	0.09	0.42	0.27	0.15	0.09	0.00
Gold ^a	0.09	0.25	0.20	0.12	0.07	0.00
Copper ^a	0.10	0.10	0.04	0.45	0.34	0.00
Silicon ^a	0.61	1.13	1.00	0.27	0.25	0.00
Silicon ^b	4.96	4.57	2.47	0.50	0.04	0.00

^a ΔE value computed between the colors corresponding to the spectral reflectances predicted by the rigorous and 1st approximate models;

^b ΔE value computed between the colors corresponding to the spectral reflectances predicted by the rigorous and 2nd approximate models.

We would like to insist on the necessity to take all reflections of light into account, even though it is often assumed, especially in computer graphics, that one or two reflections suffice to obtain accurate or physically realistic color rendering of a structured surface. Table 4 illustrates the difference between bi-hemispherical reflectances that we would obtain by considering only the rays being reflected once within the cavity (the other rays being assumed to be blocked by a neighboring facets therefore ignored), or the rays being reflected once or twice, or rays reflected up to three times, and finally the rays reflected up to four times, for a cavity made of silver at 550 nm ($n = 0.1249 + i3.3391$), silver being a highly reflective material. The reflectance values in the table are significant enough to show that it is crucial to account for all reflections, as recent studies in computer graphics also noticed, even though they used a model comparable to the one that we call here the first approximate model [38, 39].

Light interreflections in a specular only V-cavity

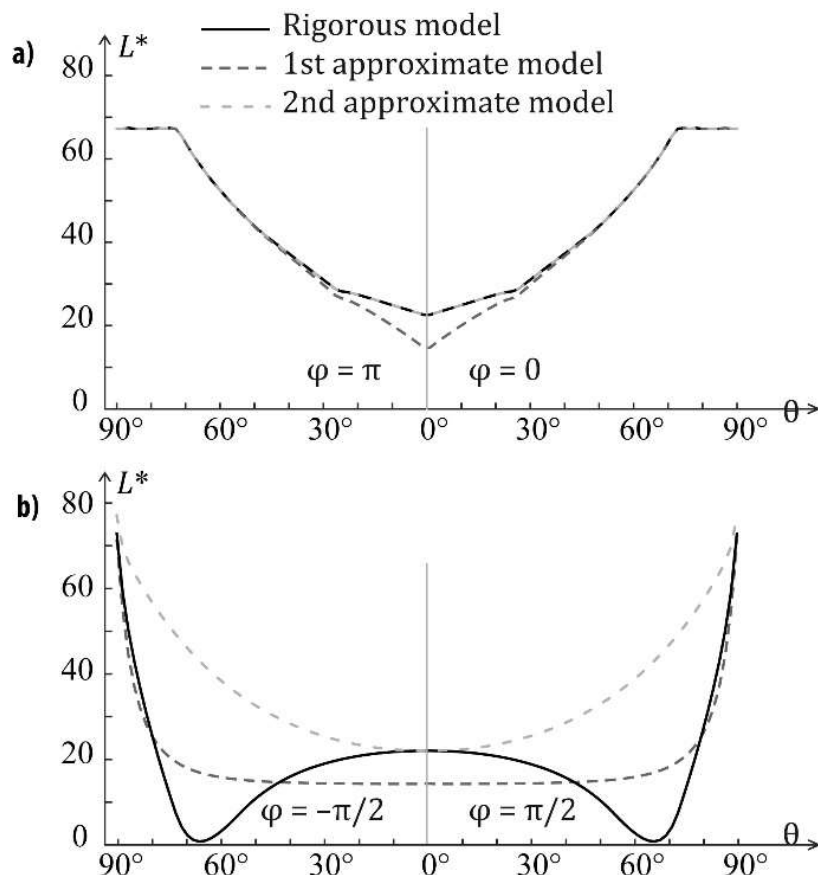


Figure 34 - Lightness L^* in the CIE1976 $L^*a^*b^*$ color space computed from the spectral reflectance of silicon according to the rigorous model and the two approximate ones for a dihedral angle of cavity of 45° , as a function of the polar observation angle θ when (a) the observation direction is perpendicular to the ridges ($\varphi = 0$ or π) and (b) when it is parallel to the ridges ($\varphi = \pi/2$ or $3\pi/2$). These curves correspond to Lightness profiles of the (a) horizontal diameter and (b) vertical diameter of the maps shown in Fig. 8.

Table 4 - Bi-hemispherical reflectance (in %) at 550 nm of a V-cavity made of silver

Number of reflections considered	Dihedral angle of the V-cavity		
	45°	60°	90°
1	13.4	24.3	54.7
2	39.0	66.7	94.4
3	71.3	92.1	
4	89.7		

4.6 Experimental verifications

After analyzing the various predictions of our presented model for specular materials, we built an experimental set-up to measure the accuracy of these predicted reflectances and try to see the correspondence with real metallic samples.

To realize this experiment, three types of samples were used. Particles of copper, gold and silver were deposited thanks to an evaporation process onto three pairs of microscope slides, one pair per metal. A stand was designed, and 3D printed in order to hold the pairs of metallic deposit and precisely form a 45° V-cavity. The most difficult part of the set-up was to create a Lambertian source of light. To do so, an integrating sphere with a 50 cm diameter coupled with two LEDs white sources were put in place. The light source were two commercial white LED lightbulbs with an unknown spectral power distribution. Thanks to the diffusion taking place in the integrating sphere, the resulting outgoing illumination is supposed to be Lambertian on the surface of the sphere. Therefore, the samples are mounted next to the sphere in order to match the edges of the V-cavity with the surface of the sphere. Indeed, the model presented earlier in this chapter makes the hypothesis of a uniform incident lighting on the plan delimited by the edges of the cavity. Finally, to perform the measurement of the hemispherical-directional reflectance of the samples, we used a hyperspectral camera from SPECIM. A schematic view of the set-up is visible on Figure 35, and picture of the sample take from the point of view of the camera is shown in Figure 36.

This camera is supplied with two high-power light sources as well as a procedure of calibration, in order to obtain correctly normalized pictures respectively to the lighting used. Instead, the chosen way of extracting reflectance measurement from the hyperspectral images is a more controlled one. We used the raw images taken by the device from a frontal point of view and selected our own white and black references in the image, for example a reflectance from the white wall of the sphere, and a reflectance from the dark background, behind the sample. In order to obtain the final measured reflectance factor $\hat{R}_{measured}$, the computation used is:

$$\hat{R}_{measured} = \frac{R_{sample} - R_{dark}}{R_{white} - R_{dark}} \quad (4.42)$$

The corresponding hemispherical-directional spectral reflectance factors were then plotted in Figure 37, for the three metallic samples. The measured reflectance factor is represented by a solid black curve. It is important to note that the direction of observation of the camera was roughly tilted by $\sim 15^\circ$ of zenith angle relatively to the optical axis, and by $\sim 15^\circ$ by turning the stand of the V-cavity. This was done in order to prevent the camera of seeing its own reflection, while having the entire V-cavity still visible. Since the images taken by the camera are “hyperspectral cubes”, meaning each pixel in the image contains a spectrum, we selected a pixel in the V-cavity that was located near the corner, in order to have a spectrum containing every reflection of the light possible.

Light interreflections in a specular only V-cavity

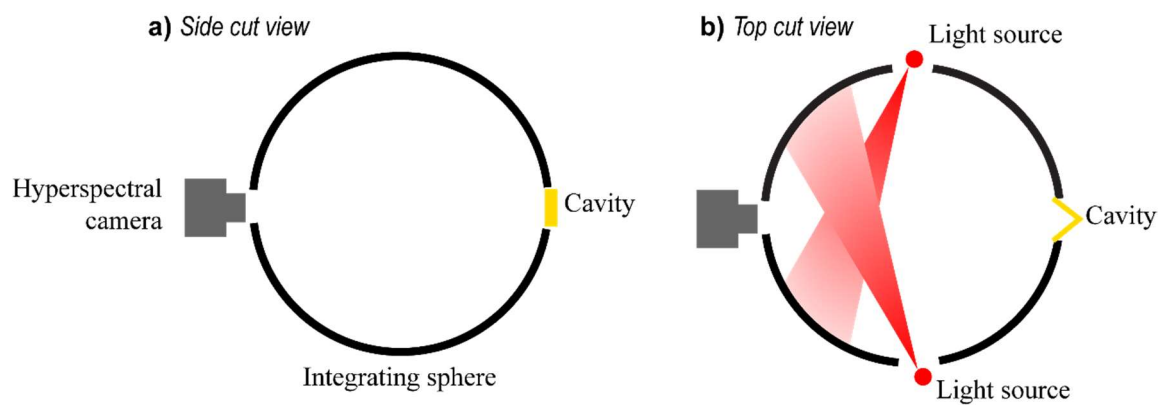


Figure 35 – Measurement set-up.

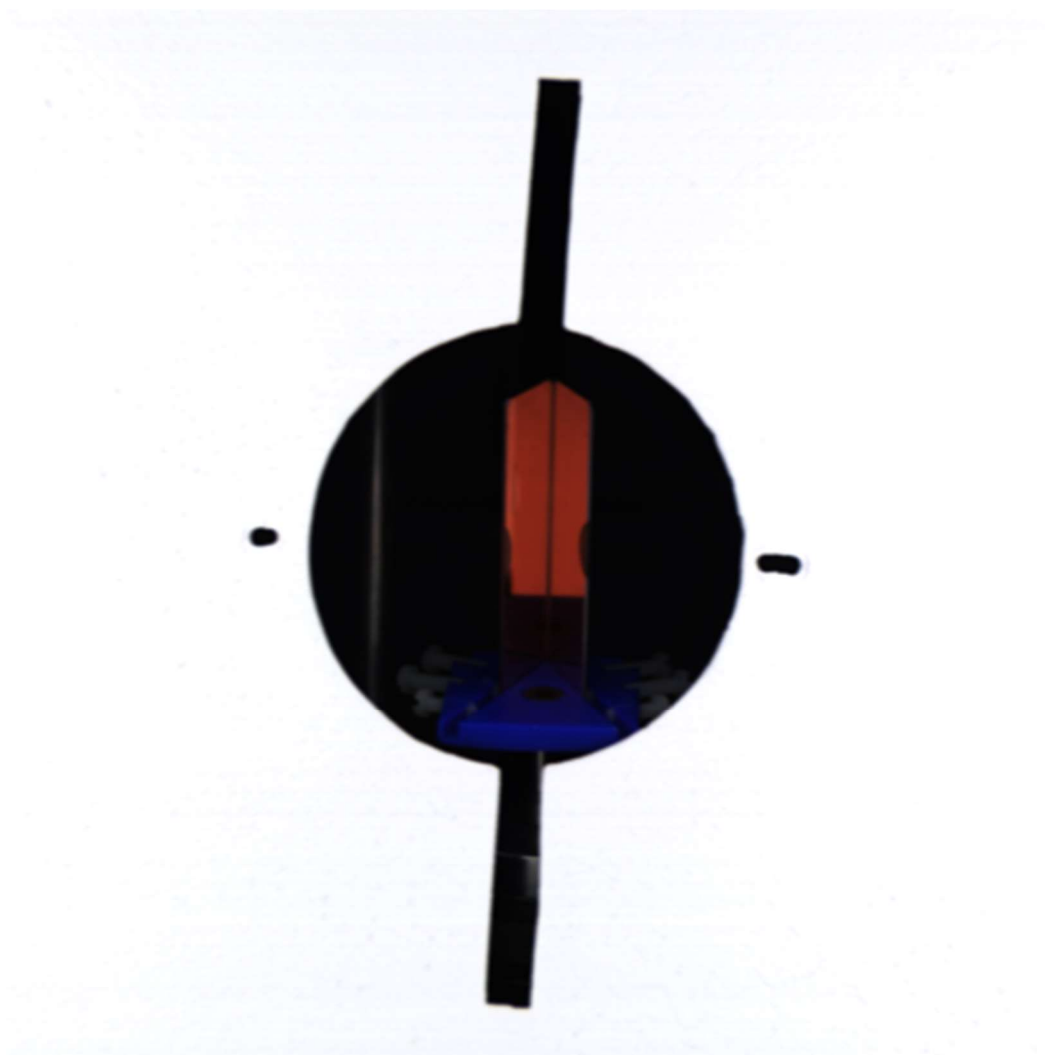


Figure 36 - 45° V-cavity made of two microscope slides with copper deposit, beside a hole of the integrating sphere. The image has been captured by the hyperspectral camera located behind another hole of the integrating sphere, and transformed into color for preview.

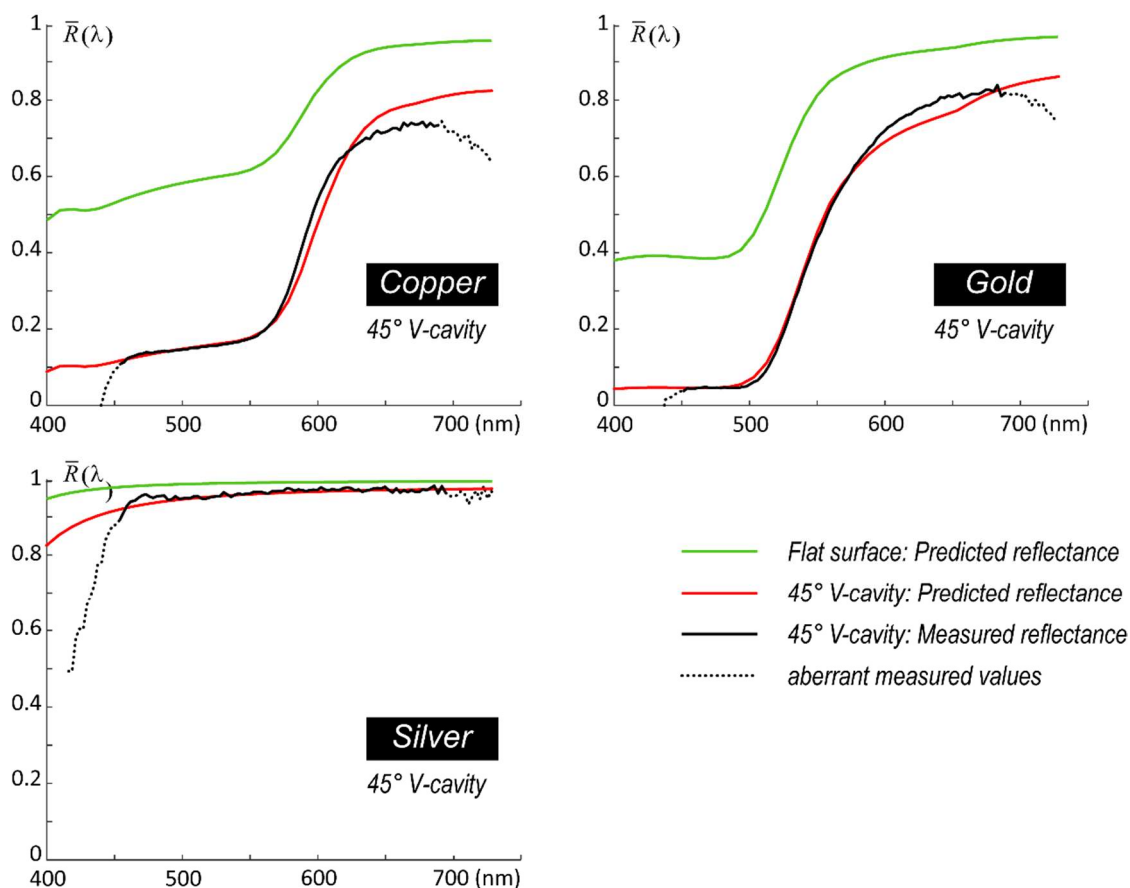


Figure 37 - Comparison between simulated (red curves) and experimental (black curves) spectral hemispherical-directional reflectances, for a 45° V-cavity made of copper, gold or silver, viewed from a direction of observation with a $\theta \approx 15^\circ$ zenith angle and a $\varphi \approx 15^\circ$ azimuth angle and taken near the fold of the cavity. The reflectance of the flat materials are shown in green line.

The corresponding predicted reflectance, taken from the hemispherical-directional reflectance maps shown earlier in section 4.4.2 are plotted in red solid curves. The optical indices used for the predictions were taken from refractiveindex.info, except for the silver, for which the index was taken from [46]. They were computed for a direction of observation using the same approximated angles. The green solid curve is the reflectance from the flat material. An offset was added to the measurement curves in order to compensate the difference in lightness between the set of data.

We can observe a good correspondence between the prediction of the model and the measured hemispherical-directional spectral reflectances. It also shows that the model we developed, implicitly considering the shadowing effect (alongside the small changes in polarization state for these three materials) can correctly predict the appearance of specular V-shaped ridges and their perceived brightness and color. It is also important to note that the part of the black solid curves that are dotted correspond to the wavelengths ranges where the measurements are deriving from the expected trend. This is mainly because white LEDs have null spectral values below 450 nm and above 700 nm, therefore

Light interreflections in a specular only V-cavity

yielding impossibilities when normalizing the data. But since the surfaces analyzed here are real, the experiment presented an interest in its realization despite the difficulties in meeting the same configurations in the experiences and the simulations.

In order to have more precise results, the experimental set-up could be improved by using an illumination calibrated especially for the hyperspectral camera we used, as well as presenting a good spectral power distribution without any wavelength band being weaker than others. The use of a more recent and fully calibrated integrating sphere could also ensure a uniform irradiance on all its surface, and especially on the sample. We also used a fabricated support for our samples that could be improved with several opto-mechanical mounts with verniers in order to better control the lighting and observation angles. Finally, we considered a 45° V-cavity sample because of its interest in our study, but 45° being a divisor of 180°, the camera was bound to see itself in the sample under a 0°:0° geometry. Using another dihedral angle such as 50° could avoid this effect.

4.7 Optical and colorimetric analysis of randomly grooved specular surfaces

Previously, we analyzed the interreflections occurring in a structured surface made of parallel V-cavities, with flat and mirror-like faces under a Lambertian illumination. The proposed model is considering the exact number of light reflections occurring in the structures, in order to accurately predict the reflectance according to the observation angle. The following section will address the use of our model, this time in the case of randomly ridged surfaces. In the first subsection we will present the approach and then argue about its interest compared to other conventional and well-known process for generating surfaces with random roughness.

4.7.1 Bi-hemispherical reflectances

The goal is to use the model for specular only V-cavity to generate surfaces with a random one-dimensional roughness, as presented in Figure 38, where on the left we see the example of the type of topography we used so far in this manuscript, and on the right, an example of parallel ridges with random apertures, simulating a random roughness.

The type of model we consider in this work deals with a characteristic size of the roughness pattern typically larger compared to the wavelength. With these considerations, the diffraction phenomenon becomes negligible. Like the work of Cook-Torrance [6], the V-cavities are distributed according to a probability function, in the present case the Beckmann distribution.

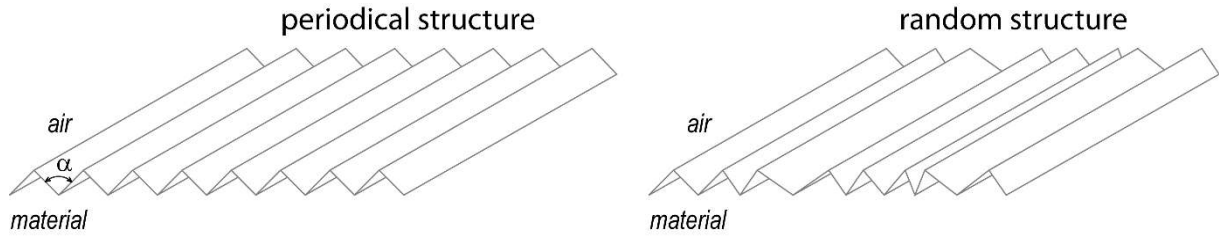


Figure 38 - Structured surface with parallel, periodical, and identical V-shaped ridges of dihedral angle α on the left, and parallel, non-periodical V-shaped ridges of random dihedral angle on the right.

The slope distribution function of Beckmann, denoted D here, is a probability function representing the distribution across the surface of the local normal vector. Most microfacets models assume that such a distribution of the slopes follows a Gaussian law. The function is isotropic, and depends only on the polar angle θ_h being the angle between the normal of the average surface and the local normal of the microfacet:

$$D(d\Omega_h) = \frac{e^{-\tan^2 \theta_h / 2m^2}}{2\pi m^2 \cos^3(\theta_h)} \quad (4.43)$$

The local normal vector, or in other words the normal vector of one of the panels of the considered V-cavity, is denoted by the differential solid angle $d\Omega_h = \sin \theta_h d\theta_h d\phi_h$. The parameter m , standard deviation of the local slope, translates the surface "roughness". In our simple case of V-cavities of infinite length along the x -axis, the angle θ_h can be obtained with:

$$\alpha = 2 \left(\frac{\pi}{2} - \theta_h \right) \quad (4.44)$$

To perform the simulations of surfaces with a one-dimensional roughness, we simply took the bi-hemispherical spectral reflectances computed earlier, and extrapolated them with the MATLAB function `interp1`, and a cubic interpolation, to generate the reflectances for every dihedral angle of V-cavity from 1° to 180° , with a step of 1° . We then pondered the generated reflectances by the Beckmann distribution for 5 different roughness: 0.01 (very smooth surface), 0.5, 0.7, 1 and 2 (extremely rough). The reflectance R_m of the resulting surface corresponds to the reflectance of each ridges weighted by its probability of being found in the surface.

$$R_m = 2\pi \int_{\theta_h=0}^{\pi/2} D(d\Omega_h) R_\alpha \sin \theta_h d\theta_h \quad (4.45)$$

with R_α being the reflectance for the V-cavity of dihedral angle α linked to the angle θ_h by Eq. (4.44). The simulated results are plotted in the Figure PF4-3 to PF4-7, pp. 36-40 of the portfolio, in the right column of each page.

Light interreflections in a specular only V-cavity

We can first observe that with $m = 0.05$, the bi-hemispherical reflectance is identical to the one of a flat mirror. Beyond this value, the reflectance diminishes as the roughness increases, to a higher extent in the spectral domain where the reflectance of the material is weak (short wavelengths for example in the case of copper). With a high m value, the V-cavities that are the most present are the ones with small apertures. The trajectory of light in them count a high number of reflections, each reflection coming with an attenuation of the incident radiance. With a very high value of m , the bi-hemispherical reflectance would near 0, meaning almost all the light is absorbed by the concavities of the surface. This leads to an increase in chroma for chromatic metals such as gold and copper, with a dramatic increase of saturation of the color, as illustrated on the L^*C^* and a^*b^* diagrams.

Our model also takes exactly into account the shadowing and masking effects, which means that no divergence is to be expected when considering high values of roughness, as opposed to other conventional approach like the one we will discuss in the next section.

4.7.2 Conventional microfacets models for rough surfaces

The approach we presented reminds the one of Torrance and Sparrow [5], later considered by Cook and Torrance [6] in computer graphics. In the same way as we developed, they use long V-cavities to compute a shadowing function, and then in a microfacet approach, they compute a distribution of these cavities. To illustrate this, one could imagine having the same kind of surface as illustrated on the left of Figure 38, repeated for each dihedral angle of aperture. Although mathematically correct, this consideration unconceivable and physically inaccurate.

To resolve this issue, the Smith method [44] is preferred in computer graphics for around 15 years, as it does not make the V-cavities intervene. The hypothesis is that the slopes of the microfacets are entirely decorrelated from each other, even the closest ones. It is a strong statement, but more realistic than Torrance and Sparrow hypothesis.

Until very recently, the microfacet based models would consider only one reflection, under the simple scattering condition. Empirical or semi-empirical solution proposals were presented. In 2016, Heitz published a correct consideration of light interreflections using the Smith approach [45]. In 2018, the same thing was also done, but this time with the Torrance and Sparrow approach [38, 39]. But the hypothesis these studies were built on remain unchanged.

This is for this reason we developed a new point of view, corresponding to the type of surface structure presented on the right of Figure 38. We consider parallel and semi-infinite V-cavities, but with an aperture following a distribution law, implicitly taking shadowing and masking into account, and being emancipated from the divergence problem of the two former approaches when considering surfaces with a high roughness. Notice that our distribution law is centered a 180° , but for representation sake, Figure 38 shows a distribution more centered around 90° .

4.8 Conclusions

In this chapter, we analyzed the interreflections occurring in a structured surface made of parallel V-cavities, with flat and mirror-like faces under a Lambertian illumination. We proposed a model accounting for the exact number of light reflections occurring in the structures, in order to accurately predict the reflectance according to the observation angle. We showed that the type of material and the dihedral angle of the cavity have a strong impact on the predicted reflectance, in particular because of the number of light reflections and the successive attenuations undergone by each ray according to the Fresnel coefficients. This is especially true for surfaces presenting concavities with a small dihedral angle: their color is darker, and in the case of chromatic materials such as gold and copper, their chroma strongly increases, even dramatically in some observation directions.

We also proposed to accurately consider the change of incidence plane at each reflection of the light, inducing a change in its polarization. Due to consideration of the shadowing effect, we offered to simulate a simple surface with random anisotropic roughness and showed that it is very similar to more classical approaches found in the literature, without showing any divergence in the case of very rough surfaces.

Then, we compared our model with two approximate versions that are simpler and faster to compute, the first one being comparable to the one that has been recently introduced in computer graphics [38, 39]. The bi-hemispherical spectral reflectance computed with these three models are very close from each other, except for silicon when the dihedral angle of cavity is small. However, the hemispherical-directional reflectances predicted by the approximate models can deviate considerably from the one predicted by the rigorous model at some observation angles, especially those for which it is probable that light has become linearly polarized during its path before striking the next facet at an angle close to the Brewster angle.

The experimentation showed a good agreement between predictions and measurements, despite a better experimental precision could be achieved.

As ridged surfaces are rather frequent in manufacturing (e.g. brushed steel objects), there is an interest in predicting accurately their appearance, with prototyping renderers developed by the computer graphics community. Even though in this manuscript the case study is focused on a specific surface topology, the influence of the number of reflections and the polarization of light stands for every patterned surface. Several extensions of this chapter study would be needed to see to which extent the color variations predicted according to the observation angle remains similar, for example when their facets are imperfect mirrors (non-flat, slightly scattering...). We can expect that these color variations are smaller than the ones drawn in this study but follow similar tendencies. Moreover, as scattering tends to decrease the effect of polarization of light, we can expect that the difference between the rigorous polarization model and the first approximate one where light remains unpolarized would decrease as well.

Chapter 5.

Light interreflections in an interfaced Lambertian V-cavity

This chapter comes back to strongly scattering materials, as in Chapter 3, but this time by considering that the interface between air and the material is smooth. The reflections and refractions of light at the interface modify consequently the interreflection model. Nevertheless, this latter can be extended in order to take into account these reflections and transmissions, included the multiple specular reflections that can occur in air between the flat interfaces, in a similar a manner as the phenomenon described in Chapter 4. To limit the complexity of the model, we consider for the simulations a frontal lighting and observation, and a V-cavity with a 45° dihedral angle. We also consider at most one possible specular reflection before the light can enter the material, when it travels across the V-cavity, and when it exits it. By considering two flat surfaces one Lambertian and the other one interfaced-Lambertian, with same reflectance, these two surfaces reflect slightly different radiance and display slightly different color once transformed into V-cavity or ridged surfaces. But the different is modest.

5.1 Introduction

In Chapter 3 we presented a model considering a Lambertian surface with a ridged structure as a way of analyzing light interreflections, shadowing and masking effects, and thus the effect of a surface topology on its appearance in terms of lightness and color. Although it allowed for a robust understanding of the multiple diffuse light reflections, considering a Lambertian material is a restrictive assumption. A corollary question is therefore to know if the model for Lambertian material is a satisfying one. In Chapter 4, we then analyzed the case of a V-cavity with mirror-like panels, to further study the influence of specular reflections, and therefore showed a drastically changing contribution to the observed radiance depending on the number of reflections involved.

Following this line of reasoning, we want to know to which extent the interface between a Lambertian and the air would influence the overall appearance of a ridged

Light interreflections in an interfaced Lambertian V-cavity

surface. In the example of sample presented in Figure 39, we can see a structure made by 2.5D printing, using a stack of white ink layers. The sample being illuminated by a frontal light is displaying light interreflections at the bottom of the structure as seen before, but if we look at a flat sample of the ink in Figure 40, we can observe that it has also a glossy aspect, on top of being scattering, suggesting a strong influence from the interface of the material. Indeed, light can be scattered by the material, but also can be reflected by the interface without entering the matter, or can be reflected multiple times between the Lambertian background and the interface before going out of the material, all these different light paths the Lambertian model does not account for.

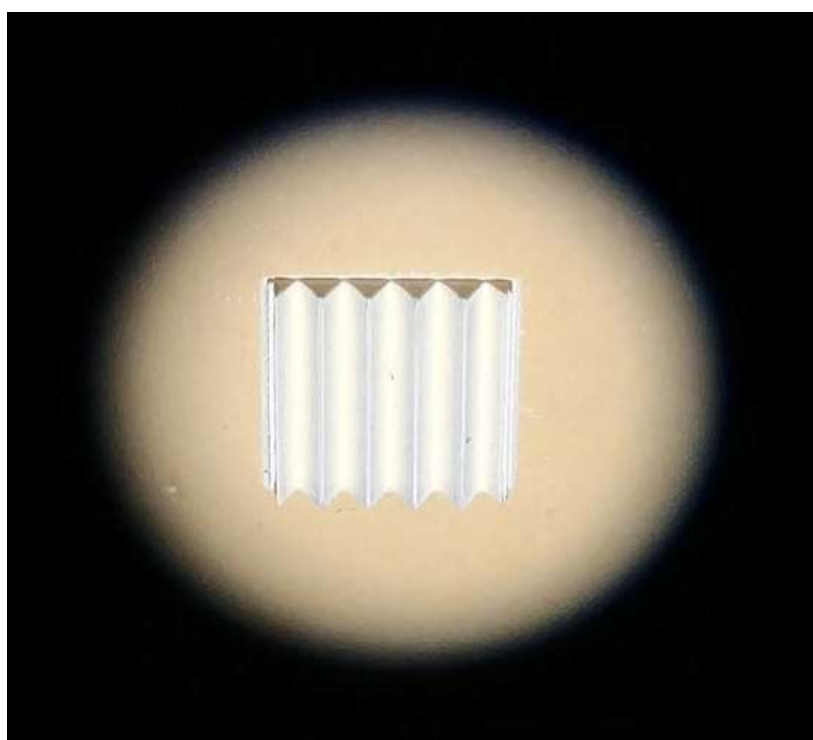


Figure 39 – 2.5D printed sample with white ink, under frontal lighting, forming a 45° V-shaped ridged surface pattern. The sample is 1x1cm, 2.4mm height with a 2mm period.



Figure 40 – Flat white sample printed with white ink used in 2.5D printing, and displaying a glossy aspect

The model presented in this chapter is dealing with a V-cavity made of a Lambertian material with an interface, such as the work developed by Meneveaux *et al.* [47] for the simulation of a rough surface with Lambertian microfacets and their interface. We developed it to quantify the discrepancy with the model presented in Chapter 3.

The Section 5.2 will draw a general overview of the proposed model, before going into the details of its components in Section 5.3, and then comment the simulation results in Section 5.4. Section 5.5 will draw the conclusions.

5.2 Overview of the model

First, light rays coming from outside can be reflected once or several times on interfaces in a specular fashion and exit the cavity without having entered the diffusing material. This light forms a "specular" reflection component which has been comprehensively presented in Chapter 4 and is added to the "diffuse" reflection component issued from the light that has entered the diffusing material at least once. It is represented by a vector \mathbf{L}_s .

The "diffuse" reflection component can be modeled by an extension of the interreflection model described in Chapter 3 for Lambertian surfaces, adapted in order to include the (possibly multiple) reflections and refractions at the interface. As in the Lambertian interreflection model, we describe radiance transfers between facets on the panels of the cavity, the facets being just beneath the interface, acting as Lambertian reflectors.

Therefore, there are several adaptations to perform:

a) Any incident radiance coming from outside must cross one interface to reach a Lambertian facet, with a Fresnel transmittance corresponding to the incidence angle (see Figure 41). Moreover, before crossing the interface, the light ray may have undergone one or more specular reflections on the panels, and the product of the corresponding Fresnel is to be considered. The possibility for a facet to received light rays from a given direction, after specular reflections or not, is given by a new shadowing function. This modifies the vector \mathbf{E}_{in} , which will be denoted as \mathbf{E}'_{in} .

b) Once the light reached a Lambertian facet, it is diffused and reflected by the Lambertian material (see Figure 42). Then, several internal reflections can take place between the material, of reflectance ρ , and the interface. This Lambertian reflectance r_i is given by Eq. (2.35). Moreover, the exitance of the facet $E_{out,j}$, including all these internal reflections and before crossing the interface, is related to its irradiance $E_{in,j}$ by using the Saunderson correction Eq. (2.44):

$$E_{out,j} = \frac{\rho}{1 - r_i \rho} E_{in,j} \quad (5.1)$$

Light interreflections in an interfaced Lambertian V-cavity

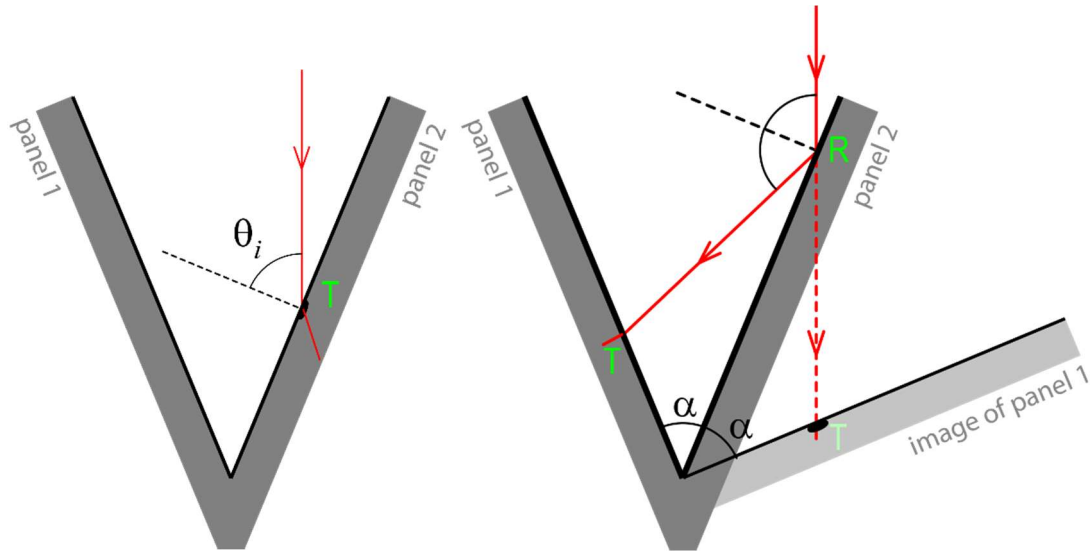


Figure 41 – Incident light ray (red) being transmitted through the interface of the Lambertian material (left) and being reflected once before being transmitted (right).

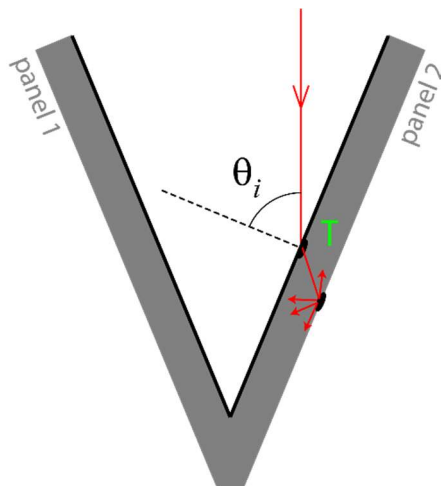


Figure 42 – Light ray (red) being scattered (small red arrows) by the Lambertian material of the V-cavity after being transmitted by the interface of the material.

c) This exitance $E_{out,j}$ is Lambertian. In any direction, the radiance striking the interface is $E_{out,j} / \pi$. When the radiance crosses the interface, the corresponding Fresnel transmittance and a factor $1/n^2$ corresponding to the change of geometrical extent between the material and air, are applied. Then, after having possibly undergone several specular reflections on the two panels, the radiance can then either exit the cavity or cross again an interface and reach another facet (see Figure 43). A masking function $M'_j(\theta, \varphi)$ determines if the ray exits the cavity. The attenuations applied to the rays exiting the cavity (Fresnel transmittance, factor $1/n^2$, and eventual Fresnel reflectances), as well as the masking function, are incorporated into a matrix \mathbf{M}'_{out} which extends the masking matrix \mathbf{M} defined in section 3.6.

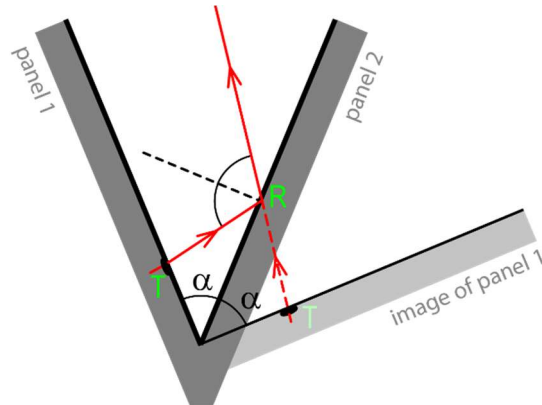


Figure 43 – Light ray (red) exiting the material, being transmitted through the interface and being reflected once before reaching the observe.

d) Once the light has entered the material, it can be reflected between the panels of the cavity. These light rays are scattered by a Lambertian facet, cross the interface (the radiance is then decreased by a factor $1/n^2$ due to a change of solid angle), travel across the V-cavity, and encounters the interface again, and then reach the Lambertian material once more to produce an irradiance (see Figure 44). A matrix \mathbf{K}' , extending the matrix \mathbf{K} of Eq. (3.11), incorporates the material-to-air and air-to-material Fresnel transmittances, the geometrical extent between the pair of facets, and the Fresnel reflectances if specular reflections between the panels occur.

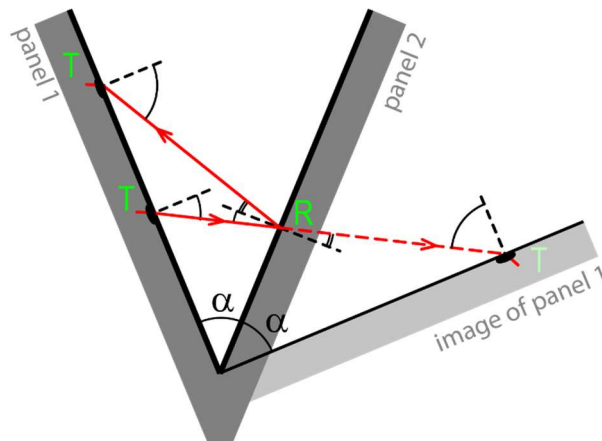


Figure 44 – Light ray (red) exiting the material before being reflected once by the interface and transmitted back into the material.

In the following sections, we propose to develop in detail the method to determine the vectors \mathbf{E}'_{in} , and \mathbf{L}_s , as well as matrices \mathbf{M}'_{out} and \mathbf{K}' . The perceived radiances from the different facets of a V-cavity made of Lambertian material, with acknowledgment of its flat interface with air, are contained into the vector \mathbf{L}' given by:

Light interreflections in an interfaced Lambertian V-cavity

$$\mathbf{L}' = \mathbf{L}_s + \mathbf{M}'_{out} \frac{\rho}{\pi(1-r_i\rho)} \left(\mathbf{I} - \frac{\rho}{\pi(1-r_i\rho)} \mathbf{K}' \right)^{-1} \mathbf{E}'_{in} \quad (5.2)$$

5.3 Components of the model

In this section, we detail the different components of Eq. (5.2). We will only consider the case of a 45° V-cavity, a frontal lighting and a frontal illumination (0:0 geometry).

5.3.1 Irradiance of the Lambertian material: vector \mathbf{E}'_{in}

We consider a collimated, frontal lighting, parallel to the z -axis, in the same manner as in Chapter 3. This lighting corresponds to a radiance L_i . As in Chapter 3, the horizontal plane (x, y) receives an irradiance denoted as E_z , which is related to by:

$$E_z = \omega_i L_i \quad (5.3)$$

where ω_i denotes the solid angle containing the radiance L_i .

Once a ray (radiance L_i) reaches a panel, with an incident angle of $\theta_{i0} = 67.5^\circ$ (see Figure 45), it produces, after refraction by the interface, an irradiance $E_i^{(0)}$ on the Lambertian material given by

$$E_i^{(0)} = \cos\theta_{i0} T_{12}(\theta_{i0}) E_z \quad (5.4)$$

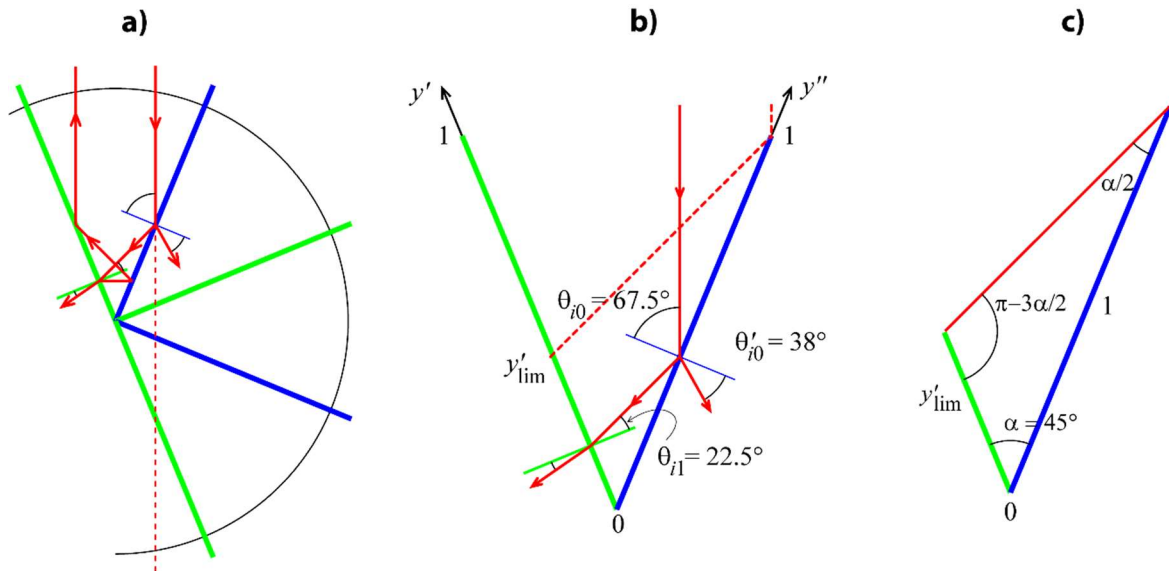


Figure 45 – Illustration of the path of the light for a frontal lighting and observation, and the limit position below which one specular reflection can happen.

Since the lighting is frontal, all facets receive this irradiance. The vector $\mathbf{E}'_{in}^{(0)}$ which gathers the facet irradiances is thus defined as:

$$\mathbf{E}_{in}^{(0)} = E_i^{(0)} (1 \ \cdots \ 1)^T \quad (5.5)$$

The light rays are also partially reflected by the interface and strike the other panel with an incident angle $\theta_{i1} = 22.5^\circ$, which produces an irradiance

$$E_i^{(1)} = \cos\theta_{i1} R_{12}(\theta_{i1}) T_{12}(\theta_{i0}) E_z \quad (5.6)$$

The facets illuminated by these rays all receive this irradiance. However, they are located below a limit position y'_{lim} , shown in Figure 45b. Since the panels have a width unity, we obtain a triangle shown in Figure 45c between the position of the limit facet j on the left panel, y'_{lim} , the edge of the right panel, $y'' = 1$, and the fold, $y' = y'' = 0$. A well-known property of the triangle is the relation between the sides and the angles. We have, in our case:

$$y'_{lim} = \frac{\sin(\alpha/2)}{\sin(\alpha + \alpha/2)} \simeq 0.414 \quad (5.7)$$

Note that, thanks to the symmetry of the configuration, same limit position would be found on the right panel.

The vector $\mathbf{E}_{in}^{(1)}$ gathering the facet irradiances associated with these rays is defined accordingly:

$$\mathbf{E}_{in}^{(1)} = E_i^{(1)} (0 \ \cdots \ 0 \underbrace{1 \ \cdots \ 1}_{\text{irradiated facets}} \ 0 \ \cdots \ 0)^T \quad (5.8)$$

These rays can also be reflected, for the second time. We could pursue the above reasoning line for these rays, but we can consider that their radiance is very low, less than 0.5% of the original radiance at the considered refractive index, here 1.5 (all reflections would have to be taken into account in the case of a metal, as demonstrated in Chapter 4). The irradiance vector of the facets on the Lambertian material is therefore given by:

$$\mathbf{E}'_{in} = \mathbf{E}_{in}^{(0)} + \mathbf{E}_{in}^{(1)} \quad (5.9)$$

Note that in case of oblique directional lighting, the number of reflections, the incident and refraction angles, and a shadowing function should be computed as a function of the orientation of the incident radiance.

5.3.2 Interreflections within the cavity: Matrix \mathbf{K}'

The entries K'_{ij} of matrix \mathbf{K}' express the ratios of the irradiance on any point of facet i to the radiances issued from the whole facet j (of infinite length and a width of $1/p$). It comprises the Fresnel transmittances associated with the crossing of the two interfaces, as well as the factor $1/n^2$, angle-independent, expressing the change of geometrical

Light interreflections in an interfaced Lambertian V-cavity

extent of the radiance by transiting from the material where it is emitted and air where it propagates. It is also possible that the light paths between the two facets includes one or several successive specular reflections at the interfaces of the panels; thus also comprises the Fresnel reflectances associated with these specular reflections.

In absence of specular reflection, a ray transiting from a point P_i and to a point P_j follows the straight line between the two points provided that the two points belong to different panels, i.e. the visibility function $V(P_i, P_j) = 1$. The geometrical extent $d^4G(x_i, x_j, y'_i, y''_j)$ is like the one derived in Chapter 3. Moreover, knowing that the light path from P_i to P_j crosses two interfaces, we incorporate the corresponding Fresnel transmittances $T_{12}(\theta_i)$ and $T_{12}(\theta_j)$ where θ_i and θ_j , given by Eq. (3.23), are the angles between the ray and the normals of the facets. The geometrical kernel between any point of facet i and facet j is therefore:

$$K_{ij}^{(0)} = \frac{1}{n^2} \int_{x=-\infty}^{\infty} \int_{y''=y'_j-1/p}^{y'_j} \frac{T_{12}(\theta_i) T_{12}(\theta_j) y'_i y'' \sin^2 \alpha dx dy''}{\left[(x_i - x)^2 + y_i'^2 + y''^2 - 2y'_i y'' \cos \alpha \right]^2} \quad (5.10)$$

Let us now consider radiances undergoing one specular reflection. Their bounding points P_i and P_j belong to the same panel (say panel 1): a condition given by $1 - V(P_i, P_j)$, which yields 1 if the two points are on the same panel, 0 otherwise. The other panel interface (panel 2) behaves as a mirror. The image of panel 1 by reflection of the mirror forms a new panel at an angle α with panel 2, and an angle 2α with panel 1. The inter-reflections that we want to model are between panel 1 and the image of panel 1.

The image P' of a point $P = (x, -y' \sin(\alpha/2), y' \cos(\alpha/2))$ on panel 1 is obtained by rotation of angle 2α around the x -axis: $P' = (x, y' \sin(3\alpha/2), y' \cos(3\alpha/2))$. The geometrical extent between P_i and the image P'_j of P_j is given by Eq. (3.24) with $\psi = 2\alpha$. The radiance associated with this extent undergoes two refractions and one reflection. The Fresnel transmittances are $T_{12}(\theta_0)$ and $T_{12}(\theta_2)$, where $\theta_0 = \theta_i$ and θ_j are again given by Eq. (3.23) with $\psi = 2\alpha$. The Fresnel reflectance associated with the specular reflection is $R_{12}(\theta_1)$, where θ_1 satisfies the equation:

$$\cos \theta_1 = \left\langle \frac{\overrightarrow{P_i P'_j}}{\| \overrightarrow{P_i P'_j} \|} \cdot \mathbf{N}_2 \right\rangle = \frac{(y'_i + y'_j) \sin \alpha}{\sqrt{(x_i - x_j)^2 + y_i'^2 + y_j'^2 - 2y'_i y'_j \cos(2\alpha)}} \quad (5.11)$$

Note that same expression for $\cos \theta_1$ is obtained if P_i and P_j are on panel 2. The geometrical kernel between any point of facet i and facet j is therefore:

$$K_{ij}^{(1)} = \frac{1}{n^2} \int_{x=-\infty}^{\infty} \int_{y''=y'_j-1/p}^{y'_j} \frac{T_{12}(\theta_0) R_{12}(\theta_1) T_{12}(\theta_2) y'_i y'' \sin^2(2\alpha) dx dy''}{\left[(x_i - x)^2 + y_i'^2 + y''^2 - 2y'_i y'' \cos(2\alpha) \right]^2} \quad (5.12)$$

Similar reasoning line can be followed for the rays having undergone $k \geq 2$ specular reflections. Their bounding points P_i and P_j belong to different panels if k is even, and the visibility function $V(P_i, P_j)$ applies; they belong to the same panel if k is odd, and the visibility function $1 - V(P_i, P_j)$ applies. The geometrical extent is still given by Eq. (3.24) with $\psi = (k+1)\alpha$. The geometrical kernel includes the two Fresnel transmittances $T_{12}(\theta_0)$ and $T_{12}(\theta_{k+1})$, and k Fresnel reflectances $R_{12}(\theta_1), \dots, R_{12}(\theta_k)$ where the angles θ_n , $0 \leq n \leq k+1$, all satisfy the equation:

$$\cos\theta_n = \frac{y_i'' \sin(n\alpha) + y_j'' \sin[(k+1-n)\alpha]}{\sqrt{(x_i - x_j)^2 + y_i'^2 + y_j'^2 - 2y_i' y_j' \cos[(k+1)\alpha]}} \quad (5.13)$$

The geometrical kernel is

$$K_{ij}^{(k)} = \frac{1}{n^2} \int_{x=-\infty}^{\infty} \int_{y''=y_j''-1/p}^{y_i''} \frac{T_{12}(\theta_0) T_{12}(\theta_{k+1}) \prod_{n=1}^k R_{12}(\theta_n) y_i' y_j'' \sin^2[(k+1)\alpha] dx dy''}{[(x_i - x)^2 + y_i'^2 + y_j''^2 - 2y_i' y_j'' \cos[(k+1)\alpha]]^2} \quad (5.14)$$

Finally, the geometrical kernel (matrix \mathbf{K}) accounting for any number of specular reflections, from 0 to the maximal number m of reflections give in appendix C, is

$$K_{ij} = \sum_{k=0}^m K_{ij}^{(k)} \quad (5.15)$$

In practice, we can only consider \mathbf{K}_0 et \mathbf{K}_1 , because in the same way as for E_{in} , the contributions of the rays that underwent two specular reflections or more are very low.

5.3.3 Exiting rays: Matrix \mathbf{M}'_{out}

The components presented so far enable to express the exitance of the different facets of the Lambertian material, through an exitance vector \mathbf{M}' given by:

$$\mathbf{M}' = \frac{\rho}{(1 - r_i \rho)} \left(\mathbf{I} - \frac{\rho}{\pi(1 - r_i \rho)} \mathbf{K}' \right)^{-1} \mathbf{E}'_{in} \quad (5.16)$$

The next step is the modeling of the transmission of radiances from the Lambertian material to the observer, thanks to a matrix \mathbf{M}'_{out} . After having crossed the interface, the rays may directly reach the observer, or undergo one, two... up to four specular reflections within the cavity before reaching the observer. For the same reason as for the irradiance vector \mathbf{E}'_{in} , we will consider only one specular reflection, by considering that the radiances attached to rays being reflected twice or more are very weak. We consider the case where the observer looks at the cavity frontally, and therefore captures only the rays emerging from it vertically, along the z axis.

Light interreflections in an interfaced Lambertian V-cavity

Regarding the rays who transit directly from the Lambertian material to the observer, their radiance correspond to a fraction $1/\pi$ of the exitance at the considered position on the Lambertian material, given by the corresponding entry of matrix \mathbf{M}' in Eq.(5.16). By crossing the interface, the geometrical extent of the radiance is changed due to the refraction and a factor $1/n^2$ is applied, as well as the Fresnel transmittance $T_{12}(\theta_{x_0})$ where $\theta_{x_0} = 67.5^\circ$ is the angle at which the radiance exits the surface towards the observer in our case. The radiance L'_j observed from facet j is therefore:

$$L'_j = \frac{T_{12}(\theta_{x_0})}{\pi n^2} M'_j \quad (5.17)$$

where M'_j denotes the j th entry of matrix \mathbf{M}' attached with this facet j . This factor $T_{12}(\theta_{x_0})/\pi n^2$ applies equally for all facets and featured on all entries on the diagonal of matrix \mathbf{M}'_{out} :

$$M'_{out,j,j} = \frac{T_{12}(\theta_{x_0})}{\pi n^2} \quad (5.18)$$

Other rays can exit the surface of a panel with an angle $\theta_{x_1} = 22.5^\circ$ from the normal of the panel in the vertical (y, z) plane, then reach the other panel with an angle $\theta_{x_0} = 67.5^\circ$ on a facet k that will be explicated later, and exit the cavity vertically along the z -axis towards the observed. This corresponds precisely to the path featured in Figure 45b, but in the opposite direction. Once again, the original radiance of these rays corresponds to a fraction $1/\pi$ of the exitance at the considered position on the Lambertian material. A factor $1/n^2$, the transmittance $T_{12}(\theta_{x_1})$, and the reflectance $R_{12}(\theta_{x_0})$ are applied. Since the observer receives this radiance from facet k , the factor $T_{12}(\theta_{x_1})R_{12}(\theta_{x_0})/\pi n^2$ is placed on the entry (k, j) of matrix \mathbf{M}'_{out} :

$$M'_{out,k,j} = \frac{T_{12}(\theta_{x_1})R_{12}(\theta_{x_0})}{\pi n^2} \quad (5.19)$$

The facet k that is reached from facet j is given by its distance y''_k from the fold between the two panels. It depends on the position of facet j on the other panel, given by its distance y'_j from the fold. Figure 46 shows the geometrical configuration by considering that facet j is on the left panel, but same result would be obtained by considering it on the right panel, by symmetry of the configuration. The position y'_{lim} associated with the edge of the right panel is the same as computed in Eq. (5.7) We thus have, according to the Thales theorem:

$$y''_k = \frac{y'_j}{y'_{lim}} \quad (5.20)$$

We could consider the rays undergoing two or more specular reflections, but their contribution would be very low, as said before.

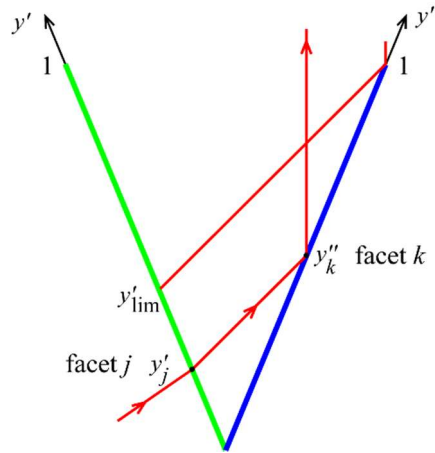


Figure 46 – Schematic view of the limit position in the V-cavity above which a specular reflection can happen when the light exits the Lambertian material

The radiance observed from the different facets is finally given by the vector:

$$\mathbf{L}_{diff} = \mathbf{M}'_{out} \frac{\rho}{\pi(1-r_i\rho)} \left(\mathbf{I} - \frac{\rho}{\pi(1-r_i\rho)} \mathbf{K}' \right)^{-1} \mathbf{E}'_{in} \quad (5.21)$$

From this radiance, it is possible to compute a reflectance factor, by dividing it with the radiance L_{ref} that is observed in the same frontal direction from a perfectly white diffuser, of reflectance unity. With an incident radiance L_i contained in a solid angle ω_i , we have:

$$L_{ref} = \frac{\omega_i L_i}{\pi} = \frac{E_z}{\pi} \quad (5.22)$$

and the reflectance factor associated with the facet j , from which the observed radiance $L_{diff,j}$ is given by the j th entry of matrix \mathbf{L}_{diff} , is:

$$\hat{R}_j = \frac{\pi}{\omega_i L_i} L_{diff,j} \quad (5.23)$$

5.3.4 Vector \mathbf{L}_s

The vector \mathbf{L}_s accounts for the light that has been reflected in a specular way in the structure, without having crossed any interface, therefore without being diffused and/or absorbed by the material. This specular component is achromatic. As we can see in Figure 45a, in our lighting-observation geometry, there exist some rays incoming frontally that can reach the observer located in the same frontal direction. These rays undergo four

Light interreflections in an interfaced Lambertian V-cavity

successive reflections, at the respective incident angles 67.5° , 22.5° , 22.5° , and 67.5° . The factor applied to incident radiance L_i , which applies on all facets in our case (due to the symmetry of our configuration), is:

$$r_s = R_{12}(67.5^\circ)R_{12}(22.5^\circ)R_{12}(22.5^\circ)R_{12}(67.5^\circ) \approx 3.3 \times 10^{-5}$$

It is therefore very low. However, this weak component may considerably affect the reflectance factors of the cavity facets, according to the solid angle ω_i of the incident radiance. Since the specularly reflected radiance is $r_s L_i$, the reflectance factor including both the diffuse and specular components is given by:

$$\hat{R}_j = \frac{\pi}{\omega_i} r_s + \frac{\pi}{\omega_i L_i} L_{diff,j} \quad (5.24)$$

Remind that $L_{diff,j}$ is proportional to $\omega_i L_i$, also denoted as E_z , because it is present in all terms composing vector \mathbf{E}'_{in} [see Eqs.(5.4) and (5.6)]. Hence, this term $\omega_i L_i$ cancels for the diffuse component of the reflectance factor, while the specular component remains inversely proportional to the incident solid angle. The specular component may therefore be very strong in comparison to the diffuse one if the incident light is very collimated, a situation which is true for any interfaced Lambertian material, even flat. In contrast, a conical illumination may generate a specular component less pronounced. Simulations with interfaces materials must therefore take into account not only the irradiance of the surface, but also the exact angular distribution of the light, more precisely its solid angle as far as it can be considered as small enough to be considered as frontal illumination. This complicates the color rendering simulations. In the following, instead of choosing an arbitrary solid angle, which would generate an achromatic specular component on the chromatic diffuse component on which our interest is focused, we decided to remove it from the simulation.

5.4 Simulations of V-cavities made with Lambertian material with an interface

We remind that the case we consider is the one of a 45° V-cavity made with a Lambertian material. The two panels of the structure possess a smooth and flat interface with air. The lighting as well as the observation direction are frontal. We also considered three cases for the material interface, with three different optical indices:

- $n = 1.001$, which is the case we used to verify the model and compare with the results given by the model of Chapter 3. Such an index is identical to having no interface at all. We did not take exactly 1 because of the discontinuity that would emerge in Fresnel's formulae in such case.

- $n = 1.33$, which we used in order to simulate a scattering material that would be covered with a varnish containing a water-based binder.
- $n = 1.5$, which is an appropriate value when considering the interface of ink with air.

The predictions given by the model are represented in Figure PF5-1 and PF5-2 with the example of the magenta spectrum, on both pages. On the top row of the first figure, we plotted the “ramp” spectra for the three optical indices, illustrating the evolution of the observed radiances as a function of the reflectance, with the distinction on left page for $n = 1.5$ between the case **a** where we do not account for any specular reflection, and **b** where one specular reflection is accounted for. The corresponding color gradients are also represented below the spectra plots.

On Figure PF5-2, we have the translation of the spectra plot into CIE 1976 L*C* diagrams, with the evolution of the ΔE_{2000} color distance across the V-cavity between the Lambertian only case, and respectively with the two other values of optical index.

The first immediate observation is that the results are identical when considering an optical index of 1, meaning the model is consistent with the version developed in Chapter 3 as expected, for Lambertian materials without an interface. The other results are a bit darker when compared with the Lambertian model and the model with an interface, where only one possible specular reflection is considered, meaning the interface is in competition with the light interreflections and tends to attenuate them, even more so with a higher optical index.

Since the lighting geometry considered in this case allows up to 4 specular reflections of the light before it can enter the material (as seen in Chapter 4), we did not take it into account due to the weakness of the purely specular component as said earlier. But it is important to know that other configurations with different solid angles, resulting in smaller number of reflections, could significantly contribute to the outgoing radiance, and therefore tend to increase the lightness and desaturate the color.

Another observation is the presence of a discontinuity in the spectra plot and in the gradient of color displayed by the Lambertian cavity with an interface, similarly to what was observed in Chapter 4, in the case of metallic and mirror like samples. This discontinuity is located exactly at the position y'_{lim} on the panel defined by Eq. (5.7) and illustrated in Figure 45b. This is due to the internal specular reflections, mostly to the ones happening before the light entering the structuring, and the ones happening after the light comes out of the material. Since these specular reflections cannot happen above y'_{lim} , a difference in the radiance displayed emerges. Consequently, this discontinuity disappears when the optical index is 1.

We can observe nonetheless that the average reflectances are similar, with a small noticeable difference in the highly absorbed wavelengths. In the case of the Lambertian model, we saw that the spectral components located in wavelength range where light is poorly reflected have a decreased lightness due to the interreflection effect. In the case of the Lambertian model with interface, we can observe that this attenuation is slightly less

Light interreflections in an interfaced Lambertian V-cavity

pronounced. This is thanks to the presence of the interface and the specular reflections contributing to a small increase of the lightness.

Another difference when accounting for the interface influence is the reflectance threshold at which the interreflections can happen. We saw in Chapter 3 that in the case of a Lambertian magenta material folded at 45° , it was around 0.93. But we can see on Figure PF5-1**b** and **c**, this threshold is located higher in both cases: 0.98 for $n = 1.33$ and 0.97 for $n = 1.5$. Consequently, we can see that the average radiance is not overpassing the reflectance of the flat surface. The interface is interfering with the occurrence of light interreflections, and at the same time contribution to a gain of radiance thanks to the specular reflections, but not as much as the radiance gain visible with the interreflection phenomenon. The added sensation of luminosity visible in Chapter 3 for some samples could be also observable for a higher optical index of interface, but it would not be as plausible and realistic as a 1.5 value in our case of Lambertian material with an interface.

Finally, Figure PF5-2 finishes to illustrate the differences. The high color distances when comparing the parts of the V-cavity that are only displaying diffuse reflections (above y'_{lim}) have an average value of 2.5 in both cases of $n = 1.33$ and 1.5, due to the presence of the interface attenuating the radiance. The distance is smaller when looking at the center of the V-cavity, where one specular reflection is considered. We can observe that the distance decreases from the case of 1.33 to 1.5, meaning the diffuse component decreases but the contribution of the specular one increases, lowering the distance between the case with an interface and without.

5.5 Conclusions

We presented a model for a surface with V-shaped ridges made of a Lambertian material, with a comprehensive computation of the light interactions happening at the interface between the air and the material, which was a problem we did not address with the model presented in Chapter 3.

The addition of an interface enables the consideration of more light reflections and transmissions happening in a real scattering material with a smooth interface as the one showed in the introduction of this chapter, which were ignored in the Lambertian only model. We discussed the possible specular reflections happening in the V-cavity before the light enters the material, during the multiple reflections process between the two panels and after the light exist the material and before reaching the observer. We also added the contribution of the multiple reflections happening between the interface and the material itself once the light has crossed the former.

The case studied was a simple one, considering only a frontal lighting and observation direction, but it was enough to simulate the appearance of such a structure. We showed that for 45° magenta V-cavity, the result is coherent with the predictions of the Lambertian model. We also showed that when considering an interface, the possible

specular reflections are contributing to the final outgoing radiance, compared to the case where only the scattered light is considered. The differences in ΔE_{2000} color distance are quite low but not negligible (>1). This leads to a specific discontinuity in the gradient of radiance and color inside the structure, depending on whether a specular reflection can happen or not before the light enters the material and after it exits. In the end, we showed that the consideration of the interface makes a difference when studying the structure influence on the perceived lightness and color, with a slightly brighter aspect and a small change in chroma. We also showed that the interface of a scattering material tends to attenuate the light interreflections effect, while adding to the radiance with the specular reflections. This attenuation is linked to the transmission coefficients of the interface.

However, this is a first approach to a complex problem in a particular case. To further the study, we would have to consider different lighting geometries as well as different observation directions, in the same fashion used in the other chapters. In fact, here 4 specular reflections were possible, rendering the purely specular component negligible. In other cases of lighting geometry, either directional or diffuse, between one and four specular reflections could happen, as shown in chapter 4, meaning a possibly greater contribution coming from an achromatic component.

Another important thing to address is also the shadowing and masking effects and their declinations throughout the multiple reflections process, but that are surely playing an important role in the appearance of a Lambertian V-cavity with an interface, and possibly increasing the difference with the Lambertian only model.

Chapter 6.

Conclusion

The study of light interreflections generated by a material surface with V-shaped ridges led us to several conclusions about the influence of a surface structure on its appearance. The simple case of a semi-infinite V-cavity periodical pattern combined with a photometric approach allowed for an in-depth study of the various mechanisms at play when modelling the appearance of such a surface.

6.1 Most relevant parameters for interreflections

We could observe that the interreflection phenomenon itself and its consequences on the ridged surface color appearance are very different according to whether the material is diffusing and matte, i.e., Lambertian, or specular like metallic mirror panels. The kind of reflectors that constitutes the panels of the cavities is definitely a crucial information which determines the interreflection process and the model that should be used.

In the case of Lambertian materials, studied in Chapter 3, the most appropriate model is based on the radiosity equation, or interreflections equation. The model is quasi-analytic, by means of a surface sampling allowing for a convenient matrix formalism, appropriate for digital computing. Visually, we can see a color gradient over the cavity even though its two panels are homogenous. Since interreflections are stronger in areas where parcels of material are the closest with other parcels, their influence is more visible at the bottom of the cavity: if the cavity is wholly and homogeneously illuminated (e.g. under frontal lighting), the bottom of the cavity is the brightest. This is not true anymore when the lighting is oblique or diffuse: the bottom of the cavity may be less or not illuminated, and the darkening that this shadowing effect induces cannot be compensated by the interreflection phenomenon. Under diffuse lighting, the bottom of the cavities is therefore the darkest. We could analyze the influence of the surface structure on color through the analysis of three parameters: the lighting geometry, the observation configuration and the shape of the structure itself. In average over the ridged surface, as viewed from afar, the light interreflections tend to modify the observed brightness by adding a gain in radiance thanks to the interreflection effect, which is striking when the material is highly reflective (albedo close to 1) and can lead in some cases to a sensation

Conclusion

of additional luminosity, as well as a more saturated color, sometimes to the point where the hue itself can shift. This gain in radiance can vanish under oblique or diffuse lighting due to the shadowing. Thus, under frontal or nearly frontal illumination where shadowing does not occur, a white or light grey ridged surface can be brighter than a flat one made of the same material; with red, magenta, or yellow material, which is bright in a certain spectral domain and darker in the rest of the spectrum, the ridged surface is brighter than the flat surface in the first spectral domain but not in the rest of the spectrum, and its color is consequently more chromatic. We could also verify that two metameric flat surfaces, having different reflectances but displaying the same color under a certain lighting, are not metameric anymore once transformed into structured surfaces. The effect of interreflection being non-linear in respect to the reflectance of the material, and this reflectance being generally a function of wavelength, the interreflections have different impacts in the different spectral wavebands. We could also simulate interesting visual effects when manipulating bi-color structures.

The second kind of structures studied in Chapter 4 is the specular V-cavity, whose lateral panels are mirrors. This model is not based on the radiosity equation but on a comprehensive description of all possible light paths, with their respective successions of reflections and change of polarization. Shadowing, usually so difficult to model in the case of randomly rough surfaces because statistical models are needed, is automatically accounted for in our model. We could predict the change of color and lightness that can be observed visually when the dihedral angle of the cavities decreases due to the number of specular reflections happening in the structure. This is particularly striking with chromatic metals such as gold and copper. The precise computation of the change of polarization state at each reflection showed that it has very little impact on the visual aspect of a ridged material, except for the case where the optical index induces a high difference between the two polarization components (ex.: silicon). Using an approximated polarization model to predict the appearance of such surfaces is satisfying.

The model that we developed for Interfaced Lambertian materials, presented in Chapter 5, is an extension of the radiosity model taking into account the reflections and transmissions of light at the interfaces, including the successive specular reflections taking place in air before reaching the Lambertian background, or after exiting it, or in the path between two material parcels. The multiple internal reflections between the diffusing material and its interface are also incorporated, in a similar way as the Saunderson model for flat interfaced Lambertian materials. Only one illumination and observation configuration has been described, the $0^\circ:0^\circ$ geometry, which prevent shadowing and masking still in need of further development. However, this configuration provides a first preview of the color difference between a Lambertian and interfaced Lambertian structured surfaces. This difference is noticeable, but rather modest. The model has the merit of being more realistic in the prediction of the appearance of scattering samples having a smooth interface with air, such as the 2.5D printed samples which were at the origin of our investigations.

6.2 Experimental verification

The experimental verification of the models has been started in the case of the specular cavities, but this work needs to be pursued. Ensuring that the structures correspond as closely as possible to the ideal case considered by the model is not easy, in particular for Lambertian materials: we must have a flat sample to get its optical properties, verify that it is a perfectly Lambertian reflector included at grazing angles, transforming a piece of this sample into a well-shaped V-cavity without waviness. If we want to measure the radiance issued from each point of the cavity and verify that the color gradients simulated are consistent with the measured ones, we need a spectral camera with good solution, and a lighting system being either perfectly collimated or perfectly diffuse (by using a large integrating sphere). The production of samples has not been possible in the time allowed for this work, but the measuring equipment has been gathered. It was used for an experimental verification for specular cavities based on mirrors of gold, copper and silver produced by coating techniques in our laboratory. The agreement between predictions and measurement was rather good attended the experimental precision that we could achieve. The experimental verification of the model for interfaced Lambertian materials is still to be done.

6.3 Further developments

The study of structured surfaces made of interfaced Lambertian materials could be continued in different directions, beyond its extension to oblique and diffuse lightings.

Firstly, the light component being only reflected in a specular fashion and without entering the material has been intentionally ignored because it depends on the solid angle of illumination, which can strongly vary according to the context or the instrument. As for flat surfaces, this achromatic light component would certainly increase the lightness of the color, decrease the chroma, and contribute to the perceived glossiness if the observer has the possibility to move around the sample. An interesting continuation of this study would be to analyze the respective contributions of this purely specular component to gloss and color, according to the large or thin solid angle used for lighting.

Secondly, it would be possible to consider a layer of transparent color material, e.g. colored ink, on top of the diffusing background. The transmittance of the layer could be incorporated into the model in addition to the transmittance of the interface. We can say that our model for bare materials with interface is equivalent to the Saunderson model when the dihedral angle of the cavities is 180° (flat surface), given by Eq. (2.44) and that we copy here:

$$R = r_e + T_{in}T_{out} \frac{\rho}{1 - r_i\rho} \quad (5.25)$$

Conclusion

where ρ is the intrinsic reflectance of the lambertian background (without interface), R the reflectance factor of the interfaced background, and r_s , r_i , T_{in} , and T_{out} are factors related to the reflections and transmission of light by the interface. Notice that the fraction in Eq. (5.25) features in the extended interreflection equation (5.2) that we also copy here:

$$\mathbf{L}' = \mathbf{L}_s + \mathbf{M}'_{out} \frac{\rho}{\pi(1-r_i\rho)} \left(\mathbf{I} - \frac{\rho}{\pi(1-r_i\rho)} \mathbf{K}' \right)^{-1} \mathbf{E}'_{in} \quad (5.26)$$

With a layer of transparent colored material on it, it would become equivalent at this flat angle to the Williams-Clapper model [23], or its simplified version proposed by Berns [48] given below, by introducing the transmittance t of the colored layer:

$$R = r_e + T_{in}T_{out} \frac{\rho t^2}{1-r_i\rho t^2} \quad (5.27)$$

The extended interreflection equation would be simply modified as follows:

$$\mathbf{L}' = \mathbf{L}_s + \mathbf{M}'_{out} \frac{\rho t^2}{\pi(1-r_i\rho t^2)} \left(\mathbf{I} - \frac{\rho t^2}{\pi(1-r_i\rho t^2)} \mathbf{K}' \right)^{-1} \mathbf{E}'_{in} \quad (5.28)$$

Following the same reasoning line, the colored layer could be a halftone layer, made of a many small ink dots distant from each other. Provided that the ink dots are small enough to assume that the halftone layer is homogenous at the scale of a cavity panel, the model could be extended in a similar way to the Clapper-Yule model [49] for (flat) halftone prints, by introducing the surface coverage of the ink layer of transmittance t :

$$R = r_e + T_{in}T_{out} \frac{\rho(1-a+at)^2}{1-r_i\rho(1-a+at^2)} \quad (5.29)$$

The extended interreflection equation would be simply modified as follows:

$$\mathbf{L}' = \mathbf{L}_s + \mathbf{M}'_{out} \frac{\rho(1-a+at)^2}{\pi[1-r_i\rho(1-a+at^2)]} \left(\mathbf{I} - \frac{\rho(1-a+at)^2}{\pi[1-r_i\rho(1-a+at^2)]} \mathbf{K}' \right)^{-1} \mathbf{E}'_{in} \quad (5.30)$$

Alternatively, if the ink dots are too large, it is still possible to sample the cavity panels into a set of small facets, each one having a certain ink transmittance according to its position in the halftone pattern, and use the interfaced version of the radiosity equation. The modelling toolbox would thus be appreciably enriched toward the color prediction of structured surfaces produced in 2.5 or 3.D printing, despite the difficulties that would necessarily arise in the confrontation between our ideal structures, perfectly shaped, and real ones.

References

1. Turbil, C., *Light Scattering from Complex Rough Surfaces*. PhD dissertation. Sorbonne Université, 2018.
2. Desage, S. F., *Contraintes et opportunités pour l'automatisation de l'inspection visuelle au regard du processus humain. Vision par ordinateur et reconnaissance de formes*. PhD dissertation. Université Grenoble Alpes, 2015. In French.
3. Page, M., *Création d'objets mats : optimisation d'un procédé d'impression en relief en termes d'apparence*. PhD dissertation. Conservatoire national des arts et métiers – CNAM, 2018. In French.
4. Phan Van Song, T., *Optical models for appearance management of printed materials*. PhD dissertation. Museum National d'Histoire Naturelle, 2018.
5. Torrance, KE, Sparrow, EM., "Theory for Off-Specular Reflection from Roughened Surfaces," *J. Opt. Soc. Am.* **57**, 1105–1114 (1967).
6. Cook, RL, Torrance, KE., "A Reflectance Model for Computer Graphics," *ACM Transactions on Graphics* **1**, 7–24 (1982)
7. Byrd, R. H., Hribar, M. E., Nocedal, J. "An interior point algorithm for large-scale nonlinear programming," *SIAM Journal on Optimization* **9**, 877 (1999).
8. Pharr, M., Jakob, W., Humphreys, G., *Physically based rendering: From theory to implementation*, Morgan Kaufmann, 2016.
9. Jensen, H. W., *Realistic image synthesis using photon mapping*, Ak Peters Natick, 2001.
10. Nayar, S. K., Ikeuchi, K., Kanade, T. "Shape from interreflections", *International Journal of Computer Vision* **6**, 173 (1991).
11. Nayar, S. K., Gong, Y. "Colored interreflections and shape recovery," in *Image Understanding Workshop*, 333–343 (1992).
12. Seitz, S. M., Matsushita, Y., Kutulakos, K. N. "A theory of inverse light transport," *Tenth IEEE International Conference on Computer Vision, ICCV 2005*, vol. 2, 1440–1447 (2005).
13. Funt, B. V., Drew, M. S., "Color space analysis of mutual illumination," *IEEE Transactions on Pattern Analysis and Machine Intelligence* **15**(12), 1319–1326 (1993).
14. Liao, M., Huang, X., Yang, R., "Interreflection removal for photometric stereo by using spectrum-dependent albedo," *IEEE Conference on Computer Vision and Pattern Recognition (CVPR)*, 689–696, (2011).
15. Fu, Y., Lam, A., Matsushita, Y., Sato, I., Sato, Y., "Interreflection removal using fluorescence," *European Conference on Computer Vision*, 203–217 (2014).

Conclusion

16. Drew, M. S., Funt, B. V., "Calculating surface reflectance using a single-bounce model of mutual reflection," *IEEE Third International Conference on Computer Vision*, 394–399 (1990).
17. Ho, J., Funt, B. V., Drew, M. S., "Separating a color signal into illumination and surface reflectance components: Theory and applications," *IEEE Transactions on Pattern Analysis and Machine Intelligence* **12**, 966–977 (1990).
18. Deeb, R. Inter-reflections in computer vision: importance, modeling & application in spectral estimation. PhD dissertation. Université de Lyon, 2018.
19. Koenderink, J.J., Van Doorn, A. "Geometrical modes as a general method to treat diffuse interreflections in radiometry," *J. Opt. Soc. Am.* **73**(6), 843–850 (1983).
20. Oren, M., Nayar, S. K., "Generalization of Lambert's reflectance model," *Proceedings of the 21st annual conference on Computer graphics and interactive techniques (SIGGRAPH '94)* 239–246 (1994).
21. Saunderson, J.L., "Calculation of the color pigmented plastics," *J. Opt. Soc. Am. A* **32**, 727-736 (1942).
22. Clapper, FR, Yule, JAC., "The Effect of Multiple Internal Reflections on the Densities of Halftone Prints on Paper," *J. Opt. Soc. Am.* **43**, 600–603 (1953).
23. Williams, FC, Clapper, FR., "Multiple Internal Reflections in Photographic Color Prints," *J. Opt. Soc. Am.* **43**, 595–597 (1953).
24. Shore, JD, Spoonhower, JP, "Reflection Density in Photographic Color Prints: Generalizations of the Williams-Clapper Transform," *J. Im. Sci. Technol.* **45**, 484–488 (2001).
25. Nicomedus, FE, Richmond, JC, Hsia, JJ. *Geometrical considerations and nomenclature for reflectance*. NBS Monograph **160**, NBS, p. 52 (1977).
26. CIE, *Colorimetry* ; CIE Technical Report, 3rd edition, 1998.
27. Kipphan, H., *Handbook of Print Media*; Springer Verlag, Berlin, 2001.
28. Perkampus, H-H., *Encyclopedia of Spectroscopy*, VCH, New York, 1995.
29. Völz, HG., *Industrial color testing: Fundamentals and techniques*; Wiley-VCH, New York, 2nd edition, 2001.
30. Elias, M, Elias, G., "Radiative transfer in inhomogeneous stratified scattering media with use of the auxiliary function method." *J. Opt. Soc. Am. A* **21**, 580-589 (2004).
31. Snyder, JP., *Map Projections – A Working Manual*. U. S. Geological Survey Professional Paper 1395; U. S. Government Printing Office, Washington, DC, 1987, pp. 182-190.
32. Kubelka, P, Munk, F., "Ein Beitrag zur Optik der Farbanstriche," *Zeitschrift für technische Physik* **12**, 593-601 (1931).
33. Kubelka, P., "New contributions to the optics of intensely light-scattering material, part I." *J. Opt. Soc. Am. A* **38**, 448-457 (1948).
34. Copyright: Vanessaezekowitz at en.wikipedia / CC BY 3.0-2.5-2.0 (<https://creativecommons.org/licenses/by/3.0-2.5-2.0-1.0>)
35. Copyright: Nilsjohan / CC BY-SA (<https://creativecommons.org/licenses/by-sa/4.0>)

36. Arfken, G., Weber H., *Mathematical Methods for Physicists*, Harcourt/Academic Press, 2000.
37. Baar, T., Shahpaski, M., Ortiz Segovia, M. "Image ghosting reduction in lenticular relief prints ", *Proc. SPIE 9018, Measuring, Modeling, and Reproducing Material Appearance*, **90180N** (2014).
38. Xie, F., Hanrahan, P. "Multiple scattering from distributions of specular v-grooves," *ACM SIGGRAPH Asia 2018 Technical Papers*, **276** (2018).
39. Lee, J.H., Jarabo, A., Jeon, D. S., Gutierrez, D., Kim, M. H. "Practical multiple scattering for rough surfaces," *ACM SIGGRAPH Asia 2018 Technical Papers*, **275** (2018).
40. Zipin, R. B. "The apparent thermal radiation properties of an isothermal V-groove with specularly reflecting walls." *J. Res. NBS C*, **70**, 275-280 (1966).
41. Mulford, R. B., Collins, N. S., Farnsworth, M. S., Jones, M. R., & Iverson, B. D., "Total hemispherical apparent radiative properties of the infinite V-groove with specular reflection," *International Journal of Heat and Mass Transfer*, **124**, 168-176 (2018).
42. Born, M., Wolf, E., *Principle of Optics*, 7th expanded ed., Pergamon, 1999, p. 47.
43. <https://refractiveindex.info/>
44. Smith, B.J. "Geometrical shadowing of a random rough surface," *IEEE Transaction on Antennas and Propagation*, **15**, 668-671 (1967).
45. Heitz, E., Hanika, J., d'Eon, E., Dachsbacher, C., "Multiple-Scattering Microfacet BSDFs with the Smith Model," *ACM Trans. Graph. (Proc. SIGGRAPH 2016)* **35**, 58 (2016).
46. Wu, Y., Zhang, C., Estakhri, N.M., Zhao, Y., Kim, J., Zhang, M., Liu, X.X., Pribil, G.K., Alù, A., Shih, C.K., Li, X., "Intrinsic optical properties and enhanced plasmonic response of epitaxial silver," *Adv. Mater.* **26**, 6106-6110 (2014)
47. Meneveaux, D., Bringier, B., Tauzia, E., Ribardièrre, M., Simonot, L., "Rendering rough opaque materials with interfaced Lambertian microfacets." *IEEE transactions on visualization and computer graphics*, **24**, 1368-1380 (2017).
48. Berns, R. S., "Spectral modeling of a dye diffusion thermal transfer printer," *J. Electron. Imaging* **2**, 359-370 (1993).
49. Clapper, F.R., Yule, J.A.C. "The effect of multiple internal reflections on the densities of halftone prints on paper." *J. Opt. Soc. Am.*, **43**, 600-603 (1953).

* * *

In addition to the present manuscript, these works are reported into four publications:

1. D. Saint-Pierre, P. Chavel, L. Simonot, and M. Hébert, "Angular reflectance model for ridged specular surfaces, with comprehensive calculation of inter-reflections and polarization," *J. Opt. Soc. Am. A* **36**, C51-C61 (2019).

Conclusion

2. D. Saint-Pierre, L. Simonot, M. Hébert, "Reflectance Computation for a Specular Only V-Cavity." *Computational Color Imaging Workshop CCIW'19* (Chiba, Japan, 25-27 March 2019 ► Young Author Best Student Paper Award) Proceedings in: Tominaga S., Schettini R., Trémeau A., Horiuchi T. (eds) *Computational Color Imaging. CCIW 2019*. Lecture Notes in Computer Science, vol 11418. Springer, Cham (2019).
3. D. Saint-Pierre, R. Deeb, D. Muselet, L. Simonot, M. Hébert, "Interréflexions lumineuses dans une V-cavité lambertienne" in *Quand la matière diffuse la lumière*, Ed. Lionel Simonot, Presse des Mines (2019).
4. D. Saint-Pierre, R. Deeb, D. Muselet, L. Simonot, M. Hébert, "Light Interreflections and Shadowing Effects in a Lambertian V-Cavity under Diffuse Illumination" IS&T Electronic Imaging Symposium, Material Appearance 2018 pp. 166-1-166-10 (Burlingame, USA, 29 January-2 February 2018).



Order number NNT: **2020LYSES041**

PhD Thesis, UNIVERSITY OF LYON
Completed at the
University Jean Monnet

Doctoral School N° 488
Sciences, Ingénierie, Santé

Publicly defended on 19/11/2020, by:
Dorian SAINT-PIERRE

PORTFOLIO
(attachment to the main manuscript)

In this portfolio, you will find the figures attached to the manuscript.

The name of the figures follows the code:

Figure PF (PortFolio) + Chapter number – Figure number

- The figures attached to Chapter 3 range from PF3-1 to PF3-15
- The figures attached to Chapter 4 range from PF4-1 to PF5-7
- The figures attached to Chapter 5 are PF5-1 and PF5-2

Dans ce portfolio, vous trouverez les figures attachées au manuscrit principal.

La dénomination des figures suit le code suivant :

Figure PF (PortFolio) + Numéro de chapitre – Numéro de figure

- Les figures du chapitre 3 allant de PF3-1 à PF3-15
- Les figures du chapitre 4 allant de PF4-1 à PF5-7
- Les figures du chapitre 5 allant : PF5-1 et PF5-2

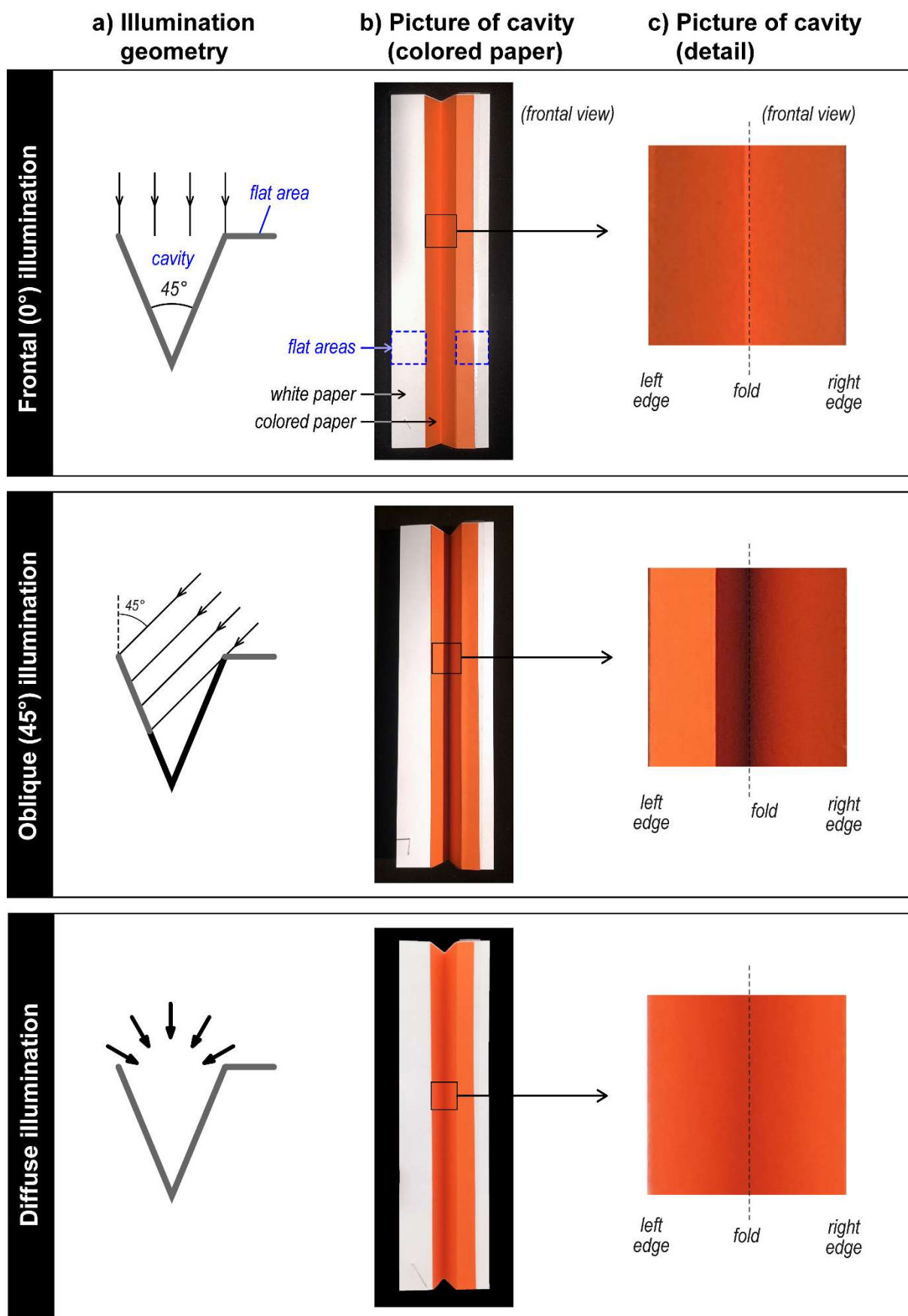
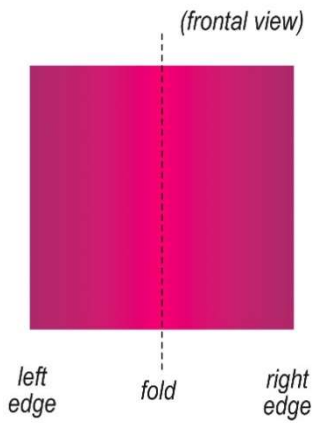
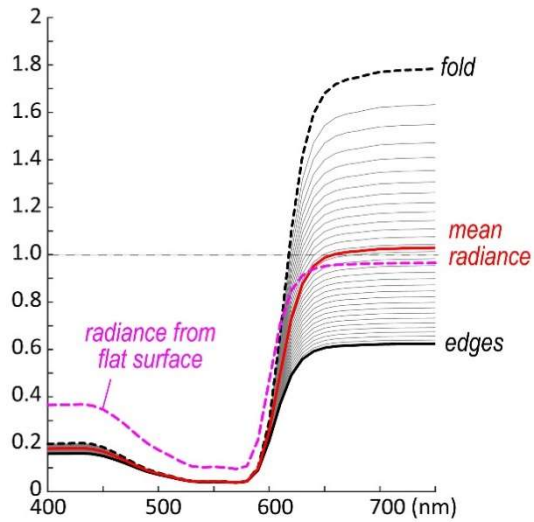


Figure PF3-1 (double page) — Illustration of the influence of the illumination geometry, by considering frontal illumination (**top row**), oblique illumination (**middle row**) and diffuse illumination (**bottom row**). **a)** Schema corresponding to the illumination geometry. **b)** Color pictures (non-calibrated) of the sample presented in Figure 4 6. **c)** Simulations of a 45° V-cavity made of magenta material. **d)** Corresponding spectra displayed by all facets across the cavity are

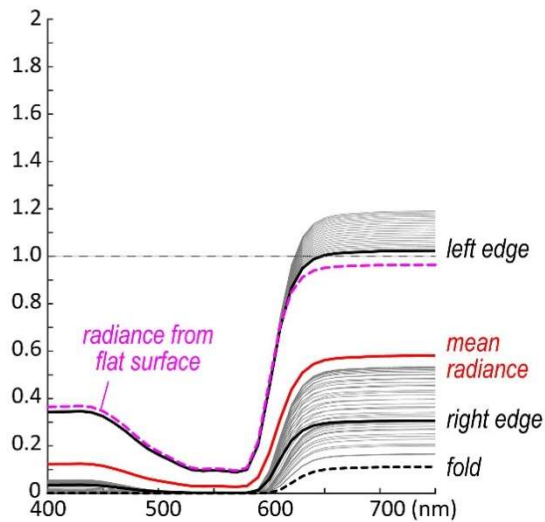
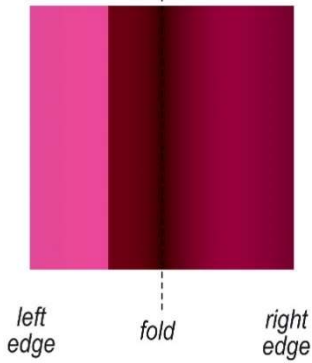
d) Simulated color gradient in a cavity



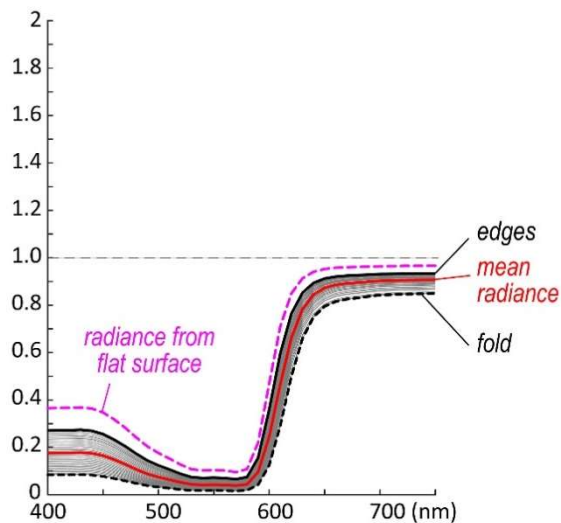
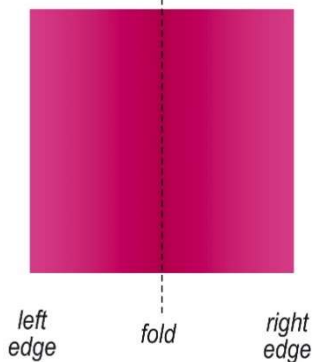
e) Simulated spectral radiances from the cavity facets



Frontal (0°) illumination



Oblique (45°) illumination

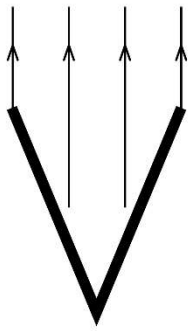


Diffuse illumination

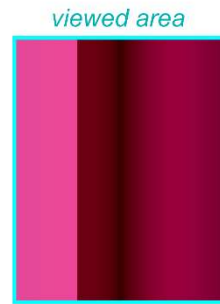
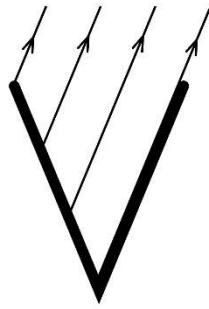
represented, with a solid line standing for a spectrum on the edge of the cavity, a dashed line representing a facet at the fold of the cavity, a dashed magenta line symbolizing the reflectance of the flat surface made with the same material, and a solid red line representing the average reflectance displayed by the cavity seen from afar, at an $(\theta, \varphi) = (0^\circ, 0^\circ)$ angle (frontal view).

Geometries where a 45°-cavity is wholly viewed

Frontal view ($\theta = 0^\circ$)



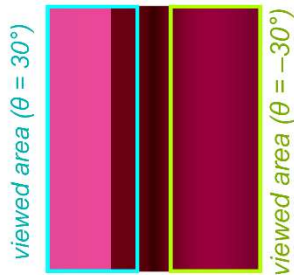
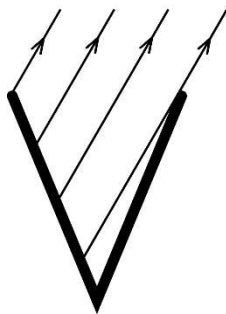
Oblique view ($\theta = 22.5^\circ$)



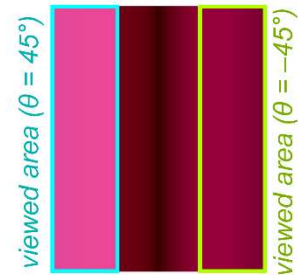
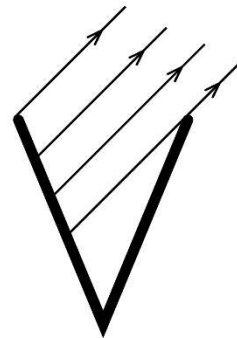
Simulated cavity
of magenta material
illuminated at 45°

Geometries where a 45°-cavity is partially viewed

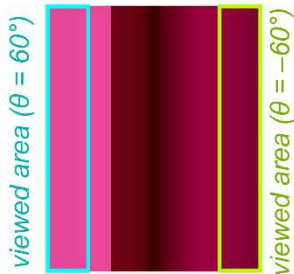
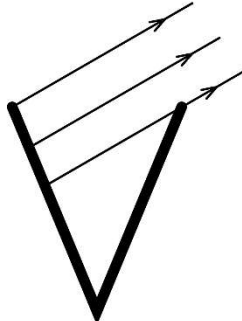
Oblique view ($\theta = 30^\circ$)



Oblique view ($\theta = 45^\circ$)



Oblique view ($\theta = 60^\circ$)



Oblique view ($\theta = 75^\circ$)

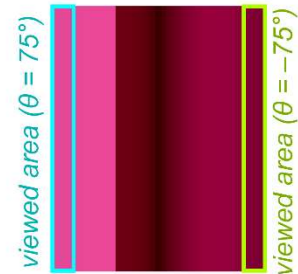
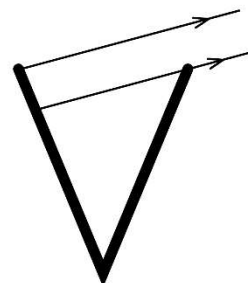


Figure PF3-2 — Visible area of a 45° magenta V-cavity, illuminated by a directional light source following the $(45^\circ, 0^\circ)$ direction, as a function of the zenithal angle of observation. The area contained in a blue rectangle stands for a positive angle, and the area in the yellow rectangle stands for a negative angle.

a) Mean spectral radiances over cavity ($\alpha = 45^\circ$)

b) (L^*, C^*) color values

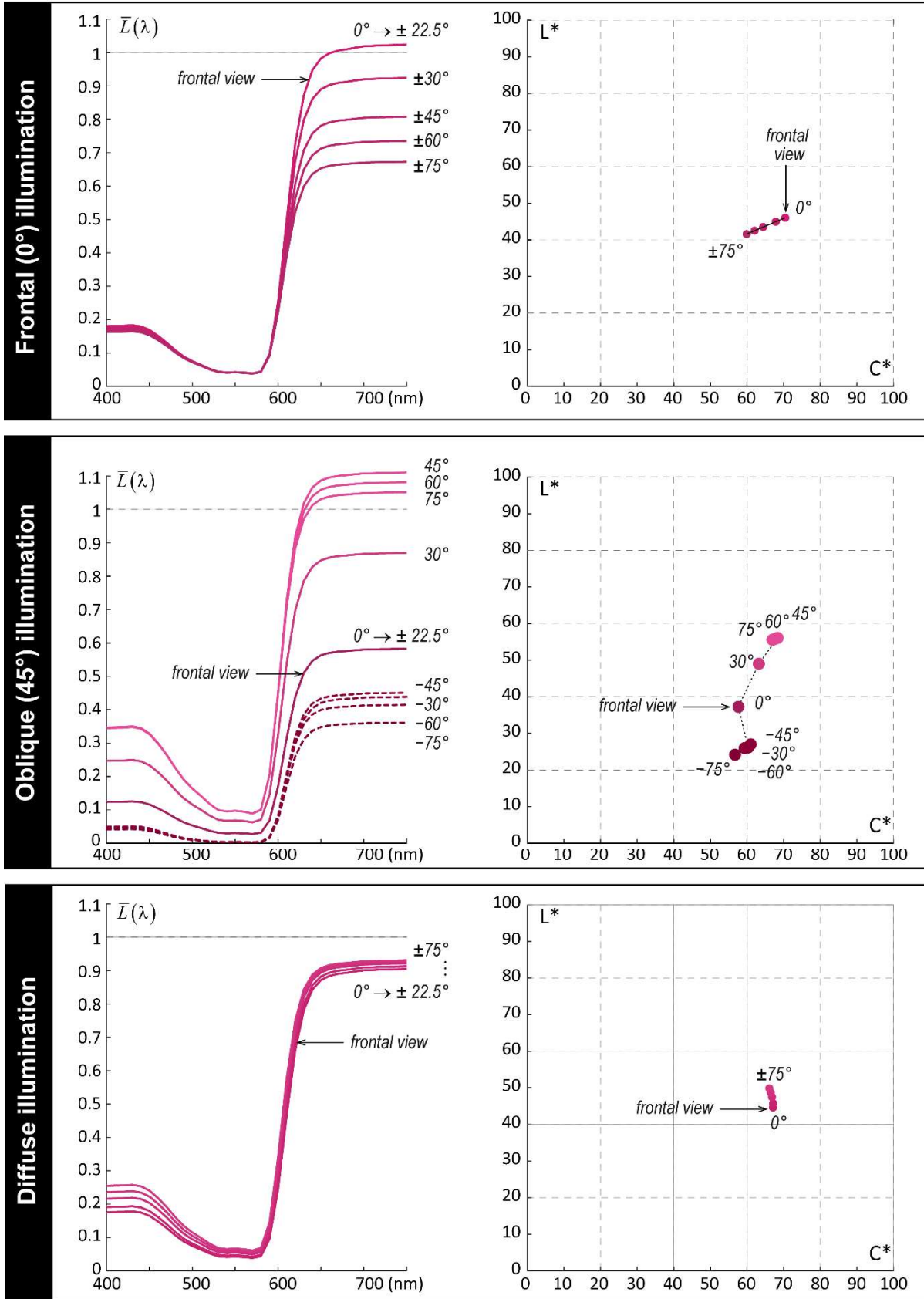
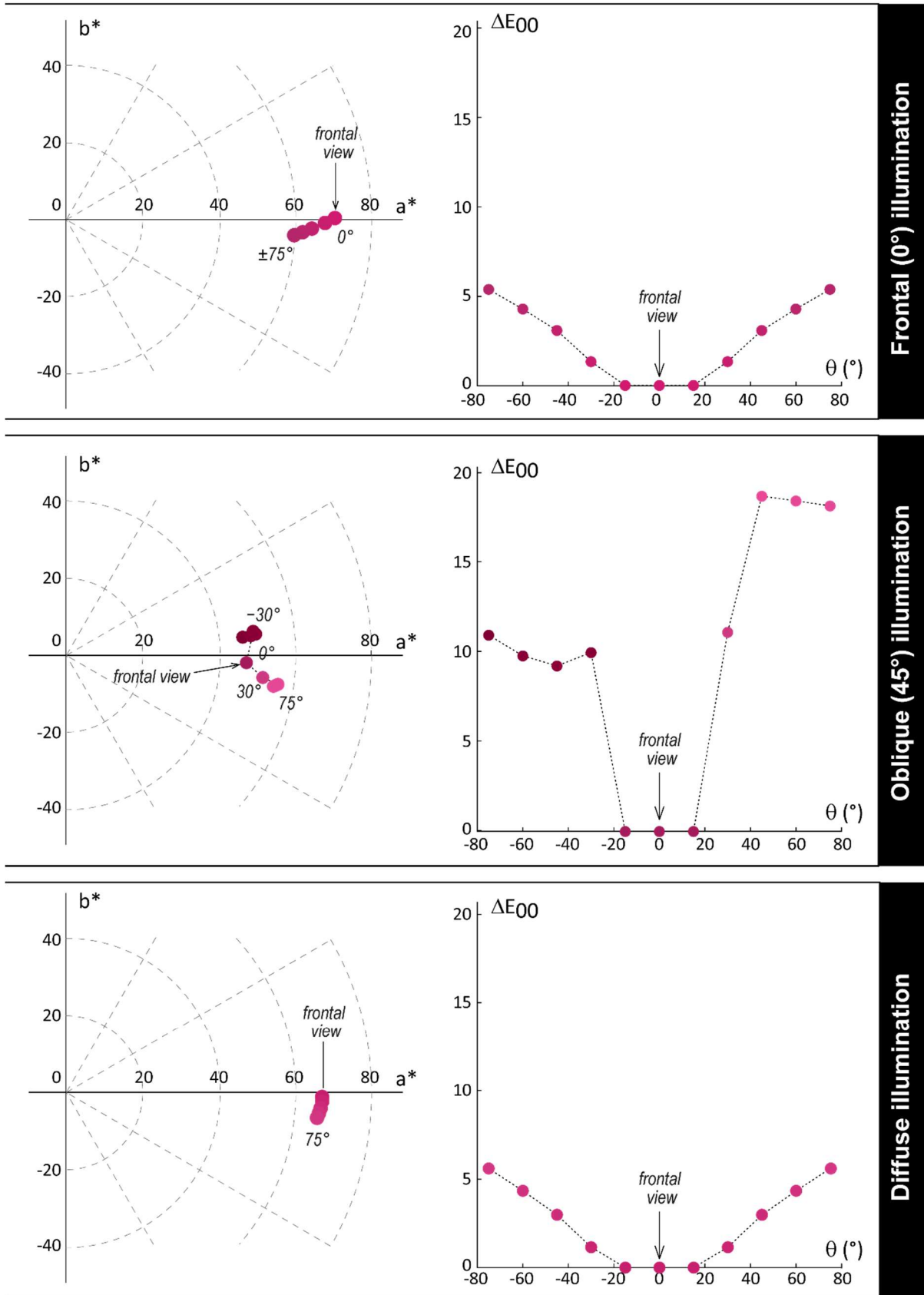


Figure PF3-3 (double page) — Simulated average spectral radiances and colors displayed under different viewing angles by a 45° magenta V-cavity under three types of illumination : frontal, oblique and collimated at 45° , and diffuse. The observation direction varies from a zenith angle of -75° to 75° in steps of 15° , with an azimuth angle of 0° . a) Spectral radiances observed: for each

c) (a^* , b^*) color values

d) Color deviation from the frontal view



zenithal angle of observation, the average spectral radiance is drawn with a solid line for the positive range, a dashed line for the negative one. **b)** Corresponding CIE1976 $L^*a^*b^*$ colors projected on the L^*C^* plane. **c)** Same colors projected on the a^*b^* plane. **d)** ΔE_{2000} color distance between each color and the one corresponding to the frontal view.

a) Mean spectral radiances over cavity

b) (L^* , C^*) color values

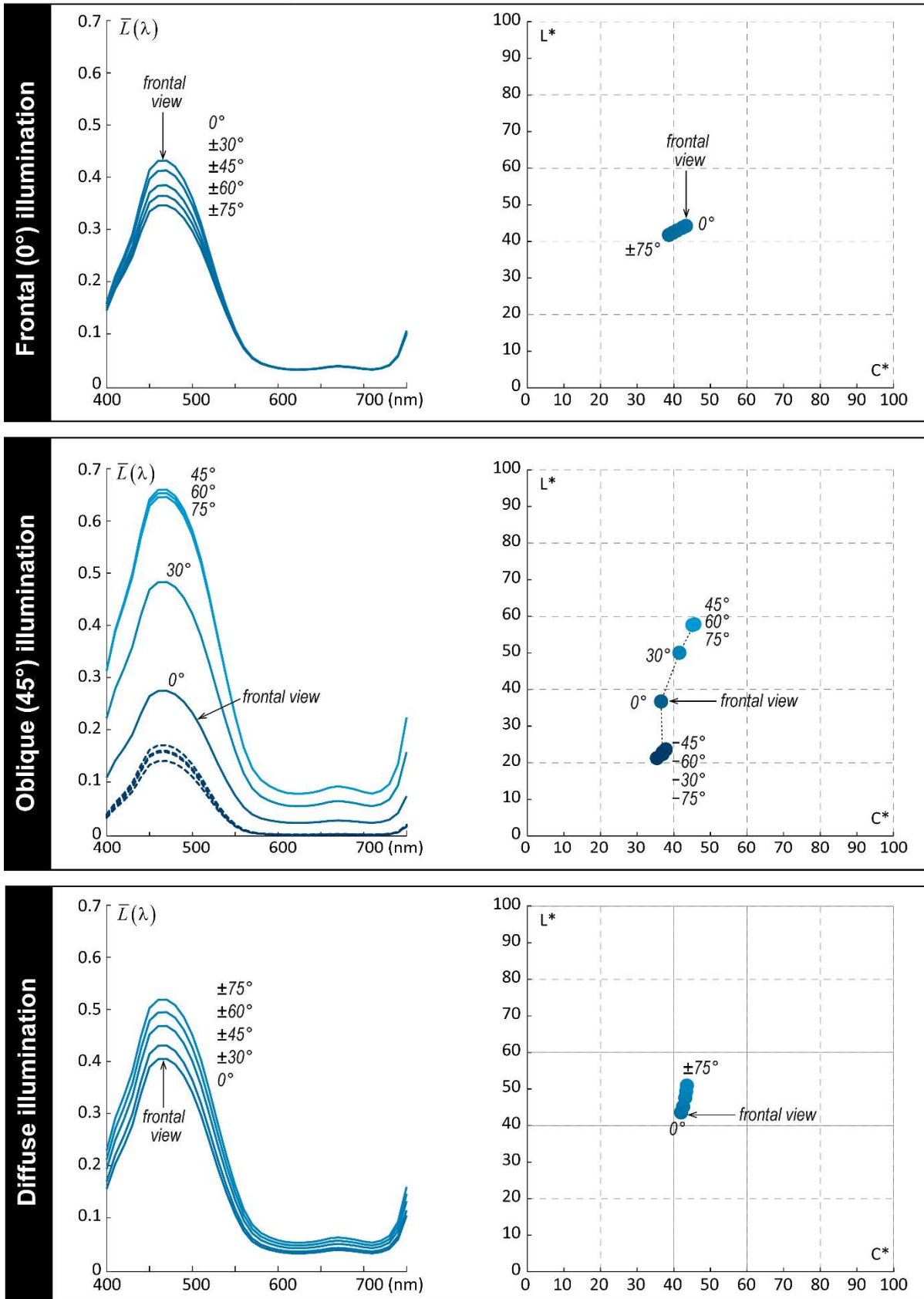
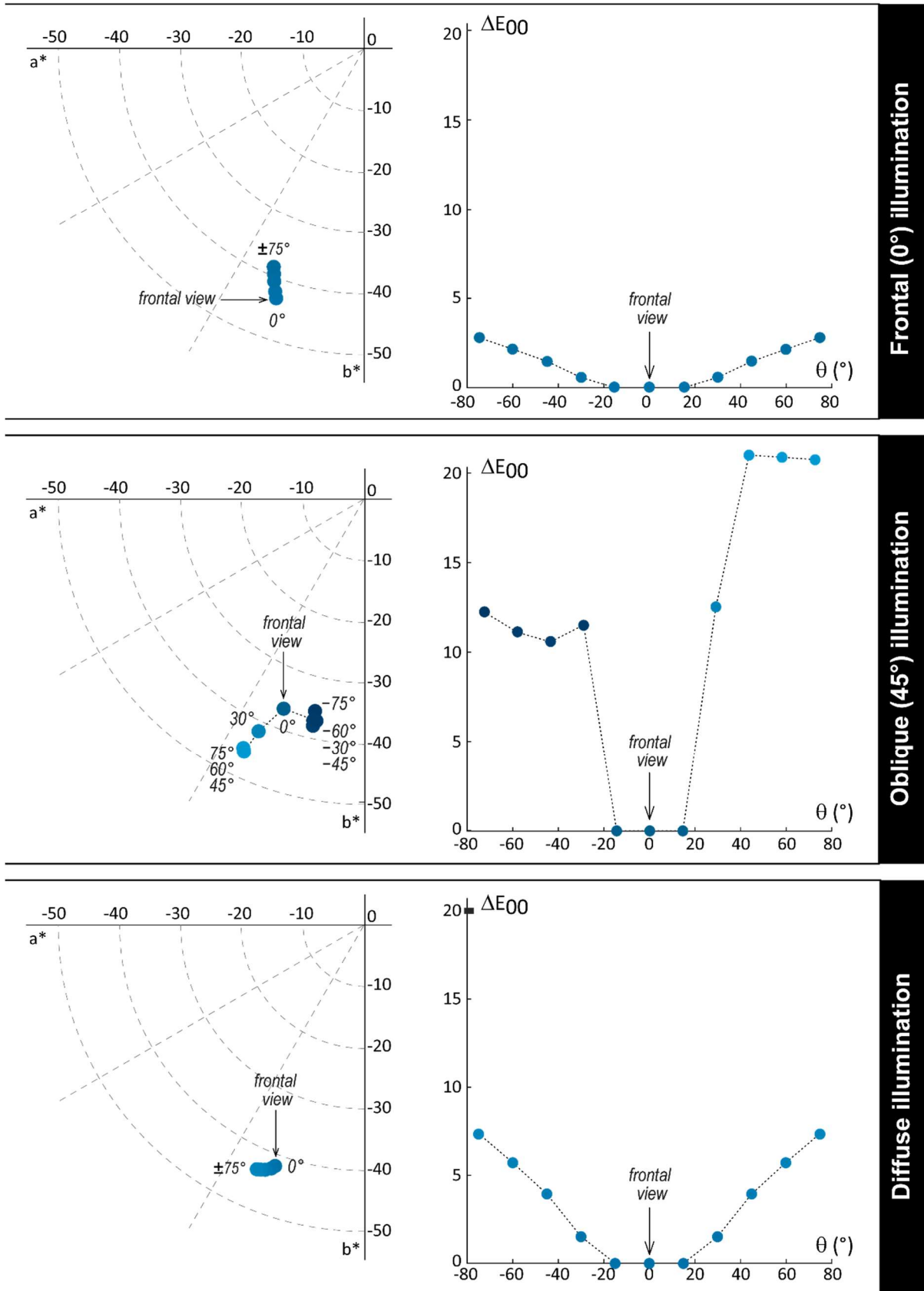


Figure PF3-4 (double page) — Simulated average spectral radiances and colors displayed under different viewing angles by a 45° cyan V-cavity under three types of illumination : frontal, oblique and collimated at 45°, and diffuse. The observation direction varies from a zenith angle of -75° to 75° in steps of 15°, with an azimuth angle of 0°. **a)** Spectral radiances observed: for each zenith

c) (a^* , b^*) color values

d) Color deviation from the frontal view



angle of observation, the average spectral radiance is drawn with a solid line for the positive range, a dashed line for the negative one. **b)** Corresponding CIE1976 $L^*a^*b^*$ colors projected on the L^*C^* plane. **c)** Same colors projected on the a^*b^* plane. **d)** ΔE_{2000} color distance between each color and the one corresponding to the frontal view.

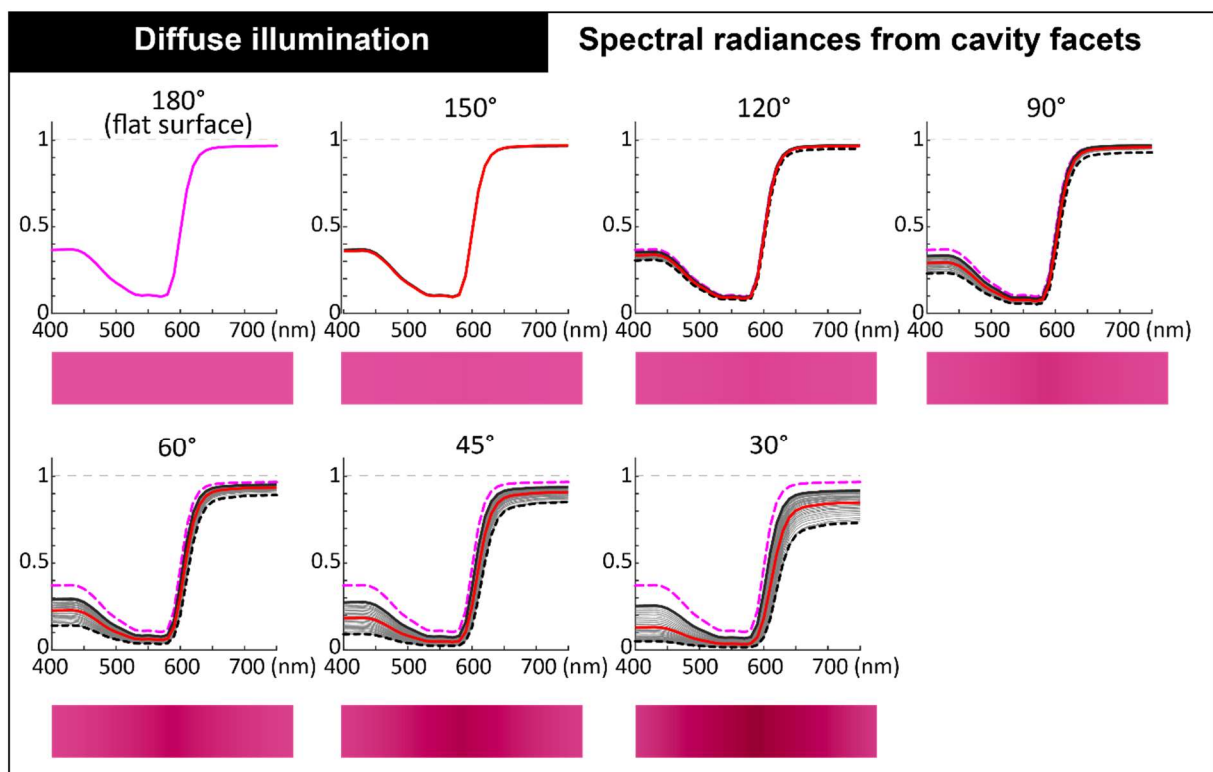
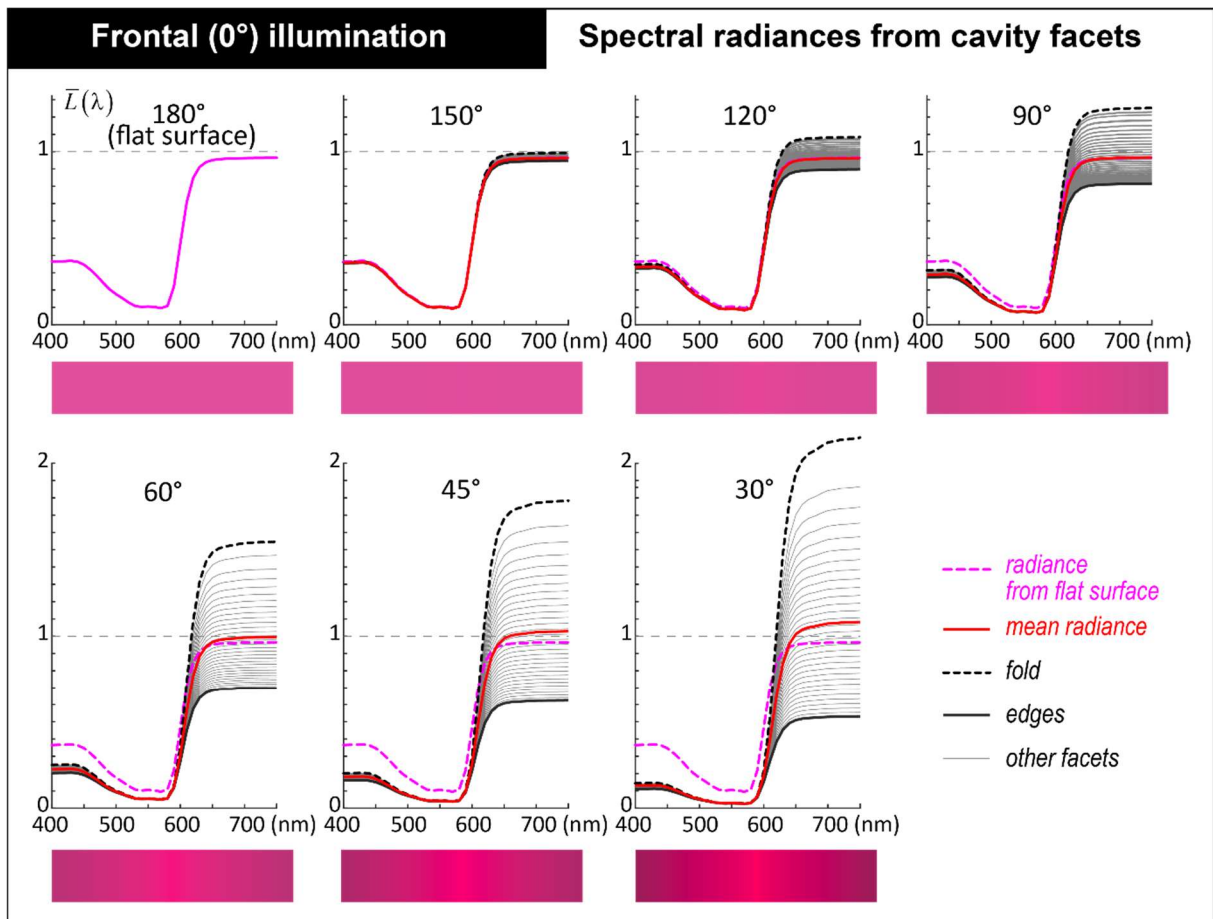


Figure PF3-5 – Simulated spectral radiances displayed by a magenta V-cavity for a dihedral angle α of 30°, 45°, 60°, 90°, 120°, 150° and 180°, under a frontal collimated lighting and a diffuse lighting. The colored rectangles are a color preview of a band of the cavity in each configuration.

a) Mean spectral radiances over cavity (frontal view)

b) (L^*, C^*) color values

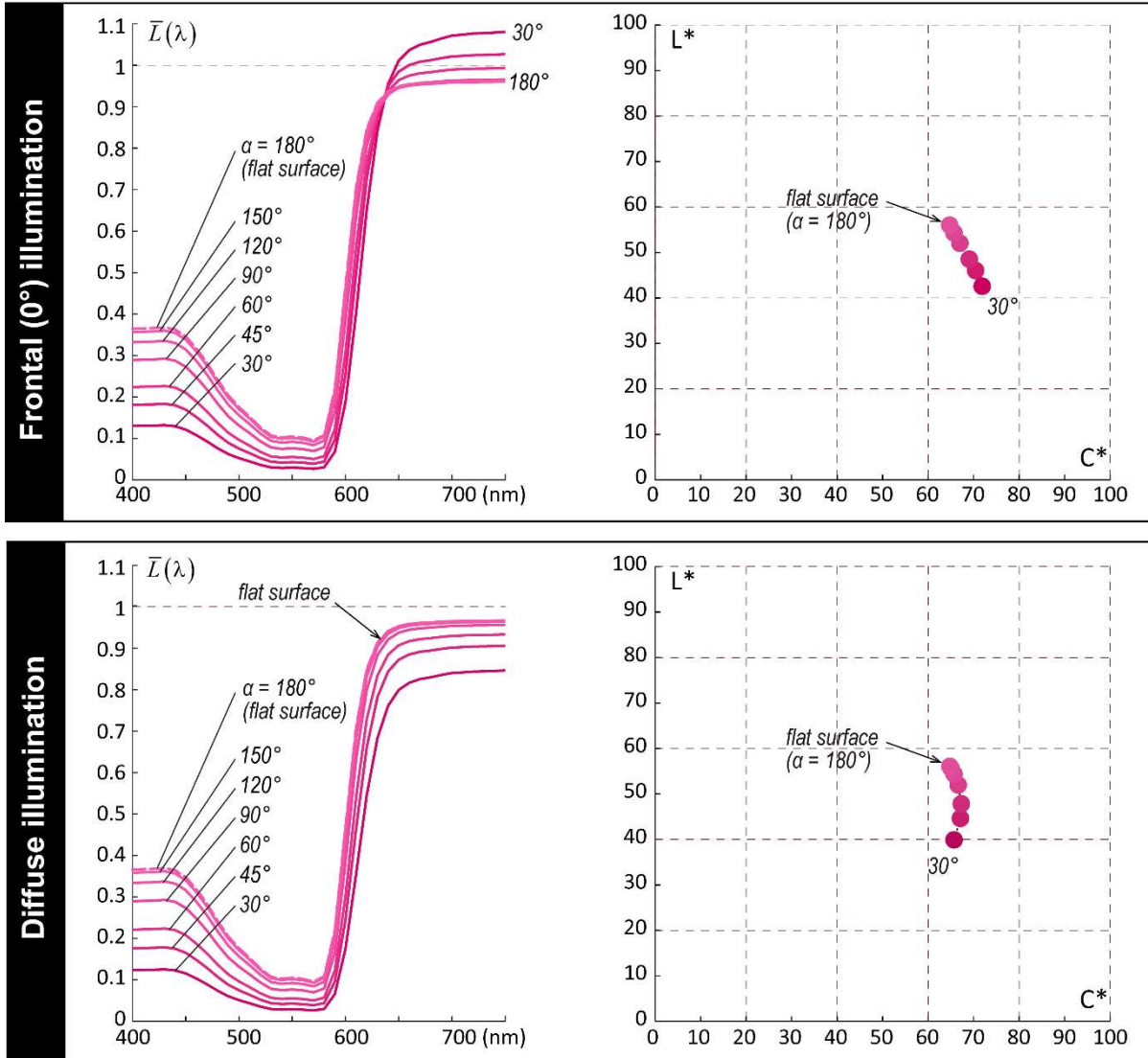
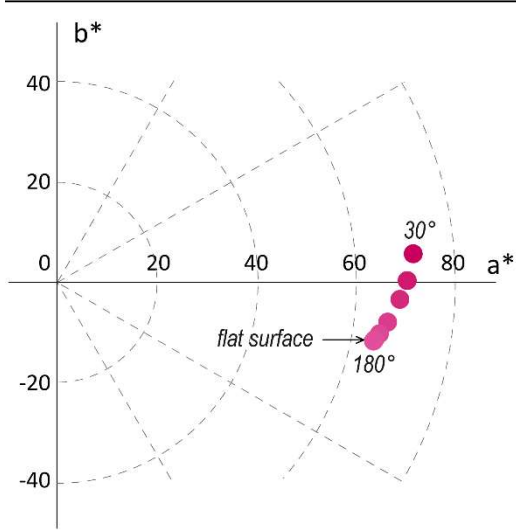
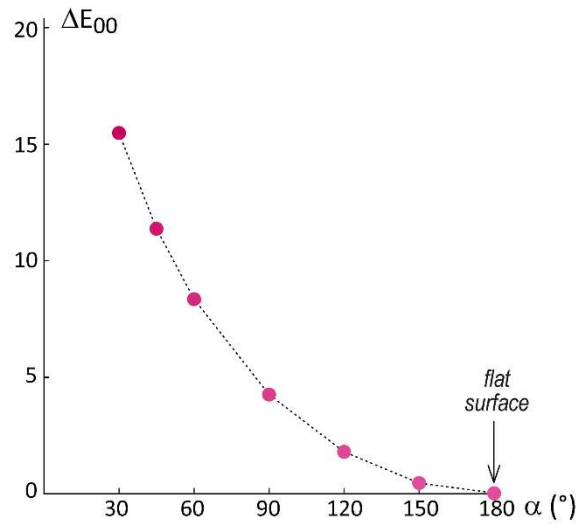


Figure PF3-6 (double page) — Simulated average spectral radiances displayed by a magenta V-cavity with a dihedral angle varying from 30° to 180° in steps of 15°, under a frontal lighting (0°, 0°) (top row) and a diffuse lighting (bottom row). a) Spectral radiances observed. b) Corresponding CIE1976 $L^*a^*b^*$ colors projected on the L^*C^* plane. c) Same colors projected on the a^*b^* plane. d) ΔE_{2000} color distance between each color and the one corresponding to the flat surface.

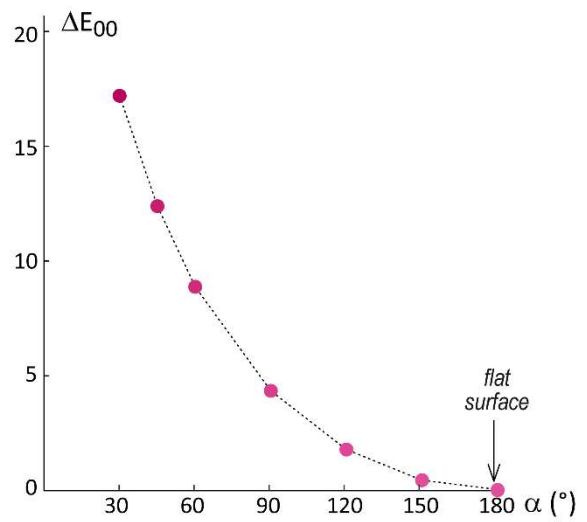
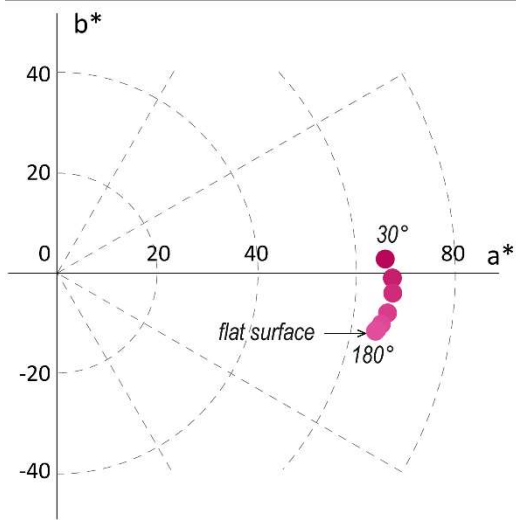
c) (a^* , b^*) color values



d) Color deviation from the flat surface



Frontal (0°) illumination



Diffuse illumination

a) Mean spectral radiances over cavity (frontal view)

b) (L^*, C^*) color values

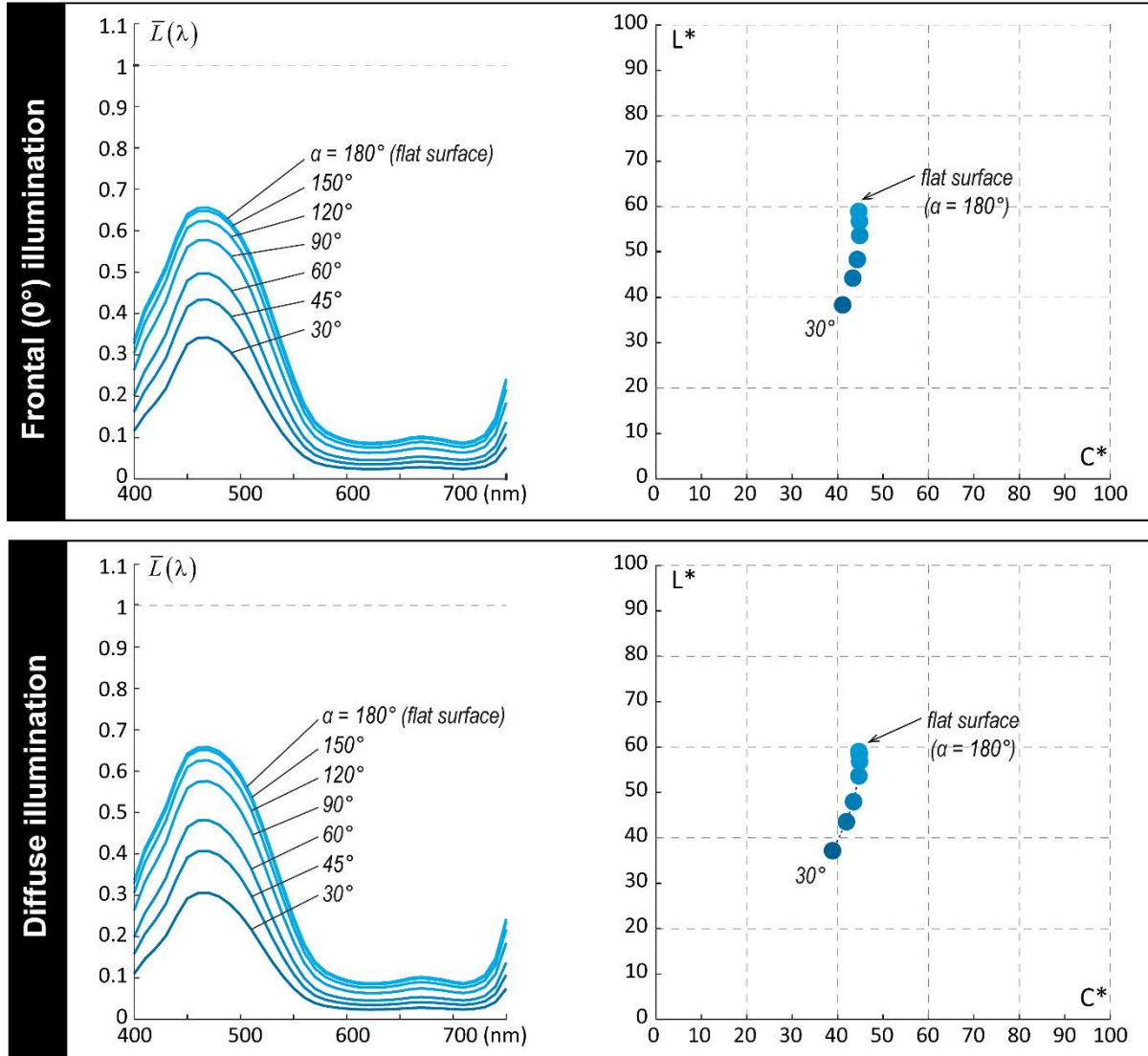
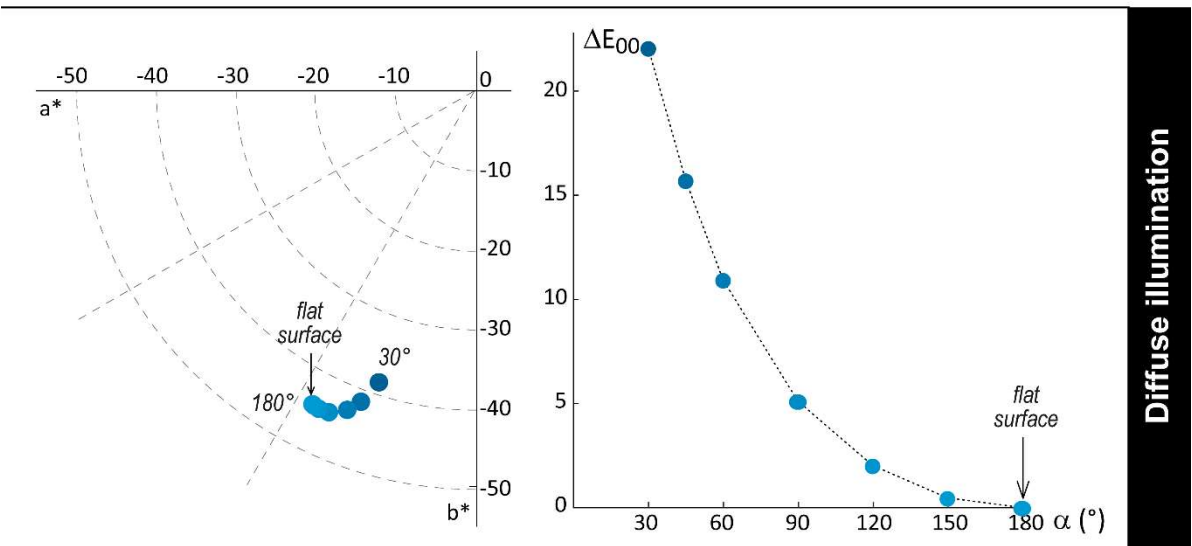
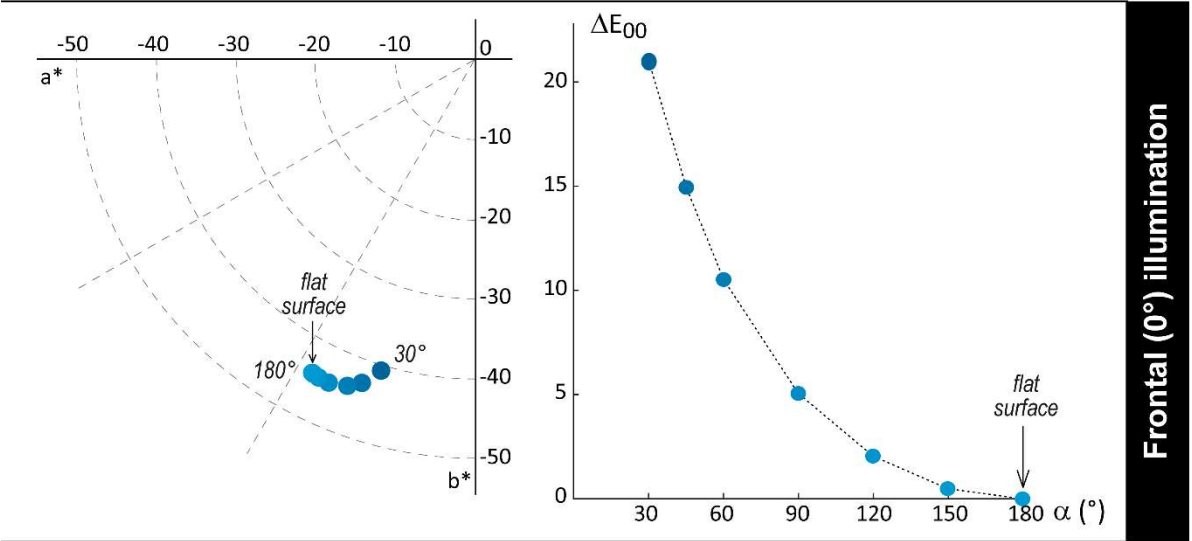


Figure PF3-7 (double page) — Simulated average spectral radiances displayed by a cyan V-cavity with a dihedral angle varying from 30° to 180° in steps of 15° , under a frontal lighting ($0^\circ, 0^\circ$) (top row) and a diffuse lighting (bottom row). a) Spectral radiances observed. b) Corresponding CIE1976 $L^*a^*b^*$ colors projected on the L^*C^* plane. c) Same colors projected on the a^*b^* plane. d) ΔE_{2000} color distance between each color and the one corresponding to the flat surface.

c) (a^* , b^*) color values

d) Color deviation from the flat surface



a) Mean spectral radiances over cavity (frontal view)

b) (L^*, C^*) color values

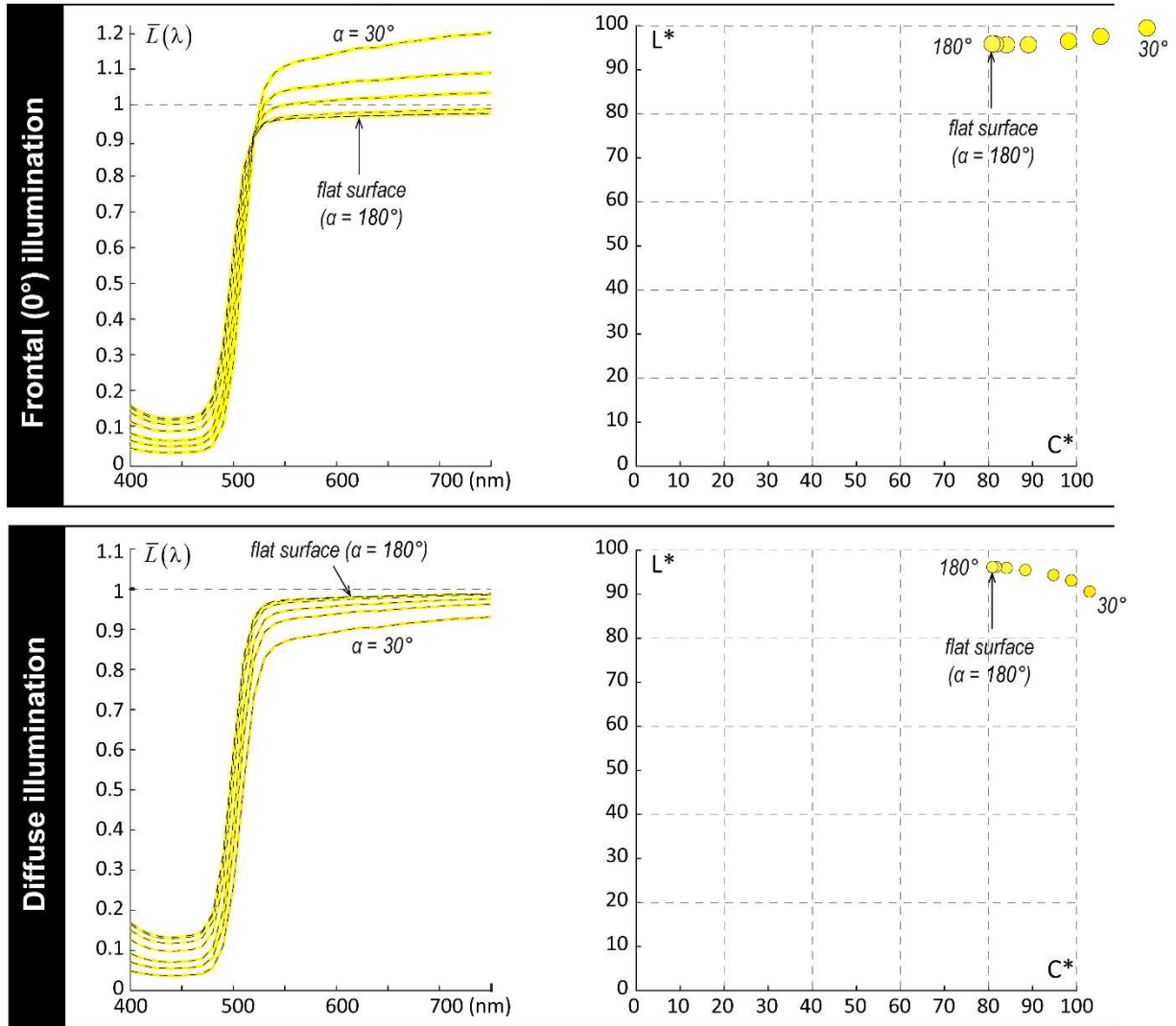
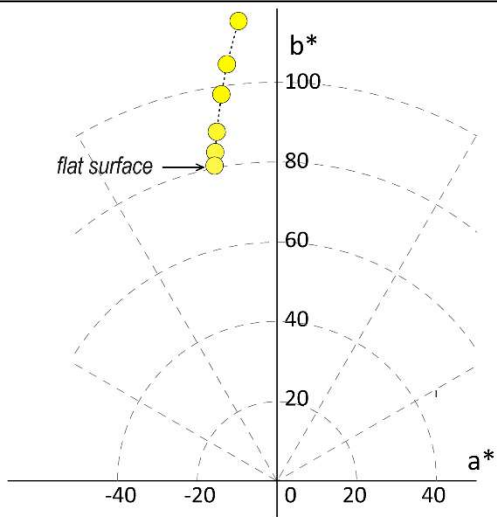
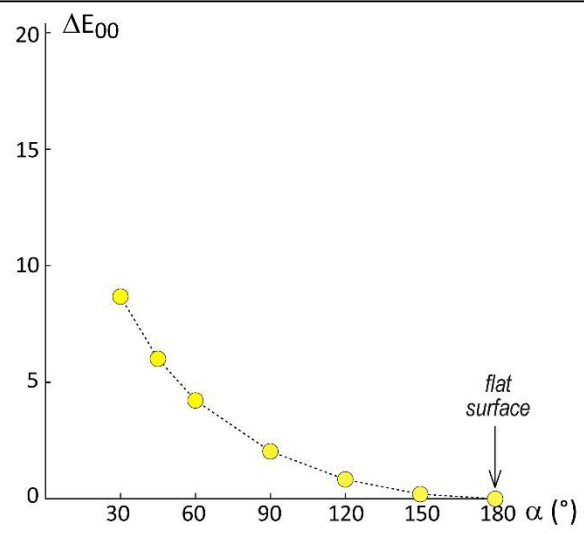


Figure PF3-8 (double page) — Simulated average spectral radiances displayed by a yellow V-cavity with a dihedral angle varying from 30° to 180° in steps of 15° , under a frontal lighting ($0^\circ, 0^\circ$) (**top row**) and a diffuse lighting (**bottom row**). **a)** Spectral radiances observed. **b)** Corresponding CIE1976 $L^*a^*b^*$ colors projected on the L^*C^* plane. **c)** Same colors projected on the a^*b^* plane. **d)** ΔE_{2000} color distance between each color and the one corresponding to the flat surface..

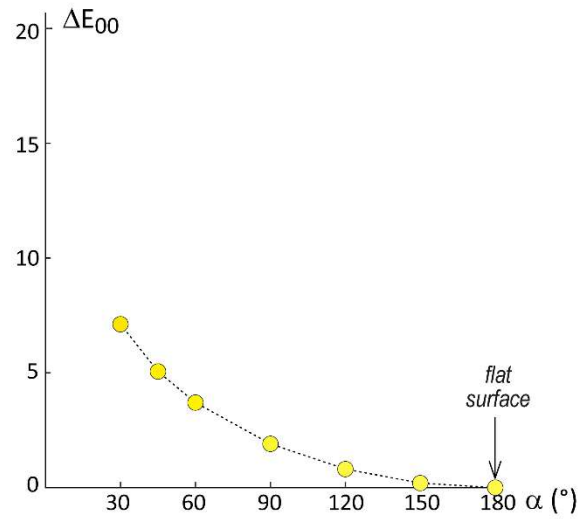
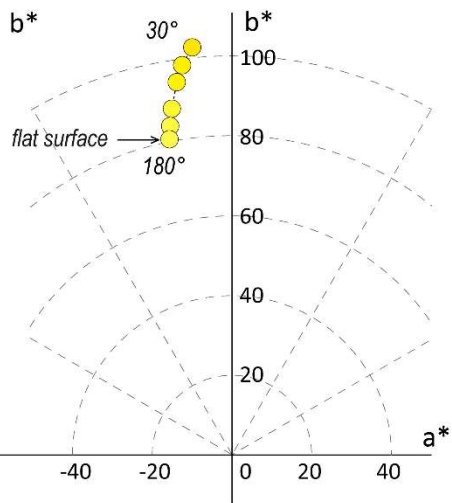
c) (a^* , b^*) color values



d) Color deviation from the flat surface



Frontal (0°) illumination



Diffuse illumination

a) Mean spectral radiances over cavity (frontal view)

b) (L^*, C^*) color values

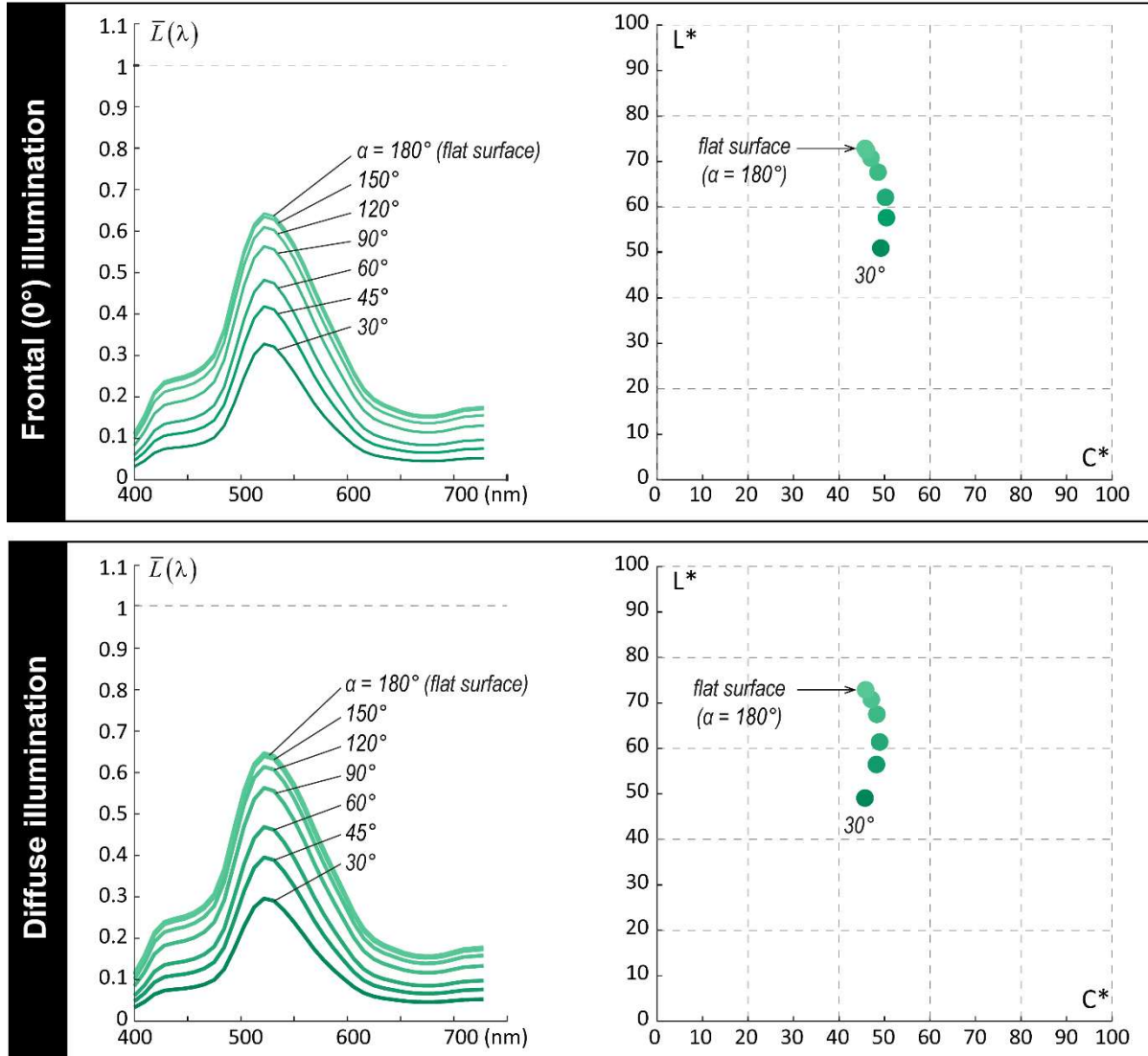
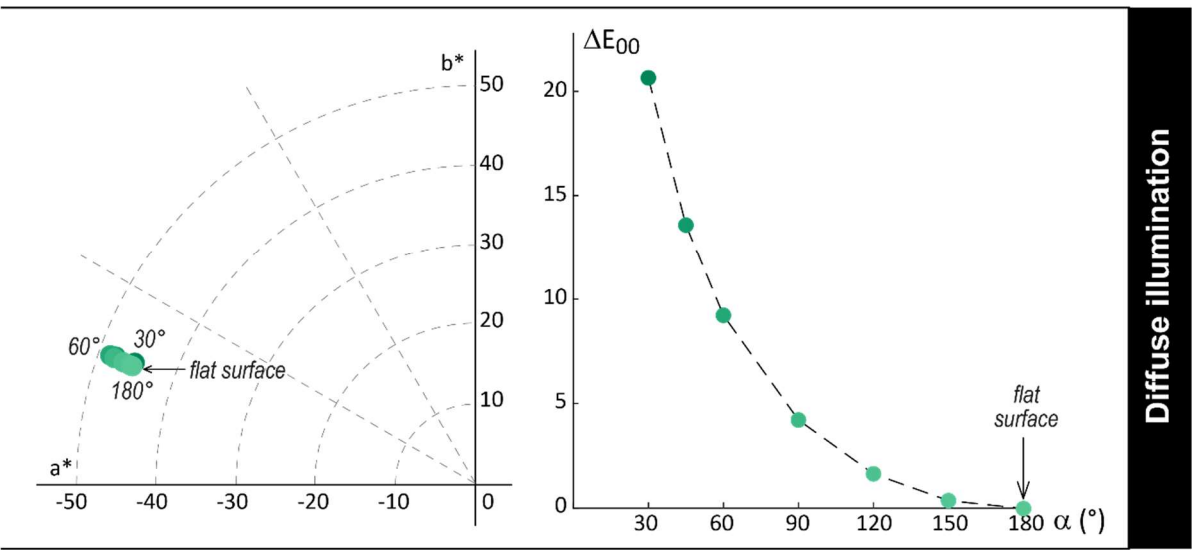
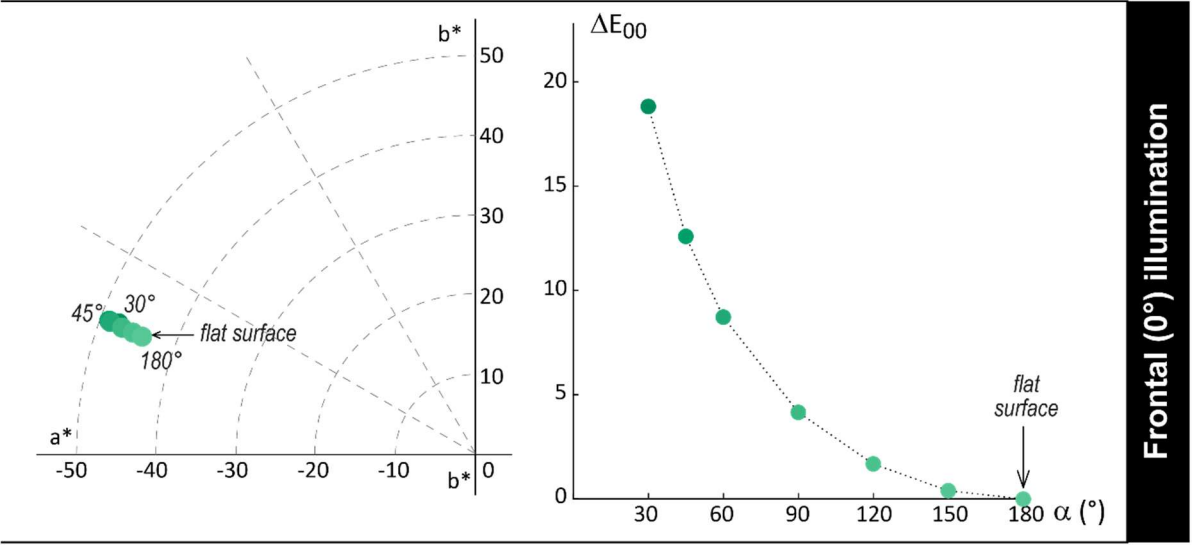


Figure PF3-9 (double page) — Simulated average spectral radiances displayed by a Munsell green V-cavity with a dihedral angle varying from 30° to 180° in steps of 15° , under a frontal lighting ($0^\circ, 0^\circ$) (top row) and a diffuse lighting (bottom row). **a)** Spectral radiances observed. **b)** Corresponding CIE1976 $L^*a^*b^*$ colors projected on the L^*C^* plane. **c)** Same colors projected on the a^*b^* plane. **d)** ΔE_{2000} color distance between each color and the one corresponding to the flat surface..

c) (a^* , b^*) color values

d) Color deviation from the flat surface



a) Mean spectral radiances over cavity (frontal view)

b) (L^*, C^*) color values

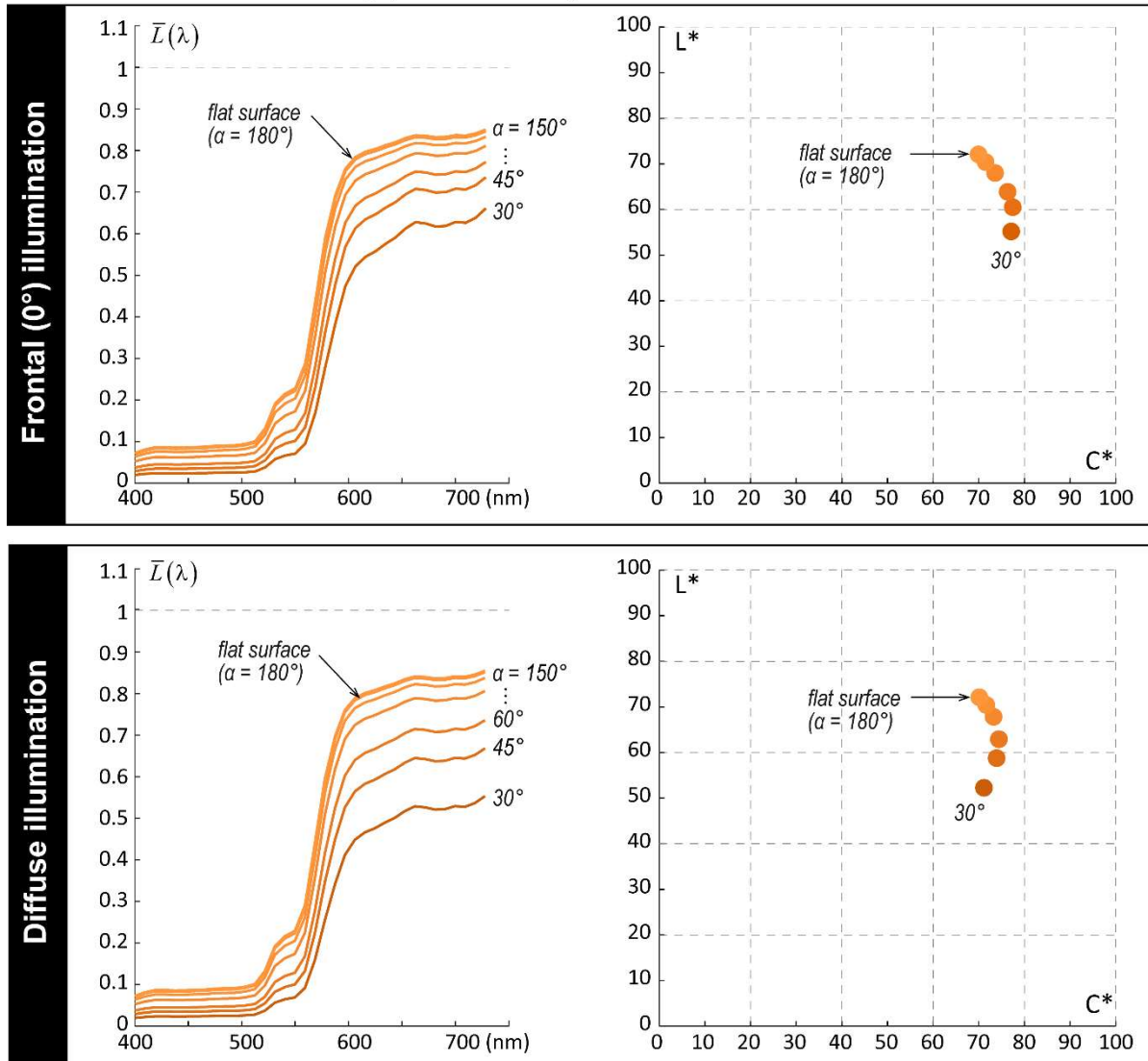
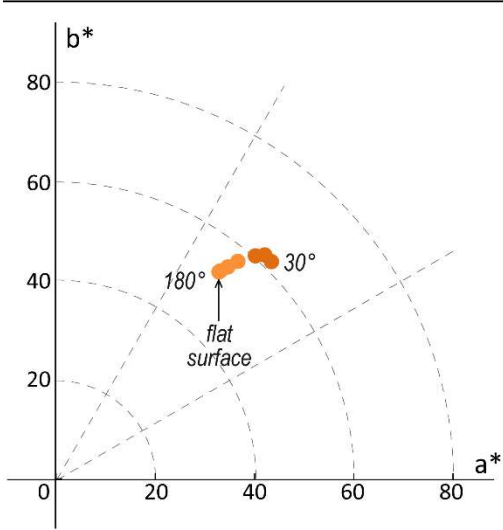
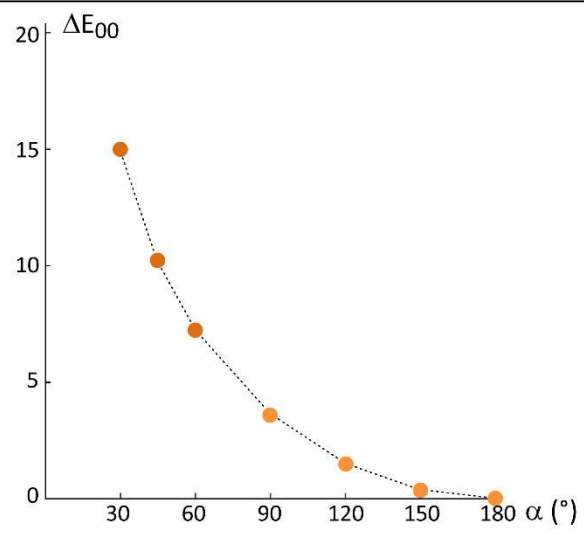


Figure PF3-10 (double page) — Simulated average spectral radiances displayed by a Munsell orange V-cavity with a dihedral angle varying from 30° to 180° in steps of 15° , under a frontal lighting ($0^\circ, 0^\circ$) (**top row**) and a diffuse lighting (**bottom row**). **a)** Spectral radiances observed. **b)** Corresponding CIE1976 $L^*a^*b^*$ colors projected on the L^*C^* plane. **c)** Same colors projected on the a^*b^* plane. **d)** ΔE_{2000} color distance between each color and the one corresponding to the flat surface..

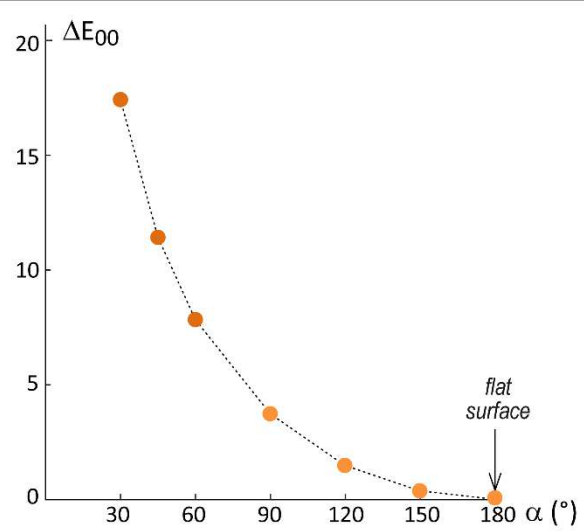
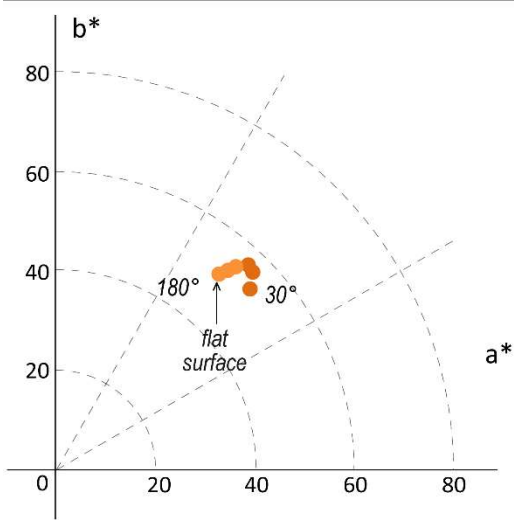
c) (a^* , b^*) color values



d) Color deviation from the flat surface



Frontal (0°) illumination



Diffuse illumination

a) Mean spectral radiances over cavity (frontal view)

b) (L^*, C^*) color values

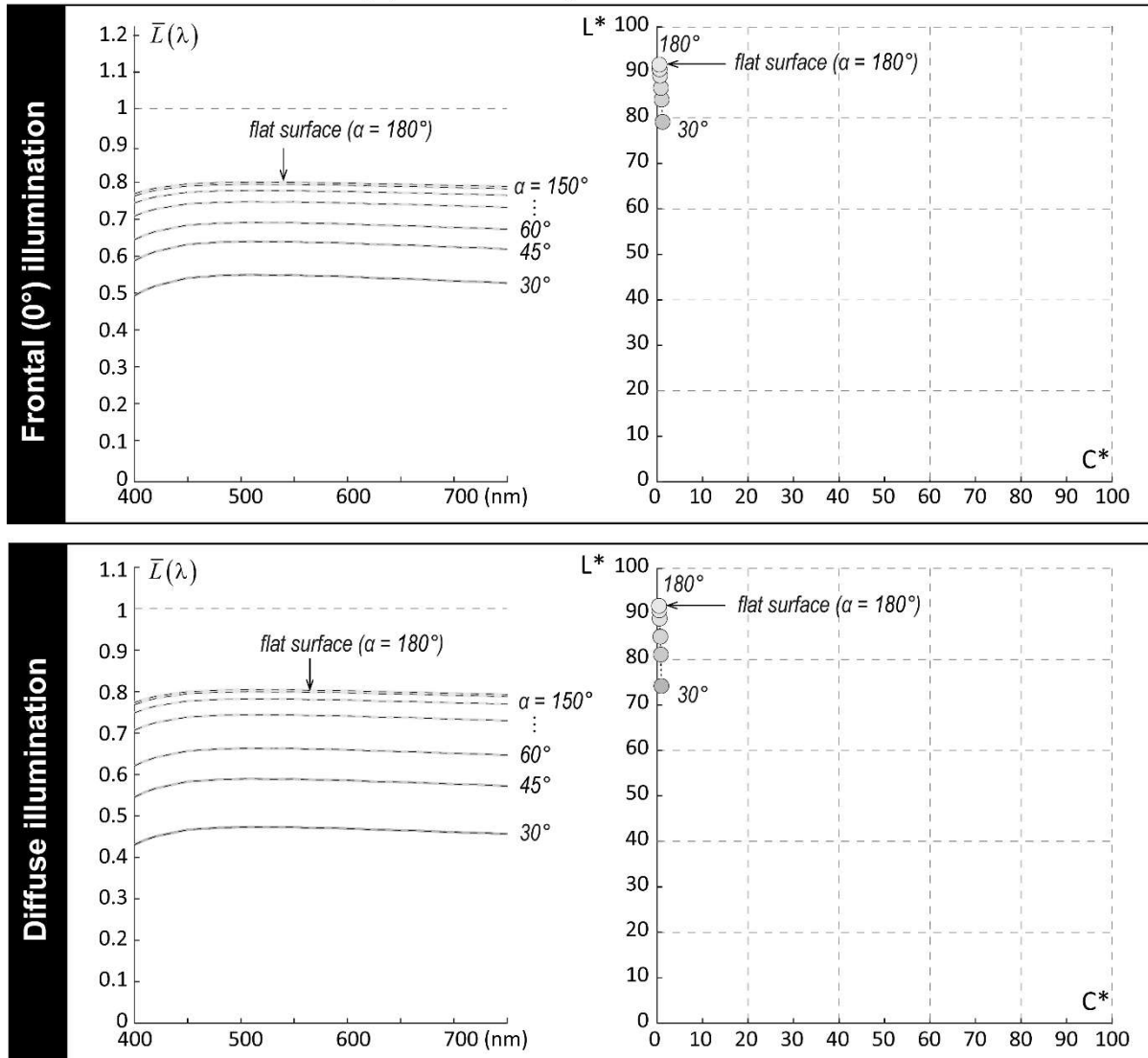
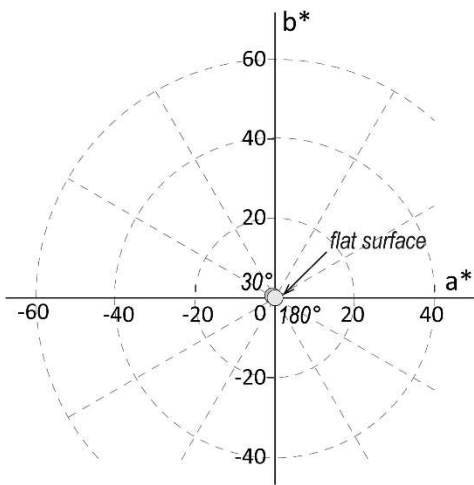
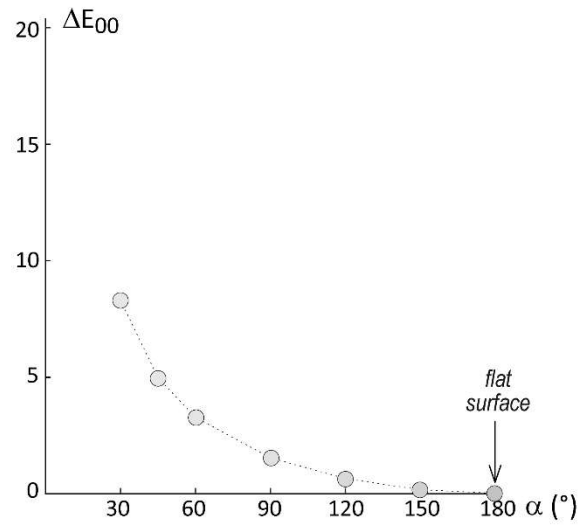


Figure PF3-11 (double page) — Simulated average spectral radiances displayed by a white V-cavity (1 sheet of paper) with a dihedral angle varying from 30° to 180° in steps of 15° , under a frontal lighting ($0^\circ, 0^\circ$) (**top row**) and a diffuse lighting (**bottom row**). **a)** Spectral radiances observed. **b)** Corresponding CIE1976 $L^*a^*b^*$ colors projected on the L^*C^* plane. **c)** Same colors projected on the a^*b^* plane. **d)** ΔE_{2000} color distance between each color and the one corresponding to the flat surface.

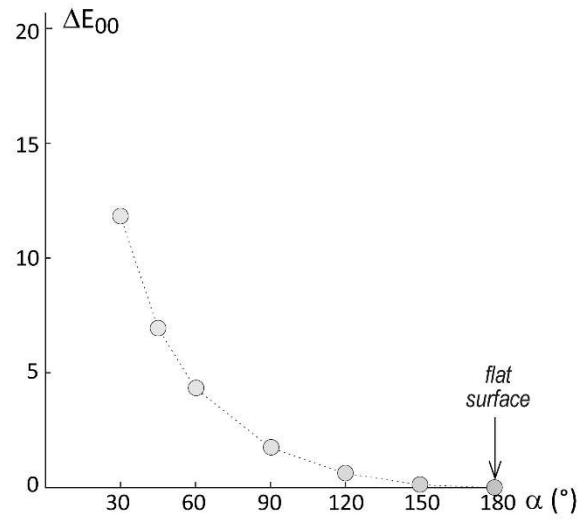
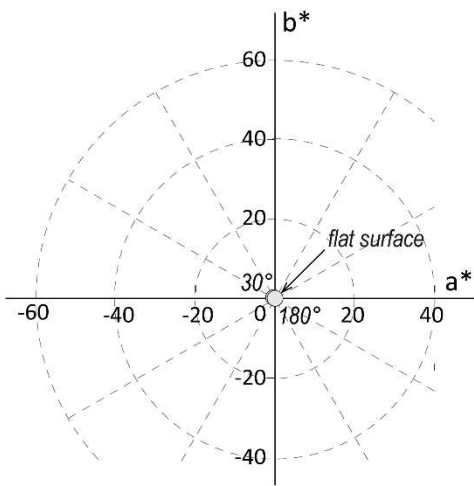
c) (a^* , b^*) color values



d) Color deviation from the flat surface



Frontal (0°) illumination



Diffuse illumination

a) Mean spectral radiances over cavity (frontal view)

b) (L^*, C^*) color values

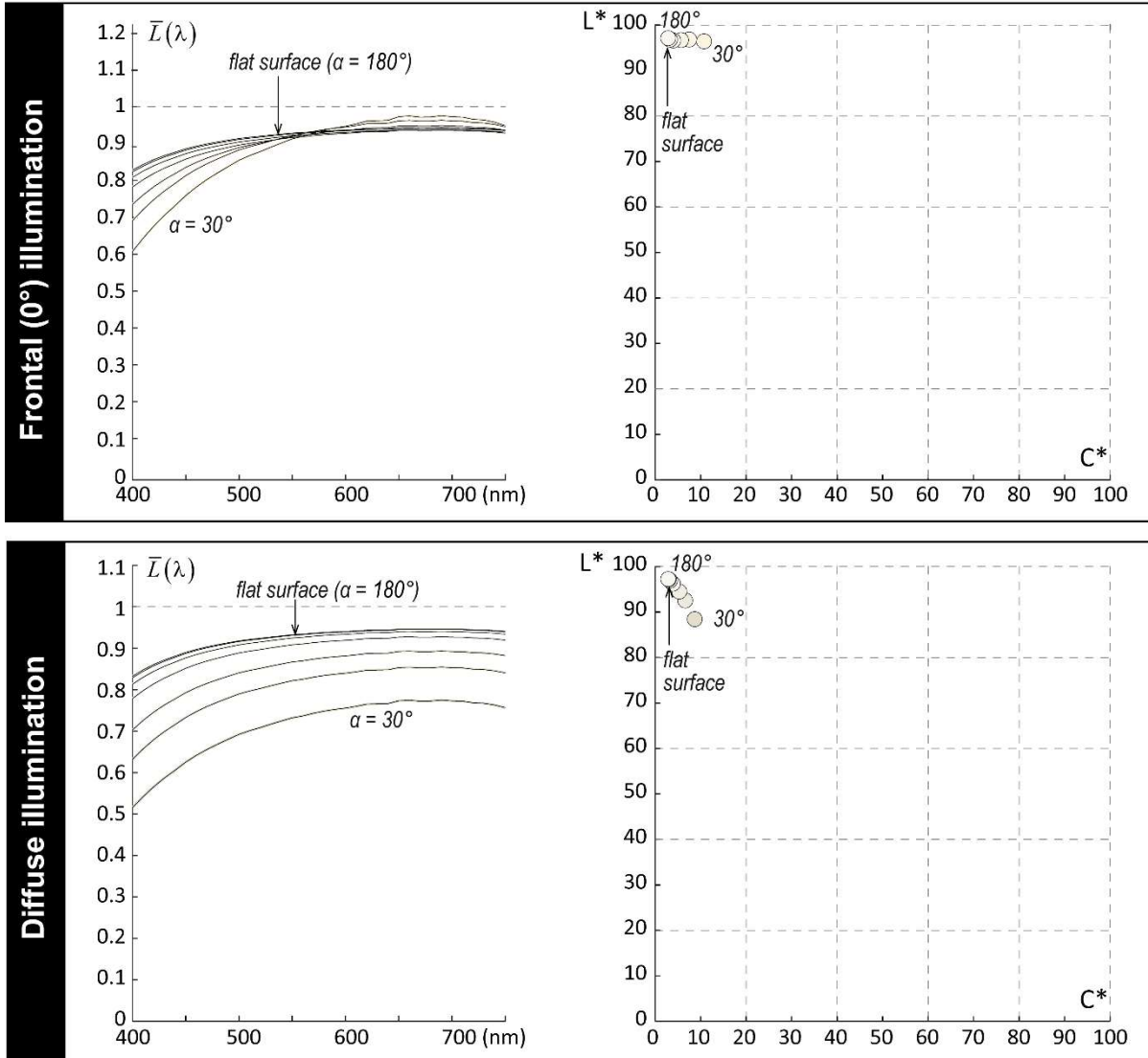
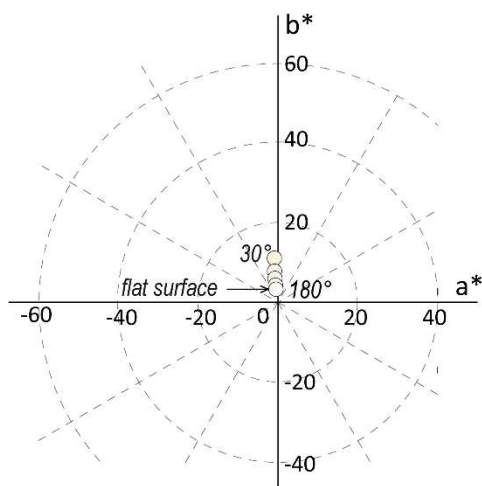
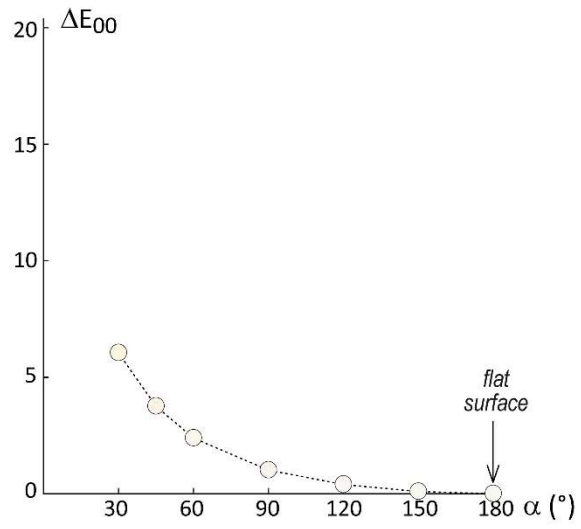


Figure PF3-12 (double page) — Simulated average spectral radiances displayed by a bright white V-cavity (5 sheets of paper) with a dihedral angle varying from 30° to 180° in steps of 15° , under a frontal lighting ($0^\circ, 0^\circ$) (top row) and a diffuse lighting (bottom row). **a)** Spectral radiances observed. **b)** Corresponding CIE1976 $L^*a^*b^*$ colors projected on the L^*C^* plane. **c)** Same colors projected on the a^*b^* plane. **d)** ΔE_{2000} color distance between each color and the one corresponding to the flat surface.

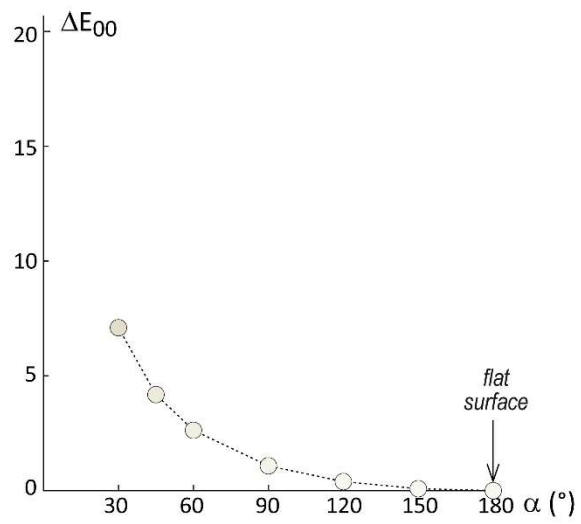
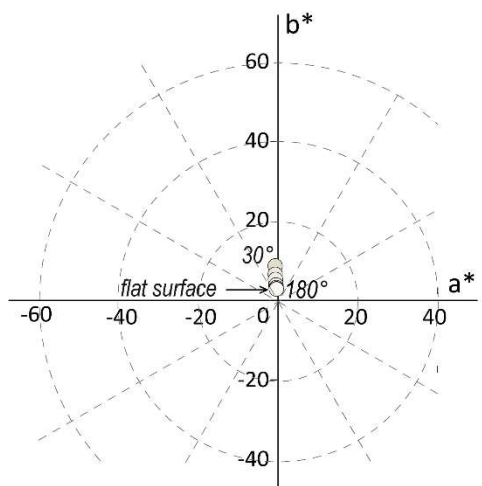
c) (a^* , b^*) color values



d) Color deviation from the flat surface



Frontal (0°) illumination



Diffuse illumination

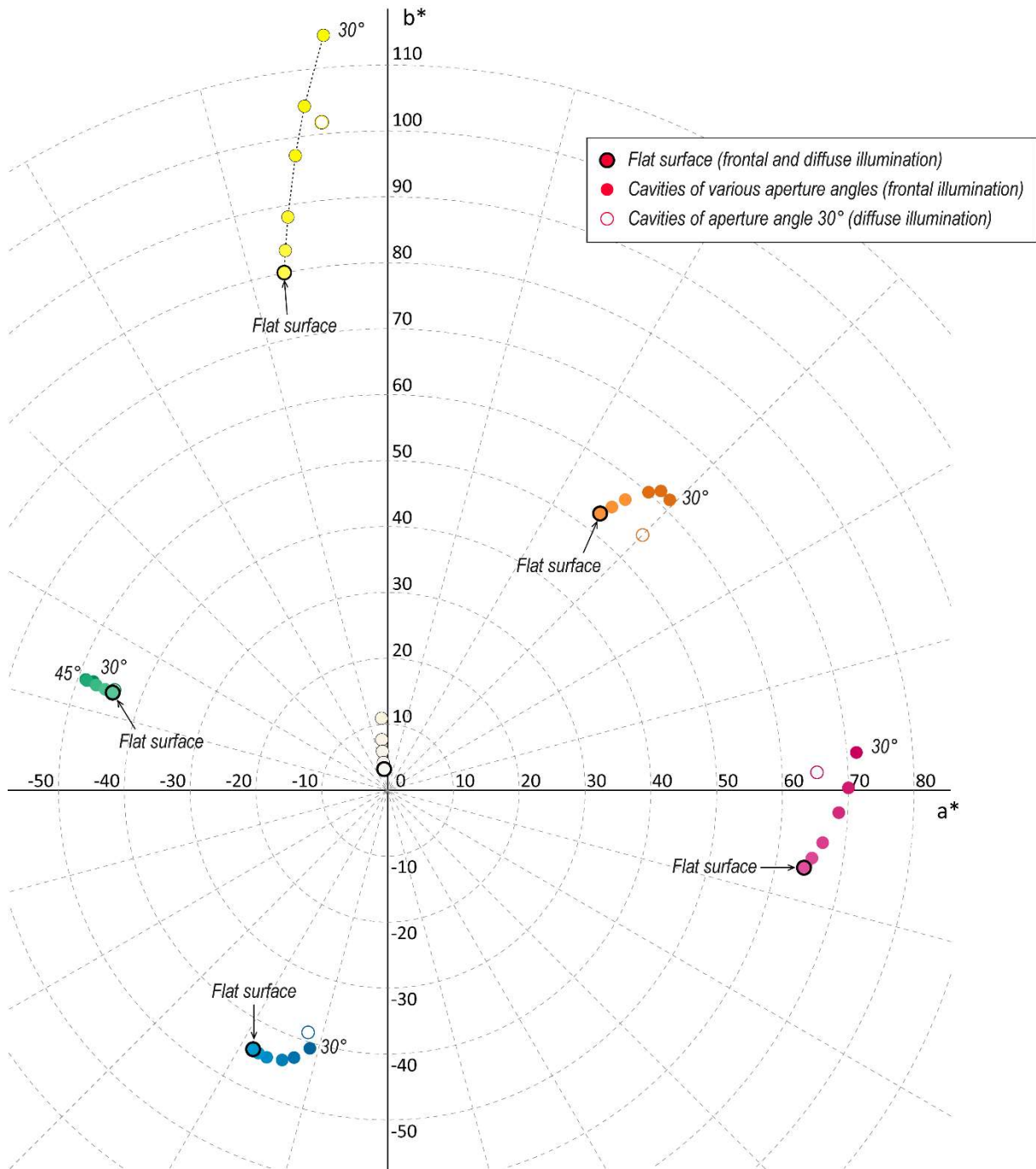
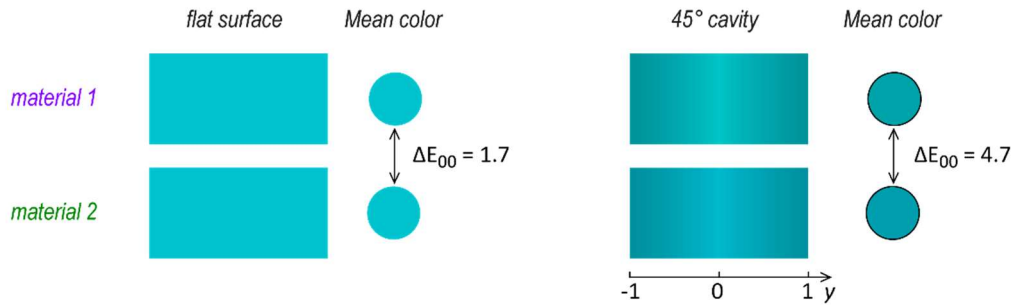


Figure PF3-13 — Simulated average CIE1976 $L^*a^*b^*$ colors of all V-cavities previously presented for both a frontal collimated lighting and a diffuse lighting; projected on the a^*b^* plane.

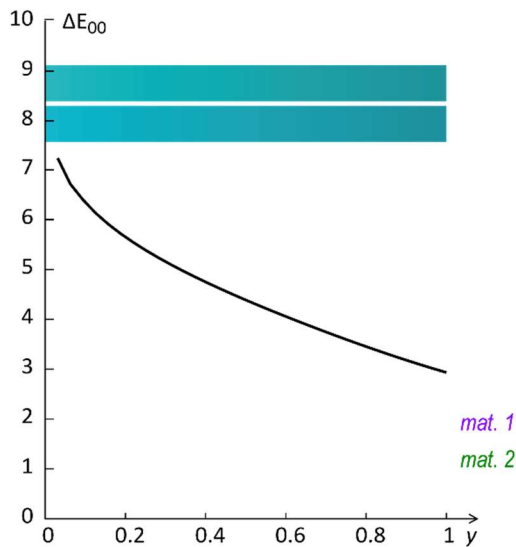
Frontal illumination

(frontal view)

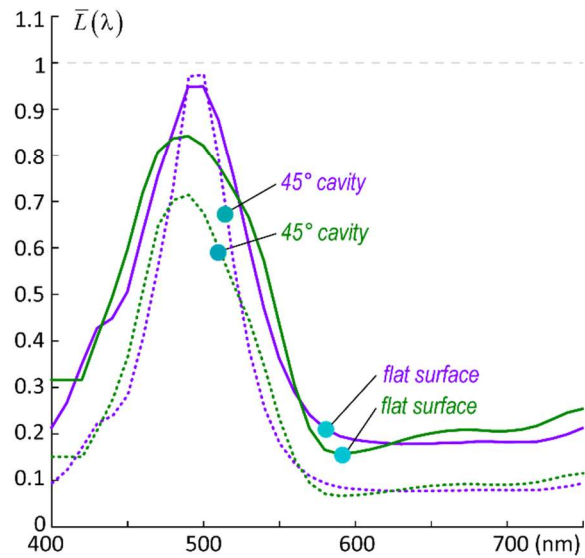
a) Color gradients



b) Point-to-point color distance in the gradients



c) Mean spectral radiances over cavity



d) (L^* , C^*) and (a^* , b^*) color values (mean and points in gradients)

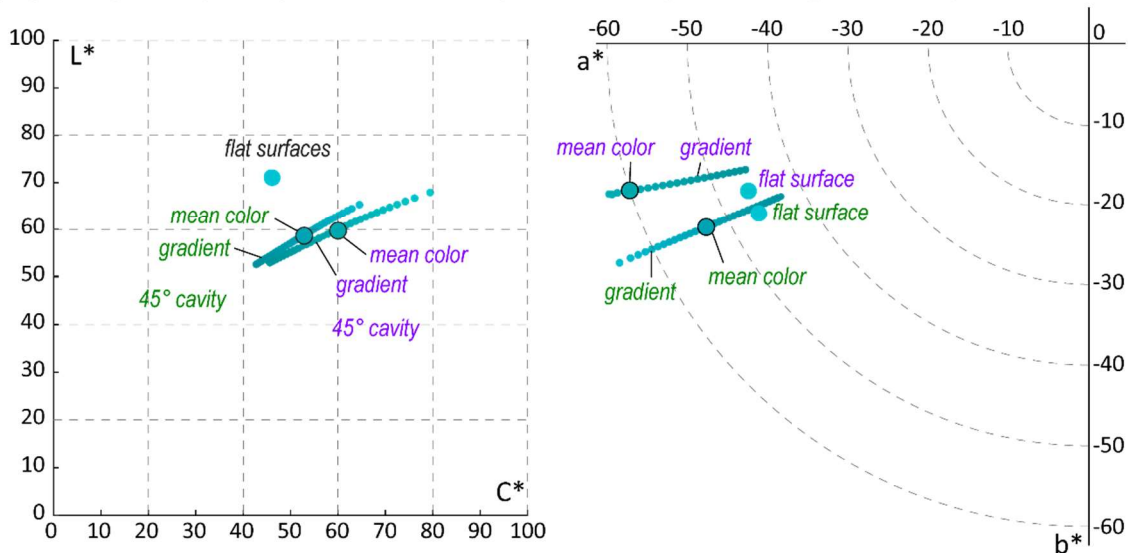
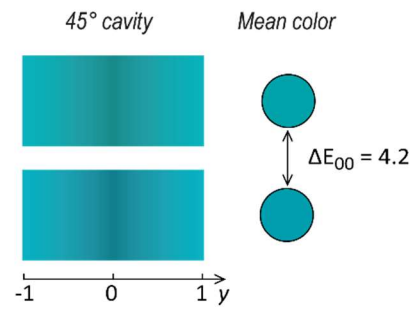
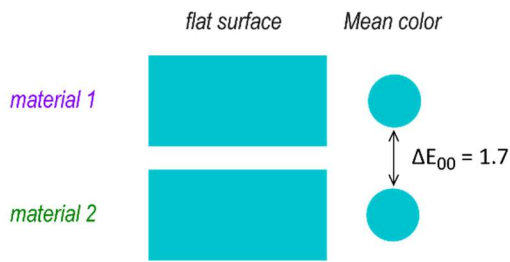


Figure PF3-14 (double page) — Simulated average spectral radiances and colors displayed by flat surfaces and 45° cavities made of two metameric materials, under frontal lighting (left page) and diffuse lighting (right page). **a)** Color previews of a band of the flat surfaces and the 45°V-cavities, their respective average color and DE2000 color distance between the two materials. **b)** Variation

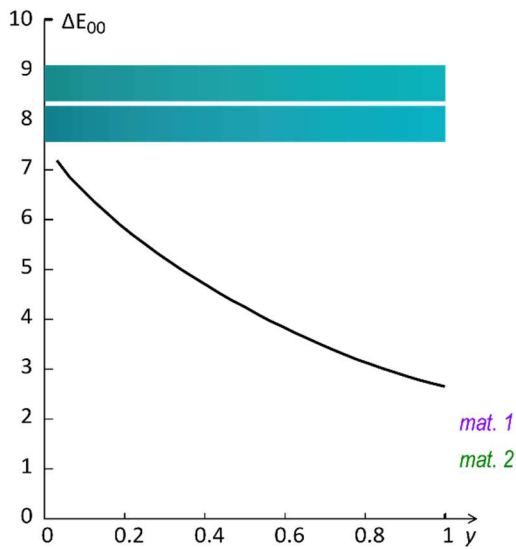
diffuse illumination

(frontal view)

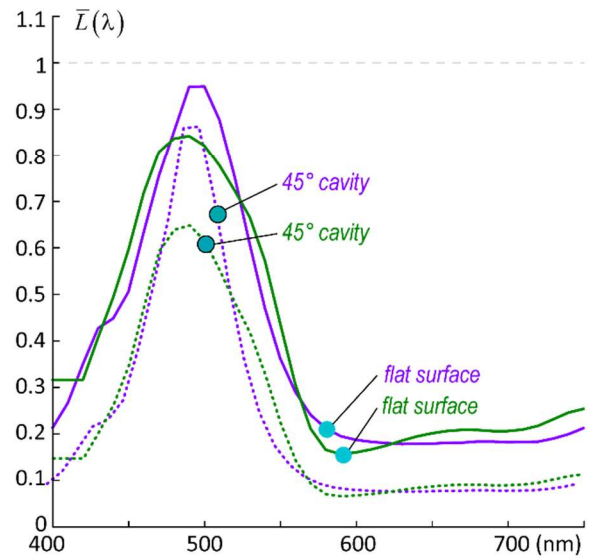
a) Color gradients



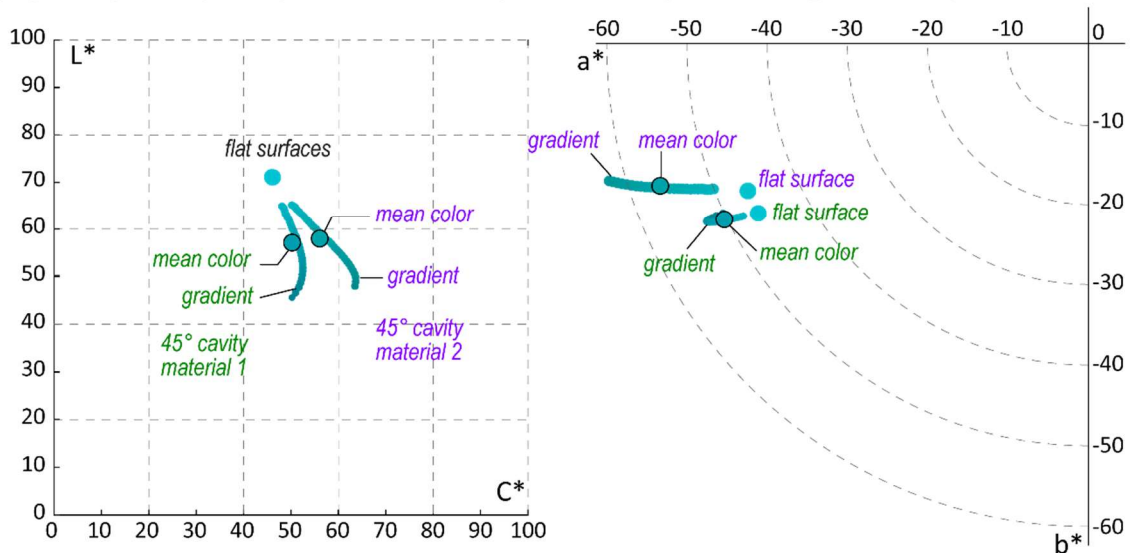
b) Point-to-point color distance in the gradients



c) Mean spectral radiances over cavity



d) (L*,C*) and (a*,b*) color values (mean and points in gradients)



of the DE2000 color distance as a function of the position in the cavity. **c)** Average spectral radiances of the four samples presented in a). **d)** Corresponding CIE 1976 L*a*b* colors projected on the L*C* plane and the a*b* plane.

Frontal (0°) illumination

Oblique (45°) illumination

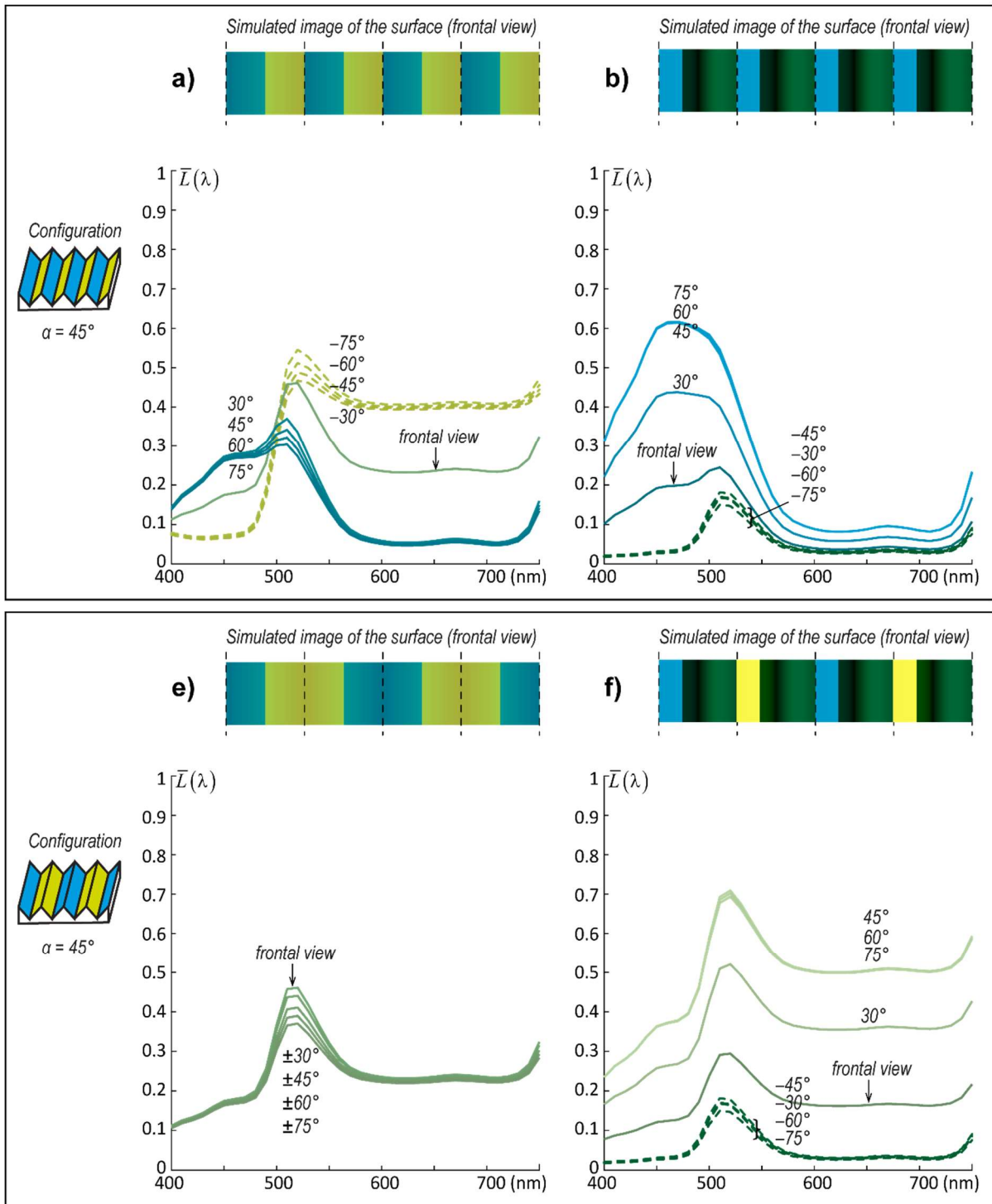
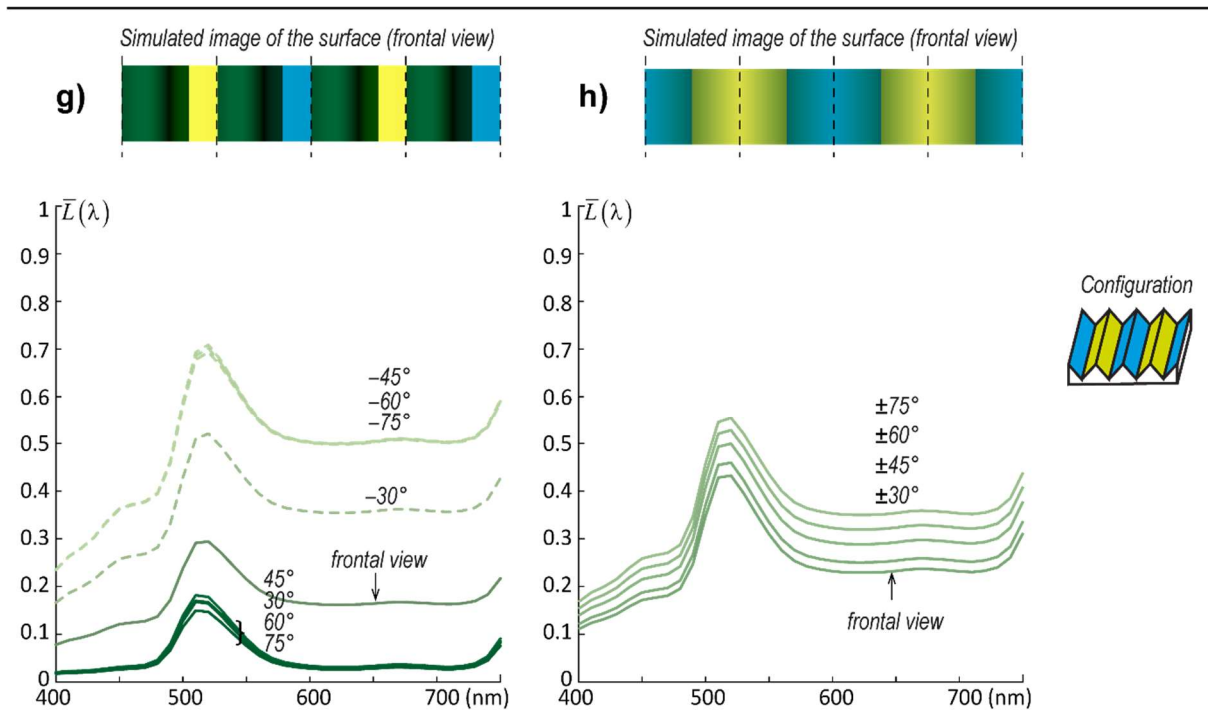
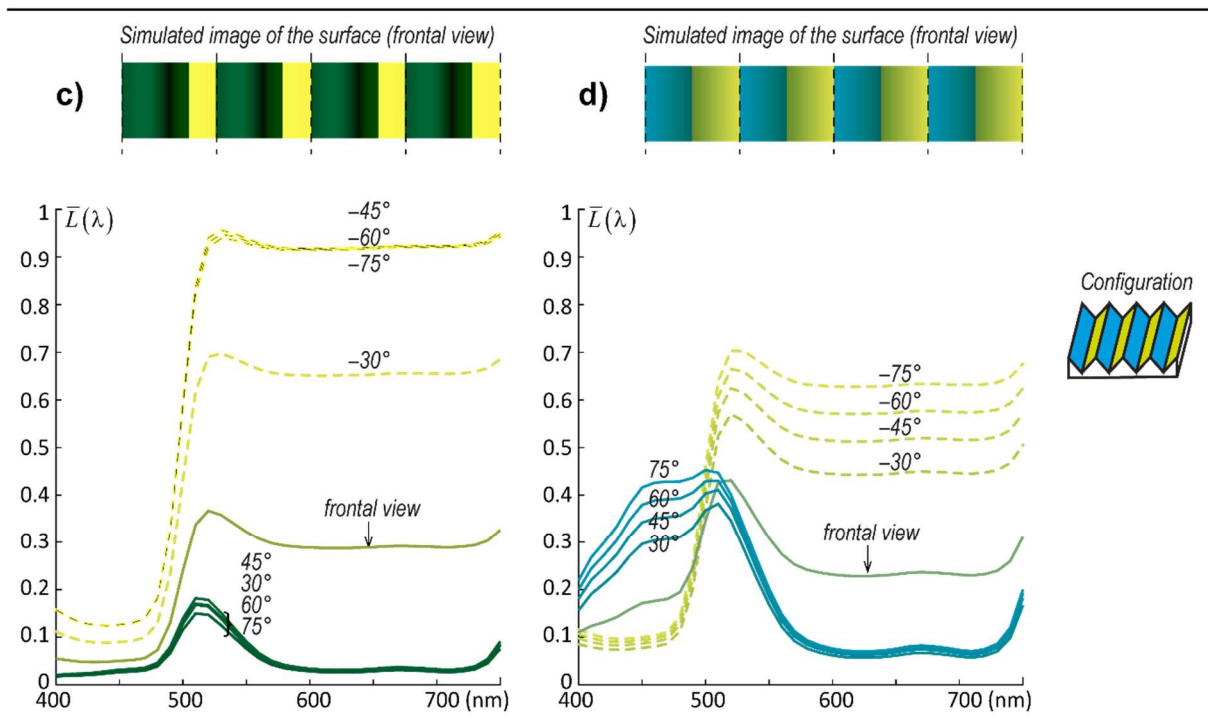


Figure PF3-15 (double page) — Spectral radiances and color previews of structured surfaces with 45° V-shaped ridges whose sides are tinted with two different colored materials always face each other, cyan and yellow, under four types of lighting: frontal (a, e), oblique at $(\theta, \phi) = (45^\circ, 0^\circ)$ (b, f) and $(\theta, \phi) = (-45^\circ, 0^\circ)$ (c, g), and diffuse (d, h). Top row (a, b, c, d): Alternation of cyan and yellow panels: the cyan panel is always on the left of the cavity, therefore the yellow panel on the right.

Oblique (-45°) illumination

Diffuse illumination



Bottom row (e, f, g, h): The cyan panel is alternatively on the left and on the right. In each case, the color preview of the structured surface is presented alongside with the average spectral radiances displayed in various directions of observation with the zenithal angle θ ranging from -75° to $\theta = 75^\circ$ and the azimuthal angle φ being 0° . The spectral corresponding to negative angles are represented with dotted lines, and the ones corresponding to positive angles with a solid line.

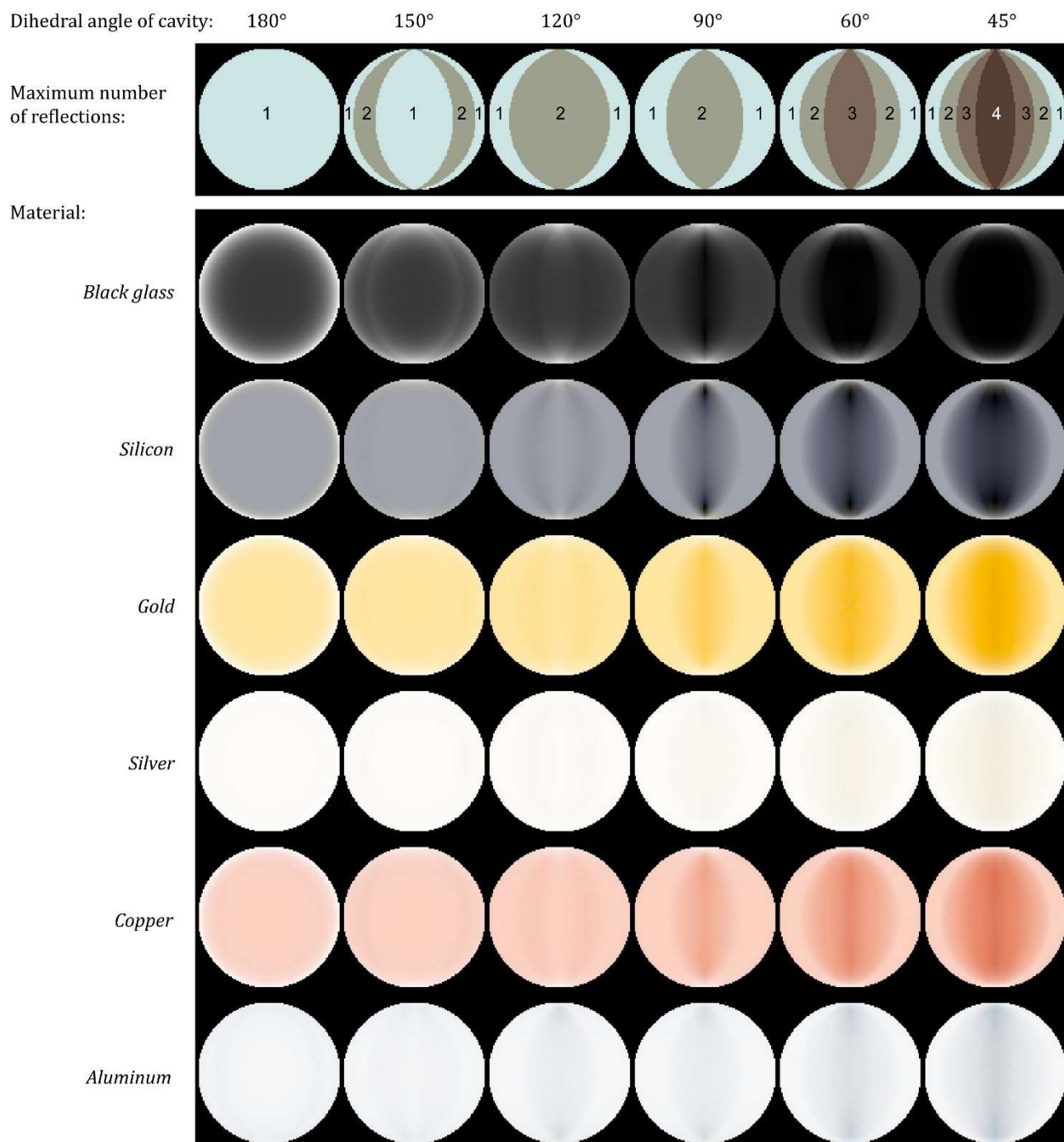


Figure PF4-1 — **Top row:** maps of the maximum number of reflections for each observation direction. **Following rows:** Color maps of hemispherical-directional reflectance for various materials, obtained with different dihedral angle of cavity, represented with the Lambert azimuthal equal area projection.

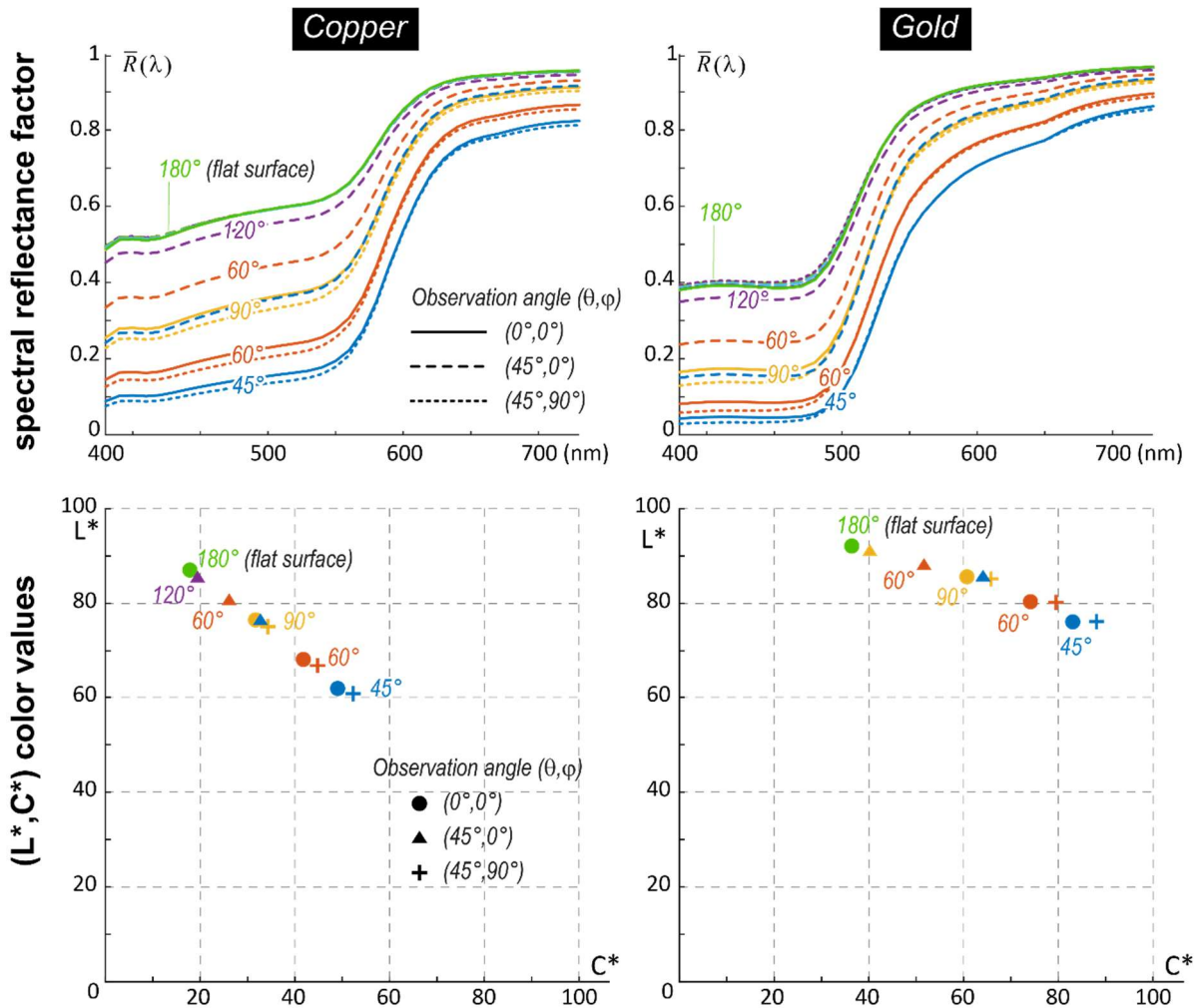


Figure PF4-2 — **Top row:** Average spectral hemispherical-directional reflectance factors displayed by two chromatic metals, copper and gold, for various dihedral angles α of cavities and various observation angles (the lighting is diffuse). **Bottom row:** Corresponding CIE1976 $L^*a^*b^*$ color values projected onto the L^*C^* plane.

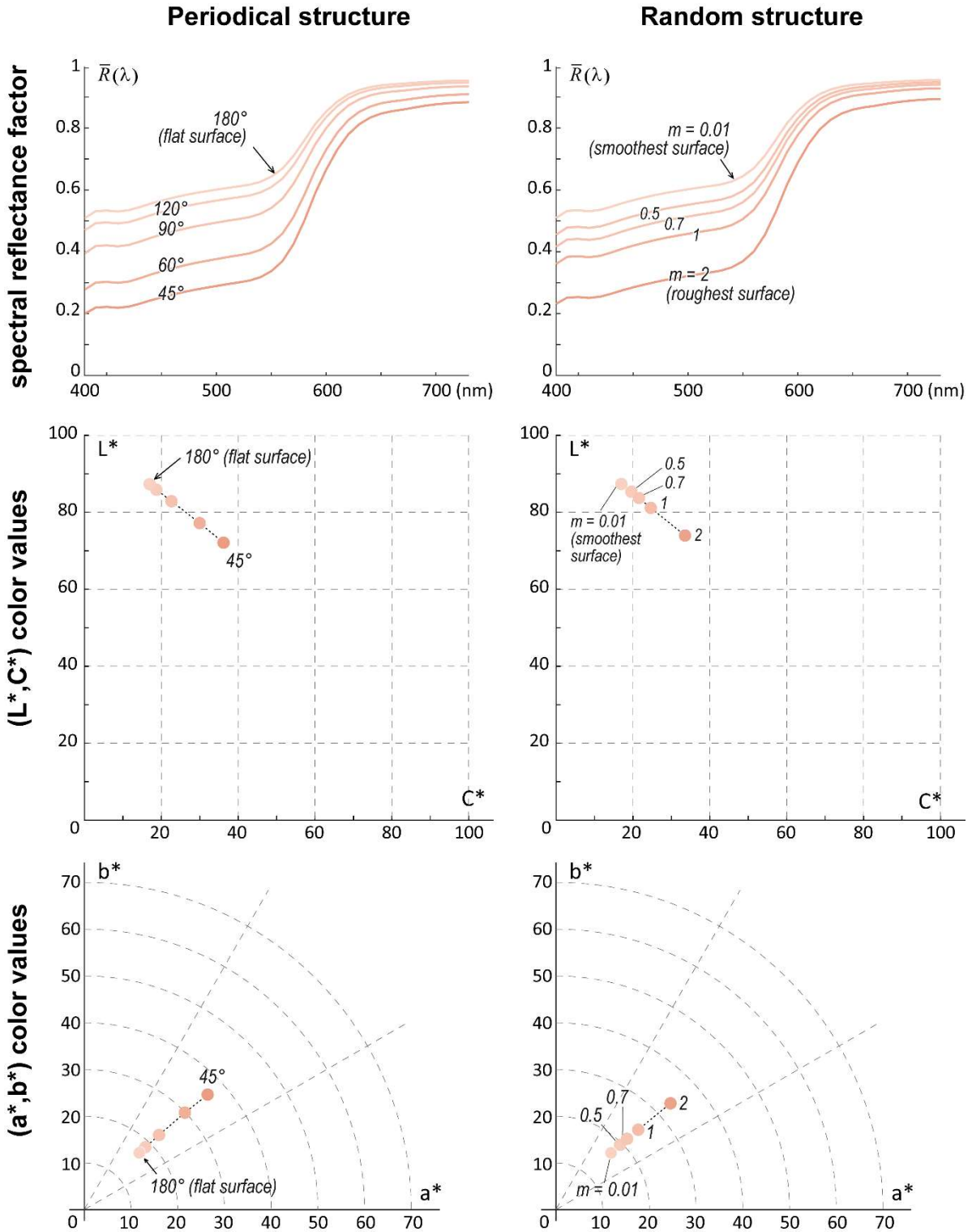


Figure PF4-3 — Average spectral bi-hemispherical reflectances (**top row**), and corresponding CIE1976 $L^*a^*b^*$ color values projected on the L^*C^* plane (**middle row**) and the a^*b^* plane (**bottom row**) of V-ridged surfaces in copper. **Left column:** the ridges are parallel and all similar (periodical structure), the different simulations rely on different dihedral angles α . **Right column:** the ridges are parallel but their dihedral angle is variable and follows a distribution function, parameterized by various roughness values.

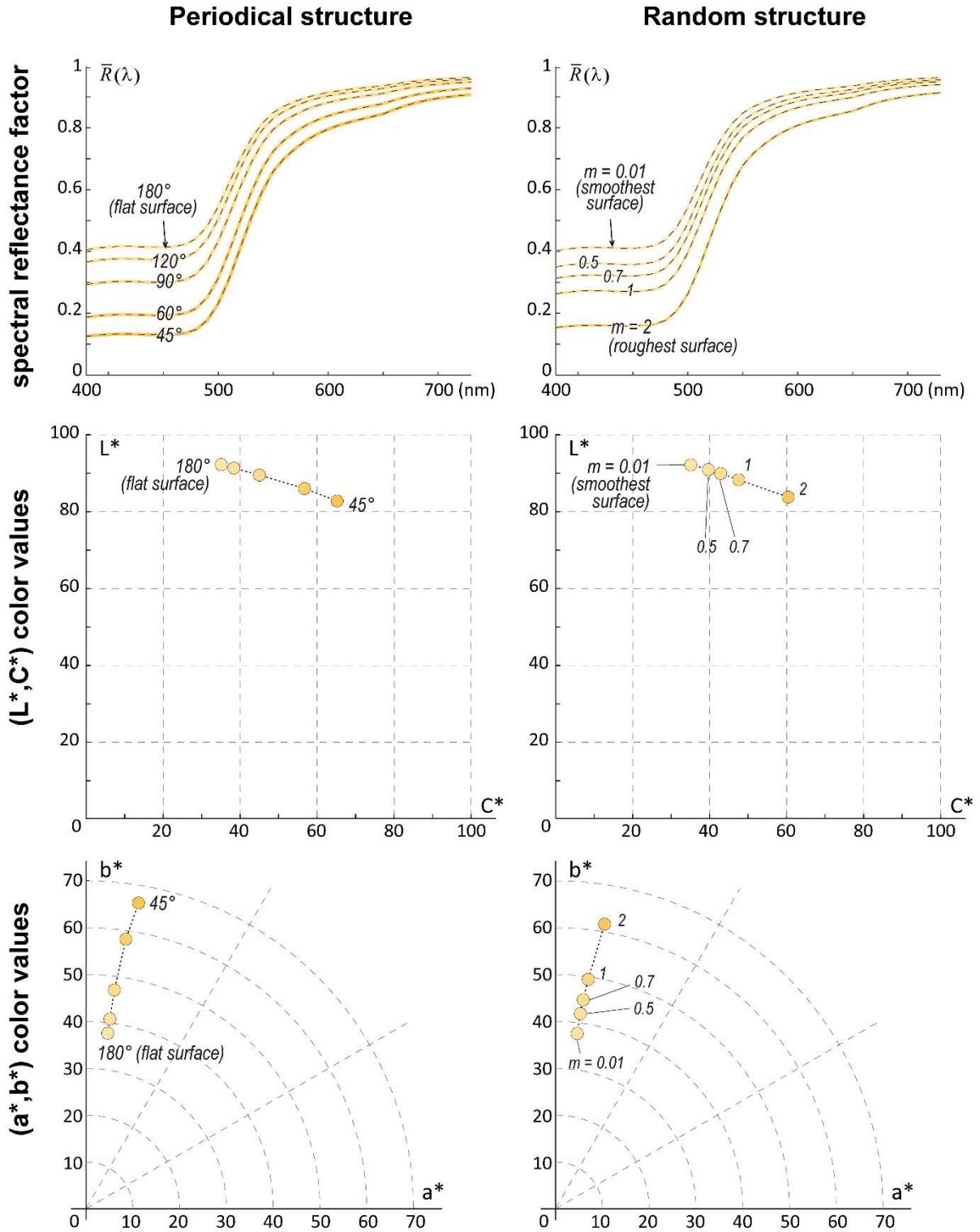


Figure PF4-4 — Average spectral bi-hemispherical reflectances (**top row**), and corresponding CIE1976 $L^*a^*b^*$ color values projected on the L^*C^* plane (**middle row**) and the a^*b^* plane (**bottom row**) of V-ridged surfaces in gold. **Left column:** the ridges are parallel and all similar (periodical structure), the different simulations rely on different dihedral angles α . **Right column:** the ridges are parallel but their dihedral angle is variable and follows a distribution function, parameterized by various roughness values.

Silver

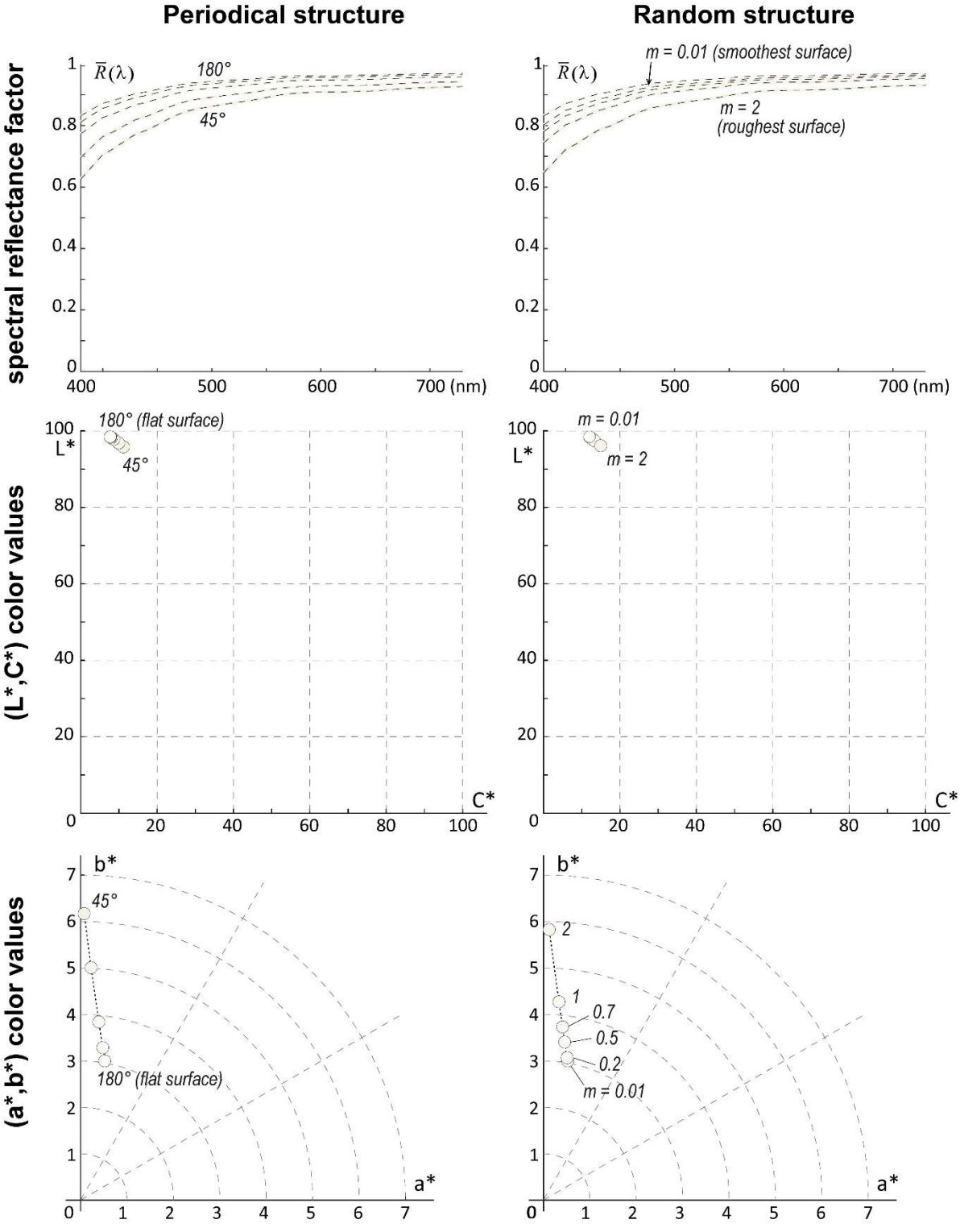


Figure PF4-5 — Average spectral bi-hemispherical reflectances (**top row**), and corresponding CIE1976 L*a*b* color values projected on the L*C* plane (**middle row**) and the a*b* plane (**bottom row**) of V-ridged surfaces in silver. **Left column:** the ridges are parallel and all similar (periodical structure), the different simulations rely on different dihedral angles α . **Right column:** the ridges are parallel but their dihedral angle is variable and follows a distribution function, parameterized by various roughness values.

Aluminum

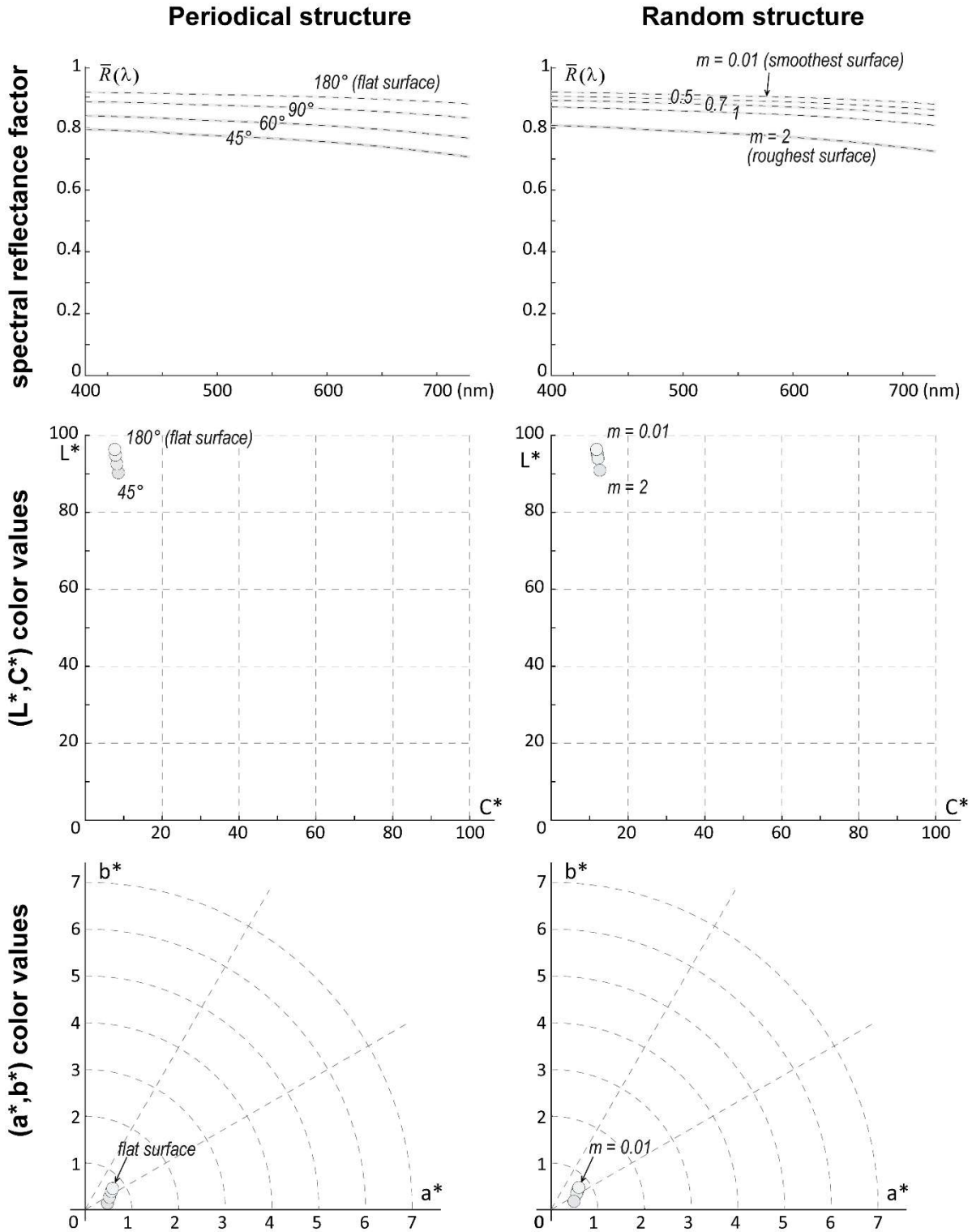


Figure PF4-6 — Average spectral bi-hemispherical reflectances (**top row**), and corresponding CIE1976 $L^*a^*b^*$ color values projected on the L^*C^* plane (**middle row**) and the a^*b^* plane (**bottom row**) of V-ridged surfaces in aluminum. **Left column:** the ridges are parallel and all similar (periodical structure), the different simulations rely on different dihedral angles α . **Right column:** the ridges are parallel but their dihedral angle is variable and follows a distribution function, parameterized by various roughness values.

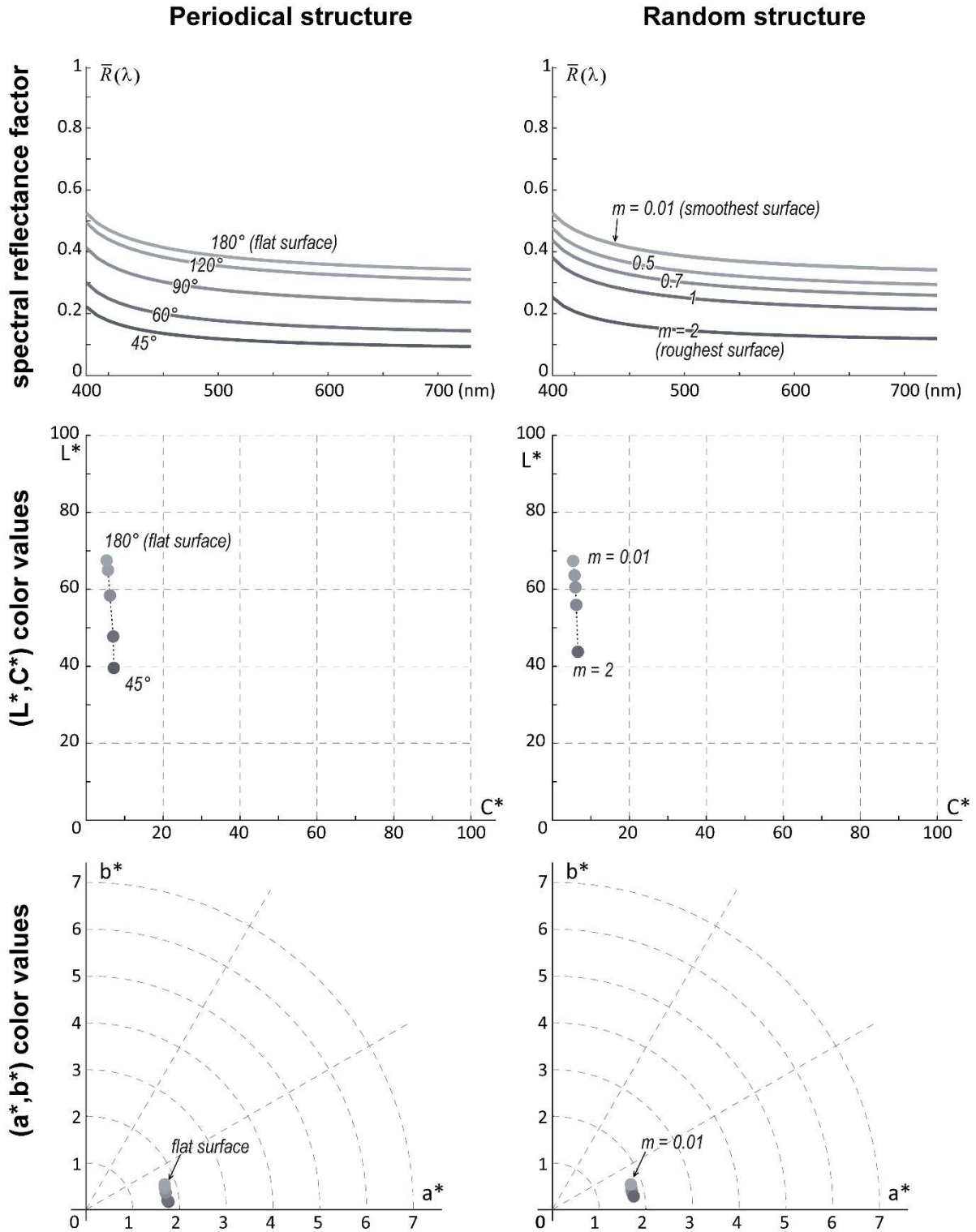


Figure PF4-7 — Average spectral bi-hemispherical reflectances (**top row**), and corresponding CIE1976 $L^*a^*b^*$ color values projected on the L^*C^* plane (**middle row**) and the a^*b^* plane (**bottom row**) of V-ridged surfaces in silicon. **Left column:** the ridges are parallel and all similar (periodical structure), the different simulations rely on different dihedral angles α . **Right column:** the ridges are parallel but their dihedral angle is variable and follows a distribution function, parameterized by various roughness values.

a) $n = 1.5$

(no specular reflection within the cavity)

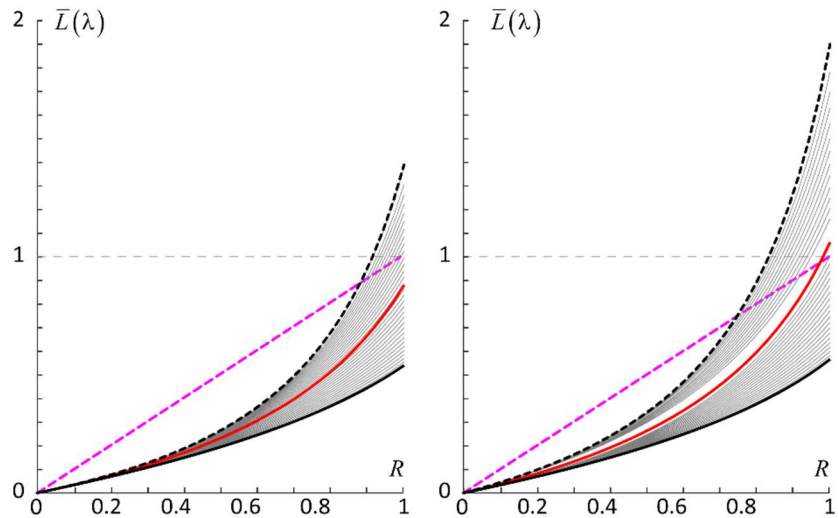
b) $n = 1.5$

Observed radiance vs reflectance R of the flat surface

(Interfaced Lambertian material,
 $\alpha = 45^\circ$,
 frontal view,
 frontal observation).

 n = refractive index

 - - - - - mean radiance from
 flat lambertian surface
 — mean radiance from
 cavity
 - - - - - Radiance from fold
 — Radiance from edges
 — Radiance from other
 facets



Spectral radiance for magenta material

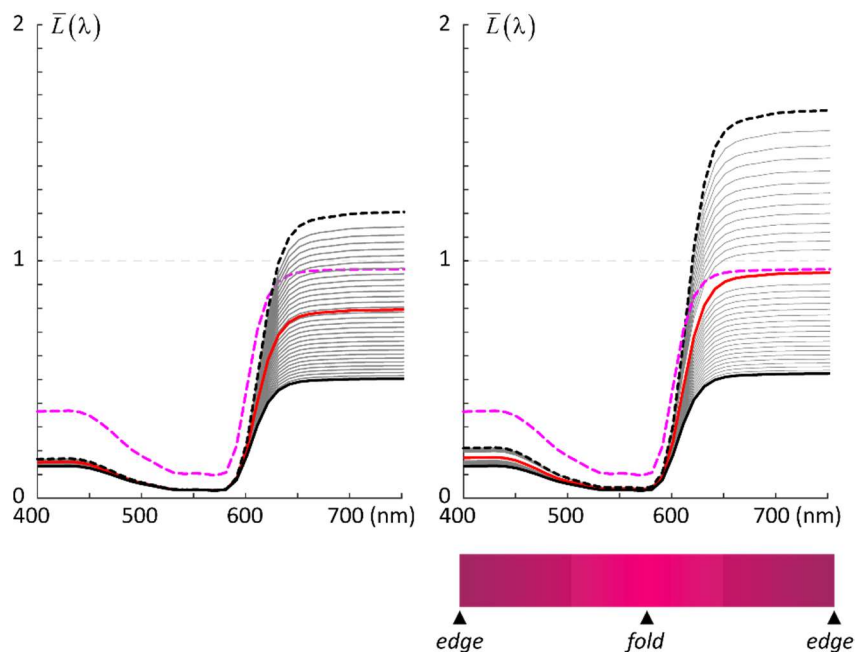
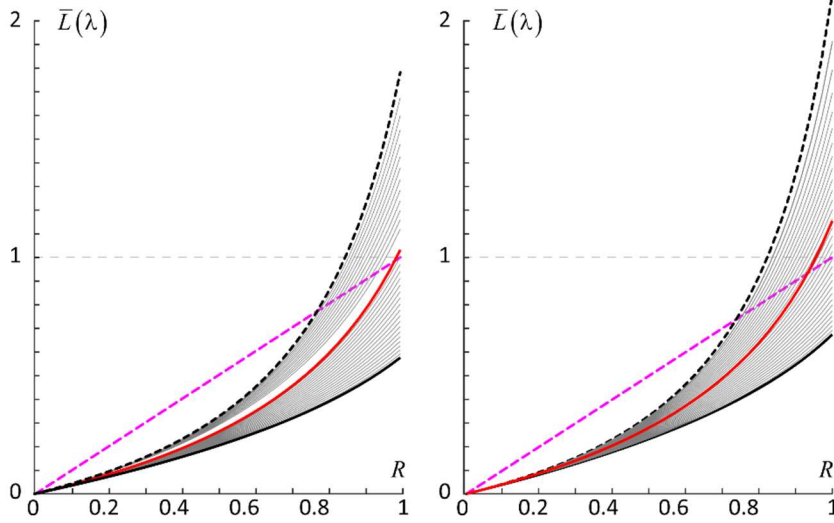


Figure PF5-1 (double page) — Comparison between spectral radiances exhibited by the facets of a 45° V-cavity made of an interfaced Lambertian material, under frontal illumination and frontal view, simulated according to various parameters. **Top row:** variation of the radiances has functions of the reflectance R of the flat surface. **Bottom row:** spectral radiances exhibited by a magenta material; the colored bands below the graphs are a color preview of a band of cavity. The simulations are computed **a)** for a relative refractive index of the interface $n = 1.5$,

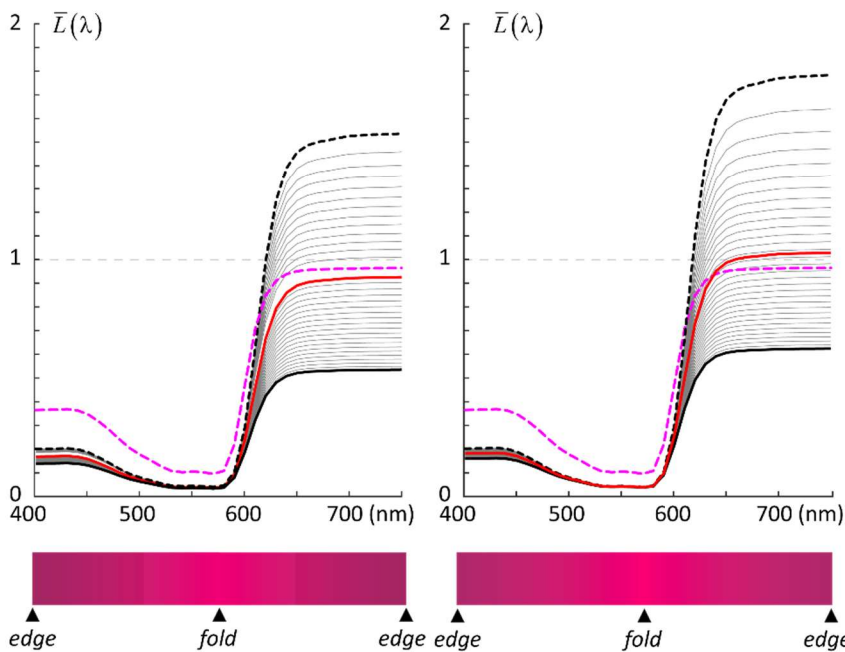
c) $n = 1.33$

d) $n = 1$

Observed radiance vs reflectance R of the flat surface



Spectral radiance for magenta material



by discarding every specular reflection within the cavity, **b)** for a relative refractive index of the interface $n = 1.5$, by taking into account the rays specularly reflected once, as allowed by the model, **c)** for a relative refractive index of the interface $n = 1.33$, with the same model as **b)**, and **d)** for a relative refractive index of the interface $n = 1$, which corresponds exactly to the (non-interfaced) Lambertian surface.

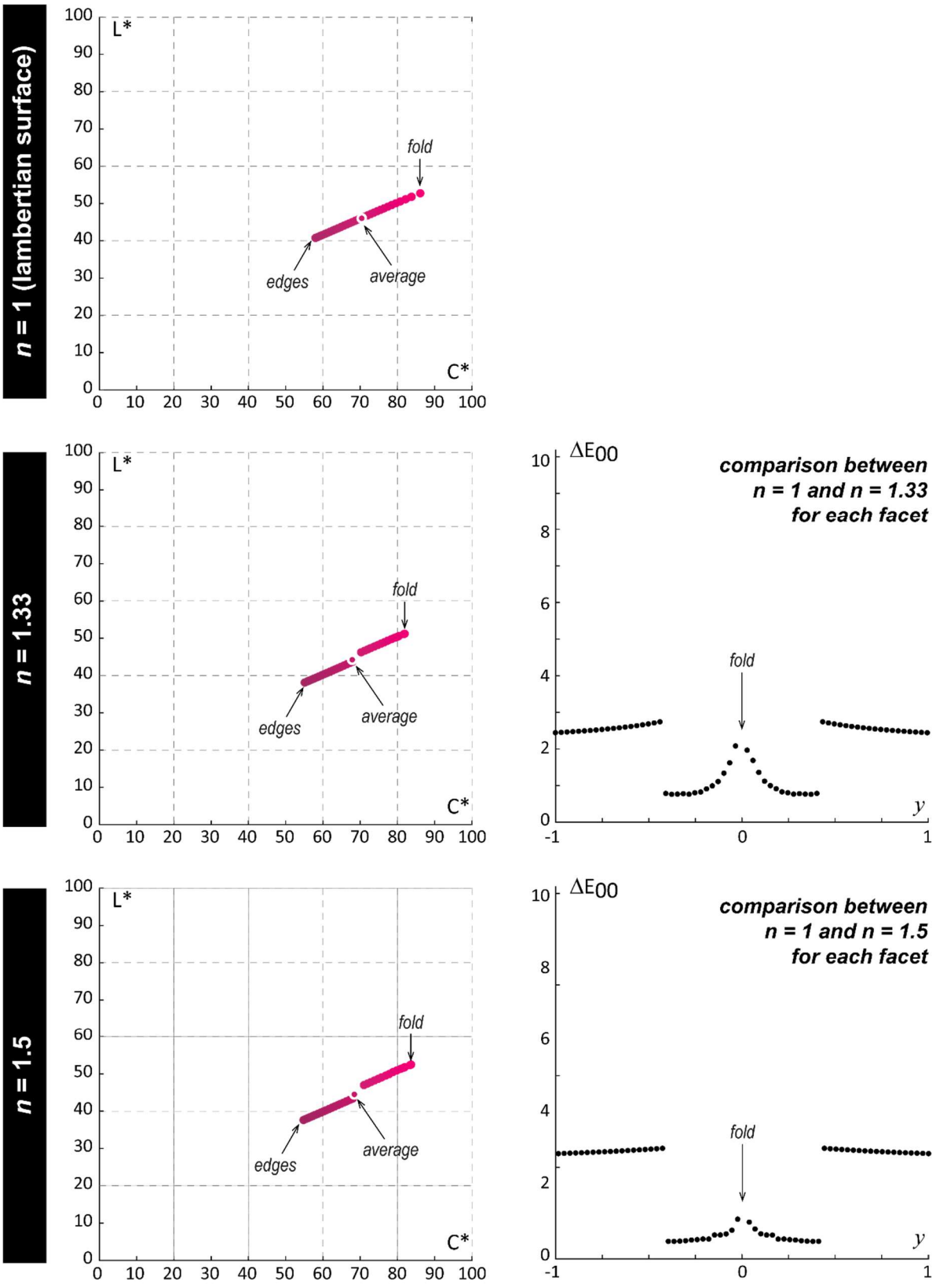


FIG PF5-2 — **Left column:** Projection on the L^*C^* plane of the CIE1976 $L^*a^*b^*$ colors displayed by the facets of an interfaced Lambertian 45° V-cavity made of magenta material when the refractive index is either 1 (**top**, which coincides with a non-interfaced Lambertian cavity), 1.33 (**middle**), or 1.5 (**bottom**). See the corresponding spectral radiances in Figure PF5-1. **Right column:** DE2000 color distance between the colors displayed by a facet when $n = 1$ and $n = 1.33$ (**middle**) or 1.5 (**bottom**), as a function of the facet position y .